Technische Universität München
Fakultät für Elektrotechnik und Informationstechnik

Traction Control via Input-Output Linearization and Stability Analysis using Parametric Lyapunov Functions

Elias Jeremias Virgil Reichensdörfer

Vollständiger Abdruck der von der Fakultät für Elektrotechnik und Informationstechnik der Technischen Universität München zur Erlangung des akademischen Grades eines

Doktors der Ingenieurwissenschaften (Dr.-Ing.)

genehmigten Dissertation.

Vorsitzender: Prof. Dr.-Ing. Wolfgang Utschick

Prüfer der Dissertation:

1. Priv.-Doz. Dr.-Ing. habil. Dirk Wollherr
2. Prof. Dr.-Ing. Naim Bajcinca

Die Dissertation wurde am 10.08.2021 bei der Technischen Universität München eingereicht und durch die Fakultät für Elektrotechnik und Informationstechnik am 28.03.2022 angenommen.

Foreword

This dissertation was created during my work as a doctoral student at BMW AG in the driving dynamics division, department of software based function development in Munich. The research was supervised at the Institute of Automatic Control Engineering, Department of Electrical and Computer Engineering at Technical University of Munich.

First, I thank Priv.-Doz. Dr.-Ing. habil. Dirk Wollherr for supervising this work and for his advice and support throughout this project.

I thank Dr.-Ing. Dirk Odenthal for supervising this work at BMW. Our discussions on traction control systems and his expertise in vehicle dynamics and robust control engineering in general had a significant influence on this work.

In addition, I thank Prof. Dr.-Ing. Naim Bajcinca for his feedback on this dissertation and for accepting to act as a second examiner.

Moreover, I thank M.Sc. Alexander Zech for our various discussion on traction control systems and for sharing his in-depth knowledge on mechanical system modeling.

Special thanks go to M.Sc. Wolfgang Degel and M.Sc. Andreas Meier for the contributions made during their Master theses and internships. I also want to thank M.Sc. Tadeas Sedlacek and M.Sc. Stefan Lupberger for many useful discussions.

Furthermore, I thank Dipl.-Ing. Torsten Müller, Dipl.-Ing. Michael Sailer and Dipl.-Ing. Bernhard Seidl for sharing their experience in embedded software development and their support with experiments and test vehicles. Also, I thank Dipl.-Ing. Marc Espenhain, Dipl.-Ing. Stefan Brandhof and Dr.-Ing. Thomas Eberl for discussions and suggestions regarding the implementation of traction control systems.

Foremost, I thank my family: my parents Katharina and Theo for their continuous support, my brothers and sisters for always creating good mood and my wife Hilda Maria for being helpful, patient and for making every day special.

Munich, December 2020 Elias Reichensdörfer

Abstract

The development of automotive vehicles over the past decades has led to engines with ever increasing power and faster dynamics. This development sets new opportunities for electronic traction control systems as new control designs are required to take advantage of the full potential of modern engines. This work proposes an approach to traction control for automotive vehicles with rear-wheel drive, front-wheel drive or on-demand four-wheel drive based on the method of input-output linearization. Three different control design models are analyzed, that apart from the actuator dynamics, the wheel dynamics and the longitudinal vehicle dynamics, take the torsional dynamics of the drivetrain into account explicitly. Global asymptotic stability of the resulting zero dynamics is shown analytically for the control laws based on these design models. Stability results are derived for the whole class of each design model by using parametric Lyapunov functions. A reformulation of the zero dynamics of the rear-wheel drive design model as a Lur'e system is proposed. It is shown how passivity based methods can be combined with the proposed class of Lyapunov functions to strengthen the results to global exponential stability and input-to-state stability. A heuristic method for Lyapunov function identification based on genetic programming is proposed and its performance is evaluated on three nonlinear example systems. The static control laws for input-output linearization are approximated by dynamic control laws for a robust implementation on the relevant control units. An experimental evaluation with different test vehicles is carried out and a comparison to traditional traction control systems is given. It is shown that the proposed traction control systems achieve better tracking performance, disturbance attenuation and damping of drivetrain oscillations.

Zusammenfassung

Die Entwicklung von Automobilen in den vergangenen Jahrzehnten hat zu Motoren mit stetig steigender Leistung und einem dynamischeren Ansprechverhalten geführt. Dadurch ergeben sich Chancen für die Entwicklung von elektronischen Traktionsregelsystemen, da neue regelungstechnische Ansätze benötigt werden, um das volle Potential von modernen Antrieben zu nutzen. In dieser Arbeit wird ein Ansatz basierend auf Ein-Ausgangs-Linearisierung vorgestellt, der sich auf Kraftfahrzeuge mit Heckantrieb, Frontantrieb oder bedarfsgesteuertem Allradantrieb anwenden lässt. Dafür werden drei verschiedene regelungstechnische Entwurfsmodelle untersucht, welche neben der Aktuatordynamik, der Raddynamik und der Fahrzeuglängsdynamik auch die Torsionsdynamik des Antriebsstrangs abbilden. Es wird globale, asymptotische Stabilität der resultierenden Nulldynamik für Traktionsregler basierend auf diesen Entwurfsmodellen nachgewiesen. Der Nachweis wird jeweils für die ganze Klasse an Entwurfsmodellen mit Hilfe von parametrischen Lyapunov-Funktionen geführt. Eine Umformulierung der Nulldynamik des Entwurfsmodells mit Heckantrieb als Lur'e System wird vorgestellt. Damit wird gezeigt, wie Methoden aus der passivitätsbasierten Regelung mit der zuvor eingeführten Klasse von Lyapunov-Funktionen kombiniert werden können, um exponentielle Stabilität und Input-to-State Stabilität nachzuweisen. Zur Identifikation von Lyapunov-Funktionen wird eine heuristische Methode basierend auf Genetischer Programmierung vorgestellt, deren Leistungsfähigkeit an drei nichtlinearen Beispielsystemen gezeigt wird. Die statischen Regelgesetze zur Ein-Ausgangs-Linearisierung werden durch dynamische Regelgesetze approximiert um eine robuste Implementierung auf den dafür relevanten Steuergeräten sicher zu stellen. Es werden Experimente in Form von Fahrversuchen in verschiedenen Testfahrzeugen und ein Vergleich zu klassischen Traktionsregelsystemen beschrieben. Dabei wird nachgewiesen, dass die vorgestellten Traktionsregelsysteme Verbesserungen bezüglich Führungsverhalten, Störgrößenunterdrückung und bei der Dämpfung von Antriebsstrangschwingungen erreichen.

Contents

Notation

Acronyms

2WD Two-wheel Drive.
4WD Four-wheel Drive.

ABS Anti-lock Braking System.
ASC Anti-slip/skid/spin Control.
ASR Anti-slip/skid/spin Regulation.
AVC Active Vibration Control.

BMW Bayerische Motoren Werke.
BNF Backus-Naur Form.

COG Center of Gravity.

DCU Driving Dynamics Control Unit.
DDFC Direct Driving Force Control.
DFC Driving Force Control.
DOA Domain of Attraction.
DOB Disturbance Observer.
DSC Dynamic Stability Control.

ECU Engine Control Unit.
ESC Electronic Stability Control.
ESP Electronic Stability Program.
ETC Electronic Transfer Case.
EV Electric Vehicle.

FRM Frequency Response Magnitude.
FWD Front-wheel Drive.

GA Genetic Algorithm.
GP Genetic Programming.

HIL Hardware-in-the-Loop.

ICE Internal Combustion Engine.
IFP Input Feed-Forward Passive.
IMC Internal Model Control.
IOL Input-Output-Linearization.
ISS Input-to-State Stable.

KYP Kalman-Yakubovich-Popov.

LMI Linear Matrix Inequality.
LPV Linear Parameter-Varying.
LQR Linear Quadratic Regulator.
LTI Linear Time-Invariant.

MFC Model Following Control.
MIMO Multiple-Input, Multiple-Output.
MPC Model Predictive Control.
MTTE Maximum Transmissible Torque Estimation.
MYC Markus-Yamabe Conjecture.

ODE Ordinary Differential Equation.
OFP Output Feedback Passive.

PD Proportional-Derivative.
PHEV Plug-in Hybrid Electric Vehicle.
PI Proportional-Integral.
PID Proportional-Integral-Derivative.

RCP Rapid Control Prototyping.
RWD Rear-wheel Drive.

SISO Single-Input, Single-Output.
SMC Sliding Mode Control.

TC Traction Control.
TCS Traction Control System.
TUM Technical University of Munich.

VDC Vehicle Dynamics Control.

Conventions

Scalars, Vectors, and Matrices

Scalars are written in italic letters, either in lower case or upper case. Vectors are written in bold italic letters in lower case. Matrices are written in bold italic letters in upper case. Elements of a vector $\boldsymbol{x}$ are denoted by x_i, the elements of a matrix $\boldsymbol{A}$ with A_{ij} for the i-th row, j-th column.

Subscripts and Superscripts

$\dot{x}$	First derivative with respect to time, shorthand for $\mathrm{d}x(t)/(\mathrm{d}t)$.
$\ddot{x}$	Second derivative with respect to time, shorthand for $\mathrm{d}^2x(t)/(\mathrm{d}t^2)$.
$\dot{\boldsymbol{x}}$	Vector of element-wise first derivatives with respect to time.
$\ddot{\boldsymbol{x}}$	Vector of element-wise second derivatives with respect to time.
$\boldsymbol{x}^T$	Transpose of $\boldsymbol{x}$.
$\boldsymbol{A}^{-1}$	Inverse matrix of $\boldsymbol{A}$.
$\boldsymbol{I}_n$	Identity matrix of size $n \times n$.
$\mathbf{1}_n$	Vector of size $n \times 1$ with all entries equal to one.
$\mathbf{0}_n$	Vector of size $n \times 1$ with all entries equal to zero.
$\mathbf{0}_{n\times m}$	Matrix of size $n \times m$ with all entries equal to zero.
$\lambda_i(\boldsymbol{A})$	The i-th eigenvalue of the real-valued square matrix $\boldsymbol{A}$.
$\lambda_{\min}(\boldsymbol{P})$	Minimum eigenvalue of the symmetric real-valued matrix $\boldsymbol{P}$.
$\lambda_{\max}(\boldsymbol{P})$	Maximum eigenvalue of the symmetric real-valued matrix $\boldsymbol{P}$.

Norms

$\lvert x\rvert$	Absolute value of the scalar x.
$\lVert\boldsymbol{x}\rVert$	Arbitrary norm of the vector $\boldsymbol{x}$.
$\lVert\boldsymbol{x}\rVert_2$	Euclidean norm of the vector $\boldsymbol{x}$.
$\lVert\boldsymbol{x}\rVert_\infty$	Maximum norm of the vector $\boldsymbol{x}$.
$\lVert\boldsymbol{L}\rVert_F$	Frobenius norm of the matrix $\boldsymbol{L}$.

Sets

$\mathbb{N}$	Natural numbers.
$\mathbb{N}_0$	Natural numbers including zero.
$\mathbb{R}$	Real numbers.
$\mathbb{R}^+$	Positive Real numbers.
$\mathbb{R}_0^+$	Positive Real numbers including zero.
$\mathbb{C}$	Complex numbers.
C^k	Set of k-times differentiable functions.
$\mathcal{K}$	Set of class $\mathcal{K}$ functions.
$\mathcal{K}_\infty$	Set of class $\mathcal{K}_\infty$ functions.
$\mathcal{KL}$	Set of class $\mathcal{KL}$ functions.
$\mathcal{D}$	Domain of attraction of a dynamical system.
Ω	Subset of the state space satisfying Lyapunov conditions.
Ω_c	Subset of the domain of attraction.
$\mathcal{N}$	Nonterminals of a context free grammar.
Σ	Terminals of a context free grammar.
$\mathcal{P}$	Production rules of a context free grammar.
$\emptyset$	Empty set.

Symbols

Main Symbols for General Control Systems

t	Time.
$\boldsymbol{x}$	State vector of dimension $n \times 1$.
$\boldsymbol{u}$	Input vector of dimension $m \times 1$.
$\boldsymbol{y}$	Output vector of dimension $p \times 1$.
$\boldsymbol{f}$	Vector field of the system.
$\boldsymbol{h}$	Measurement functions of the system.

Main Symbols for Traction Control

a_0	Reference model coefficient for weighting angular velocity.
a_1	Reference model coefficient for weighting angular acceleration.
A_{st}	Vehicle frontal area.
a_x	Longitudinal acceleration of the vehicle.
a_y	Lateral acceleration of the vehicle.
b_0	Reference model coefficient for weighting outer controller.
B_f	Pacejka stiffness factor of the front axle tires.
B_r	Pacejka stiffness factor of the rear axle tires.
C_f	Pacejka shape factor of the front axle tires.
C_r	Pacejka shape factor of the rear axle tires.
c_w	Aerodynamic drag coefficient.
c_{xf}	Longitudinal slip stiffness of the front axle tires.
$\underline{c}_{xf}$	Lower bound for the longitudinal slip stiffness of the front wheels.
$\bar{c}_{xf}$	Upper bound for the longitudinal slip stiffness of the front wheels.
c_{xr}	Longitudinal slip stiffness of the rear axle tires.
$\underline{c}_{xr}$	Lower bound for the longitudinal slip stiffness of the rear wheels.
$\bar{c}_{xr}$	Upper bound for the longitudinal slip stiffness of the rear wheels.
d_c	Aggregated drivetrain torsional damping constant (rear).
d_e	Aggregated drivetrain torsional damping constant (front).
$\Delta\phi_c$	Twist angle between crankshaft and rear axle.
$\Delta\phi_e$	Twist angle between electronic transfer case and front axle.
e_1	Control error for the first controlled system output.
e_2	Control error for the second controlled system output.
ϵ	Smoothing parameter for normalization speed.
F_w	Aerodynamic drag force.
F_{xf}	Friction force between front axle tires and road.
$F_{xf,0}$	Front tires friction force at zero front axle angular velocity.
F_{xr}	Friction force between rear axle tires and road.
F_{zf}	Normal force on the front axle.
F_{zr}	Normal force on the rear axle.
g	Gravitational acceleration.
i_a	Gear ratio of the automatic transmission case.
i_E	Total gear ratio between main engine and front axle.
i_f	Gear ratio of the front axle differential.
i_G	Total gear ratio between main engine and rear axle.
i_r	Gear ratio of the rear axle differential.
J_c	Aggregated moment of inertia of the drive side.
J_e	Aggregated moment of inertia of the electronic transfer case.

J_{eq}	Equivalent rotational inertia of the rear axle as a function of wheel slip.
J_f	Front axle moment of inertia.
J_r	Rear axle moment of inertia.
k_c	Aggregated drivetrain torsional stiffness (rear).
k_d	Derivative gain of proportional-integral-derivative (PID) controller.
k_e	Aggregated drivetrain torsional stiffness (front).
k_i	Integral gain of PID controller.
k_p	Proportional gain of PID controller.
l_f	Distance from the front axle to the center of gravity of the vehicle.
l_r	Distance from the rear axle to the center of gravity of the vehicle.
λ_{xf}	Average wheel slip of the front axle wheels.
$\lambda_{xf,d}$	Target wheel slip for the front axle.
$\lambda^{+}_{xf,\text{peak}}$	Wheel slip at which the front tires attain the positive peak tire force.
$\lambda^{-}_{xf,\text{peak}}$	Wheel slip at which the front tires attain the negative peak tire force.
λ_{xr}	Average wheel slip of the rear axle wheels.
$\lambda_{xr,c}$	Slip calculated with crankshaft instead rear axle angular velocity.
$\lambda_{xr,d}$	Target wheel slip for the rear axle.
$\lambda^{+}_{xr,\text{peak}}$	Wheel slip at which the rear tires attain the positive peak tire force.
$\lambda^{-}_{xr,\text{peak}}$	Wheel slip at which the rear tires attain the negative peak tire force.
m	Vehicle mass.
$\mathcal{M}_5$	Synthesis model of 5-th order for vehicles with two-wheel drive.
$\mathcal{M}_7$	Synthesis model of 7-th order for vehicles with four-wheel drive.
$\mathcal{M}_9$	Synthesis model of 9-th order for vehicles with four-wheel drive.
μ	Coefficient of friction between tire and driving surface.
$\mu_{\max}$	Upper bound for the friction coefficient.
$\mu_{\min}$	Lower bound for the friction coefficient.
ω_c	Crankshaft angular velocity.
$\omega_{c,d}$	Target angular velocity of the crankshaft, scaled to wheel level.
ω_e	Electronic transfer case output speed.
ω_f	Front axle angular velocity.
ω_r	Rear axle angular velocity.
$\omega^{+}_{r,\text{peak}}$	Optimal rear axle speed with respect to traction.
r_1	Target speed for the first system output.
r_2	Target speed for the second system output.
r_f	Radius of the front axle wheels.
r_r	Radius of the rear axle wheels.
ρ	Air density.
σ_a	Boolean signal indicating controller active status.
σ_s	Boolean signal indicating controller saturation.
T_{driver}	Requested drive torque by the driver.
T_e	Electronic transfer case torque.
$T_{e,d}$	Desired electronic transfer case torque.
T_f	Drive torque of a single front wheel.
T_m	Main engine torque.
$T_{m,d}$	Desired main engine torque.
T_r	Drive torque of a single rear wheel.
τ_d	Filter time constant of PID controller.
τ_e	Time constant of electric motor for electronic transfer case.
τ_m	Motor time constant
$\tau_{m,d}$	Time delay of the main engine.

τ_s	Sample time of the traction control system.
$\widetilde{u}_1$	Arbitrated control signal between driver and traction control system.
$\bar{u}_1$	Saturated control signal.
u_1	First control input of the control design models, equal to $T_{m,d}$.
$u_{1,d}$	Portion of the first control input generated by the drivetrain torsion.
u_2	Second control input of the traction control system, equal to $T_{e,d}$.
v_0^*	Minimum value of the smoothed normalization speed.
v_1	Output signal of the reference model corresponding to the first output.
v_2	Output signal of the reference model corresponding to the second output.
v_{nf}	Smoothed normalization speed of the front axle.
v_{nr}	Smoothed normalization speed of the rear axle.
v_x	Longitudinal vehicle velocity (speed when focus is on forward drive).
w_1	Output signal of the PID controller for the first output.
w_2	Output signal of the PID controller for the second output.
x_1	Main engine torque, equal to T_m.
x_2	Twist angle between crankshaft and rear axle, equal to $\Delta\phi_c$.
x_3	Crankshaft angular velocity, equal to ω_c.
x_4	Rear axle angular velocity, equal to ω_r.
x_5	Longitudinal vehicle velocity, equal to v_x.
x_6	Electronic transfer case torque, equal to T_e.
x_7	Front axle angular velocity, equal to ω_f.
x_8	Twist angle between electronic transfer case and front axle, equal to $\Delta\phi_e$.
x_9	Electronic transfer case output speed, equal to ω_e.
y_1	First output, equal to ω_c/i_G.
y_2	Second output, for the $\mathcal{M}_7$ model $y_2 = \omega_f$, for the $\mathcal{M}_9$ model $y_2 = \omega_e/i_f$.

Main Symbols for Genetic Programming

C	Ephemeral random constant for generation of expressions.
F	Fitness value.
$\mathcal{G}$	Context free grammar.
k_{node}	Factor for scaling the maximum number of expression nodes.
$\mathcal{S}$	Start symbol of a context free grammar.
N_{node}	Maximum number of nodes per expression.
N_s	Maximum number of stages per fitness computation.
N_x	Number of state space samples per stage.
$\boldsymbol{X}_s$	Matrix of size $(2N_xN_s) \times n$ with state space samples.

Additional Matrix-related Symbols

$\det(\boldsymbol{A})$	Determinant of the square matrix $\boldsymbol{A}$.
$\operatorname{diag}(a_1, \ldots, a_n)$	Diagonal matrix of size $n \times n$ with diagonal entries $a_1, \ldots, a_n$.
$\boldsymbol{H}_V(\boldsymbol{x})$	Hessian matrix of $V(\boldsymbol{x})$ evaluated at $\boldsymbol{x}$.
$\boldsymbol{J}_{\boldsymbol{f},\boldsymbol{x}}(\boldsymbol{x}^*, \boldsymbol{u}^*)$	Jacobian of $\boldsymbol{f}(\boldsymbol{x}, \boldsymbol{u})$ with respect to $\boldsymbol{x}$ evaluated at $\boldsymbol{x} = \boldsymbol{x}^*$, $\boldsymbol{u} = \boldsymbol{u}^*$.
$\operatorname{rank}(\boldsymbol{A})$	Rank of the square matrix $\boldsymbol{A}$.

Miscellaneous Symbols

$\circ\!\!-\!\!\bullet$	Laplace transform.
$\Re(s)$	Real part of the complex variable s.
$\operatorname{sec}[\boldsymbol{K}_1, \boldsymbol{K}_2]$	Stability sector.

List of Figures

List of Tables

1 Introduction

1.1 Motivation

Traction control systems (TCSs) are an important part of electronic stability control systems of automotive vehicles. Such control systems are very effective at reducing traffic accidents [178] and, according to the World Health Organization, the most important regulation of the United Nations for crash avoidance by preventing traffic accidents is the regulation on electronic stability control [281, p. 47]. Besides improving drivability and overall driving stability, modern TCSs also increase acceleration performance and improve driving comfort by dampening drivetrain oscillations. TCSs achieve this by constantly monitoring and evaluating the current driving situation and the wheel speeds. When a critical situation is detected, namely the wheels start to spin, the requested drive torque from the driver is reduced by the TCS in order to maximize the transmitted traction force between the tires and the driving surface.

While TCSs have existed for decades, they received increasing interest in the past years, which can be explained by the development of electric motors and modern, highly supercharged combustion engines with continuously increasing power, responsiveness and high dynamics. These conditions offer opportunities for control design, as new approaches are required to make full use of the powerful new generation of actuators. The present work is a contribution in this direction and studies a control architecture where the speed control loop of the TCS is partitioned directly on the engine control unit (ECU), not on the driving dynamics control unit (DCU) as in traditional TCSs. This can be advantageous, as it reduces time delay due to asynchronous communication of different control units and thereby, increases bandwidth of the closed loop system. One of the main challenges for the control design itself is the nonlinearity of the forces transmitted by the tires. We approach this problem by an analytic control design based on the method of input-output-linearization (IOL) for controlling the wheel slip and drivetrain dynamics. In order to cover both vehicles with two-wheel drive (2WD) and vehicles with on-demand four-wheel drive (4WD) torque bias systems using an electronic transfer case (ETC), the IOL based control design is carried out for three different control design models, which explicitly model the torsional dynamics of the drivetrain.

For safety-critical systems like TCSs, a formal stability analysis followed by an experimental evaluation which confirms the theoretical analysis is essential. We prove stability analytically for TCSs based on the exact IOL of wheel slip and drivetrain dynamics for vehicles with 2WD and 4WD in order to show that the overall structure of the control designs is suitable for the task from a theoretical perspective. Parts of the static control laws for IOL are approximated with high pass filters, in order to enable a robust implementation for the available sensor setup on a microprocessor. The 2WD control design and one of the 4WD control designs are evaluated in test vehicles on different maneuvers to evaluate their practical performance and demonstrate stability and robustness also for a real-world implementation experimentally.

The stability analysis of the zero dynamics resulting from the IOL of the single-input, single-output (SISO) 2WD also raises further questions. Since the zero dynamics can be reformulated as a third order multiple-input, multiple-output (MIMO) Lur'e system with two inputs and two outputs, the question arises whether the Markus-Yamabe conjecture (MYC), while false in general, might be true for this system class. Two methods are derived to analyze existing counterexamples to the MYC, showing that this question remains open. In the following, the research contributions are listed and the structure of this work is stated.

1.2 Contributions and Outline

The main research contributions of this work can be summarized as follows.

1. TCS designs for vehicles with 2WD and on-demand 4WD torque bias systems by IOL.
2. Proof of global, exponential stability of the resulting class of time-variant zero dynamics.
3. Proof of input-to-state stability of the resulting class of time-variant internal dynamics.
4. A passivity based analysis using a Lur'e system reformulation of the 2WD zero dynamics.
5. Analysis of this Lur'e system in the context of the Kalman conjecture and the MYC.
6. Methods for input/output dimension analysis of Lur'e systems.
7. Application of genetic programming (GP) for Lyapunov functions synthesis to TCSs.
8. Comparison in the frequency domain of the IOL based control design with PID control.
9. Experimental validation of the control designs in different test vehicles.

Items 1-3 describe results from the control design and stability analysis of the TCSs. Items 4-6 summarize findings from a Lur'e formulation of the 2WD zero dynamics. Item 7 describes the first application of GP to Lyapunov function synthesis for the zero dynamics of a TCS with torsional drivetrain dynamics. Items 8 and 9 provide an analysis and experimental validation of the IOL based TCSs. The remainder of this dissertation is organized as follows.

Chapter 2 gives an introduction to traction control systems and an overview of the current state of the art. The focus is set on the control design perspective and the most commonly used control design methods for TCSs are reviewed. The architectures of DCU based and ECU based traction control are discussed and the gap in the state of the art addressed in this work is derived. Furthermore, some preliminaries on control theory and optimization with GP are presented.

Chapter 3 presents TCSs for vehicles with 2WD and on-demand 4WD torque bias systems based on IOL of three different design models, considering the torsional dynamics of the drivetrain explicitly. A method to parameterize the reference dynamics of the TCS based on a reduced model is presented. We derive classes of parametric Lyapunov functions for the resulting zero dynamics and show global asymptotic stability for all vehicle parameters and time-varying, bounded friction coefficients. Also, details for a practical implementation of the TCSs are given.

Chapter 4 presents a reformulation of the zero dynamics of the 2WD TCS in Lur'e system form. Passivity based methods are then combined with the class of parametric Lyapunov functions from Chapter 3 to show global exponential stability of the zero dynamics and input-to-state stability of the internal dynamics of the TCS. This analysis raises the question whether the MYC is true for third order systems with two inputs and two outputs. We propose two methods for testing if the input or output dimension of a Lur'e system is reducible and apply them to existing counterexamples to the MYC, leading to a new open question.

Chapter 5 presents a novel heuristic method for Lyapunov function identification based on the optimization method of GP. The method is applied to two benchmark systems and the zero dynamics of the 2WD TCS. It is demonstrated that the method is able to find a valid Lyapunov function for the two benchmark systems and that it is able to approximate a valid Lyapunov function for the zero dynamics of the 2WD TCS.

Chapter 6 starts with an experimental validation of the 2WD design model. Following, a benchmark PID controller is designed which is used for a comparison with the IOL based TCS, based on a frequency domain analysis. Moreover, the TCS is analyzed with respect to tracking performance and disturbance attenuation. Thereafter, an experimental evaluation of the 2WD and 4WD TCSs in different test vehicles is presented. Also, a comparison of the proposed TCS with a DCU based TCS and an ECU based benchmark TCS is included.

Chapter 7 summarizes and discusses the results of this work. Based on the discussed findings, a conclusion is drawn and an outlook for future work is given.

In the following, an overview of the state of the art of traction control and a review of different control design methods that have been proposed in literature for TCSs is given.

2 State of the Art

Summary. *This chapter gives an overview of the field of traction control in terms of control architectures and control methods. Open questions and problems of existing solutions are discussed and the identified research gap is derived. Moreover, the required preliminaries on control theory and genetic programming are summarized.*

2.1 Traction Control Systems

2.1.1 Fundamentals of Traction Control Systems

Traction control systems have the goal of improving driving stability, performance and comfort. The reason for the need of TCSs is, that the torque that can be transmitted to the road is limited by the friction force between the tires and the road. The motor torque, which is requested by the driver by actuating the throttle, however, is practically independent of road conditions. Hence, if the driver requests significantly more drive torque than is transmittable to the road, the remaining torque will accelerate the wheels disproportionately to the vehicle speed and so the wheels will start to spin. This is potentially dangerous, as spinning wheels also reduce transmittable forces in lateral direction and therefore decrease steerability of the vehicle, which can result in accidents. In longitudinal direction, spinning wheels reduce the force transmitted to the road as well, such that on a slippery road with low friction coefficient, the force might be even too low for driveaway, but at least will deteriorate acceleration performance. Finally, spinning wheels will also affect driving comfort in a negative way, while mechanical stress might damage drivetrain components in the long term. Therefore, it is important to control the drive torque to an appropriate level, that takes road conditions into consideration. Even experienced drivers cannot do this as efficiently and reliable as when electronically controlled, which is the task of TCSs. To understand the basic physical characteristics of TCSs, we first analyze the fundamental dynamics and properties of the tire-road contact in a control oriented way.

In the state of the art, the most common synthesis model used for control design is the 2-state model, which includes the angular velocity ω_r of a single wheel (or an axle)[1] and the longitudinal speed of the vehicle, v_x. Reduced to the most essential relations, the longitudinal dynamics during acceleration in forward direction can be expressed by, cf. [142, 266],

$$J_r\dot{\omega_r} = T_m i_G - r_r F_{xr}(\lambda_{xr}, \mu) \tag{2.1a}$$

$$m\dot{v}_x = F_{xr}(\lambda_{xr}, \mu) - F_w(v_x) \tag{2.1b}$$

$$\lambda_{xr} = (r_r\omega_r - v_x)/(r_r\omega_r)\,, \text{ with } r_r\omega_r \geq v_x > 0. \tag{2.1c}$$

Here, T_m is the motor torque applied to the rear axle[2] with inertia J_r and total gear ratio i_G, F_{xr} is the tire force transmitted to the driving surface with friction coefficient μ, while λ_{xr} denotes the longitudinal wheel slip and $F_w = (1/2)\rho c_w A_{st} v_x|v_x|$ the aerodynamic drag force[3].

[1] Some publications consider a quarter car model [112, 113], others a half-car model [302, 307]. The 2-state model is suitable for both cases and the choice mainly depends on whether a traditional drivetrain with a driven axle of in-wheel motors for each wheel are used.

[2] Here, we assume a vehicle with rear-wheel drive. The model however is analogously applicable to vehicles with front-wheel drive.

[3] Some publications consider only a relatively low vehicle speed, such that $F_w \approx 0$, so the aerodynamic drag force can be neglected [71, 210]. Other publications include additional loss terms, like rolling resistance or grade resistance [36, 93, 205]. However, the basic principles remain the same despite of these variations.

Moreover, m is the vehicle mass, r_r the rear wheel radius, ρ the air density, c_w the aerodynamic drag coefficient and A_{st} the vehicle frontal area, compare [83, pp. 97–100]. An explicit formula for F_{xr} will be given later, as it is not required to describe the basic dynamical behavior of TCSs. To analyze some properties of the 2-state model and the tire-road contact, a descriptive example maneuver, displayed in Figure 2.1, is worked through in detail in the following.

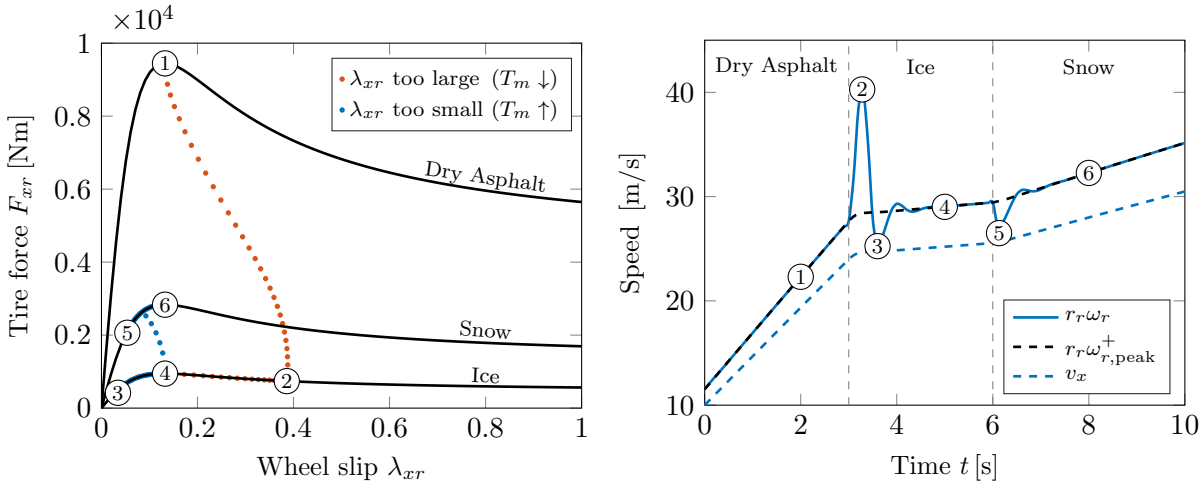

(a) Nonlinear friction force.

(b) Wheel speed and vehicle speed.

Figure 2.1: Connection between tire force, drive torque, wheel speed, vehicle speed and wheel slip.

The main nonlinearity of the plant (2.1) is the friction force F_{xr}, which is transmitted to the road by the lever arm of the contact patch that is formed by the vertical load of the vehicle on the pneumatic rubber tires. This force depends primarily on the tire parameters, the normal force on the tire, the road conditions and the wheel slip [128, pp. 17–20], which is the relative difference between translatory and angular velocity of the wheel [200, pp. 19–32]. Figure 2.1a shows a model representation of this force as a function of wheel slip, for three different types of friction coefficients (dry asphalt, snow and ice), using the Pacejka tire model [219]. As can be seen in Figure 2.1a, the tire force has a maximum at $\lambda^+_{xr,\text{peak}} \approx 0.15$, so maximum longitudinal traction is achieved if $\lambda_{xr} = \lambda^+_{xr,\text{peak}}$. Figure 2.1b shows an example longitudinal maneuver, starting at $v_x = 10\,\text{m/s}$ on dry asphalt. The dashed blue line shows the vehicle speed v_x, the solid blue line the wheel speed ω_r, converted to m/s via the rear tire radius r_r. Finally, the dashed black line denotes the optimal wheel speed $\omega^+_{r,\text{peak}}$ in m/s, corresponding to the maximum of the tire friction curve, calculated by solving (2.1c) for ω_r and inserting $\lambda^+_{xr,\text{peak}}$ for λ_{xr}.

At the beginning of the example maneuver, from $t = 0$ to $3\,\text{s}$, indicated by ①, the wheel speed is at its optimum value (solid blue and dashed black line coincide), so the maximum tire force is achieved as the ① in Figure 2.1a shows. The motor torque T_m is just right in this phase and therefore, the achieved traction and acceleration is at maximum. At $t = 3\,\text{s}$, the underground changes from dry asphalt to ice (in this example, μ is rate limited to ± 3 units per second), so the previously optimal motor torque T_m is now too large, which leads to significant overshoot of ω_r, at point ②, corresponding to a wheel slip $\lambda_{xr} \approx 0.4$. Figure 2.1b also shows the trajectory of the tire force on the force curves as dotted curve. By reducing the motor torque appropriately ($T_m \downarrow$), after an undershoot at point ③, the optimal operating point is restored approximately at ④. At $t = 6\,\text{s}$, the friction coefficient increases again, as the underground changes from ice to snow. Consequently, the motor torque T_m is now too small, leading to an undershoot at point ⑤. After increasing the motor torque again ($T_m \uparrow$), the desired operating point is restored again at $t \approx 8\,\text{s}$, indicated with ⑥. This is basically how TCSs operate and how the fundamental dynamics of the tire-road contact during acceleration are connected with each other.

In practice, many other things have to be considered and, for example, calculating the optimal wheel slip, or wheel speed, respectively, cannot be done just by maximizing F_{xr}. As an example for the generation of the optimal setpoint, lateral acceleration due to steering, as well as uncertainties of tire and vehicle parameters or additional environmental conditions, like road inclination or side wind gust, have to be taken into account, among other effects. However, the term TCS here refers to the control of wheel slip, or an equivalent angular velocity, while the target value is provided by a higher level controller [275, 55]. Since this work focuses on the inner speed control loop, the availability of a higher level controller is assumed to be given. There exist different brand names in the literature for a system that implements such a controller, like vehicle dynamics control (VDC) [275], electronic stability program (ESP) [201] or dynamic stability control (DSC) [54, 55], while a commonly used general term is electronic stability control (ESC) [64]. The modularity of ESC, with the TCS as an important subsystem, allows the separate design of the ESC system for the vehicle motion and both TCSs and anti-lock braking systems (ABSs) for the wheel motion, as will be further discussed from an architectural viewpoint in Section 2.1.2.

In the discussed longitudinal maneuver, it was not mentioned who or what modified the motor torque T_m in order to maximize traction. This detail was left unspecified intentionally, as it is not necessary for understanding the physical principles of traction control. In practice however, there is an interaction with the driver, as under normal conditions the driver is the controller and directly commands the motor torque. The TCS acts as a limiter on the requested torque by the driver and is activated only if too large wheel slip values are detected so that the requested force could not be transmitted to the road anyway, see [53, 287] and [302]. It can further be noted that reducing the motor torque is not the only possibility to decelerate spinning wheels, as this can be achieved by using wheel brakes, for example. Various TCSs use a combination of torque reduction and brake control [8, 179], differential lock systems [254] or 4WD on-demand torque bias systems [220]. An overview and a discussion of such systems are provided in [254]. In this work, focus is set on engine control, as in modern vehicles with an internal combustion engine (ICE), the required torque reduction can be performed using the fast firing path, while electric vehicles (EVs) have even higher bandwidth. Hence, in terms of actuator dynamics, braking is not required. For some maneuvers involving lateral dynamics or inhomogeneous friction coefficients, combined brake or differential lock control are still necessary. Existing state of the art control systems can be used for this purpose in combination with the TCSs of this work.

From a control perspective, an interesting state transformation of the 2-state model (2.1) is rewriting the system dynamic in terms of the wheel slip instead of angular velocity. Since the longitudinal wheel slip λ_{xr} is a function of these state variables, their relationship can be used to derive a differential equation for the wheel slip, cf. [36], given by

$$\dot{\lambda}_{xr} = -\frac{v_x F_{xr}}{J_r \omega_r^2} - \frac{\dot{v}_x}{r_r \omega_r} + \frac{i_G v_x}{r_r J_r \omega_r^2} T_m = f(\lambda_{xr}, v_x, \mu) + g(\lambda_{xr}, v_x) T_m \,, \tag{2.2}$$

where

$$f(\lambda_{xr}, v_x, \mu) = -\frac{(1-\lambda_{xr})\big(\dot{v}_x J_r + r_r^2 F_{xr}(1-\lambda_{xr})\big)}{v_x J_r} \text{ and } g(\lambda_{xr}, v_x) = \frac{r_r i_G (1-\lambda_{xr})^2}{v_x J_r} \,. \tag{2.3}$$

The equation $\dot{\lambda}_{xr} = f(\lambda_{xr}, v_x, \mu) + g(\lambda_{xr}, v_x) T_m$ then replaces (2.1a) in the 2-state model. The decelerating case for ABSs can be derived analogously [136]. This formulation is a more direct approach to traction control, as it fits best to a TCS that directly controls the wheel slip λ_{xr}. However, as will be discussed in Section 2.1.2, an indirect approach that controls angular velocity instead can be the preferable solution in practice.

Generally, the dynamics in a TCS can be divided into "fast" (wheel during slipping) and "slow" (vehicle) contributions, as the inertia of the wheels are significantly smaller than the inertia of the vehicle. In the next section, an overview of the two mainly used control architectures for TCSs in the automotive industry is given. The summary focuses on the control aspects of these architectures and how modern TCSs are implemented in a cascaded control architecture.

2.1.2 Traction Control Architectures

An important aspect of a TCS is that its fundamental dynamics during control evolve at very different time scales. This is mainly because the inertia of vehicle and wheels are at different scales. Furthermore, the nonlinear friction force between the tire and the road accelerates the vehicle and decelerates the wheels. If the requested driving torque significantly exceeds the maximum transmittable force, the wheels start spinning, which decreases the transmitted force. These properties can also be seen by looking at the 2-state model (2.1) in Section 2.1.1. On a road with low friction coefficient, the $r_r F_{xr}$ term in (2.1a) becomes neglectable compared to T_m, if the requested torque is large. Moreover, $\dot{v}_x$ is scaled by the vehicle mass m, which is several orders of magnitude larger than the inertia J_r used for scaling $\dot{\omega}_r$. Hence, v_x generally evolves significantly slower than ω_r, which is also the main reason why v_x is often used as a scheduling parameter in gain-scheduled control designs for TCSs and ABSs [53, 136, 235].

A consequence of this is not only the suitability of TCSs for gain-scheduling approaches, but also the cascaded control structure that is traditionally used as a basis of traction control. The control task is separated into two cascaded loops, where the outer loop controls the vehicle driving dynamics and the inner loop the faster wheel speeds. The general building blocks of this control architecture, which is widely adopted in the automotive industry, are shown in Figure 2.2 and are also described in detail by van Zanten *et al.* [275]. Here, it can also be seen how the cascaded control loops are distributed over two different control units. The outer control loop, responsible for the driving dynamics, is located on the DCU. The DCU takes into account several measured and observed quantities relevant for the vehicle motion, like for example yaw rate or lateral acceleration and computes a target wheel slip from these quantities, which serves as a setpoint for the inner control loop. This setpoint is chosen such that the traction force F_{xr} is maximized. In the traditional architecture for TCSs, the traction controller is located on the DCU, where it computes a corrective torque from the deviation of the wheel slip (or speed, equivalently) from its setpoint, which is then transmitted to the ECU, in [275] also referred to as motor management system. The ECU then realizes the computed torque for example by controlling the ignition angle [54], see [151, pp. 68–69] or the throttle valve [275], see also [27, pp. 172–174].

This cascaded control architecture arises naturally from the facts that the control system depends on state variables with very different dynamics and that the traction force, which should be maximized, directly depends on the wheel slip. However, while the cascaded structure is meant to separate "slow" and "fast" parts of the dynamics, both the driving dynamics controller and the traction controller are implemented on the DCU, as indicated in Figure 2.2. Since in this setup the driving dynamics controller and the traction controller run with the same sampling time and a communication delay between DCU and ECU due to synchronization is present, the full advantages of a truly cascaded control structure cannot be achieved.

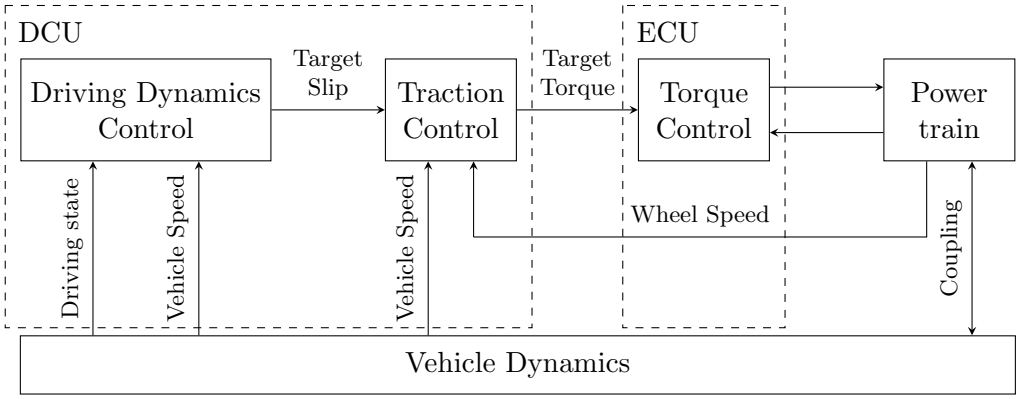

Figure 2.2: Traditional traction control architecture partitioned on the DCU, adapted from [305].

One way to resolve this is a change in architecture and to partition the inner control loop directly on the ECU, an approach that came up recently [130, 264, 291, 305]. Figure 2.3 shows the components of this ECU-based, or engine-based TCS. The communication delay between ECU and DCU is considered less critical in this architecture, because a signal with significantly lower dynamics is transmitted. In the DCU-based architecture in Figure 2.2, the torque transmitted to the ECU can change rapidly, for example due to a sudden change of the friction coefficient of the road. In the ECU-based design, only the setpoint of the wheel speed is transmitted, which has the dynamics of the vehicle speed. The ECU-based architecture has further advantages, as on the ECU, it is natural to control angular velocity, which can be directly calculated from the wheel slip using the vehicle speed and the tire radius. Hence, the DCU only calculates a traction maximizing target wheel slip, which is converted to an angular velocity and then transmitted to the ECU. In addition, on the ECU, the engine speed (scaled to wheel level) instead of the wheel speed can be used for feedback, which is sampled at high rates. Therefore, the ECU-based architecture achieves fast and cascaded control with a stricter modularization of reference speed generation on the DCU and traction control on the ECU.

The cascaded structure using angular velocity as setpoint for the inner control loop is described in [69], though without details regarding the partitioning on different control units. Hrovat *et al.* use this structure to compare throttle-only with throttle and spark control, based on a PID controller [114, pp. 87–92] and also investigate linear quadratic regulator (LQR) and model predictive control (MPC) for TCSs [115]. However, there are no details about the control unit architecture included as emphasis is set on the physical modeling of the plant in [114]. König *et al.* propose a TCS based on a variant of feedback linearization combined with gain-scheduling and remark in their conclusion that performance could potentially be further improved by partitioning the traction controller on the ECU [153, 154]. Jaime *et al.* demonstrate the advantages of an ECU-based TCS with proportional-derivative (PD) control in comparison to a traditional DCU-based TCS, by evaluating both approaches in a test vehicle [130]. Syrnik also investigates an ECU-based TCS with a PID controller in a test vehicle and analyzes stability based on a linearized plant model [264]. Zech *et al.* apply a proportional controller as an active vibration control (AVC) system for damping of drivetrain oscillations with an ECU-based TCS [291].

Only few works on ECU-based traction control use IOL and take torsional drivetrain dynamics into account explicitly. Early works on this topic are our publications [300, 305, 304, 306] and our joint work with Zech *et al.* [307], which is focused on model validation of the proposed TCS, an approach that has also been extended by Zech *et al.* to plug-in hybrid electric vehicles (PHEVs), see [290]. In the following, a literature review of the state of the art of traction control is presented, focusing especially on the methods used for control design and whether these methods were approved in a test vehicle or in simulation only.

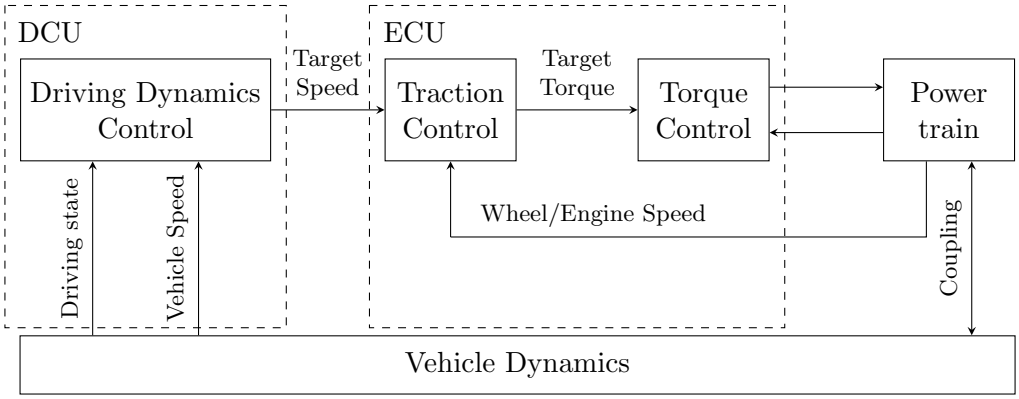

Figure 2.3: Engine-based architecture with traction control partitioned on the ECU, adapted from [305].

2.1.3 Traction Control Design Methods

Before discussing the different state of the art control methods used for designing TCSs, a short overview of some early works on the subject is given. Due to the novelty of TCSs at that time, there was greater focus on fundamental, general design decisions, rather than analytic control design. The first industrialized automotive TCS was the Max-Trac system in the 1971 Buick Riviera, documented in the corresponding manual [77]. On the webpage where this manual was still available at the time of writing, it is stated that the system was dropped again in 1973, as it was not sophisticated enough [193].

An early work describing TCSs as an extension to ABSs is by Gerstenmeier [79]. It can be noted that in the literature TCSs are also known as anti-slip/skid/spin control (ASC) or anti-slip/skid/spin regulation (ASR), respectively, whereas in [79] only the term ASR is used. There, it is discussed how the ABSs of that time could be extended to the accelerating case, while architecture, software design and diagnostics are in focus. However, no explicit controller design is carried out and the paper can be considered as more of an outlook, since neither simulation results nor validation in test vehicles of the discussed concepts are provided. In the same year, Bleckmann *et al.* describe an extension of an ABS to traction control and show that the hill climbing ability of a vehicle can be improved significantly by using a TCS [18]. Additionally, they focus on a description of the mechanical components, the interaction with ABS and the failsafe concept, rather than on analytic control design. Maisch *et al.* also discuss differences between TCSs using engine control or engine and brake control, as well as differential lock control [188]. However, no details about the control design or results are included; it is only stated that the system can improve performance and stability. Crossley evaluates a TCS on different maneuvers in a simulation model including torsional drivetrain dynamics, but without stating the actual control structure, only that the controller was tuned to achieve the desired response [48]. Asami *et al.* proposed and evaluated a proportional-integral (PI) controller for traction control in a test vehicle, investigating both engine only and combined engine and brake control [12]. They show that acceleration performance and cornering stability can be improved by the TCS. An extension of this system is proposed by Ise *et al.*, including an extensive evaluation in a test vehicle [120]. There, the integral of the estimated brake pressure is subtracted from the output of the PI controller. They state that this modification prevents the interference between engine and brake control.

The work by van Zanten *et al.* also describes TCSs as an important subsystem of their VDC system [276, 275, 274]. The VDC system compares quantities like yaw rate and sideslip angle to nominal values that are derived from the traditional linear single-track model by Rieckert and Schunck [241]. From this system, a nominal wheel slip is communicated to the TCS as a reference signal, which uses a PID controller to compute a nominal engine torque that is transmitted to the ECU. In addition to the PID controller which operates on the wheel speeds, a PI controller contributing to a torque portion which controls the speed difference between left and right driven wheels is proposed. It is further stated that both controllers are nonlinear, as their parameters are adjusted in real time based on the engine state and the transmission ratio in order to compensate for a variable response time of the engine. However, other than this general statement, no further details on this adaptation mechanism are provided. The efficiency of the system is demonstrated both in simulation and in test vehicles.

As can be seen in these early works on TCSs, PID control and its variations were already a popular control method at the beginning of the development of the first TCSs. In the following, different methods that are used for traction control in the state of the art are analyzed, ranging from PID control, model following control, maximum transmittable torque estimation, fuzzy logic control to sliding mode control, input-output linearization and flatness-based control, among others. Thereafter, a discussion about the state of the art control design methods for TCSs is given and the research questions addressed in this work are stated.

PID Control

As already mentioned in the previous summary of early works on TCSs, PID control has already been used from the beginning in some of the first TCSs. In the following, a short overview about additional publications dealing with TCSs and ABSs based on traditional PID control, including some problem specific extensions, is given.

Park and Kim evaluate the performance and robustness of a TCS based on PID control during cornering in simulation [221]. Wu *et al.* evaluate PID control for traction control on a test bench [282], while Jin *et al.* evaluate a PID based TCS in a test vehicle with four in-wheel motors [135]. Magallan *et al.* propose a sliding-mode observer for estimating the maximum transmittable torque, based on the LuGre tire model [31], combined with a PID controller for traction control [187]. In [186], driving force control (DFC) is proposed for traction control of a 4WD EV with four in-wheel motors. There, a cascaded control loop is constructed, with an integral controller in the outer loop, which controls the observed driving force such that it tracks the target force. The target force is distributed to the four wheels using an online least squares method. Finally, the inner loop controls individual wheel speeds using PI controllers. Amada and Fujimoto further propose direct driving force control (DDFC), where the intermediate wheel speed control loop is omitted and the observed force is controlled directly by a controller based on pole placement, augmented with integral action [9]. Fujimoto *et al.* provide a comparison between DFC and DDFC, drawing the conclusion that DDFC achieves higher bandwidth and, hence, better performance [72]. Both DFC and DDFC are similar to the model-based control designs discussed on the next page but are included here, as their main feedback component in the inner control loop is PI and integral control.

For many industrial processes, internal model control (IMC) design results in either PI or PID controllers–a property which has been used to derive IMC-based tuning rules for both PI and PID controllers [244]. In [273], these tuning rules are evaluated in simulation for a TCS. Zhao *et al.* combine a sliding mode observer for the tire force with a recursive least square algorithm for estimating tire parameters, the friction coefficient and a PID controller for the motor torque [293]. Gain-scheduling of PI parameters, in combination with an iterative tuning mechanism for ABSs is proposed in [235]. Vasiljevic *et al.* use linearization about operating points and PI control in combination with a road condition estimator, which is used for a road condition dependent feed-forward term. The TCS is evaluated in simulation and with a hardware-in-the-loop (HIL) system [277, 278]. Zhou *et al.* propose a model predictive controller for motion control, where the wheel slips are treated as virtual inputs, while a PID controller is used for traction control and evaluated with a HIL system [294]. Alexander and Vacca combine PID control for a TCS with an extremum seeking algorithm that aims at maximizing the traction force by adapting the setpoint for the PID controller [8]. The PID controller is used in conjunction with an electro-hydraulic brake actuator in order to avoid wheel spinning, while the TCS is evaluated both in simulation and on a wheel loader as a test vehicle. One work that consider the torsional dynamics of the drivetrain explicitly during the control design process is [181]. There, a Notch filter is implemented in series with both a feed-forward and a feedback PI controller, in order to attenuate the resonance frequency of the driveline.

There also exist different publications proposing PID control for 4WD on-demand torque bias systems. Lee [166] combines a PI controller with an adaptation law of the controller gains and a forgetting factor. Moreover, Panzani *et al.* [220] use proportional control for torque distribution with a controlled ETC. An application of a PD controller to front-to-rear distribution in a vehicle with four electric in-wheel motors using torque vectoring is presented in [131].

In summary, a variety of TCSs based on PID control exists–ranging from standard PID control, over combinations with model based approaches like DFC and DDFC, to methods involving gain-scheduling or extremum seeking algorithms.

Model Following Control and Maximum Transmittable Torque Estimation

While PID control has been used for the design of TCSs, various publications also investigate the methods of model following control and maximum transmittable torque estimation. One of the first designs in this category is the model following control (MFC) design proposed by Hori *et al.* and also evaluated in a test vehicle in [113]. MFC is closely related to the well-known internal model control, as it uses feedback of the difference of process and model output. In contrast to standard IMC however, the feedback channel in MFC contains an additional high-pass filter, since, according to Hori *et al.*, only the high frequency response is required for traction control, while no Q-Filter is used in the forward path. The model itself is based on the idea that the equivalent inertia of the wheel J_{eq} can be interpreted as a function of wheel slip by

$$J_{\text{eq}} = J_r + mr_r^2(1 - \lambda_{xr}), \text{ with } \lambda_{xr} \in [0, 1]. \tag{2.4}$$

The intuition behind (2.4) is, that when $\lambda_{xr} \approx 0$, the torque applied to the wheel has to accelerate both the wheel inertia J_r and the vehicle mass m, mapped to an aggregated inertia by the tire radius r_r so that $J_{\text{eq}} \approx J_r + mr_r^2$. However, when $\lambda_{xr} \approx 1$, the wheels spin almost freely, and so $J_{\text{eq}} \approx J_r$. For the internal model, the first case is used (assuming $\lambda_{xr} \approx 0$), such that the difference between the actual and the internal model wheel speed is close to zero in standard driving situations (small wheel slip), but significant when the wheels start to spin. Further experimental evaluations of MFC are presented by Sakai *et al.* [249]. Akiba *et al.* compare MFC to wheel slip control using a MIMO transfer function, considering left and right wheels separately, where the transfer function matrix was obtained by linearization [7]. Their conclusion is that the slip-based controller performs better than MFC in the considered maneuvers, however, in contrast to MFC, also requires the wheel slip and thereby the vehicle speed v_x. A detailed study on MFC and direct wheel slip control using a PI controller is also provided by Hori in [112], which considers maneuvers with lateral dynamics, although no direct comparison of the two approaches is given therein. Kawabe proposes an extension to MFC, by using an MPC based PID controller in the feedback path, instead of the MFC formulation [147]. A comparison with MFC is given in simulation, with the conclusion that the MPC based PID controller yields better acceleration performance than MFC.

Another model-based approach is maximum transmissible torque estimation (MTTE) by Yin *et al.* [287]. MTTE is based on calculating the maximum transmissible torque from the estimated friction force, which is obtained by solving the differential equation of the wheel angular acceleration for the tire force, including an additional tuning factor. In [287], a simulative and experimental comparison with MFC is provided as well, with the conclusion that MTTE outperforms MFC in the considered maneuvers. Hu and Yin also give a study on MTTE in conjunction with yaw moment control [117], where they show in simulation that yaw moment control can be improved using MTTE. Li *et al.* propose a combination of MTTE for controlling the front wheels and sliding mode control (SMC) for the rear wheels and evaluate their concept in simulation [174]. Ewin investigates the interaction of an MTTE-based TCS with its outer loop driving dynamics control system in a test vehicle [62]. Borrelli *et al.* use MPC based on a 2-state model for traction control [21]. It can be noted that this is also one of the few papers, where the engine speed is used in the 2-state model, instead of the wheel speed. However, the drivetrain is nevertheless modeled as stiff, so the only difference is that the engine speed is scaled by the total gear ratio, a constant parameter. They also consider discretization and time delay in the design process and evaluate the TCS in simulation and in a test vehicle. For the 4WD case, MFC was proposed by Chen *et al.* and also evaluated in a test vehicle [40].

In summary, the discussed control designs MFC and MTTE are built upon the 2-state model and neglect torsional dynamics of the drivetrain in the control design. Combinations with other control methods like SMC exist, as well as predictive control designs based on MPC.

Sliding Mode Control

Several authors propose SMC to approach the traction control problem. Tan and Tomizuka [267] derive SMC for TCSs and ABSs using a linearized, discretized 2-state synthesis model. The SMC is combined with a linear feedback term, called "minor" feedback, in order to reduce chattering. Further, they evaluate the braking case in an experimental test cell. A theoretical investigation of the dynamics of the continuous 2-state model under SMC, where it is for example shown that the sliding surface can be reached from any initial state, is given by Tan and Chin [266]. Fan *et al.* use a similar SMC for a TCS for tracked vehicles with an additional low-pass filter for the signum term in the control law, in order to further reduce chattering and evaluate the system in simulation [63]. Canudas de Wit and Tsiotras evaluate the TCS based on SMC by [63] in simulation and compare different static and dynamic tire models with each other [30]. In [141], SMC is proposed for both wheel slip control in a TCS and for the torque production process of the engine, while both [133] and [295] evaluate SMC for vehicles with four individual wheel drives and [269] compares SMC to MTTE, all of them using simulation.

Colli *et al.* compare SMC with a fuzzy controller, which is used to control the gradient of the normalized tire force on a test bench [47]. Their conclusion is that SMC provides better performance than the fuzzy controller. Ferrera and Vecchio [65] propose two variants of SMC for traction control, namely sub-optimal and super-twisting SMC, and compare both in simulation, with the conclusion that both approaches provide comparable performance. Further simulative evaluation of this approach, combined with a sliding mode observer to estimate the nonlinear tire force, can be found in [11]. Super-twisting SMC is also applied to the braking case by Hamzah *et al.* [101], where it is evaluated in simulation against first order SMC, with the result that super-twisting SMC avoids chattering. De Castro *et al.* propose a TCS based on SMC combined with a conditional integrator, which switches from an ideal SMC design to a PI controller when the controlled variable is close to its setpoint [52]. Also, a simplified estimator for an upper bound of the tire force, based on the requested torque by the driver, is proposed there. They evaluate the TCS in simulation and on different maneuvers in a test vehicle. The combination of SMC with a conditional integrator is also used in [261], where the tire force is estimated online by approximating the Burckhardt tire model [27, pp. 24–35], using a linear combination of basis functions. The TCS is evaluated in simulation.

Kuntanapreeda proposes a PI nonlinearity observer for estimating the tire friction force, in combination with SMC [163] and super-twisting SMC [164]. Both approaches are evaluated in simulation and on a single-wheel test rig, considering different maneuvers. Siampis *et al.* combine MPC for the reference generation of the wheel slip with SMC, which is used for tracking the reference trajectory [253]. They also implement their control scheme on hardware in order to ensure real-time capability and evaluate the approach in simulation. Nam *et al.* use adaptive SMC for a vehicle with four in-wheel motors with a driving force observer and evaluate the TCS in a test vehicle [206, 207]. Moreover, He *et al.* compare different inter-axle torque distribution strategies based on SMC in simulation [105]. Han *et al.* propose SMC for hybrid 4WD vehicles [102], where instead of the sign of the wheel slip error, the sign of the estimated rate of change of the tire force and the sign of the wheel speed is used, while the TCS is evaluated in simulation. Also torque-bias systems have been considered for traction control using SMC. Ham and Lee for example propose SMC for vehicles with 4WD drivetrain and torque-bias systems and compare SMC against a controller based on lookup tables in simulation [100].

In summary, various approaches based on SMC have been proposed for traction control. Most investigations are built upon variations of the 2-state model, while particular effort has been made to deal with the chattering phenomenon of first order SMC. Also, since the proposed SMC schemes generally require the nonlinear tire friction force, or at least bounds on the force and its time-derivative, SMC has been combined with various tire force estimation algorithms.

Fuzzy Logic Control and Rule Based Systems

Another common design method is fuzzy logic control. In fuzzy logic control, the control signals are generated based on measured or observed system states, which are mapped to logical variables that can take any value between 0 and 1. This mapping process is called fuzzification. The produced fuzzy logical variables are then passed through a rule processor, where the designer has to incorporate knowledge about the control system. After that, a defuzzifier maps the result back to a control signal. This method has been widely applied, also in combination with PID control, to both TCSs and ABSs.

Lee and Tomizuka compare an adaptive sliding-mode control, which requires a tire force model, with a fuzzy logic control approach which operates without such a model [167]. The comparison is carried out in simulation, with the result that the model-based SMC design results in better performance, if an accurate tire model is available. Kathun *et al.* use a test bench for the design of a fuzzy controller, based on the rate of change of the wheel slip and the observed load torque [150]. A fuzzy PID approach is used in [177], where the variables used for fuzzification are the wheel slip and its rate of change. The fuzzy logic adapts the proportional gain of the PID controller, while integral and derivative gains remain constant. They compare their fuzzy logic controller with a PID controller in a test vehicle and show in experiments that the fuzzy logic controller achieves better performance than a standard PID controller. Cai *et al.* compare a fuzzy logic controller with a heuristic rule based control system [29]. Here, the ratio of the wheel acceleration and the motor torque and the rate of change of this ratio are used as variables for fuzzification. The evaluation is done in simulation, where the fuzzy logic controller shows better performance compared to the rule based approach. Jalali *et al.* use the deviation of the wheel slip from its setpoint and its rate of change as variables for the fuzzification process for both a TCS and an ABS [132]. The performance of the fuzzy logic controller is evaluated on various maneuvers in simulation and on a HIL test bench including an operator-in-the-loop driving simulator.

Li *et al.* propose a control structure, where a PID controller is used in parallel with a fuzzy logic controller [172], using the front left and front right wheel slips for fuzzification to compute a confidence level of the friction coefficient. This confidence level is combined with several model based rules to produce the final base torque, which is added to the PID controller. The approach is evaluated on a HIL test bench and in a test vehicle and compared to a standard PID controller, with the result that the fuzzy logic improves driving performance. Additional investigations of this approach are presented in [173]. Dahmani *et al.* propose a fuzzy PI control design for traction control where the output of the PI controller is scaled by the friction coefficient, estimated using a Takagi-Sugeno fuzzy representation of the nonlinear vehicle model [49], which is also applied to a four-wheel active steering system [50]. In both publications, a stability analysis is performed based on the analysis from Tseng *et al.*, which is based on linear matrix inequalities [271]. However, the control system is evaluated in simulation only. Liu and Jin combine sliding mode control for the driving torque with a fuzzy controller which uses the wheel brakes for traction control [179]. They describe a two-step procedure, where first the brake pressure from the fuzzy controller is applied and second the driving torque is adapted by the sliding mode controller. Variables used for fuzzification are the deviation of the wheel slip from its target value and the rate of change of this deviation. Experiments in a test vehicle and on different maneuvers are presented. Hu *et al.* finally propose fuzzy logic control for traction control of vehicles with 4WD torque-bias systems, where fuzzy logic controllers are used for the driving torque, the torque distribution and the brake torque, respectively [116]. Further references of vehicle dynamics control, TCSs and ABSs using fuzzy logic control can be found in the review paper [272].

In summary, fuzzy logic control for TCSs and ABSs mainly differs by the variables used for fuzzification and whether the fuzzy algorithm is used for control directly or in conjunction with other controllers. However, stability and drivetrain oscillation analyzes are rarely considered.

Input-Output Linearization and Flatness-Based Control

Following we review publications proposing feedback linearization or flatness-based control for TCSs. The different variants of linearization by feedback, like input-output linearization or full state feedback linearization, all aim at finding a control law that cancels out nonlinearities in the system equations, such that the resulting system has linear behavior. The most prevalent of these methods in the context of TCSs and ABSs is input-output linearization. The method itself was proposed by Isidori *et al.* [126, 127], see also [28] and [123].

For input-output linearization techniques in TCSs, the 2-state model (2.1a)-(2.1c) is widely used. Assuming $v_x > 0$ and $0 \leq \lambda_{xr} < 1$, so that $g(\lambda_{xr}, v_x) \neq 0$, the nonlinearities in (2.2) can be canceled out by defining the control input T_m as

$$T_m = \frac{v - \lambda_{xr} - \tau f(\lambda_{xr}, v_x, \mu)}{\tau g(\lambda_{xr}, v_x)} \tag{2.5a}$$

$$\Rightarrow \dot{\lambda}_{xr} = (v - \lambda_{xr})/\tau \,, \tag{2.5b}$$

so the linearized slip dynamics are given by a first order lag element with time constant τ and new, virtual input v. This method has been used, with slight variations, in the publications by Guo *et al.* [93] and Ningfeng *et al.* [210], where the control law was evaluated in simulation. The ABS case can be treated analogously and has been considered in [138] with a first order lag element for the hydraulic brake actuator model. Zhang and Ordonez evaluate an IOL based controller for an ABS combined with an extremum seeking algorithm in simulation [292].

The main difficulty with applying these approaches in practice is that the control law (2.5a) depends on the nonlinear and uncertain tire force, which cannot be measured directly in vehicles that are equipped with standard sensors. A model based computation of the tire force in (2.5a) is not only challenging due to uncertainties in tire parameters and vehicle load, but also because of the dependency on the uncertain and time-varying friction coefficient of the road. Using the measured longitudinal vehicle acceleration a_x to compute F_{xr} does not scale to situations where the distribution of the tire forces is relevant, like vehicles with 4WD. Moreover, using a_x for the $\dot{v}_x$ term in (2.5a) is problematic, as on roads with nonzero slope, a_x deviates from $\dot{v}_x$ due to gravity [121, pp. 156–157]. Chapuis *et al.* published one of the few works where a TCS based on IOL is evaluated in a real test vehicle and additionally compared to PID control and a flatness-based approach [36]. The IOL approach is based on the 2-state wheel slip model (2.2) and uses an estimate of the tire force based on a linearization of the tire force around different operating points, assuming a constant friction coefficient. The controllers are evaluated on a longitudinal acceleration maneuver, starting from standstill on a road with asymmetric friction coefficients. The flatness-based controller is also evaluated in simulation by Chapuis *et al.* [37]. For ABSs, a design based on IOL with an additional two-position controller for compensation of the hydraulic brake actuator hysteresis can be found in [121, pp. 146–168]. Moreover, the estimation of the longitudinal speed of the vehicle is addressed there, compare [121, pp. 155–159], as well as the generation of the target speed for the considered ABS, see [121, pp. 159–163]. The concept based on an ABS variant of the 2-state model is evaluated in a test vehicle and achieves a shorter stopping distance compare to a conventional ABS, see [121, pp. 163–167].

Mousavi *et al.* provide a simulation study of different control approaches for ABSs, including feedback linearization, SMC and adaptive fuzzy SMC [202]. The controller based on feedback linearization is derived based on a 2-state vehicle model with an additional first order actuator model. The tire force is calculated with a fixed friction coefficient using the Burckhardt tire model [27, pp. 24–35]. While the feedback linearization controller achieves short stopping times on different road conditions, it shows large undershoots after sudden changes of the friction coefficient. Also, while performance is comparable to SMC on wet asphalt and snow, the feedback linearization controller shows more oscillations on ice compared to the other methods. Therefore, other designs might be necessary to further increase robustness.

Different approaches have been proposed in order to address the tire force dependency issue of the linearizing control law. One example is the work on ABSs by Mirzaeinejad and Mirzaei [198], where feedback linearization is combined with MPC and integral action. Also, they use slightly different reference dynamics for $\dot{\lambda}_{xr}$ in (2.5b), namely an integrator with first order lag, adapted from [103]. There, the gain of the integrator is defined as the (constant) slip value which maximizes the traction force. Zhang and Ordonez solve an ABS variant of (2.1a) for F_{xr}, which is then computed using the measured vehicle acceleration, neglecting aerodynamic drag [292]. Geamanu *et al.* [76] propose flatness-based control for longitudinal tracking control of the vehicle speed with a TCS and an ABS based on SMC. The tire force is estimated by solving (2.1a) for F_{xr}, but no details are provided how the $\dot{\omega}_r$ term itself is obtained. Both [36, 37] and [76] use the vehicle speed as flat system output. The main difference between [36, 37] and [76] is that the latter uses the flatness-based controller not directly for the TCS, but for tracking the vehicle speed. The TCS is based on SMC, combined with an estimation algorithm for the friction coefficient of the road. Furthermore, Fuji and Fujimoto combine a slip-ratio estimator with IOL and compare it to a PI controller in simulation and in a test vehicle [71]. They test two methods for computing $\dot{\omega}_r$ for the tire force. The first is by approximating the derivative with a high-pass filter, the second by estimating the derivative based on the target wheel slip and the motor torque. However, both designs show more oscillations than a PI controller. The authors derive the need for a nonlinear control design based on IOL by the reasoning that a PI controller can result in instability, however no formal stability analysis is carried out for the IOL based control design. A similar design with comparable results can also be found in the work by Fujimoto *et al.* [73].

Stability of the zero dynamics, resulting from a control design for an ABS based on IOL for a 2-state model is investigated in detail by Nakakuki *et al.* [205]. Since in case of a 2-state model, the relative degree of the system is 1, the zero dynamics are a scalar system, which simplifies stability analysis. The controller is combined with an adaptation law to estimate uncertain parameters in real time. However, the adaptive controller is only evaluated in simulation and outperforms a standard PI controller only at low speed [205]. Nyandoro *et al.* [212] use IOL for ABS based on a 2-state model, which is evaluated in simulation only. They derive stability of the scalar zero dynamics based on physical interpretation. Although no explicit Lyapunov function is given, the result follows immediately from their analysis, as the wheel slip is defined as a system output. Hence, for the zero dynamics, by output zeroing follows that $\lambda_{xr} = 0 \Rightarrow F_{xr} = 0$, so the scalar zero dynamics reduce to the aerodynamic drag force, which eventually decelerates the system to the origin. Nyandoro *et al.* also extended this approach to an ABS with an active suspension system, which is modeled by a 6-state dynamical system with two inputs (brake torque and active suspension force) and two outputs (wheel slip and suspension travel) [211]. While this is one of the few works which considers a higher order system for ABS using IOL, the drivetrain is still based on the 2-state model, and the control law also contains the tire force. The nonlinear portion of the zero dynamics reduces to the zero dynamics of the 2-state case in [212].

Summarizing, the state of the art for IOL of TCSs uses almost exclusively variations of the 2-state model for control synthesis. Extensions so far included first order actuator dynamics [138] or active suspension systems for ABSs [211]. However, torsional dynamics of the drivetrain have not yet been considered explicitly for control design based on IOL, except in our recent work [300, 305, 304, 307] and extensions thereof proposed by our colleagues [57, 58, 182, 183]. There exists work using IOL for torque converters using synthesis models including torsional dynamics [97]. However, the vehicle model there is based on a model published in [156], which assumes that the wheel speed is directly proportional to the vehicle speed, so wheel slip dynamics are neglected. Rebouh *et al.*, [240] use IOL for control of a permanent magnet synchronous motor in an EV with a detailed model of the motor. However, only the nonlinearity of the motor itself is linearized there, while the load torque, containing the nonlinear tire force, is not considered during control design, but treated as perturbation. Hence, it can be noted that these publications do not address the traction control problem directly, as their focus is different.

Other Approaches and Active Vibration Control

Various other methods have been applied to the design of traction control systems for automotive vehicles. Fujimoto *et al.* propose a control design based on a disturbance observer (DOB), where the tire force is treated as uncertain inertia variation [74, 75]. They also analyze the effect of time delay and evaluate the TCS in a test vehicle. Li *et al.* use an observer for the back electromotive force, treating the nonlinear friction force as an inertia variation and evaluate the controller in a test bench [176]. Backstepping is proposed by Tai and Tomizuka for both TCSs and ABSs, based on the 2-state vehicle model with an additional first order lag as actuator model [265]. For the control law, they assume a linear tire force model and evaluate the TCS in simulation. Adaptive backstepping based on the 2-state model is proposed for ABSs and evaluated in simulation by He *et al.* [107]. Stability is analyzed with barrier Lyapunov functions, the control laws depend on the tire force. Adaptive control is applied by Kececi *et al.*, using a model with the vehicle speed and yaw rate as states, which is evaluated in simulation [148]. Kirchner and Southward evaluate adaptive control, based on knowledge of partial derivatives of the tire forces in simulation [152]. A DOB in conjunction with a recursive least squares estimator of the vehicle mass, based on the 2-state model, is proposed in [239] and evaluated on a test bench. Marino *et al.* propose stochastic control based on an extended Kalman filter for the 2-state model, in order to maximize the nonlinear tire force, which is evaluated in simulation [189]. A comparative simulation study of five different methods for TCSs (MTTE, SMC, second order SMC, H_∞ control and gain-scheduled PI) is carried out in [53], with the conclusion that gain-scheduled PI and H_∞ control result in the best performance.

Active vibration control (AVC) has been used in combination with TCSs as well. For example, the authors of [53] analyze for their simulation study the AVC from Rodriguez *et al.*, see [245], in order to validate their model and to damp drivetrain oscillations. The AVC is a PD controller, which takes the difference between engine and wheel speed as input and computes a torque for oscillation damping. The controller is designed based on an analysis of the poles of a linear model by treating the nonlinear tire force as a perturbation, or alternatively as a linear parameter-varying (LPV) system, cf. [285]. An AVC design based on proportional feedback of the speed difference between engine and wheel speed is considered by Götting and De Doncker in conjunction with a TCS, cf. [91]. Götting also proposes state feedback for AVC [90, pp. 81–122] and analyzes several such designs in simulation and on a test bench [90, pp. 124–135]. Zech *et al.* propose an AVC design with proportional feedback for a TCS using the ECU based architecture described in Section 2.1.2, which is evaluated in a test vehicle [291]. Baumann *et al.* propose a Smith-Predictor in combination with a Luenberger observer and a PD controller for controlling the predicted speed difference [17]. They also evaluate their AVC design in a test vehicle, while the control design is based on a root locus analysis of a linear design model. Moreover, there exist numerous publications dealing with AVC of general drive systems that are not specific to automotive applications, see for example [111] and [251, pp. 1188–1291].

It can further be noted that the presented state of the art on TCSs focuses on the traction control loop, where typically wheel speed/wheel slip or engine speed is the controlled variable. A variety of publications are dealing with the design of the driving dynamics controller, where for example the yaw rate of the vehicle is controlled and the target slip for the inner traction control loop is computed. Early publications dealing with this topic are [54, 55, 276, 275, 274], see for example also [106, 218] as well as [121, pp. 169–211] and [27, pp. 167–190]. A detailed review of TCSs and ABSs can be found in the survey paper by Ivanov *et al.* [129].

This concludes the review of the state of the art of the methods for design of TCSs. In the following, some of the open questions identified during this review are discussed, which describe a research gap in the current state of the art on TCSs that is addressed by this work. The contributions and novel aspects of the present work, with some of its aspects and related methods published in [300, 301, 302, 303, 304, 305, 306, 307], are detailed in the following.

2.1.4 Identified Problems and Research Gap

Considering the review of the state of the art of TCSs from Section 2.1.2 and Section 2.1.3, it is evident that some interesting facets have not been considered yet in the literature. The following items characterize the current state of the art on TCS.

1. TCS design by input-output linearization is based almost exclusively on the 2-state model.
2. Torsional dynamics of the drivetrain are rarely considered in the design phase.
3. Stability of zero dynamics of TCSs is shown only for the 2WD case using the 2-state model.
4. No passivity or robustness analysis of zero dynamics with torsional dynamics is available.
5. Few experimental evaluations of TCSs that consider ECU-based architectures exist.

Items 1 and 2 also apply more generally to TCS design, as more sophisticated models for controller design than the 2-state model are rarely used. Damping of torsional dynamics of the drivetrain is an essential feature of TCSs, which is one reason why separated active vibration control systems have been proposed [53, 245, 291]. However, a TCS that incorporates such a mechanism by a control design based on IOL for both vehicles with 2WD and on-demand 4WD drivetrains using torque bias systems has not been proposed yet, except in our recent publications [300, 304, 305, 306, 307]. In this work, the control design is further investigated and the analysis extended in several directions. Item 3 is of interest since it is required for safety critical systems like TCSs to ensure stability of a novel control concept. Previous work on input-output linearization for TCSs so far considered mainly vehicles with 2WD and stability analyses of the 2-state model. Also, robustness with respect to parameter variations and external disturbances, like a time-varying friction coefficient, is essential to guarantee the suitability of the concept. Item 4 is of theoretical interest, as the nonlinear friction curve that models friction between tire and road shows the characteristic shape of a sector-bounded, memoryless nonlinearity. Despite that fact, no such analysis exists in the literature on TCSs. Finally, Item 5 is of practical interest, as many publications present simulation results only. For example, the survey paper [129] states that only 24% of the therein considered literature presents experimental evaluation in real test vehicles. Taking furthermore into account the analytic control design based on IOL and a design model with torsional drivetrain dynamics, the architectural change discussed in Section 2.1.2 and vehicles with 4WD on-demand torque bias systems, it is found that no experimental evaluation in the current state of the art has considered this setup previously. Such an evaluation is presented in Chapter 6.

Additionally, it is investigated how optimization with GP can be applied for Lyapunov function synthesis for the stability analysis of traction control zero dynamics including torsional drivetrain dynamics. This partially addresses Item 3 as well, as the main challenge for stability analysis of nonlinear dynamical systems is the problem of finding a suitable Lyapunov function. While GP has been applied to Lyapunov function synthesis, see Chapter 5, we present a new heuristic for evaluating the fitness of potential Lyapunov functions in a GP setting.

These findings constitute a research gap in the literature of TCSs for automotive vehicles which justifies the goals set for this dissertation as listed in Chapter 1. We aim to close this gap by addressing the previously mentioned issues explicitly. Moreover, the investigations regarding stability and passivity of the zero dynamics of TCSs, including torsional drivetrain dynamics, have led to some general questions regarding the applicability of the Kalman conjecture and the Markus-Yamabe conjecture for a specific class of nonlinear systems. While these conjectures are well researched, the zero dynamics resulting from the TCS design constitute the interesting special case of a third order Lur'e system with two inputs and two outputs, which has previously not been considered explicitly. In the following chapter, some preliminaries on control theory, with the focus on Lyapunov stability, absolute stability and control design by input-output linearization is given. Thereafter, a short introduction to optimization with GP is presented.

2.2 Preliminaries on Control Theory

2.2.1 Stability of Linear and Nonlinear Systems

This section gives some background information on the control theoretic concepts used in this work, which is mainly based on our summary in [303] and the standard textbooks by Khalil [149], Franklin *et. al* [70], Doyle *et al.* [60], Slotine and Li [256], Ackermann *et al.* [1] and Ogata [216]. First, consider the nonlinear system of autonomous ordinary differential equations (ODEs)

$$\dot{\boldsymbol{x}}(t) = \boldsymbol{f}\big(\boldsymbol{x}(t)\big)\,, \text{ with } \dot{\boldsymbol{x}}(t) = \begin{bmatrix} \dot{x}_1(t) \\ \dot{x}_2(t) \\ \vdots \\ \dot{x}_n(t) \end{bmatrix}, \boldsymbol{x}(t) = \begin{bmatrix} x_1(t) \\ x_2(t) \\ \vdots \\ x_n(t) \end{bmatrix} \text{ and } \boldsymbol{f}\big(\boldsymbol{x}(t)\big) = \begin{bmatrix} f_1\big(\boldsymbol{x}(t)\big) \\ f_2\big(\boldsymbol{x}(t)\big) \\ \vdots \\ f_n\big(\boldsymbol{x}(t)\big) \end{bmatrix}. \tag{2.6}$$

Here, $\boldsymbol{x}(t) \in \mathbb{R}^n$ is a state vector, $\boldsymbol{f} : \mathbb{R}^n \to \mathbb{R}^n$ a C^1 vector field, while $\dot{x}_i(t) \stackrel{\text{def}}{=} \mathrm{d}x_i(t)/(\mathrm{d}t)$ denotes the derivative of $x_i(t)$ with respect to time t for $i \in \{1, 2, \ldots, n\}$.

Remark 1. *To shorten notation, as long as it is clear from the context, the explicit dependence on time will be omitted for the state vector and the later defined input and output vectors.*

In this work, stability properties of TCSs with isolated equilibrium are investigated, therefore the required preliminaries on stability analysis of nonlinear dynamical systems are stated.

Definition 1. *(Equilibrium) A state vector $\boldsymbol{x}^* \in \mathbb{R}^n$ is called equilibrium of (2.6) if $\boldsymbol{f}(\boldsymbol{x^*}) = \boldsymbol{0}_n$.*

There exist various different notions of stability in the literature, see for example Khalil [149, pp. 111–222], Sontag [259] and Doyle *et al.* [60, pp. 31–40]. First, focus is set on stability in the sense of Lyapunov and its stronger versions, asymptotic and exponential stability, respectively.

Definition 2. *(Lyapunov stability, cf. [149, p. 149]) Let $\boldsymbol{x}^*$ be an equilibrium of system (2.6). Then $\boldsymbol{x}^*$ is called stable in the sense of Lyapunov if for every $\epsilon > 0$, $\exists \delta(\epsilon, t_0) : \|\boldsymbol{x}(t_0)\| < \delta \Rightarrow \|\boldsymbol{x}(t)\| < \epsilon\,, \forall t \geq t_0$. As shorthand, $\boldsymbol{x}^*$ is also just called (Lyapunov) stable.*

Definition 3. *(Asymptotic stability, cf. [149, p. 149]) An equilibrium $\boldsymbol{x}^*$ of system (2.6) is called asymptotically stable if it is Lyapunov stable and $\exists k > 0 : \lim_{t\to\infty} \boldsymbol{x}(t) \to \boldsymbol{x}^*\,, \forall \|\boldsymbol{x}(t_0)\| < k$.*

Definition 4. *(Exponential stability, cf. [149, p. 150]) An equilibrium $\boldsymbol{x}^*$ of system (2.6) is called exponentially stable if $\exists c_d, r_d, x_d > 0 : \|\boldsymbol{x}(t)\| \leq c_d \|\boldsymbol{x}(t_0)\| \exp(-r_d(t - t_0))\,, \forall \|\boldsymbol{x}(t_0)\| < x_d$.*

A system like (2.6) is called stable in the sense of Lyapunov [185], if its trajectories remain bounded. However, this does not yet guarantee that they converge to an equilibrium state. Asymptotic stability gives the additional guarantee that trajectories converge to an equilibrium for $t \to \infty$. Exponential stability finally guarantees that this convergence is "fast", in especially that the norm of the state vector $\|\boldsymbol{x}(t)\|$, can be bounded by an exponentially decaying function. An important concept for stability analysis of nonlinear dynamical systems is definiteness.

Definition 5. *(Definiteness of real-valued functions, cf. [149, p. 117]) Let $X_0 \subseteq \mathbb{R}^n$ be a connected set with $\boldsymbol{0}_n \in X_0$, $X = X_0 \setminus \{\boldsymbol{0}_n\}$, $V : \mathbb{R}^n \to \mathbb{R}$ with $V(\boldsymbol{0}_n) = 0$. Then, V is called:*

- *Positive definite on X_0 if $V(\boldsymbol{x}) > 0\,, \forall \boldsymbol{x} \in X$, denoted with $V(\boldsymbol{x}) \succ 0$.*
- *Positive semi-definite on X_0 if $V(\boldsymbol{x}) \geq 0\,, \forall \boldsymbol{x} \in X$, denoted with $V(\boldsymbol{x}) \succeq 0$.*
- *Negative definite on X_0 if $V(\boldsymbol{x}) < 0\,, \forall \boldsymbol{x} \in X$, denoted with $V(\boldsymbol{x}) \prec 0$.*
- *Negative semi-definite on X_0 if $V(\boldsymbol{x}) \leq 0\,, \forall \boldsymbol{x} \in X$, denoted with $V(\boldsymbol{x}) \preceq 0$.*
- *Indefinite otherwise.*

An important class of real-valued functions for investigating stability of dynamical systems are so-called quadratic forms.

Definition 6. *(Quadratic form, cf. [149, p. 117]) A function $V : \mathbb{R}^n \to \mathbb{R}$ is called a quadratic form if it can be written as a polynomial of degree two like*

$$V(\boldsymbol{x}) = \sum_{i=1}^{n}\sum_{j=1}^{n} p_{ij}x_i x_j = \boldsymbol{x}^T \begin{bmatrix} p_{11} & p_{12} & \cdots & p_{1n} \\ p_{21} & p_{22} & \cdots & p_{2n} \\ \vdots & \vdots & \ddots & \vdots \\ p_{n1} & p_{n2} & \cdots & p_{nn} \end{bmatrix} \boldsymbol{x} = \boldsymbol{x}^T \boldsymbol{P} \boldsymbol{x} \tag{2.7}$$

with $\boldsymbol{P} = \boldsymbol{P}^T \in \mathbb{R}^{n\times n}$, so $p_{ij} = p_{ji}$ for all $i, j \in \{1, 2, \ldots, n\}$.

One convenient property of quadratic forms is, that their definiteness can be evaluated by testing the definiteness of their associated $\boldsymbol{P}$ matrix. This leads to the next definition.

Definition 7. *(Definiteness of real-valued matrices, cf. [149, p. 117]) Let $\boldsymbol{x} \in \mathbb{R}^n$. A symmetric, real-valued matrix $\boldsymbol{P} = \boldsymbol{P}^T \in \mathbb{R}^{n\times n}$ is called, following Definition 5:*

- *Positive definite if $\boldsymbol{x}^T\boldsymbol{P}\boldsymbol{x} \succ 0$, denoted with $\boldsymbol{P} \succ 0$.*
- *Positive semi-definite if $\boldsymbol{x}^T\boldsymbol{P}\boldsymbol{x} \succeq 0$, denoted with $\boldsymbol{P} \succeq 0$.*
- *Negative definite if $\boldsymbol{x}^T\boldsymbol{P}\boldsymbol{x} \prec 0$, denoted with $\boldsymbol{P} \prec 0$.*
- *Negative semi-definite if $\boldsymbol{x}^T\boldsymbol{P}\boldsymbol{x} \preceq 0$, denoted with $\boldsymbol{P} \preceq 0$.*
- *Indefinite otherwise.*

One interpretation of this definition is, that definiteness is a generalization of signedness from scalar values to symmetric, real-valued matrices. It can be evaluated for example by looking at the eigenvalues of $\boldsymbol{P}$ or by the Sylvester criterion [149, p. 117]. Definiteness is an important property, as it is a requirement for Lyapunov function candidates.

Definition 8. *(Lyapunov function candidate) A function $V : X_0 \to \mathbb{R}$ is called a Lyapunov function candidate if $V(\boldsymbol{x}) \succ 0\,, \forall \boldsymbol{x} \in X_0$, following Definition 5.*

Given a Lyapunov function candidate, its evolution along system trajectories can be evaluated.

Definition 9. *(Derivative along solution trajectories, cf. [149, p. 114]) Let $V : \mathbb{R}^n \to \mathbb{R}$ and $\boldsymbol{f} : \mathbb{R}^n \to \mathbb{R}^n$ with $\boldsymbol{x}^T = \begin{bmatrix} x_1 & x_2 & \ldots & x_n \end{bmatrix}$ and $\boldsymbol{f}(\boldsymbol{x})^T = \begin{bmatrix} f_1(\boldsymbol{x}) & f_2(\boldsymbol{x}) & \ldots & f_n(\boldsymbol{x}) \end{bmatrix}$. Then, the derivative of V along the trajectories of (2.6) is given by*

$$\dot{V}(\boldsymbol{x}) \overset{\text{def}}{=} \frac{\partial V(\boldsymbol{x})}{\partial \boldsymbol{x}} \boldsymbol{f}(\boldsymbol{x}) = \sum_{i=1}^{n} \frac{\partial V(\boldsymbol{x})}{\partial x_i} f_i(\boldsymbol{x})\,. \tag{2.8}$$

In the control engineering literature, common synonyms are orbital, directional or time derivative.

This leads to the established notion of Lyapunov functions.

Definition 10. *(Lyapunov function, cf. [149, p. 116]) Let $X_0 \subseteq \mathbb{R}^n$ with $\mathbf{0}_n \in X_0$ and let (2.6) be such that $\boldsymbol{f}(\mathbf{0}_n) = \mathbf{0}_n$. A C^1 function $V : X_0 \to \mathbb{R}$ is called a Lyapunov function for (2.6) if:*

- *It is a Lyapunov function candidate, so $V(\boldsymbol{x}) \succ 0$ in X_0 following Definition 8.*
- *Its time derivative $\dot{V}(\boldsymbol{x}) \preceq 0$ in X_0, following Definitions 5 and 9.*

Additionally, if $X_0 = \mathbb{R}^n$, then V is sometimes called a global Lyapunov function and if $X_0 \neq \mathbb{R}^n$ then V is sometimes called a local Lyapunov function of the system (2.6).

The level sets of a Lyapunov function that satisfy these conditions, form invariant sets. This means that trajectories that start in such a set will remain there for all time. If the inequality on the time derivative is strict such that $\dot{V}(\boldsymbol{x}) \prec 0$ for some level sets of V, then these level sets are subsets of the so-called domain of attraction (DOA).

Definition 11. *(Domain of attraction, cf. [149, p. 122]) Let $\boldsymbol{\varphi}(t, t_0, \boldsymbol{x}_0)$ denote the solution of system (2.6) starting at t_0 with initial condition $\boldsymbol{x}_0$. Let, without loss of generality, $\mathbf{0}_n$ be an equilibrium. Then,*

$$\mathcal{D} \stackrel{\text{def}}{=} \{t_0 \in \mathbb{R}_0^+, \boldsymbol{x}_0 \in \mathbb{R}^n : \lim_{t\to\infty} \boldsymbol{\varphi}(t, t_0, \boldsymbol{x}_0) = \mathbf{0}_n\} \tag{2.9}$$

is called the DOA of $\mathbf{0}_n$. Common synonyms in the literature for the DOA are basin of attraction or region of convergence/stability.

A subset of the DOA, $\Omega_0 \subseteq \Omega_c \subseteq \mathcal{D}$ of (2.6) can be computed given a Lyapunov function V by

$$\Omega_0 \subseteq \Omega_c \stackrel{\text{def}}{=} \{\boldsymbol{x} \in \Omega : V(\boldsymbol{x}) < c\}\,, \tag{2.10}$$

where $\Omega \stackrel{\text{def}}{=} \{\boldsymbol{x} \in \mathbb{R}^n : V(\boldsymbol{x}) > 0, \dot{V}(\boldsymbol{x}) \leq 0\} \cup \{\mathbf{0}_n\}$, Ω_c is assumed to be bounded and Ω_0 is the maximal connected component of the level set Ω_c with $\mathbf{0}_n \in \Omega_0$. If the set $\{\boldsymbol{x} \in \Omega_c : \dot{V}(\boldsymbol{x}) = 0\}$ within Ω_c contains no solutions of (2.6) except the zero solution, then $\mathbf{0}_n$ is asymptotically stable and Ω_0 is a subset of the DOA, cf. [256, pp. 72–73]. By the Lyapunov stability theorems, see [185] and [149, pp. 112–126], the origin of (2.6) is stable if there exists a Lyapunov function according to Definition 10. For global (asymptotic) stability, the conditions $V(\boldsymbol{x}) \succ 0$ and $\dot{V}(\boldsymbol{x}) \preceq 0$ (or rather $\dot{V}(\boldsymbol{x}) \prec 0$) must hold for all $\boldsymbol{x} \in \mathbb{R}^n$ and additionally, V must be radially unbounded.

Definition 12. *(Radially unbounded function, cf. [149, p. 123]) A function $V : \mathbb{R}^n \to \mathbb{R}$ is called radially unbounded if from $\|\boldsymbol{x}\| \to \infty$ follows that $V(\boldsymbol{x}) \to \infty$.*

For example, a quadratic form like (2.7) is always radially unbounded if it is positive definite. The methods discussed so far can also be applied to the analysis of non-autonomous systems, when $\boldsymbol{f} : [0, \infty) \times \mathbb{R}^n \to \mathbb{R}^n$ is an explicit function of time with

$$\dot{\boldsymbol{x}} = \boldsymbol{f}(t, \boldsymbol{x})\,. \tag{2.11}$$

If $\exists V(t, \boldsymbol{x})$ with $W_1(\boldsymbol{x}) \leq V(t, \boldsymbol{x}) \leq W_2(\boldsymbol{x})$ with $W_1(\boldsymbol{x}) \succ 0$, $W_2(\boldsymbol{x}) \succ 0$ and time derivative

$$\dot{V}(t, \boldsymbol{x}) \stackrel{\text{def}}{=} \frac{\partial V(t, \boldsymbol{x})}{\partial t} + \frac{\partial V(t, \boldsymbol{x})}{\partial \boldsymbol{x}} \boldsymbol{f}(t, \boldsymbol{x}) \leq -W_3(\boldsymbol{x})\,, \tag{2.12}$$

where $W_3(\boldsymbol{x}) \succeq 0$, each condition being true for all $\boldsymbol{x} \in X_0$, then (2.11) is stable, if $W_3(\boldsymbol{x}) \succ 0$ then it is also asymptotically stable. These results hold globally if $X_0 = \mathbb{R}^n$ and W_1 is radially unbounded [149, pp. 147–155]. Finally, exponential stability for system (2.11) can be asserted if

$$k_1 \|\boldsymbol{x}\|^\alpha \leq V(t, \boldsymbol{x}) \leq k_2 \|\boldsymbol{x}\|^\alpha \tag{2.13a}$$

$$\dot{V}(t, \boldsymbol{x}) \leq -k_3 \|\boldsymbol{x}\|^\alpha \tag{2.13b}$$

where $k_1, k_2, k_3, \alpha > 0$. The norm of the system trajectories is then guaranteed to be bounded by the exponentially decaying function

$$\|\boldsymbol{x}(t)\| \leq c_d \|\boldsymbol{x}(t_0)\| \exp\left(-r_d(t - t_0)\right), \tag{2.14}$$

compare [149, p. 154]. In (2.14), the decay coefficient c_d and decay rate r_d are given by

$$c_d = (k_2/k_1)^{1/\alpha} \tag{2.15a}$$

$$r_d = k_3/(k_2\alpha)\,. \tag{2.15b}$$

If conditions (2.13a)-(2.13b) hold for all $\boldsymbol{x} \in \mathbb{R}^n$, then global exponential stability follows. A useful extension to the Lyapunov stability theorems is LaSalle's invariance principle [256, pp. 68–73], which can be used to show asymptotic stability of (2.6) even if $\dot{V}$ is only negative semi-definite, as already indicated by the statements below Equation (2.10). Let

$$S \stackrel{\text{def}}{=} \{\boldsymbol{x} \in \mathbb{R}^n : \dot{V}(\boldsymbol{x}) = 0\}\,. \tag{2.16}$$

If no trajectory other than the zero solution can stay in S, then the system is asymptotically stable, see also [149, pp. 126–129]. A limitation of the invariance principle is, that it can only be applied to autonomous systems like (2.6), but not to time-varying systems like (2.11).

An important class of dynamical systems are linear time-invariant (LTI) systems, which are ODEs of the form

$$\dot{\boldsymbol{x}} = \boldsymbol{A}\boldsymbol{x} \tag{2.17}$$

with $\boldsymbol{x} \in \mathbb{R}^n$ and $\boldsymbol{A} \in \mathbb{R}^{n\times n}$. These systems have the advantage that there exist many theoretical and practical results in the literature dealing with LTI systems, making analysis of such systems often significantly easier than for general nonlinear systems like (2.6). For example, the stability analysis can be done by solving the Lyapunov equation, which gives an explicit Lyapunov function for the system (2.17).

Definition 13. *(Lyapunov equation, cf. [149, pp. 135–137]) Let $\boldsymbol{A} \in \mathbb{R}^{n\times n}$ and $\boldsymbol{Q} = \boldsymbol{Q}^T \in \mathbb{R}^{n\times n}$ with $\boldsymbol{Q} \succ 0$. Then,*

$$\boldsymbol{A}^T\boldsymbol{P} + \boldsymbol{P}\boldsymbol{A} = -\boldsymbol{Q} \tag{2.18}$$

is called Lyapunov equation in the symmetric matrix variable $\boldsymbol{P} = \boldsymbol{P}^T \in \mathbb{R}^{n\times n}$, with $\boldsymbol{P} \succ 0$.

This equation has a unique positive definite solution $\boldsymbol{P}$ for every $\boldsymbol{Q} \succ 0$ only if (2.17) is asymptotically stable[4]. A Lyapunov function for (2.17) is then given by $V(\boldsymbol{x}) = \boldsymbol{x}^T\boldsymbol{P}\boldsymbol{x}$ with the negative definite time derivative $\dot{V}(\boldsymbol{x}) = -\boldsymbol{x}^T\boldsymbol{Q}\boldsymbol{x}$. From this it can also be seen that every asymptotically stable LTI system is globally exponentially stable, as for a positive definite $\boldsymbol{P}$, it holds that $\lambda_{\min}(\boldsymbol{P})\boldsymbol{x}^T\boldsymbol{x} \leq \boldsymbol{x}^T\boldsymbol{P}\boldsymbol{x} \leq \lambda_{\max}(\boldsymbol{P})\boldsymbol{x}^T\boldsymbol{x}$ and so also that $-\boldsymbol{x}^T\boldsymbol{Q}\boldsymbol{x} \leq -\lambda_{\min}(\boldsymbol{Q})\boldsymbol{x}^T\boldsymbol{x}$ where $\lambda_{\min}(\cdot)$ and $\lambda_{\max}(\cdot)$ denote the minimum and maximum eigenvalue of its symmetric, matrix valued argument [149, p. 145]. Since $\boldsymbol{P}$ and $\boldsymbol{Q}$ are symmetric, their eigenvalues are real numbers. The Lyapunov equation is also closely related to the eigenvalues of the system matrix $\boldsymbol{A}$ of (2.17), as it has a positive definite solution if and only if $\boldsymbol{A}$ is Hurwitz [149, pp. 133–137].

Definition 14. *(Hurwitz matrix, cf. [246, 118]) A matrix $\boldsymbol{A} \in \mathbb{R}^{n\times n}$ is called Hurwitz matrix if $\Re\big(\lambda_i(\boldsymbol{A})\big) < 0\,, \forall i \in \{1,\dots,n\}$, where $\lambda_i(\boldsymbol{A})$ denotes the i-th eigenvalue of $\boldsymbol{A}$ and $\Re(\cdot)$ the real part of its complex argument.*

An important property of an LTI system (2.17) is, that it is globally exponentially stable if and only if $\boldsymbol{A}$ is Hurwitz. However, for control not only stability of unforced systems like (2.6) or (2.17) is of interest, but especially the analysis of systems with inputs, like

$$\dot{\boldsymbol{x}} = \boldsymbol{f}(t, \boldsymbol{x}, \boldsymbol{u})\,. \tag{2.19}$$

Here, $\boldsymbol{x} \in \mathbb{R}^n$ is the state, $\boldsymbol{u} \in \mathbb{R}^m$ the input of the system, while $\boldsymbol{f} : [0,\infty) \times \mathbb{R}^n \times \mathbb{R}^m \to \mathbb{R}^n$ is the vector field. It is assumed that $\boldsymbol{f}$ is piecewise continuous in t, locally Lipschitz in $\boldsymbol{x}$ and $\boldsymbol{u}$ and that $\boldsymbol{f}(t, \boldsymbol{0}_n, \boldsymbol{0}_m) = \boldsymbol{0}_n$. Given a system like (2.19), it is of interest to verify that bounded inputs are guaranteed to result in bounded states. Generally, this property cannot be concluded by looking at the unforced system with $\boldsymbol{u} = \boldsymbol{0}_m$ only, as (2.19) can be unstable even if the unforced system is globally exponentially stable [149, pp. 174–175]. This motivates the notion of input-to-state stable (ISS) stability, first proposed by Sontag [258]. For this property, the definition of comparison functions is convenient.

Definition 15. *(Comparison functions, cf. [149, p. 144]) Let $\alpha : [0,a) \to [0,\infty)$ and $\beta : [0,a) \times [0,\infty] \to [0,\infty)$ be continuous functions. Then:*

- *The function α belongs to class $\mathcal{K}$ if $\alpha(0) = 0$ and it is strictly increasing.*
- *The function α belongs to class $\mathcal{K}_\infty$ if it is in class $\mathcal{K}$ with $a = \infty$ and $\lim_{r\to\infty} \alpha(r) \to \infty$.*
- *The function β belongs to class $\mathcal{KL}$ if $\forall q \in \mathbb{R}_0^+$, $\beta(r,q)$ is in class $\mathcal{K}$ and $\forall r \in [0,a)$, the function is decreasing and $\lim_{q\to\infty} \beta(r,q) \to 0$.*

[4] Positive definiteness of $\boldsymbol{Q}$ is not strictly required, as it is sufficient to take $\boldsymbol{Q} = \boldsymbol{C}^T\boldsymbol{C} \succeq 0$ (positive semi-definite) with $(\boldsymbol{A}, \boldsymbol{C})$ observable, in order to ensure that Equation (2.18) has a positive definite solution [149, p. 137].

The ISS property can be defined with the help of these classes of comparison functions.

Definition 16. *(Input-to-state stability, cf. [149, p. 175]) The system (2.19) is called input-to-state stable (ISS) if there exists a class $\mathcal{KL}$ function β and a class $\mathcal{K}$ function γ such that $\forall \boldsymbol{x}_0 \in \mathbb{R}^n$ and piecewise continuous bounded $\boldsymbol{u}(t)$, the inequality*

$$\|\boldsymbol{x}(t)\| \leq \beta(\|\boldsymbol{x}_0\|, t) + \gamma(\|\boldsymbol{u}(\tau)\|_\infty) \tag{2.20}$$

is satisfied for all $t \geq 0$, where $\|\boldsymbol{u}(\tau)\|_\infty \stackrel{\text{def}}{=} \sup_{0\leq\tau\leq t} \|\boldsymbol{u}(t)\|$.

One way to formally show this inequality holds is by the use of ISS-Lyapunov functions, which can be similarly used for proving stability as in the unforced case.

Definition 17. *(ISS-Lyapunov function, cf. [149, p. 176]) A C^1 function $V : [0, \infty) \times \mathbb{R}^n \to \mathbb{R}$ is called an ISS-Lyapunov function for (2.19) if $\alpha_1(\|\boldsymbol{x}\|) \leq V(t, \boldsymbol{x}) \leq \alpha_2(\|\boldsymbol{x}\|)$ and*

$$\dot{V}(t, \boldsymbol{x}, \boldsymbol{u}) \stackrel{\text{def}}{=} \frac{\partial V(t, \boldsymbol{x})}{\partial t} + \frac{\partial V(t, \boldsymbol{x})}{\partial \boldsymbol{x}} \boldsymbol{f}(t, \boldsymbol{x}, \boldsymbol{u}) \leq -W_3(\boldsymbol{x}) \,, \forall \|\boldsymbol{x}\| \geq \rho(\|\boldsymbol{u}\|) > 0 \tag{2.21}$$

where α_1, α_2 are in class $\mathcal{K}_\infty$, ρ is in class $\mathcal{K}$, W_3 is continuous and $W_3(\boldsymbol{x}) \succ 0$ on $\mathbb{R}^n$.

If there exists an ISS-Lyapunov function for a system (2.19), then the system is ISS with gain function $\gamma = \alpha_1^{-1} \circ \alpha_2 \circ \rho$. When the system is autonomous, this sufficient condition for input-to-state stability is also necessary [149, p. 176].

While the properties discussed so far deal with dynamical systems in the time domain, another important tool for control engineering is the frequency domain. Considering an LTI system in the time domain of the form

$$\dot{\boldsymbol{x}} = \boldsymbol{A}\boldsymbol{x} + \boldsymbol{B}\boldsymbol{u} \tag{2.22a}$$

$$\boldsymbol{y} = \boldsymbol{C}\boldsymbol{x} + \boldsymbol{D}\boldsymbol{u} \,, \tag{2.22b}$$

with state $\boldsymbol{x} \in \mathbb{R}^n$, input $\boldsymbol{u} \in \mathbb{R}^m$, output $\boldsymbol{y} \in \mathbb{R}^p$, system matrix $\boldsymbol{A} \in \mathbb{R}^{n\times n}$, input matrix $\boldsymbol{B} \in \mathbb{R}^{n\times m}$, output matrix $\boldsymbol{C} \in \mathbb{R}^{p\times n}$ and feedthrough matrix $\boldsymbol{D} \in \mathbb{R}^{p\times m}$. This system can be converted from the time domain to a rational transfer function matrix in the frequency domain using the Laplace transformation [70, pp. 479–612].

Definition 18. *(Rational transfer function matrix, cf. [70, p. 503]) Given an LTI system as in (2.22). Its transfer function matrix is given by $\boldsymbol{G}(s) = \boldsymbol{C}(s\boldsymbol{I}_n - \boldsymbol{A})^{-1}\boldsymbol{B} + \boldsymbol{D}$, where $\boldsymbol{I}_n$ denotes the $n \times n$-identity matrix and $s = \sigma + j\omega \in \mathbb{C}$ the complex Laplace variable.*

This enables the use of various frequency domain tools for system analysis and design. It can be noted that while (2.22) might appear to be only useful for purely linear systems, this representation is often useful for nonlinear systems as well. Considering a nonlinear system like

$$\dot{\boldsymbol{x}} = \boldsymbol{f}(\boldsymbol{x}, \boldsymbol{u}) \tag{2.23a}$$

$$\boldsymbol{y} = \boldsymbol{h}(\boldsymbol{x}, \boldsymbol{u}) \,, \tag{2.23b}$$

again with state $\boldsymbol{x} \in \mathbb{R}^n$, input $\boldsymbol{u} \in \mathbb{R}^m$, output $\boldsymbol{y} \in \mathbb{R}^p$, vector field $\boldsymbol{f} : \mathbb{R}^n \times \mathbb{R}^m \to \mathbb{R}^n$ and measurement function $\boldsymbol{h} : \mathbb{R}^n \times \mathbb{R}^m \to \mathbb{R}^p$, where $\boldsymbol{f}, \boldsymbol{h} \in C^1$ and equilibrium at $\boldsymbol{x}^*, \boldsymbol{u}^*$ such that $\boldsymbol{f}(\boldsymbol{x}^*, \boldsymbol{u}^*) = \boldsymbol{0}_n$. Then, (2.23) can be approximated locally around that equilibrium by $\delta\dot{\boldsymbol{x}} = \boldsymbol{A}\delta\boldsymbol{x} + \boldsymbol{B}\delta\boldsymbol{u}$, $\delta\boldsymbol{y} = \boldsymbol{C}\delta\boldsymbol{x} + \boldsymbol{D}\delta\boldsymbol{u}$ with $\delta\boldsymbol{x} = \boldsymbol{x} - \boldsymbol{x}^*$, $\delta\boldsymbol{u} = \boldsymbol{u} - \boldsymbol{u}^*$ and $\delta\boldsymbol{y} = \boldsymbol{y} - \boldsymbol{h}(\boldsymbol{x}^*, \boldsymbol{u}^*)$. Moreover, $\boldsymbol{A} = \boldsymbol{J}_{\boldsymbol{f},\boldsymbol{x}}(\boldsymbol{x}^*, \boldsymbol{u}^*)$, $\boldsymbol{B} = \boldsymbol{J}_{\boldsymbol{f},\boldsymbol{u}}(\boldsymbol{x}^*, \boldsymbol{u}^*)$, $\boldsymbol{C} = \boldsymbol{J}_{\boldsymbol{h},\boldsymbol{x}}(\boldsymbol{x}^*, \boldsymbol{u}^*)$, $\boldsymbol{D} = \boldsymbol{J}_{\boldsymbol{h},\boldsymbol{u}}(\boldsymbol{x}^*, \boldsymbol{u}^*)$ where

$$\boldsymbol{J}_{\boldsymbol{f},\boldsymbol{x}}(\boldsymbol{x}^*, \boldsymbol{u}^*) \stackrel{\text{def}}{=} \left[\frac{\partial \boldsymbol{f}(\boldsymbol{x}, \boldsymbol{u})}{\partial \boldsymbol{x}}\right]\Big|_{\boldsymbol{x}=\boldsymbol{x}^*, \boldsymbol{u}=\boldsymbol{u}^*} \tag{2.24}$$

denotes the Jacobian of $\boldsymbol{f}$ with respect to $\boldsymbol{x}$, evaluated at $\boldsymbol{x} = \boldsymbol{x}^*$, $\boldsymbol{u} = \boldsymbol{u}^*$. This technique, known as Jacobian linearization [256, p. 207], approximates the nonlinear functions in (2.23) by neglecting higher order terms of their Taylor series, see [256, pp. 53–57] and [149, pp. 51–54].

By the linearization method of Lyapunov, also known as indirect or first method of Lyapunov, the nonlinear system (2.23) has a locally exponentially stable equilibrium at $\boldsymbol{x} = \boldsymbol{x}^*$, $\boldsymbol{u} = \boldsymbol{u}^*$ if $\boldsymbol{A} = \boldsymbol{J}_{\boldsymbol{f},\boldsymbol{x}}(\boldsymbol{x}^*, \boldsymbol{u}^*)$ is Hurwitz. This provides a theoretical justification for the (local) validity of nonlinear system approximations based on Jacobian linearization [256, pp. 53–57].

The advantage of a transfer function representation of the system is, that there exist numerous intuitive tools for control system analysis and design. Examples include Bode diagrams, cf. [216, pp. 403–427], Nyquist plots, cf. [216, pp. 427–443], root-locus plots, cf. [216, pp. 270–290] or the Ziegler-Nichols tuning rules for PID controller design, cf. [216, pp. 568–577]. Also, there are formulas available for interconnections of transfer functions, cf. [216, pp. 17–29]. It can be noted that Definition 18 applies for general MIMO LTI systems, having an $m \times p$ transfer function matrix $\boldsymbol{G}(s)$. For the remainder of this introduction we focus on SISO transfer functions $G(s)$, such that $m = p = 1$. Following, we consider the closed loop block diagram shown in Figure 2.4.

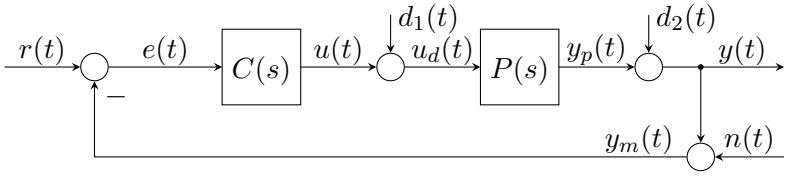

Figure 2.4: Single-input, single-output closed loop control system [303].

Here, $P(s)$ is the plant transfer function and $C(s)$ the transfer function of the controller. Furthermore, r is the reference input, e the control error, u the controller output, d_1 the input or load disturbance, u_d the plant input, y_p the plant output, d_2 the output disturbance, y the system output, n a measurement noise signal and y_m the measured system output. One relevant question, assuming first $d_1(t) = d_2(t) = n(t) = 0$, is whether the output can asymptotically track the reference input, such that $y(t) \to r(t)$ as $t \to \infty$. If $r(t)$ is a polynomial of degree k, like $r(t) = t^k/k!$, the steady-state control error depends on the system type number.

Definition 19. *(Linear system type number, cf. [216, pp. 225–226]) Let $G(s) = N(s)/D(s)$ be a rational SISO transfer function where $N(s)$ and $D(s)$ are polynomials in s. The multiplicity of the root $s = 0$ of $D(s)$ is the system type number of $G(s)$. If $s = 0$ is not a root of $D(s)$, the system type number is zero. A system with system type number $d \in \mathbb{N}_0$ is called a type d system.*

For example, the double integrator $1/s^2$ is a type 2 system, while a low-pass of the form $1/(s+1)$ is a type 0 system. The system type number can be used to obtain the error constant and steady state error of the closed loop system from Figure 2.4.

Definition 20. *(Error constant and steady-state error, cf. [70, pp. 217–219]) Given the LTI close loop control system from Figure 2.4. Let $d_1(t) = d_2(t) = n(t) = 0$ and $r(t) = H(t)t^k/k!$ with $k \in \mathbb{N}_0$ and $H(t)$ the Heaviside (unit step) function. Let further $d \in \mathbb{N}_0$ denote the system type number of the open loop transfer function $L(s) = C(s)P(s)$. Then, the error constant K_d and steady-state error e_{ss} of the system are*

$$K_d = \lim_{s \to 0} s^d L(s) \tag{2.25a}$$

$$e_{ss} = \lim_{t \to \infty} e(t) = \lim_{s \to 0} \frac{s^d}{s^d + K_d} \frac{1}{s^k}\,. \tag{2.25b}$$

In the literature, K_0, K_1 and K_2 are also called position, velocity and acceleration error constants.

So if $k = 0$ then $r(t)$ is a unit step and hence $L(s) = C(s)P(s)$ should be a type 1 system in order to guarantee that the asymptotic tracking error (2.25b) approaches zero, so $e_{ss} = 0$.

More generally, the classification with type numbers can be considered as a special case of the so-called internal model principle, which is the basis for IMC. It states that in order to achieve tracking with zero asymptotic error, generally, a model that describes the reference signal is required, cf. [70, pp. 573–585]. In this work, focus is set on tracking of ramp-like reference trajectories, as this is the main use-case for TCSs. Table 2.1 shows the steady state errors of some reference signals, indicating that a TCS that controls angular velocity should realize an open loop type 2 system in order to achieve zero asymptotic tracking error with $e_{ss} = 0$.

Table 2.1: Steady-state errors for reference signals, adapted from Ogata [216, p. 230].

Reference Signal	**Step**	**Ramp**	**Parabola**	**Cubic curve**
Mechanical Interpretation	Position	Velocity	Acceleration	Jerk
System type d	e_{ss} [m]	e_{ss} [m/s]	e_{ss} [m/s^2]	e_{ss} [m/s^3]
Type 0	$1/(1+K_0)$	∞	∞	∞
Type 1	0	$1/K_1$	∞	∞
Type 2	0	0	$1/K_2$	∞
Type 3	0	0	0	$1/K_3$

However, tracking is not the only task of a control system. In general, $d_1(t)$, $d_2(t)$ and $n(t)$ in Figure 2.4 are nonzero, so good rejection of disturbances and measurement noise is required as well. One approach to achieve this is with sensitivity functions, also called "gang of four" ("gang of six" if a reference signal filter is added to the block diagram in Figure 2.4).

Definition 21. *(Gang of four, cf. [262, pp. 177–214]) Let $C(s)$ and $P(s)$ be controller and plant in feedback connection as shown in Figure 2.4. Denote with $L(s) = C(s)P(s)$ the open loop transfer function. Define:*

- $T(s) = L(s)/(1 + L(s))$, *the complementary sensitivity function.*
- $S(s) = 1/(1 + L(s))$, *the sensitivity function.*
- $S_C(s) = C(s)/(1 + L(s))$, *the input/load disturbance function.*
- $S_P(s) = P(s)/(1 + L(s))$, *the output disturbance sensitivity function.*

Generally, a closed loop system as shown in Figure 2.4 can be stable for $d_1(t) = d_2(t) = n(t) = 0$, but is actually unstable for nonzero disturbances or measurement noise. Systems that do not have this problem are called internally stable. A necessary and sufficient condition for internal stability is provided by the following definition.

Definition 22. *(Internal stability, cf. [1, p. 137]) Let $L(s) = C(s)P(s)$ be the open loop transfer of the setup in Figure 2.4. The closed loop system is internally stable, if and only if:*

- *The transfer function $1 + L(s)$ has no zeros with $\Re(s) \geq 0$.*
- *No pole-zero cancellation occurs in $\Re(s) \geq 0$ when forming the product $C(s)P(s)$.*

This definition can be extended to internal Γ-stability, which requires the transfer function poles s_i being located in a specific region $\Gamma \subseteq \{s_i \in \mathbb{C} : \Re(s_i) < 0\}$ for performance specifications.

Definition 23. *(Internal Γ-stability, cf. [1, p. 137]) Given the same setup as in Definition 22. The closed loop system is internally Γ-stable, if and only if:*

- *The transfer function $1 + L(s)$ has no zeros with $\Re(s) \notin \Gamma$.*
- *No pole-zero cancellation occurs outside of Γ when forming the product $C(s)P(s)$.*

This is relevant for shaping the response of the system. Figure 2.5a shows an example Γ-region. The vertical line imposes a minimum response time, while the circle restricts the maximum bandwidth. The two sloped lines constrain the damping of the system.

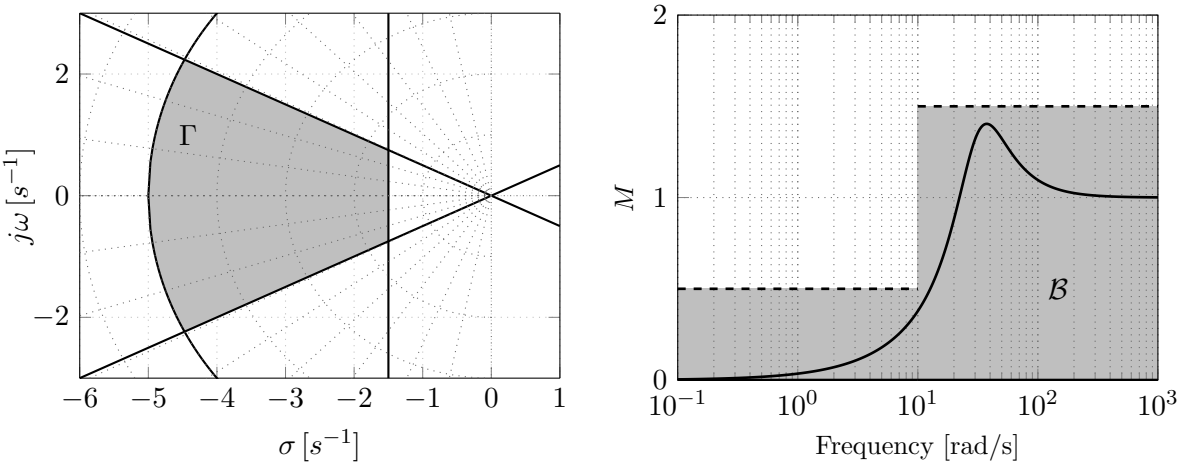

(a) Example Γ-region in grey. **(b)** Example $\mathcal{B}$-region in grey.

Figure 2.5: Example regions for transfer function performance specifications [303].

Another common method for performance specification is to constrain the frequency response magnitude (FRM) of a system to realize a specific behavior over a frequency range.

Definition 24. *(Frequency response magnitude, cf. [1, p. 132]) The FRM of a transfer function $F(s)$ in a frequency interval $\Omega_{\text{int}} = \{\omega \in \mathbb{R}_0^+ : 0 \leq \omega^- \leq \omega \leq \omega^+\}$ is $M_F = \sup_{\omega \in \Omega_{\text{int}}} |F(j\omega)|$.*

The FRM of a transfer function can then be constrained, as an additional design goal, to be located in some region $\mathcal{B}$, which is defined in terms of its boundary function.

Definition 25. *($\mathcal{B}$-region, cf. [1, pp. 139–140]) The $\mathcal{B}$-region, with boundaries $\partial\mathcal{B}_i : \Omega_{\text{int}} \to \mathbb{R}_0^+$, $i \in \{1, 2\}$ in the (ω, M) plane, is given by $\mathcal{B} = \{(\omega, M) \in \Omega_{\text{int}} \times \mathbb{R}_0^+ : \partial\mathcal{B}_1(\omega) < M < \partial\mathcal{B}_2(\omega)\}$.*

The boundary function can be defined for example by piecewise horizontal line segments or in terms of the frequency response of another transfer function [1, pp. 139–140]. This leads to the definition of $\mathcal{B}$-stability of a transfer function on a certain frequency interval.

Definition 26. *($\mathcal{B}$-stability, cf. [1, p. 149]) A transfer function $F(s)$ is called $\mathcal{B}$-stable in the frequency interval Ω_{int} if $|F(j\omega)| \in \mathcal{B}\,, \forall\omega \in \Omega_{\text{int}}$.*

Figure 2.5b shows an example $\mathcal{B}$-region and the FRM of a sensitivity function $S(s)$ which is $\mathcal{B}$-stable with respect to that specific region. There are different tuning rules available to achieve good tracking, disturbance attenuation and noise rejection with limited control effort by definition of appropriate FRMs. For example, good tracking in the frequency range $0 \leq \omega \leq \omega_S$ as well as output disturbance attenuation is achieved if $|S(j\omega)| \ll 1\,, \forall\omega \in [0, \omega_S]$, while input disturbances are attenuated within the same range if $|S_P(j\omega)| \ll 1\,, \forall\omega \in [0, \omega_S]$ and measurement noise is rejected in the range $\omega_T \leq \omega < \infty$ if $|T(j\omega)| \ll 1\,, \forall\omega \in [\omega_T, \infty)$, see [1, pp. 138–141]. In general, these are competing design goals, so the control engineer has to choose a compromise between performance and robustness [1, pp. 147–148], see also [215] and [214, pp. 27–62].

This concludes the preliminaries on stability analysis of general nonlinear systems in the time domain and linear systems in the frequency domain. In the following, an introduction to the more specific system class of so-called Lur'e systems and the concept of absolute stability is given. Also, the related concepts of passivity, positive-realness and the Kalman-Yakubovich-Popov Lemma are briefly discussed. These will be important for the stability analysis of the proposed TCSs.

2.2.2 Absolute Stability, Lur'e Systems and Passivity

In this section, some background on absolute stability of Lur'e systems and passivity is given. It is based on the summary of the state of the art in our publication [306], which is mainly based on the textbook by Khalil [149]. The term "absolute stability" is strongly linked with a specific class of nonlinear dynamical systems, the so-called Lur'e systems, first proposed by Lur'e and Postnikow in 1944 [184]. This system class will play an important role for the stability analysis of TCSs. Figure 2.6 shows the structure of a general Lur'e system, which consists of an LTI system in negative feedback with a memoryless, static but possibly time-varying, nonlinear function that is subject to a sector condition.

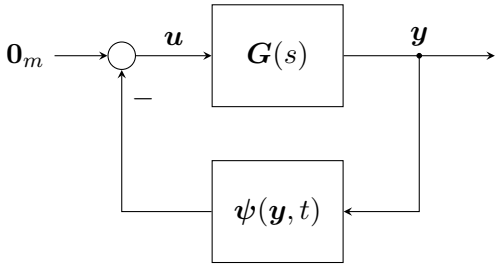

Figure 2.6: General feedback structure of a Lur'e system [306].

This feedback connection can be expressed in the time domain, with $\boldsymbol{x} \in \mathbb{R}^n$, $\boldsymbol{u} \in \mathbb{R}^m$, $\boldsymbol{y} \in \mathbb{R}^p$, $\boldsymbol{A} \in \mathbb{R}^{n\times n}$, $\boldsymbol{B} \in \mathbb{R}^{n\times m}$, $\boldsymbol{C} \in \mathbb{R}^{p\times n}$, $\boldsymbol{D} \in \mathbb{R}^{p\times m}$ and $\boldsymbol{\psi} : \mathbb{R}^p \times \mathbb{R}_0^+ \to \mathbb{R}^m$ by

$$\dot{\boldsymbol{x}} = \boldsymbol{A}\boldsymbol{x} + \boldsymbol{B}\boldsymbol{u} \tag{2.26a}$$
$$\boldsymbol{y} = \boldsymbol{C}\boldsymbol{x} + \boldsymbol{D}\boldsymbol{u} \tag{2.26b}$$
$$\boldsymbol{u} = -\boldsymbol{\psi}(\boldsymbol{y},t)\,, \tag{2.26c}$$

where $(\boldsymbol{A},\boldsymbol{B})$ is controllable and $(\boldsymbol{A},\boldsymbol{C})$ observable. Moreover, the algebraic loop $\boldsymbol{u} = -\boldsymbol{\psi}(\boldsymbol{y},t)$ must have a unique solution $\forall t, \boldsymbol{u}$ and $\boldsymbol{G}(s) = \boldsymbol{C}(s\boldsymbol{I}_n - \boldsymbol{A})^{-1}\boldsymbol{B} + \boldsymbol{D}$ is square ($m = p$) and proper. Finally, the nonlinearity $\boldsymbol{\psi}$ is locally Lipschitz in $\boldsymbol{y}$, piecewise continuous in t, satisfies $\boldsymbol{\psi}(\mathbf{0}_p, t) = \mathbf{0}_m\,, \forall t \in \mathbb{R}_0^+$ and, in addition, a so-called sector condition [149, p. 264]. In literature, there are two commonly used conditions, the first one is sector boundedness.

Definition 27. *(Sector boundedness, cf. [149, pp. 232–233]) Let $\boldsymbol{\psi} : \mathbb{R}^p \times \mathbb{R}_0^+ \to \mathbb{R}^m$ be a memoryless function with $\boldsymbol{\psi}(\mathbf{0}_p, t) = \mathbf{0}_m\,, \forall t \in \mathbb{R}_0^+$ and $\boldsymbol{K} = \boldsymbol{K}_2 - \boldsymbol{K}_1 = \boldsymbol{K}^T \succ 0$ with $\boldsymbol{K}_1$, $\boldsymbol{K}_2 \in \mathbb{R}^{p\times p}$ and $m = p$. Then, $\boldsymbol{\psi}$ is said to belong to the sector:*

- $[\mathbf{0}, \boldsymbol{\infty}]$*, if* $\boldsymbol{y}^T\boldsymbol{\psi}(\boldsymbol{y},t) \geq 0$*, denoted with* $\boldsymbol{\psi} \in \operatorname{sec}[\mathbf{0}, \boldsymbol{\infty}]$.
- $[\boldsymbol{K}_1, \boldsymbol{\infty}]$*, if* $\boldsymbol{y}^T\big(\boldsymbol{\psi}(\boldsymbol{y},t) - \boldsymbol{K}_1\boldsymbol{y}\big) \geq 0$*, denoted with* $\boldsymbol{\psi} \in \operatorname{sec}[\boldsymbol{K}_1, \boldsymbol{\infty}]$.
- $[\mathbf{0}, \boldsymbol{K}_2]$*, if* $\boldsymbol{\psi}(\boldsymbol{y},t)^T\big(\boldsymbol{\psi}(\boldsymbol{y},t) - \boldsymbol{K}_2\boldsymbol{y}\big) \leq 0$*, denoted with* $\boldsymbol{\psi} \in \operatorname{sec}[\mathbf{0}, \boldsymbol{K}_2]$ *where* $\boldsymbol{K}_2 = \boldsymbol{K}_2^T \succ 0$.
- $[\boldsymbol{K}_1, \boldsymbol{K}_2]$ *if* $\big(\boldsymbol{\psi}(\boldsymbol{y},t) - \boldsymbol{K}_1\boldsymbol{y}\big)^T\big(\boldsymbol{\psi}(\boldsymbol{y},t) - \boldsymbol{K}_2\boldsymbol{y}\big) \leq 0$*, denoted with* $\boldsymbol{\psi} \in \operatorname{sec}[\boldsymbol{K}_1, \boldsymbol{K}_2]$.

These inequalities are supposed to hold for all $\boldsymbol{y} \in \mathbb{R}^p$ and $t \in \mathbb{R}_0^+$. The dimension indices for zero and the infinite sectors (both of dimension $p \times p$) are omitted here for a more compact notation.

A function $\boldsymbol{\psi} \in \operatorname{sec}[\mathbf{0}, \boldsymbol{\infty}]$ is also called passive. Functions belonging to the other sectors mentioned in Definition 27 can be transformed to the sector $[\mathbf{0}, \boldsymbol{\infty}]$ by appropriate input-feedforward and output feedback loop transformation, see [149, pp. 228–233] and [149, pp. 264–270]. Therefore, a function $\boldsymbol{\psi} \in \operatorname{sec}[\boldsymbol{K}_1, \boldsymbol{\infty}]$ is also called input feed-forward passive (IFP), while a function $\boldsymbol{\psi} \in \operatorname{sec}[\mathbf{0}, \boldsymbol{K}_2]$ is also called output feedback passive (OFP).

The sector conditions are visualized for the SISO case, when $p = m = 1$, as follows. Figure 2.7a displays an example nonlinearity, which is sector bounded like $\big(\psi(y) - k_1 y\big)\big(\psi(y) - k_2 y\big) \leq 0$ with

$0 < k_1 < k_2 < \infty$, such that $\psi \in \text{sec}[k_1, k_2]$. In Figure 2.7a it can be seen that such a function is restricted to the first and third quadrant and passes through the origin. As indicated in Figure 2.1a, this applies to the nonlinear tire friction force, a fact that will be used later.

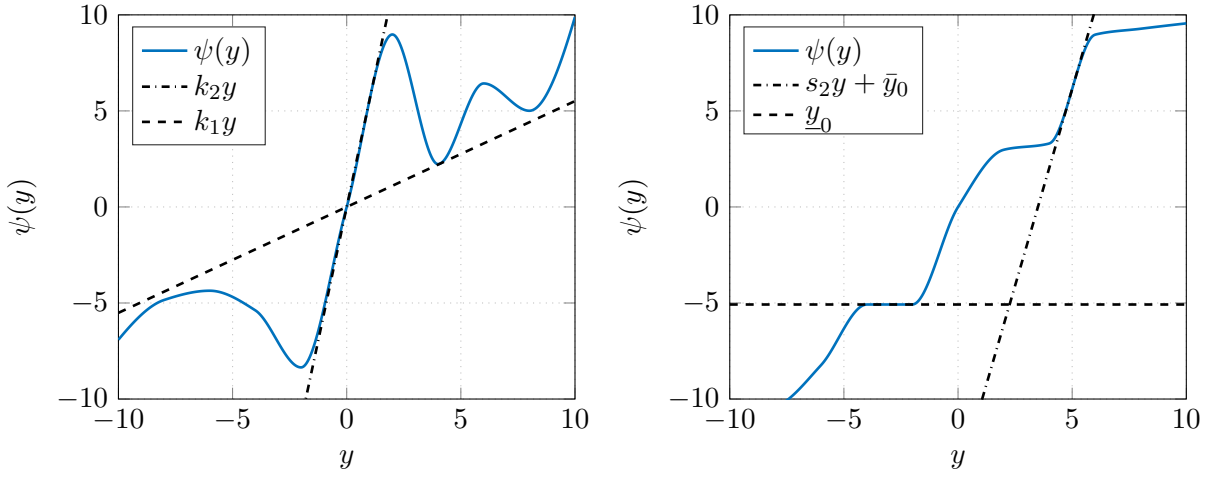

(a) Sector bounded ψ.

(b) Slope restricted ψ.

Figure 2.7: Examples of a sector bounded and a slope restricted nonlinear static function [306].

Figure 2.7b shows an example of the second commonly used, more restrictive sector condition, which requires that the nonlinearity is slope restricted.

Definition 28. *(Slope restrictedness, cf. [109]) Let* $\boldsymbol{\psi} : \mathbb{R}^p \to \mathbb{R}^m$ *with* $\boldsymbol{\psi}(\mathbf{0}_p) = \mathbf{0}_m$, $m = p$ *and* $(\boldsymbol{\psi}(\boldsymbol{y}) - \boldsymbol{\psi}(\hat{\boldsymbol{y}}) - s_1(\boldsymbol{y} - \hat{\boldsymbol{y}}))^T(\boldsymbol{\psi}(\boldsymbol{y}) - \boldsymbol{\psi}(\hat{\boldsymbol{y}}) - s_2(\boldsymbol{y} - \hat{\boldsymbol{y}})) \leq 0\,, \forall \boldsymbol{y}, \hat{\boldsymbol{y}} \in \mathbb{R}^p$ *with* $0 \leq s_1 < s_2 < \infty$. *Then* $\boldsymbol{\psi}$ *is called slope restricted to the interval* $[s_1, s_2]$, *denoted with* $\partial\boldsymbol{\psi} \in \text{sec}[s_1, s_2]$.

In the SISO case with $m = p = 1$, this reduces to the more commonly used definition, given by the inequality $s_1 \leq \big(\psi(y) - \psi(\hat{y})\big)/(y - \hat{y}) \leq s_2\,, \forall y, \hat{y} \in \mathbb{R}$ with $y \neq \hat{y}$, see also [3]. Figure 2.7b shows an example of a slope restricted function ψ with $\partial\psi \in \text{sec}[0, s_2]$, while the two tangent lines indicate its minimum and maximum slope, respectively. These sector conditions have motivated the notion of absolute stability of Lur'e systems.

Definition 29. *(Absolute stability, cf. [149, p. 265]) A Lur'e system (2.26a)-(2.26c) is called absolutely stable with respect to a sector condition if it is uniformly globally asymptotically stable for all nonlinear functions* $\boldsymbol{\psi} : \mathbb{R}^p \times \mathbb{R}_0^+ \to \mathbb{R}^m$, *with* $p = m$, *that satisfy the sector condition.*

Absolute stability can be considered as a strong robustness property, as it guarantees global asymptotic stability not only for a single, but rather for a whole class of nonlinear functions that satisfy the sector condition. The stability analysis of Lur'e systems motivated numerous subsequent research directions. Two famous early examples are the Aizerman conjecture [5] and the Kalman conjecture [143], two conjectures about stability of Lur'e systems that will be discussed in more detail in Section 4.4. One reason for the research interest in Lur'e systems is their practical relevance, as various systems can be expressed in the form (2.26a)-(2.26c). For example, LTI systems with control signal saturation and anti-windup [155], deadzone nonlinearity [171] or mechanical systems with stick-slip friction [51] can be analyzed with this formulation. The absolute stability of a Lur'e system can be analyzed for example with the circle criterion by Sandberg [250] and Zames [288], or for SISO nonlinearities that do not depend on time explicitly, by the Popov criterion [232]. For example, by the circle criterion, the Lur'e system (2.26) is absolutely stable if $\boldsymbol{\psi} \in \text{sec}[\boldsymbol{K}_1, \boldsymbol{K}_2]$, with $\boldsymbol{K} = \boldsymbol{K}_2 - \boldsymbol{K}_1 = \boldsymbol{K}^T \succ 0$ following Definition 27 and the transfer function $\big(\boldsymbol{I}_p + \boldsymbol{K}_2\boldsymbol{G}(s)\big)\big(\boldsymbol{I}_p + \boldsymbol{K}_1\boldsymbol{G}(s)\big)^T$ is strictly positive real [149, pp. 264–266].

Before stating the definition of the positive realness, the more general concept of passivity of dynamical systems is defined. This property is similar to the sector boundedness from Definition 27, which can be analogously applied to dynamical systems.

Definition 30. *(Passivity, cf. [149, p. 236]) A nonlinear system as defined in (2.23) is called passive if* $\exists V \in C^1$ *with* $V : \mathbb{R}^n \to \mathbb{R}$ *and* $V(\boldsymbol{x}) \succeq 0\,, \forall \boldsymbol{x} \in \mathbb{R}^n$ *such that* $\boldsymbol{u}^T\boldsymbol{y} \geq \dot{V}(\boldsymbol{x}, \boldsymbol{u})$ *is satisfied for all* $\boldsymbol{x} \in \mathbb{R}^n, \boldsymbol{u} \in \mathbb{R}^m$*. It is called strictly passive if* $\boldsymbol{u}^T\boldsymbol{y} \geq \dot{V}(\boldsymbol{x}, \boldsymbol{u}) + W(\boldsymbol{x})$ *for some function* W *with* $W(\boldsymbol{x}) \succ 0$ *on* $\mathbb{R}^n$*. The function* V *is also called a storage function of (2.23).*

Here, $\dot{V}(\boldsymbol{x}, \boldsymbol{u})$ is defined analogously to (2.21). Passivity is a useful property, because first, it is preserved for certain interconnections of different passive systems [149, pp. 245–259] and second, it can be used for stability analysis under certain conditions [149, pp. 241–245]. The closely related concept of positive realness, applicable for LTI systems, is defined as follows.

Definition 31. *(Positive realness, cf. [149, pp. 237–238]) Let* $\boldsymbol{G}(s)$ *be a square, proper, rational transfer function matrix. Then,* $\boldsymbol{G}(s)$ *is positive real if*

- *The poles of all entries of* $\boldsymbol{G}(s)$ *are located in* $\Re(s) \leq 0$*.*
- *The matrix* $\boldsymbol{G}(j\omega) + \boldsymbol{G}^T(-j\omega) \succeq 0\,, \forall \omega \in \mathbb{R}$ *such that* $j\omega$ *is not a pole of any entry of* $\boldsymbol{G}(s)$*.*
- *All purely imaginary poles* $j\omega$ *of each entry of* $\boldsymbol{G}(s)$ *are simple poles and* $\lim_{s \to j\omega}(s - j\omega)G(s)$ *is a positive semi-definite Hermitian matrix.*

Furthermore, $\boldsymbol{G}(s)$ *is called strictly positive real if* $\exists \varepsilon > 0$ *such that* $\boldsymbol{G}(s - \varepsilon)$ *is positive real.*

It can be noted that an LTI system (2.22) with $(\boldsymbol{A}, \boldsymbol{B})$ controllable and $(\boldsymbol{A}, \boldsymbol{C})$ observable is (strictly) passive if it is (strictly) positive real. One way to evaluate positive realness of a given LTI system is by the Kalman-Yakubovich-Popov Lemma [144, 284].

Definition 32. *(Kalman-Yakubovich-Popov (KYP) Lemma, cf. [149, pp. 240–241]) Given an LTI system as in (2.22) with* $p = m$*, such that its associated transfer function matrix* $\boldsymbol{G}(s)$ *is square. Let* $(\boldsymbol{A}, \boldsymbol{B})$ *be controllable and* $(\boldsymbol{A}, \boldsymbol{C})$ *observable. Then* $\boldsymbol{G}(s)$ *is strictly positive real if and only if* $\exists \boldsymbol{P} \in \mathbb{R}^{n \times n}$ *with* $\boldsymbol{P} = \boldsymbol{P}^T \succ 0$*,* $\boldsymbol{L} \in \mathbb{R}^{n \times m}$*,* $\boldsymbol{W} \in \mathbb{R}^{m \times m}$ *and* $\varepsilon > 0$ *such that*

$$\boldsymbol{A}^T\boldsymbol{P} + \boldsymbol{P}\boldsymbol{A} = -\boldsymbol{L}^T\boldsymbol{L} - \varepsilon\boldsymbol{P} \tag{2.27a}$$

$$\boldsymbol{P}\boldsymbol{B} = \boldsymbol{C}^T - \boldsymbol{L}^T\boldsymbol{W} \tag{2.27b}$$

$$\boldsymbol{W}^T\boldsymbol{W} = \boldsymbol{D} + \boldsymbol{D}^T\,. \tag{2.27c}$$

Remark 2. *The transfer function matrix* $\boldsymbol{G}(s)$ *is positive real if and only if these conditions hold for* $\varepsilon = 0$*. This result is sometimes called the Positive Real Lemma, see [149, p. 240], while other authors use it interchangeably with the KYP Lemma [25, pp. 70–71].*

The Equations (2.27) of the KYP Lemma can be efficiently evaluated numerically by reformulating them into a single linear matrix inequality (LMI), see [25, p. 71, pp. 93–94] and then using a standard LMI solver. The KYP Lemma is one out of many important results that were derived in the context of absolute stability. To give just one more example, the S-Lemma [283] can be mentioned as well, which considers the solvability of quadratic equations that appear during the S-Procedure, cf. Aizerman and Gantmacher [6]. Ultimately, these research directions led to the notion of positive real functions and passivity [280, 25], as well as methods based on dynamic multipliers [289, 43] or an approach based on integral quadratic constraints [196]. For a historical overview of the topic, see also [34].

This concludes the introduction to absolute stability of Lur'e systems and passivity. While the preliminaries so far were focused on analysis of dynamical systems, the following section gives a short introduction to the nonlinear control design method of input-output-linearization (IOL). This is the main method that will be used for an analytic derivation of the control laws of the proposed TCSs. The application of IOL to the design of TCSs and and the stability analysis of these designs will be the topic of Chapter 3.

2.2.3 Input-Output-Linearization

In this section, the nonlinear control design method of input-output-linearization (IOL) is briefly reviewed. Although the name might suggest that IOL is similar to Jacobian linearization which was already discussed in Section 2.2.1, these two methods differ fundamentally. The reason is that with IOL, the system dynamic is not approximated by a linear system in a vicinity of an operating point, but instead a feedback law is used to actively render the system linear in a region of the state space, potentially the whole $\mathbb{R}^n$. In the context of TCSs, this technique was already mentioned as a (theoretical) option to control the 2-state model (2.1), if the tire force would be available for feedback, compare (2.5a)-(2.5b). However, in this example the control input could be used directly to cancel out the nonlinearity. So the question naturally arises whether this compensation of nonlinearities by the control input is still possible if the input enters a different ODE than the nonlinearity. For example, this would be the case if actuator dynamics are added to (2.1). Indeed, this is still possible for a class of systems, and one systematical method to achieve this is IOL. Similar methods based on state feedback linearization that deal with finding a control law which linearizes the full dynamics were proposed even earlier than IOL by Brockett [24], see also [123, pp. 528–534] and [162] for an historical overview.

The method of IOL, which instead of linearizing the full dynamics, linearizes only the input-output relationship of a system, was first considered by Isidori and Krener [126]. Other early publications on this topic are by Isidori and Ruberti [127] and Byrnes and Isidori [28], see also the survey [162]. This introduction is based on the textbooks by Isidori [123, 124, 125] and partially also on [2, 149]. For the introduction to the method of IOL we consider the following class of input-affine nonlinear MIMO dynamical systems

$$\dot{\boldsymbol{x}} = \boldsymbol{f}(\boldsymbol{x}) + \boldsymbol{G}(\boldsymbol{x})\boldsymbol{u} \tag{2.28a}$$

$$\boldsymbol{y} = \boldsymbol{h}(\boldsymbol{x}) \tag{2.28b}$$

with state $\boldsymbol{x} \in \mathbb{R}^n$, input $\boldsymbol{u} \in \mathbb{R}^m$, output $\boldsymbol{y} \in \mathbb{R}^p$ and $m = p$. Furthermore, $\boldsymbol{f} : \mathbb{R}^n \to \mathbb{R}^n$ is the part of the vector field that depends only on the system state, while $\boldsymbol{G} : \mathbb{R}^n \to \mathbb{R}^{n\times m}$ is a matrix field affine in $\boldsymbol{u}$. Finally, $\boldsymbol{h} : \mathbb{R}^n \to \mathbb{R}^p$ is the measurement function. One concept that will be useful for the notation of the IOL method is the Lie derivative.

Definition 33. *(Lie derivative, cf. [123, p. 8]) The Lie derivative of a function $h : \mathbb{R}^n \to \mathbb{R}$ along the vector field $\boldsymbol{f} : \mathbb{R}^n \to \mathbb{R}^n$ is denoted by $L_{\boldsymbol{f}}h(\boldsymbol{x})$. More generally, the k-th derivative of h along $\boldsymbol{f}$ and the derivative of h, first along $\boldsymbol{f}$ and second along $\boldsymbol{g} : \mathbb{R}^n \to \mathbb{R}^n$ are given by*

$$L_{\boldsymbol{f}}^k h(\boldsymbol{x}) = \frac{\partial\big(L_{\boldsymbol{f}}^{k-1}\big)}{\partial \boldsymbol{x}}\boldsymbol{f}(\boldsymbol{x}) \text{ and } L_{\boldsymbol{g}}L_{\boldsymbol{f}}\boldsymbol{h}(\boldsymbol{x}) = \frac{\partial\big(L_{\boldsymbol{f}}h(\boldsymbol{x})\big)}{\partial \boldsymbol{x}}\boldsymbol{g}(\boldsymbol{x}) \tag{2.29}$$

respectively, where $L_{\boldsymbol{f}}^1 h(\boldsymbol{x}) = L_{\boldsymbol{f}}h(\boldsymbol{x}) = \sum_{i=1}^n f_i(\boldsymbol{x})\partial h(\boldsymbol{x})/(\partial x_i)$ and $L_{\boldsymbol{f}}^0 h(\boldsymbol{x}) = h(\boldsymbol{x})$.

This provides a compact notation for derivatives of real-valued functions along vector fields. For example, the derivative of the Lyapunov function along solution trajectories, given by (2.8) in Definition 9, can be written as $\dot{V}(\boldsymbol{x}) = L_{\boldsymbol{f}}V(\boldsymbol{x})$. Informally, the IOL method can be summarized as follows: differentiate each system output $y_j\,, \forall j \in \{1, 2, \ldots, m\}$ until any component of $\boldsymbol{u}$ appears; redefine the highest occurring derivative of each y_j as new, virtual input v_j; this gives a linear system of m equations which is to be solved for u_j. The control law derived by this method linearizes the input-output relationship of the system and results in a substitute linear system with virtual control inputs $v_1, v_2, \ldots, v_m$. This informal description leaves several important questions unanswered, like where this algorithm comes from, when it is actually applicable and whether global asymptotic stability can be guaranteed for a control law based on this method. The goal of this review is to provide answers to these questions by a brief overview of the basics of IOL. One concept that will be needed for this is the (vector) relative degree of a system.

The (vector) relative degree of a general MIMO system of the form (2.28) can be defined with the help of the Lie derivative from Definition 33 as follows.

Definition 34. *(Relative degree and vector relative degree, cf. [123, pp. 219–220]) A system as defined in (2.28) with* $\boldsymbol{G}(\boldsymbol{x}) = \begin{bmatrix}\boldsymbol{g}_1(\boldsymbol{x}) & \boldsymbol{g}_2(\boldsymbol{x}) & \dots & \boldsymbol{g}_m(\boldsymbol{x})\end{bmatrix}$ *and* $\boldsymbol{g}_j(\boldsymbol{x}) \in \mathbb{R}^n, \forall j \in \{1, 2, \dots, m\}$ *has vector relative degree* $\boldsymbol{r} = \begin{bmatrix}r_1 & r_2 & \dots & r_m\end{bmatrix}$ *at* $\boldsymbol{x}_0 \in \mathbb{R}^n$ *if*

- $L_{\boldsymbol{g}_j} L_{\boldsymbol{f}}^k h_i(\boldsymbol{x}) = 0$ *with* $k < r_i - 1, \forall i, j \in \{1, 2, \dots, m\}, \forall \boldsymbol{x}$ *in a neighborhood of* $\boldsymbol{x}_0$.
- *The decoupling matrix* $\boldsymbol{A}(\boldsymbol{x}) \in \mathbb{R}^{m \times m}$ *is nonsingular at* $\boldsymbol{x}_0$*, with* $\boldsymbol{A}(\boldsymbol{x})$ *given by*

$$\boldsymbol{A}(\boldsymbol{x}) = \begin{bmatrix} L_{\boldsymbol{g}_1} L_{\boldsymbol{f}}^{r_1-1} h_1(\boldsymbol{x}) & L_{\boldsymbol{g}_2} L_{\boldsymbol{f}}^{r_1-1} h_1(\boldsymbol{x}) & \dots & L_{\boldsymbol{g}_m} L_{\boldsymbol{f}}^{r_1-1} h_1(\boldsymbol{x}) \\ L_{\boldsymbol{g}_1} L_{\boldsymbol{f}}^{r_2-1} h_2(\boldsymbol{x}) & L_{\boldsymbol{g}_2} L_{\boldsymbol{f}}^{r_2-1} h_2(\boldsymbol{x}) & \dots & L_{\boldsymbol{g}_m} L_{\boldsymbol{f}}^{r_2-1} h_2(\boldsymbol{x}) \\ \vdots & \vdots & \ddots & \vdots \\ L_{\boldsymbol{g}_1} L_{\boldsymbol{f}}^{r_m-1} h_m(\boldsymbol{x}) & L_{\boldsymbol{g}_2} L_{\boldsymbol{f}}^{r_m-1} h_m(\boldsymbol{x}) & \dots & L_{\boldsymbol{g}_m} L_{\boldsymbol{f}}^{r_m-1} h_m(\boldsymbol{x}) \end{bmatrix}. \tag{2.30}$$

The value $r = \sum_{i=1}^{m} r_i$ *is called total relative degree of (2.28) at* $\boldsymbol{x}_0$*. In the SISO case, when* $m = 1$*,* $r = r_1$ *is called relative degree of (2.28) at* $\boldsymbol{x}_0$*.*

The elements r_i of the vector $\boldsymbol{r}$ can be interpreted as the number of differentiations of the i-th output y_i that is required such that the r_i-th derivative of y_i depends on at least one element of the input vector $\boldsymbol{u}$, cf. [123, p. 221]. It can be noted that the (vector) relative degree of a system might not be well defined, namely if some entries of $\boldsymbol{r}$ do not exist. This is for example the case if the corresponding output is independent of $\boldsymbol{u}$, see [149, p. 511]. It can be noted that the (vector) relative degree in general is a local concept for a neighborhood of some $\boldsymbol{x}_0 \in \mathbb{R}^n$, for example an equilibrium. However, for the TCSs considered in this work, the conditions from Definition 34 are satisfied globally. Therefore, we assume for the remainder of this introduction that the relative degree of the considered systems is well defined and uniform and that the decoupling matrix is nonsingular and that both of these conditions are true for all $\boldsymbol{x} \in \mathbb{R}^n$. For more details on the differences between local and global applicability of IOL, see for example [123, pp. 219–277, pp. 427–460]. Another important concept for IOL is that of a diffeomorphism, which is a potentially nonlinear change of coordinates of a system, defined as follows.

Definition 35. *(Diffeomorphism, cf. [123, p. 11]) A function* $\boldsymbol{\phi} : \mathbb{R}^n \to \mathbb{R}^n$ *is called a global diffeomorphism on* $\mathbb{R}^n$ *if there exists* $\boldsymbol{\phi}^{-1}$ *such that* $\boldsymbol{\phi}^{-1}\big(\boldsymbol{\phi}(\boldsymbol{x})\big) = \boldsymbol{x}, \forall \boldsymbol{x} \in \mathbb{R}^n$ *and* $\boldsymbol{\phi}, \boldsymbol{\phi}^{-1} \in C^\infty$*.*

One possibility to test whether a given function $\boldsymbol{\phi}$ is a global diffeomorphism is by evaluating the determinant of its Jacobian matrix: if $\boldsymbol{\phi}$ is a smooth bijection and $\det\big(\boldsymbol{J}_{\boldsymbol{\phi},\boldsymbol{x}}(\boldsymbol{x})\big) \neq 0, \forall \boldsymbol{x} \in \mathbb{R}^n$, then $\boldsymbol{\phi}$ is a global diffeomorphism. It can be noted that if $\boldsymbol{\phi}$ is linear, then it suffices to examine the Jacobian for being nonsingular. A diffeomorphism is used for IOL in order to transform the original system into Byrnes-Isidori normal form. This system representation basically solves the already mentioned problem that generally not all nonlinearities that affect the system output can be directly canceled out by an input in the original representation. For each output $y_j, \forall j \in \{1, 2, \dots, m\}$ this is achieved by a state transformation that shifts those nonlinearities into one differential equation that is also directly affected by the input vector $\boldsymbol{u}$. The input can then be used to compensate the nonlinearities and provide a new, virtual input to the differential equations which are reduced to a chain of integrators, except for those that have no direct effect on the output $\boldsymbol{y}$. Alternatively, a linear reference model can be imposed on the dynamics [123, pp. 290–291]. This procedure, which is fundamental for IOL, was inspired by the so-called structure algorithm due to Silverman [255], see also [123, pp. 282–289, pp. 531–532] and [125, pp. 252–263] for a detailed review. In the following, we state the generic diffeomorphism that is generally used for IOL, where the original system states are denoted with $\boldsymbol{x} \in \mathbb{R}^n$ and the states of the transformed system states with $\boldsymbol{\xi} \in \mathbb{R}^n$ such that $\boldsymbol{\xi} = \boldsymbol{\phi}(\boldsymbol{x})$ and $\boldsymbol{x} = \boldsymbol{\phi}^{-1}(\boldsymbol{\xi})$ for all $\boldsymbol{x}, \boldsymbol{\xi}$. Then, it is shown how the linearizing control law is derived from the transformed system.

The state transformation from $\boldsymbol{x}$-coordinates to $\boldsymbol{\xi}$-coordinates can be defined as

$$\boldsymbol{\xi} = \begin{bmatrix} \xi_1 \\ \xi_2 \\ \vdots \\ \xi_{r_1} \\ \xi_{r_1+1} \\ \xi_{r_1+2} \\ \vdots \\ \xi_{r_1+r_2} \\ \vdots \\ \xi_{r-r_m} \\ \xi_{r-r_m+1} \\ \vdots \\ \xi_r \\ \xi_{r+1} \\ \xi_{r+2} \\ \vdots \\ \xi_n \end{bmatrix} = \boldsymbol{\phi}(\boldsymbol{x}) = \begin{bmatrix} \phi_1(\boldsymbol{x}) \\ \phi_2(\boldsymbol{x}) \\ \vdots \\ \phi_{r_1}(\boldsymbol{x}) \\ \phi_{r_1+1}(\boldsymbol{x}) \\ \phi_{r_1+2}(\boldsymbol{x}) \\ \vdots \\ \phi_{r_1+r_2}(\boldsymbol{x}) \\ \vdots \\ \phi_{r-r_m}(\boldsymbol{x}) \\ \phi_{r-r_m+1}(\boldsymbol{x}) \\ \vdots \\ \phi_r(\boldsymbol{x}) \\ \phi_{r+1}(\boldsymbol{x}) \\ \phi_{r+2}(\boldsymbol{x}) \\ \vdots \\ \phi_n(\boldsymbol{x}) \end{bmatrix} = \begin{bmatrix} h_1(\boldsymbol{x}) \\ L_{\boldsymbol{f}} h_1(\boldsymbol{x}) \\ \vdots \\ L_{\boldsymbol{f}}^{r_1-1} h_1(\boldsymbol{x}) \\ h_2(\boldsymbol{x}) \\ L_{\boldsymbol{f}} h_2(\boldsymbol{x}) \\ \vdots \\ L_{\boldsymbol{f}}^{r_2-1} h_2(\boldsymbol{x}) \\ \vdots \\ h_m(\boldsymbol{x}) \\ L_{\boldsymbol{f}} h_m(\boldsymbol{x}) \\ \vdots \\ L_{\boldsymbol{f}}^{r_m-1} h_m(\boldsymbol{x}) \\ \phi_{r+1}(\boldsymbol{x}) \\ \phi_{r+2}(\boldsymbol{x}) \\ \vdots \\ \phi_n(\boldsymbol{x}) \end{bmatrix}, \tag{2.31}$$

see [123, pp. 222–223] or [2, pp. 329–333]. The functions $\phi_i \, \forall i \in \{r+1, r+2, \ldots, n\}$ can be chosen freely, with the restriction that $\boldsymbol{\phi}$ must be a diffeomorphism. Such functions are guaranteed to exist at least locally in a neighborhood of $\boldsymbol{x}_0$ [123, pp. 222–223]. Evaluating $\dot{\boldsymbol{\xi}} = \mathrm{d}\boldsymbol{\phi}(\boldsymbol{x})/(\mathrm{d}t)$ and inserting $\boldsymbol{x} = \boldsymbol{\phi}^{-1}(\boldsymbol{\xi})$ results in the Byrnes-Isidori normal form,

$$\dot{\boldsymbol{\xi}} = \begin{bmatrix} \dot{\xi}_1 \\ \dot{\xi}_2 \\ \vdots \\ \dot{\xi}_{r_1} \\ \dot{\xi}_{r_1+1} \\ \dot{\xi}_{r_1+2} \\ \vdots \\ \dot{\xi}_{r_1+r_2} \\ \vdots \\ \dot{\xi}_{r-r_m} \\ \dot{\xi}_{r-r_m+1} \\ \vdots \\ \dot{\xi}_r \\ \dot{\xi}_{r+1} \\ \dot{\xi}_{r+2} \\ \vdots \\ \dot{\xi}_n \end{bmatrix} = \begin{bmatrix} \xi_2 \\ \xi_3 \\ \vdots \\ L_{\boldsymbol{f}}^{r_1} h_1\big(\boldsymbol{\phi}^{-1}(\boldsymbol{\xi})\big) + \sum_{j=1}^{m} L_{\boldsymbol{g}_j} L_{\boldsymbol{f}}^{r_1-1} h_1\big(\boldsymbol{\phi}^{-1}(\boldsymbol{\xi})\big) u_j \\ \xi_{r_1+2} \\ \xi_{r_1+3} \\ \vdots \\ L_{\boldsymbol{f}}^{r_2} h_2\big(\boldsymbol{\phi}^{-1}(\boldsymbol{\xi})\big) + \sum_{j=1}^{m} L_{\boldsymbol{g}_j} L_{\boldsymbol{f}}^{r_2-1} h_2\big(\boldsymbol{\phi}^{-1}(\boldsymbol{\xi})\big) u_j \\ \vdots \\ \xi_{r-r_m+2} \\ \xi_{r-r_m+3} \\ \vdots \\ L_{\boldsymbol{f}}^{r_m} h_m\big(\boldsymbol{\phi}^{-1}(\boldsymbol{\xi})\big) + \sum_{j=1}^{m} L_{\boldsymbol{g}_j} L_{\boldsymbol{f}}^{r_m-1} h_m\big(\boldsymbol{\phi}^{-1}(\boldsymbol{\xi})\big) u_j \\ L_{\boldsymbol{f}} \phi_{r+1}\big(\boldsymbol{\phi}^{-1}(\boldsymbol{\xi})\big) + \sum_{j=1}^{m} L_{\boldsymbol{g}_j} \phi_{r+1}\big(\boldsymbol{\phi}^{-1}(\boldsymbol{\xi})\big) u_j \\ L_{\boldsymbol{f}} \phi_{r+2}\big(\boldsymbol{\phi}^{-1}(\boldsymbol{\xi})\big) + \sum_{j=1}^{m} L_{\boldsymbol{g}_j} \phi_{r+2}\big(\boldsymbol{\phi}^{-1}(\boldsymbol{\xi})\big) u_j \\ \vdots \\ L_{\boldsymbol{f}} \phi_n\big(\boldsymbol{\phi}^{-1}(\boldsymbol{\xi})\big) + \sum_{j=1}^{m} L_{\boldsymbol{g}_j} \phi_n\big(\boldsymbol{\phi}^{-1}(\boldsymbol{\xi})\big) u_j \end{bmatrix} \tag{2.32}$$

It is not always possible to choose the functions $\phi_i \, , \forall i \in \{r+1, r+2, \ldots, n\}$ such that the last $n-r$ equations of (2.32) are independent of $\boldsymbol{u}$. Such functions exist locally if the distribution spanned by the $\boldsymbol{g}_j \, , \forall j \in \{1, 2, \ldots, m\}$ is involutive near $\boldsymbol{x}_0$. However, this part is not problematic for the TCSs considered in this work, so we refer the reader to [123, pp. 222–223] for more details.

Considering the first r equations in (2.32), it becomes apparent that the coefficients of the $u_j\,, \forall j \in \{1, 2, \ldots, m\}$ in the r_i-th row are the (r_i, j) entry of $\boldsymbol{A}(\boldsymbol{x})$ from (2.30), see [123, p. 224]. Now the remaining nonlinearities in the first r equations can be eliminated, which leads to a system of linear equations $\boldsymbol{v} = \boldsymbol{A}\big(\boldsymbol{\phi}^{-1}(\boldsymbol{\xi})\big)\boldsymbol{u} + \boldsymbol{b}\big(\boldsymbol{\phi}^{-1}(\boldsymbol{\xi})\big)$ that has the solution

$$\boldsymbol{u} = -\boldsymbol{A}^{-1}\big(\boldsymbol{\phi}^{-1}(\boldsymbol{\xi})\big)\big[\boldsymbol{b}\big(\boldsymbol{\phi}^{-1}(\boldsymbol{\xi})\big) - \boldsymbol{v}\big] = -\boldsymbol{A}^{-1}(\boldsymbol{x})\big[\boldsymbol{b}(\boldsymbol{x}) - \boldsymbol{v}\big]\,. \tag{2.33}$$

Here, $\boldsymbol{v}^T = \begin{bmatrix} v_1 & v_2 & \ldots & v_m \end{bmatrix}$ are the virtual inputs to the linearized subsystem and $\boldsymbol{b}$ is a vector that collects the remaining $L_{\boldsymbol{f}}^{r_i} h_i\big(\boldsymbol{\phi}^{-1}(\boldsymbol{\xi})\big)\,, \forall i \in \{1, 2, \ldots, m\}$ from (2.32) as

$$\boldsymbol{b}\big(\boldsymbol{\phi}^{-1}(\boldsymbol{\xi})\big)^T = \begin{bmatrix} L_{\boldsymbol{f}}^{r_1} h_1\big(\boldsymbol{\phi}^{-1}(\boldsymbol{\xi})\big) & L_{\boldsymbol{f}}^{r_2} h_2\big(\boldsymbol{\phi}^{-1}(\boldsymbol{\xi})\big) & \ldots & L_{\boldsymbol{f}}^{r_m} h_m\big(\boldsymbol{\phi}^{-1}(\boldsymbol{\xi})\big) \end{bmatrix}\,. \tag{2.34}$$

This leads to m decoupled integrator chains where the j-th chain consists of r_j integrators with v_j as new input. Since this renders the first r equations of (2.32) linear, these equations can be globally exponentially stabilized by static state feedback of the first r states of $\boldsymbol{\xi}$ or any other appropriate method from linear control theory.

If $r = n$, then the feedback law (2.33) linearizes the whole system. However, in general $r < n$ so the last $n - r$ equations of (2.32) will still be nonlinear. While these equations do not affect the output $\boldsymbol{y}$, they are still required to be stable in order for the controller to work in practice. For further analysis, partition the state as $\boldsymbol{\zeta}^T = \begin{bmatrix} \zeta_1 & \zeta_2 & \ldots & \zeta_r \end{bmatrix} = \begin{bmatrix} \xi_1 & \xi_2 & \ldots & \xi_r \end{bmatrix}$ and $\boldsymbol{z}^T = \begin{bmatrix} z_1 & z_2 & \ldots & z_{n-r} \end{bmatrix} = \begin{bmatrix} \xi_{r+1} & \xi_{r+2} & \ldots & \xi_n \end{bmatrix}$ for the next two definitions.

Definition 36. *(External dynamics, cf. [2, p. 332]) Let* $\dot{\boldsymbol{\zeta}}^T = \begin{bmatrix} \dot{\zeta}_1 & \dot{\zeta}_2 & \ldots & \dot{\zeta}_r \end{bmatrix}$ *be given by*

$$\dot{\boldsymbol{\zeta}} = \begin{bmatrix} \zeta_2 & \zeta_3 & \ldots & v_1 & \zeta_{r_1+2} & \zeta_{r_1+3} & \ldots & v_2 & \ldots & \zeta_{r-r_m+2} & \zeta_{r-r_m+3} & \ldots & v_m \end{bmatrix}^T\,, \tag{2.35}$$

as a result of taking the first r equations of (2.32), after inserting (2.33) where (2.32) is derived from (2.28) by the described procedure. Then, (2.35) are the external dynamics of (2.28).

The external dynamics, as already discussed, can be stabilized by the static state feedback $\boldsymbol{v} = -\boldsymbol{K}\boldsymbol{\zeta}$, so by using only the states $\boldsymbol{\zeta}$ of the external dynamics and an appropriate gain matrix $\boldsymbol{K} \in \mathbb{R}^{m \times r}$. Next, let $\boldsymbol{q}(\boldsymbol{\zeta}, \boldsymbol{z}, \boldsymbol{v})^T = \begin{bmatrix} q_1(\boldsymbol{\zeta}, \boldsymbol{z}, \boldsymbol{v}) & q_2(\boldsymbol{\zeta}, \boldsymbol{z}, \boldsymbol{v}) & \ldots & q_{n-r}(\boldsymbol{\zeta}, \boldsymbol{z}, \boldsymbol{v}) \end{bmatrix}$ and

$$q_\ell(\boldsymbol{\zeta}, \boldsymbol{z}, \boldsymbol{v}) = L_{\boldsymbol{f}} \phi_{r+\ell}\big(\boldsymbol{\phi}^{-1}(\boldsymbol{\xi})\big) + \sum_{j=1}^{m} L_{\boldsymbol{g}_j} \phi_{r+\ell}\big(\boldsymbol{\phi}^{-1}(\boldsymbol{\xi})\big) u_j\,, \forall \ell \in \{1, 2, \ldots, n-r\}\,, \tag{2.36}$$

where the u_j in (2.36) are inserted according to (2.33) such that (2.36) generally depends on $\boldsymbol{v}$. Furthermore, note that $\boldsymbol{\xi}^T = \begin{bmatrix} \boldsymbol{\zeta} & \boldsymbol{z} \end{bmatrix}$, so separating the first two arguments of q_ℓ as done in (2.36) is always possible. Then, the internal dynamics can be defined.

Definition 37. *(Internal dynamics, cf. [2, p. 332]) Let (2.36) be given by the described procedure applied to (2.28). Then,*

$$\dot{\boldsymbol{z}} = \boldsymbol{q}(\boldsymbol{\zeta}, \boldsymbol{z}, \boldsymbol{v}) = \begin{bmatrix} \dot{z}_1 \\ \dot{z}_2 \\ \vdots \\ \dot{z}_{n-r} \end{bmatrix} = \begin{bmatrix} q_1(\boldsymbol{\zeta}, \boldsymbol{z}, \boldsymbol{v}) \\ q_2(\boldsymbol{\zeta}, \boldsymbol{z}, \boldsymbol{v}) \\ \vdots \\ q_{n-r}(\boldsymbol{\zeta}, \boldsymbol{z}, \boldsymbol{v}) \end{bmatrix}\,, \tag{2.37}$$

with $q_\ell\,, \forall \ell \in \{1, 2, \ldots, n-r\}$ *given by (2.36), are called the internal dynamics of (2.28).*

This definition is general in the sense that $\boldsymbol{q}$ can depend on $\boldsymbol{v}$. As mentioned previously, this can be avoided by choosing the functions $\phi_i\,, \forall i \in \{r+1, r+2, \ldots, n\}$ appropriately. Then, $\boldsymbol{q}$ depends only on $\boldsymbol{\zeta}$ and $\boldsymbol{z}$. For the TCSs considered in this work, such a choice was readily possible, so the internal dynamics analyzed in this work in the context of traction control are independent of the virtual input $\boldsymbol{v}$. Since $\boldsymbol{q}$ is generally a nonlinear vector field, analyzing stability of (2.37) can be difficult. The zero dynamics, while still nonlinear in general, describe the internal dynamics but without inputs from the external dynamics. Therefore, stability of the zero dynamics is often studied first, while the internal dynamics are then analyzed in a subsequent step.

The zero dynamics of a nonlinear system of the form (2.28) can then be defined in terms of its internal dynamics from Definition 37.

Definition 38. *(Zero dynamics, cf. [123, pp. 162–164]) Given a nonlinear system of the form (2.28) with internal dynamics (2.37). Then, its zero dynamics are given by*

$$\dot{\boldsymbol{z}} = \boldsymbol{q}(\mathbf{0}_r, \boldsymbol{z}, \mathbf{0}_m)\,, \tag{2.38}$$

which are the internal dynamics evaluated at $\boldsymbol{\zeta} = \mathbf{0}_r$ and also $\boldsymbol{v} = \mathbf{0}_m$, if (2.37) depends on $\boldsymbol{v}$.

The zero dynamics are the part of the system dynamic, that emerges from an input $\boldsymbol{u}$ forcing the outputs to $\boldsymbol{y} = \mathbf{0}_p$, with $m = p$, for all time and for all initial conditions, see also [123, pp. 162–172]. For the control law (2.33) to be feasible in practice, the zero dynamics should at least be locally stable, preferable globally asymptotically stable. This property is also called globally minimum-phase because of its relation to the transfer function zeros in the LTI case.

Definition 39. *(Globally minimum-phase systems, cf. [125, p. 178]) Given a system of the form (2.28) with $\boldsymbol{f}(\mathbf{0}_n) = \mathbf{0}_n$, $\boldsymbol{h}(\mathbf{0}_n) = \mathbf{0}_n$ and a constant (vector) relative degree of $r < n$ for all $\boldsymbol{x} \in \mathbb{R}^n$. Assume a global diffeomorphism (2.31) exists. Then, (2.28) is said to be globally minimum phase if the equilibrium $\boldsymbol{z} = \mathbf{0}_{n-r}$ of its zero dynamics is globally asymptotically stable.*

One might think that if both the external and the zero dynamics of a system are globally asymptotically stable, that the whole system is globally exponentially stable as well because $\boldsymbol{\zeta} \to \mathbf{0}_r$ for $t \to 0$. While this is true locally, it is generally not the case for all initial conditions due to the so called peaking phenomenon, see for example [263] for details. A condition that excludes this possibility is that the system is strongly minimum-phase, meaning that its internal dynamics are ISS.

Definition 40. *(Strongly minimum-phase systems, cf. [125, p. 178]) Given a system of the form (2.28) with the assumptions of Definition 39. Assume further that the diffeomorphism was chosen such that the internal dynamics do not depend on $\boldsymbol{v}$. Then, the system (2.28) is called strongly minimum-phase if its internal dynamics are ISS, with $\boldsymbol{\zeta}$ interpreted as an input vector.*

From this follows that strongly minimum-phase systems can always be globally asymptotically stabilized by the control law (2.33), see also [125, pp. 394–395]. Generally, these methods can not only be applied for stabilization of nonlinear systems but also for reference tracking, see for example [123, pp. 387–416] and [149, pp. 540–545], and also for disturbance decoupling [123, pp. 184–189]. Finally, it can be noted that the method of IOL assumes that the nonlinearities in (2.33) are known, which might pose challenges regarding robustness. Another assumption is, that it is actually desirable to cancel out the nonlinearities. Depending on the problem, each of these assumptions might be problematic, cf. [149, pp. 539–540] for a discussion. It is therefore often advisable to augment the linearized substitute system with an additional outer controller in order to increase robustness and to carefully evaluate the closed loop system in simulation, with tools from linear control theory and specifically designed experiments in order to ensure that the real-world system is well behaved.

This concludes the summary of the nonlinear control design method of IOL and some of its particularities regarding stability analysis. It can be noted that in the above definitions and remarks it is just stated that stability of the overall closed loop system can be asserted, for example by showing that the internal dynamics are ISS. However, as already mentioned, this might be difficult to achieve in practice, as the internal dynamics generally are nonlinear. Finding an appropriate Lyapunov function for a given nonlinear system can be a challenging task, depending on the concrete structure of the system. In this work, additionally to the TCSs, a novel heuristic method based on GP which searches for Lyapunov functions is proposed. Therefore, a brief introduction to genetic algorithms (GAs), which form the basis of GP, as well as the general GP algorithm itself, is given in the following.

2.3 Optimization based on Genetic Programming

2.3.1 Preliminaries on Evolutionary Algorithms

In this section, a brief overview of GAs and GP is given, which will be used later in this work for a new heuristic method of constructing Lyapunov functions for general nonlinear systems of the form (2.6). First, some preliminaries on optimization by GAs are given. For this introduction, we focus on the problem of unconstrained nonlinear function minimization over the non-negative integers, which takes the form

$$\min_{\boldsymbol{x}} F(\boldsymbol{x}) \tag{2.39}$$

with $\boldsymbol{x} \in \mathbb{N}_0^n$ and $F : \mathbb{N}_0^n \to \mathbb{R}$. Without further knowledge about F, this can be a very difficult problem and even if F is known, it might be impossible to solve (2.39) analytically. In that case, a randomized heuristic search method like a GA might be useful to find a solution that is "good enough". The method of GAs was introduced by Holland [110] in 1975 and is based on the idea of simulating the natural selection process of a population. It can be noted that there are numerous other randomized search methods to approach the problem of global function minimization, compare [85] and [104, pp. 187–202] for an overview. Also, GAs are not limited to problems of the form (2.39), but can be used for constrained optimization [104, pp. 51–66], multiple objective optimization [104, pp. 97–101] or optimization over the reals instead of the integers [104, pp. 51–65], for example. The general optimization process of a GA is depicted in Figure 2.8.

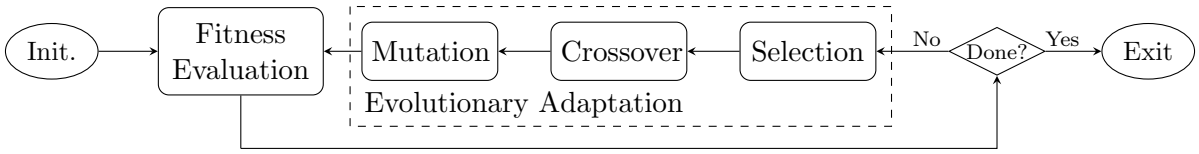

Figure 2.8: Flow-chart of a GA with the standard genetic operators [303].

The main steps of the optimization process of a genetic algorithm, adapted from [303], can be summarized as follows, compare also [199, pp. 7–8] and [104, pp. 27–49].

1. **Initialization**: Candidate solutions, also called *individuals*, are initialized randomly. The set of individuals is called the *population* of the GA.
2. **Fitness evaluation**: A *fitness value* is assigned to each individual, which represents the value to be optimized. In a GA setting, F in (2.39) is called *fitness function*.
3. **Selection**: A portion of the population is *selected* randomly to enter the next generation, while a higher fitness value leads to a higher selection probability.
4. **Crossover**: New individuals are formed by *recombination* of the selected individuals in order to replace individuals that were previously not selected.
5. **Mutation**: The new individuals from the crossover step are *mutated*, meaning that they are modified randomly according to some mutation rate.

These steps are repeated until a previously specified stopping criterion is met. One such iteration is also called a *generation* [104, p. 38]. Standard stopping criteria are for example a maximum number of generations or fitness function evaluations, a threshold for the fitness value or that the average fitness does not change significantly for a number of generations. We consider a simple example to illustrate the steps of the optimization process. Given

$$F_e(\boldsymbol{x}) = x_1^2 + x_2^2 + x_3^2 + x_4^2 \tag{2.40}$$

with $\boldsymbol{x}^T = \begin{bmatrix} x_1 & x_2 & x_3 & x_4 \end{bmatrix}$ and $\boldsymbol{x} \in \mathbb{N}_0^4$. Solving (2.39) for this F_e is trivial, as the unique global minimum is attained at the origin, but it is well suited to explain the main steps of a GA.

Before starting, we fix the population size for this example to $N_p = 3$. The first step is initialization, so we draw three random individuals, meaning we define 3 vectors by drawing each entry of these vectors from a the uniform integer distribution with support $[0, 9]$. This is an arbitrary choice and of course other distributions or initialization techniques can be used. The individuals and their fitness values according to (2.40) are listed in Table 2.2.

Table 2.2: Example population, fitness values and ranking at generation $i = 1$.

k	**Individual no.** k	**Fitness Value** $F_e(\boldsymbol{x}_{k,i})$	**Ranking** $\text{rank}(k, i)$
1	$\boldsymbol{x}_{1,1}^T = [6 \quad 9 \quad 7 \quad 1]$	167	2
2	$\boldsymbol{x}_{2,1}^T = [9 \quad 8 \quad 7 \quad 6]$	230	3 (worst fitness)
3	$\boldsymbol{x}_{3,1}^T = [7 \quad 0 \quad 6 \quad 3]$	94	1 (best fitness)

Here, $\boldsymbol{x}_{k,i}$ denotes the k-th individual of the i-th generation. Assume that evaluating the stopping criterion does not lead to termination of the process. Then, the next step is selection, for which we define for now that in each generation two individuals are selected for crossover and one is removed. In this example, we choose rank selection, which means that each individual is assigned a selection probability proportional to its rank within the population. The rank is determined by the fitness value, where the individual with best fitness value is assigned the first rank by $\text{rank}(3, 1) = 1$ and the other individuals $\text{rank}(1, 1) = 2$ and $\text{rank}(2, 1) = 3$ accordingly, as depicted in the last column of Table 2.2. The selection probability of the k-th individual $\boldsymbol{x}_{k,i}$ at generation i can then be computed by

$$P(k, i) = \frac{2(1 - s_p)\,\text{rank}(k, i) + s_p(1 + N_p) - 2}{N_p(N_p - 1)}\,, \tag{2.41}$$

where $s_p \in [1, 2]$ is called the selection pressure, compare [85, pp. 122–123]. It can be noted that the definition in [85, p. 122] assumes a rank of N_p being assigned to the individual with the best fitness while (2.41) assumes the rank of the fittest individual as 1. In the considered example, taking $s_p = 3/2$ gives $P(1, 1) = 1/3$, $P(2, 1) = 1/6$ and $P(3, 1) = 1/2$ as selection probabilities. Since the third individual has the best fitness, it has the highest probability of being selected, namely 50% in this example. However, this also means that sometimes individuals with lower fitness are selected. For example, a possible result of performing a selection based on these computed probabilities is that the second and third individual are selected, although $F_e(\boldsymbol{x}_{1,1}) < F_e(\boldsymbol{x}_{2,1})$, so the first individual is removed from the population despite a better fitness value. This mechanism allows GAs to escape from local minima while still being biased towards exploiting the currently best found solutions. The standard selection could even remove the fittest individual from the population. Since this can be undesired, often a certain *elitism* rate is defined, which excludes the fittest individuals from the selection process and transfers them automatically to the next generation. Numerous other methods to implement selection exist, compare for example [85, pp. 120–123] and [199, pp. 124–128].

After removing the first individual and selecting individuals 2 and 3, the crossover operation is used to construct new individuals. Here, typically two of the previously selected individuals are paired, often randomly according to some distribution. Then a new individual is constructed by using data from both of these individuals. This can be interpreted as the analogue of inheritance from one generation to the next. The process is usually repeated until the number of individuals in the population is N_p again. Although methods exist that try to adapt the population size during the optimization [199, pp. 131–132], in this work the population size is kept constant during the optimization. One crossover method is cut and splice crossover, which "splits" the two selected vectors at a randomly chosen point and creates a new individual by concatenating

the first part of the first individual with the second part of the second individual. This process is illustrated for the considered example by

$$\boldsymbol{x}_{2,1}^T = \begin{bmatrix} 9 & 8 & | & 7 & 6 \end{bmatrix} \quad \text{(parent)} \tag{2.42a}$$

$$\boldsymbol{x}_{3,1}^T = \begin{bmatrix} 7 & 0 & | & 6 & 3 \end{bmatrix} \quad \text{(parent)} \tag{2.42b}$$

$$\implies \widetilde{\boldsymbol{x}}_{1,2}^T = \begin{bmatrix} 7 & 0 & 7 & 6 \end{bmatrix} \quad \text{(offspring, before mutation).} \tag{2.42c}$$

Various other methods for implementing crossover exist, compare for example [199, pp. 128–129] and [104, pp. 56–60]. The previously selected individuals are then transferred directly to the next generation like $\boldsymbol{x}_{2,2}^T = \boldsymbol{x}_{2,1}^T$ and $\boldsymbol{x}_{3,2}^T = \boldsymbol{x}_{3,1}^T$. For the new individuals however, a mutation operation is performed before they are added to the next generation, like

$$\boldsymbol{x}_{1,2}^T = M(\widetilde{\boldsymbol{x}}_{1,2})^T = \begin{bmatrix} 7 & 0 & \not{7}\,1 & 6 \end{bmatrix} \quad \text{(offspring, after mutation),} \tag{2.43}$$

where $M : \mathbb{N}_0^n \to \mathbb{N}_0^n$ denotes a mutation operator, which typically involves some randomness. One example is single point mutation, where a random entry of the individual is replaced with a random number drawn from some previously defined distribution. Alternatively, the value could also be added or subtracted, as long as the result being a non-negative integer is guaranteed. The process of mutation itself is typically invoked randomly, according to some mutation rate. In our example, mutation happens for $\widetilde{\boldsymbol{x}}_{1,2}$ and replaces the third entry of $\widetilde{\boldsymbol{x}}_{1,2}$ with the number 1, as indicated in (2.43). This completes the first generation of the example. The second generation, its corresponding individuals and their fitness values are shown in Table 2.3. There, it can be seen that now the first individual is the fittest individual in the population, so one iteration of the process from Figure 2.8 led to an improvement of the solution here. This might not always be the case; for example, the mutation could have also replaced the second entry of $\widetilde{\boldsymbol{x}}_{1,2}$ with number of 8 for example, such that the resulting fitness of 198 would be worse than the one of $\boldsymbol{x}_{1,1}$. However, as it has a lower selection probability, it is more likely to be removed in subsequent generations than fitter individuals, which biases the GA towards better solutions.

Table 2.3: Example population, fitness values and ranking at generation $i = 2$.

k	**Individual no.** k	**Fitness Value** $F_e(\boldsymbol{x}_{k,i})$	**Ranking** $\text{rank}(k, i)$
1	$\boldsymbol{x}_{1,2}^T = [7 \quad 0 \quad 1 \quad 6]$	86	1 (best fitness)
2	$\boldsymbol{x}_{2,2}^T = [9 \quad 8 \quad 7 \quad 6]$	230	3 (worst fitness)
3	$\boldsymbol{x}_{3,2}^T = [7 \quad 0 \quad 6 \quad 3]$	94	2

Again, numerous other methods for implementing mutation in GAs exist, see [85, pp. 126–127] and [104, pp. 43–44]. Repeating this process will eventually further improve the fitness value here. While there are no guarantees of convergence or error bounds for a GA minimizing an arbitrary function, it can be used as a heuristic that sometimes finds a good enough solution or even the global optimum. As indicated by the above example, a GA has many different parameters that require careful and problem dependent adjustment. Also, the discussed genetic operators like crossover and mutation only represent the most commonly used operators. More operators have been proposed in the literature, compare [199, p. 130].

The traditional GA described above can be a useful tool for parameter tuning, not only for integer valued functions, but of course also for functions over the reals. However, applications like curve fitting require the designer to choose a specific structure before the actual optimization. The GA then optimizes the parameters of this structure, but not the structure itself. In order to overcome this limitation, different methods have been proposed already. In the following section, a short summary of one such method, genetic programming, is given, which can be considered as an extension of traditional GAs.

2.3.2 Optimization with Genetic Programming

Genetic Programming is an optimization algorithm similar to the traditional GA, but with the difference that it not only optimizes parameters of a fixed, predefined structure, but the structure itself. Genetic programming was proposed by Koza, see for example [157, 158]. This method usually represents individuals in the form of syntax trees instead of the common real-valued or integer-valued vector representation of GAs [231, p. 9], although alternative representations like linear GP have been proposed as well [231, pp. 61–68]. The genetic operators described in Section 2.3.1 can be defined analogously for tree structures, cf. [231, pp. 9–17]. The method has been used early for control design [159, 160]. More control applications can be found in [61], while [231, pp. 111–130] lists different applications of GP.

In this work, we focus on a variant of GP which uses a context free grammar for representation of individuals, see for example [195] and [231, pp. 53–57]. The grammar provides the basic building blocks and the rules how to combine these blocks to form a syntactically valid candidate solution, which can then be evaluated with a suitable fitness function. As such, the grammar represents a high level description of the expected structure of a solution and hence is a degree of freedom that the user has to choose appropriately for the corresponding optimization problem. A formal definition of a context free grammar reads as follows.

Definition 41. *(Context free grammar, cf. [209, p. 5]) A context free grammar $\mathcal{G}$ is the four-tuple $\mathcal{G} = (\mathcal{N}, \Sigma, \mathcal{P}, \mathcal{S})$, where $\mathcal{N}$ is the finite set of nonterminals, Σ the finite set of terminals such that $\mathcal{N} \cap \Sigma = \emptyset$, $\mathcal{S} \in \mathcal{N}$ is the start symbol and $\mathcal{P}$ is the finite set of production rules. Elements of $\mathcal{P}$ are ordered pairs (A, α) with $A \in \mathcal{N}$ and $\alpha \in (\mathcal{N} \cup \Sigma)^*$ where the asterisk denotes the Kleene closure of $(\mathcal{N} \cup \Sigma)$ and production rules are written $A \mapsto \alpha$.*

While this definition is very general and allows for example the definition of the grammar of a programming language, in this work we focus on the synthesis of mathematical expressions. An example grammar suitable for this purpose can be defined as $\mathcal{G}_e = (\mathcal{N}_e, \Sigma_e, \mathcal{P}_e, \mathcal{S}_e)$ with $\mathcal{S}_e = \langle e \rangle$, $\mathcal{N}_e = \{\langle e \rangle, \langle o \rangle, \langle v \rangle, \langle c \rangle\}$, $\Sigma_e = \{+, -, \times, x_1, x_2, 1, 2, 3, (,), ,\}$. A compact notation commonly used to denote the production rules is the Backus-Naur Form (BNF), compare [13, 14]. The production rules $\mathcal{P}_e$ used in the example here are defined in BNF as

$$\langle e \rangle \mapsto \langle o \rangle(\langle e \rangle, \langle e \rangle) \mid \langle v \rangle \mid \langle c \rangle \tag{2.44a}$$

$$\langle o \rangle \mapsto + \mid - \mid \times \tag{2.44b}$$

$$\langle v \rangle \mapsto x_1 \mid x_2 \tag{2.44c}$$

$$\langle c \rangle \mapsto 1 \mid 2 \mid 3\,, \tag{2.44d}$$

where $\mid$ denotes disjunction, meaning for example that in (2.44), the nonterminal $\langle v \rangle$ can be mapped to either x_1 or x_2. The syntax tree notation for operators is $+(a, b) = a+b$, $-(a, b) = a-b$ and $\times(a, b) = ab$. The example grammar $\mathcal{G}_e$ represents the rules to form expressions of up to two variables x_1, x_2 and three constants 1, 2, 3, involving (potentially nested) addition, subtraction and multiplication. With this definition, the initialization of a population can be illustrated. As an example, we consider the two traditional techniques of "full" and "grow" initialization [231, pp. 11–14]. For full initialization, the user defines a desired target tree depth, for example two. Then, random non-terminals are drawn until the tree depth of two is reached, drawing in this example only non-terminals that allow recursive mapping, which is here only $\langle e \rangle \mapsto \langle o \rangle(\langle e \rangle, \langle e \rangle)$. Non-terminals are replaced with random terminals, leading to an expression tree where each leaf has a depth of 2. For example, we start with $\langle o \rangle(\langle e \rangle, \langle e \rangle)$, draw a random operator to obtain $+(\langle e \rangle, \langle e \rangle)$, then draw a random recursive non-terminal for $+(\langle o \rangle(\langle e \rangle, \langle e \rangle), \langle e \rangle)$. This process is repeated until each branch of the tree has the desired depth, for example $+(\times(x_1, x_1), \times(2, x_2))$ which represents the function $x_1^2 + 2x_2$. The grow initialization technique works similarly, with the only difference that branches are allowed to terminate before reaching a maximum depth and could therefore also produce $+(x_1, \times(2, x_2))$, representing the function $x_1 + 2x_2$.

In order to generate an initial population with higher diversity, the two initialization techniques can be combined, leading to the "ramped half-and-half" initialization, where one half of the population is initialized using full and one half using grow initialization, see [231, pp. 11–14]. Fitness evaluation is done by evaluating the generated expression within the user defined fitness function. Selection is performed in the same way as for traditional GAs, see Section 2.3.1. Crossover is performed by copying one individual and replacing a subtree of its expression tree with a subtree of another individual, where both nodes are chosen at random [231, pp. 15–17]. This process is depicted in Figure 2.9, where the abstract syntax trees on the left and in the middle represent two example individuals chosen by the selection mechanism. Two nodes are chosen at random, according to a user defined distribution, in this example indicated by a bold border in Figure 2.9. A new tree is formed by copying the subtree above the selected node of the first tree and appending the subtree copied from the selected node of the second tree as shown in Figure 2.9. The abstract syntax tree on the right represents the offspring generated by this crossover operation. Crossover points are not constrained in this work by the grammar to have the same underlying non-terminal, as for example suggested in [195], see also [231, pp. 53–55].

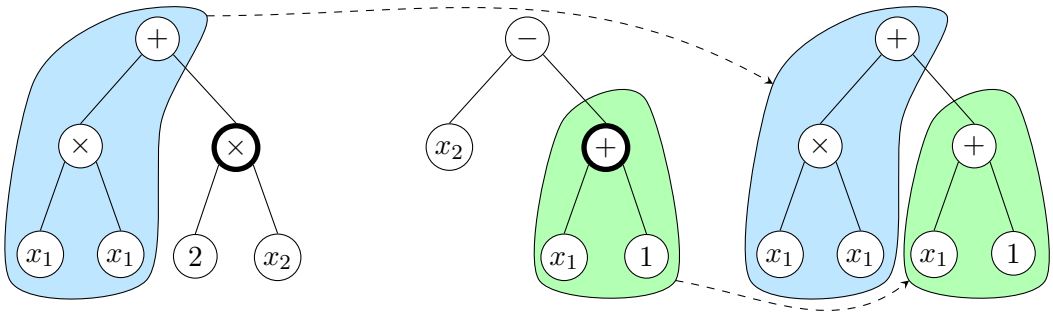

Figure 2.9: Example of the crossover operation used in the GP algorithm, derived from [231, p. 16].

For mutation, we use the two common methods of subtree mutation and point mutation, see also [231, pp. 15–17]. Subtree mutation denotes the operation of replacing a randomly chosen subtree of the considered expression with a randomly generated subtree. In this work, we use the grow initialization technique described above to generate the random subtree. Point mutation denotes the operation of selecting some nodes at random and replacing the terminal symbol of these nodes with a randomly drawn compatible terminal. For example, given the expression $+(x_1, 1)$ which corresponds to $x_1 + 1$, point mutation could randomly choose the $+$ node and replace it with either $+$, $-$ or $\times$, as these are available terminals from the underlying non-terminal $\langle o \rangle$, according to the production rule (2.44b). In this introduction we focus on the mutation and crossover methods that are used in Chapter 5 of this work. Various other methods for implementing mutation and crossover operations in GP exist, compare for example [231, pp. 42–46]. Optionally, a symbolic simplification of the generated tree can be performed before the fitness evaluation [231, p. 46]. For this purpose, we apply a basic simplification method that only combines constants, so for example $+(x_1, +(1, 1))$ is simplified to $+(x_1, 2)$.

Moreover, it can be noted that constants are not a fixed set of numbers like in the example grammar $\mathcal{G}_e$ from above. Instead, a terminal representing a so-called ephemeral random constant is included in the grammar, cf. [231, p. 20]. When a production rule during creation of the tree leads to this terminal, a random value is drawn for generating the constant. Since every individual maintains its own pool of constants, point mutation can alter these constants without affecting other individuals in the population.

This concludes the literature review. In the next chapter, a control design for TCSs based on IOL is proposed, followed by a detailed stability analysis. The zero dynamics of the 2WD TCS will be used thereafter to test a heuristic method for Lyapunov function identification by GP.

3 Traction Control and Vibration Damping via Input-Output-Linearization

Summary. *This chapter describes the methodical approaches taken in this thesis to solve the traction control problem for vehicles with 2WD and on-demand 4WD with torque-bias systems. The main contributions are:*

1. *A TCS based on input-output linearization for vehicles with 2WD and on-demand 4WD torque bias systems, including a model for reference dynamics generation.*
2. *A detailed derivation and analysis of the control laws obtained from three longitudinal models of different complexity for traction control.*
3. *Proof of global, asymptotic, parameter-independent stability of the resulting zero dynamics using a novel family of parametric, quadratic Lyapunov functions.*

Moreover, a new modification of the wheel slip, applicable for local stability analysis, is proposed. This chapter is partially based on our previous publications [305, 304, 307] and [300].

3.1 Objectives for the Traction Control System

The goal of the control design, as stated in Chapter 1, is to enable the usage of the IOL technique for traction control without the need of estimating uncertain quantities like tire parameters or the friction coefficient of the road in the inner control loop on the ECU. This is important in order to ensure robustness of the control design. The main objectives regarding performance, usability and robustness, adapted from [305], are listed in the following.

1. Tracking of the reference speeds commanded from the DCU with zero asymptotic error.
2. Damping of drivetrain vibrations and compensation of drivetrain inertia.
3. Attenuation of external disturbances like variations of the friction coefficient of the road.
4. Scalability of the TCS for vehicles with 2WD and on-demand 4WD torque bias systems.
5. Stability of the control design, by analytic proof and experimental evaluation.
6. Robustness of these five objectives with respect to parameter uncertainty, time-varying disturbances and a wide range of operating conditions.

The remainder of this chapter shows how these objectives are achieved with the proposed control design. In the following section, different synthesis models suitable for control design are proposed. These form the basis of the following control design with the input-output linearization technique. It is shown how this method can be applied for control design of TCSs for both vehicles with 2WD and vehicles with on-demand 4WD torque bias systems. Thereafter, a detailed stability analysis of the resulting nonlinear zero dynamics using Lyapunov techniques is presented. For this analysis a novel family of parametric, quadratic Lyapunov functions is proposed which can be used to show global, asymptotic stability of the resulting zero dynamics for all possible vehicle parameters. These results are developed further in Chapter 4, while the experimental evaluation of the proposed TCSs is provided in Chapter 6.

The 2WD synthesis model is a result of our joint work with Zech *et al.* [307], while we proposed the 7-state 4WD synthesis model in [300], see also [297] for an earlier, lower-order variant of this model. The 9-state 4WD synthesis model proposed in this work represents a natural extension of this model. Following, the 2WD synthesis model is described.

3.2 Modeling of Longitudinal Vehicle Dynamics

3.2.1 Synthesis Model for 2WD Drivetrains

For control design, three different synthesis models which describe the relevant dynamics for traction control are discussed in the following. Based on these models, the control laws are derived in the subsequent section for vehicles with 2WD and on-demand 4WD with torque-bias systems. In addition to the 2WD case, two different variants for the 4WD case are proposed, each with different advantages, resulting in a total of three synthesis models for control design. This section is partially based on our previously published work [300, 305, 307].

First, the synthesis model used for control design of TCSs for vehicles with 2WD is presented. The actuator dynamics for the torque build-up of the motor are modeled by a first order lag element with

$$\tau_m \dot{T}_m = T_{m,d} - T_m. \tag{3.1}$$

Here, τ_m is the time constant of the actuator, $T_{m,d}$ is the requested torque and T_m the actual torque provided by the motor. For an electric motor, this is a common model for control design of TCSs [113]. Generally, ICEs have more complicated, nonlinear dynamics if the whole operating range is considered, see [151, pp. 75–97] or [122, pp. 31–47]. However, the controller is only active if the requested torque by the driver exceeds the maximum achievable torque. A TCS generally reduces the requested torque by the driver and can make use of the fast firing path during transients. Therefore, during active control, Equation (3.1) can be used for the actuator dynamics of combustion engines in TCSs, as well [305, 291]. The drivetrain is modeled as a single torsion spring by

$$\Delta\dot{\phi}_c = \omega_c/i_G - \omega_r \tag{3.2}$$

$$J_c\dot{\omega}_c = T_m - 2\,T_r/i_G \tag{3.3}$$

$$T_r = k_c\Delta\phi_c + d_c(\omega_c/i_G - \omega_r)\,. \tag{3.4}$$

Here, ω_c and ω_r are the angular velocities of the crankshaft and the rear axle, respectively, while $\Delta\phi_c$ denotes the twist angle of the spring and J_c the aggregated inertia of the drive side. Moreover, $i_G = i_a i_r$ is the total gear ratio from the motor to the rear axle, i_a the gear ratio of the automatic transmission case and i_r the gear ratio of the differential on the rear axle. The torque on the rear axle is $2\,T_r$, generated through the torsion spring with aggregated torsional stiffness k_c and damping factor d_c. The factor 2 in (3.3) enters, because the spring constants k_c and d_c are typically identified using torque sensors on individual wheels. Next, the equations for the rear axle are given by

$$J_r\dot{\omega}_r = 2\,T_r - r_r F_{xr} \tag{3.5}$$

$$F_{xr} = \mu F_{zr}\sin\big(C_r\arctan(B_r\lambda_{xr})\big) \tag{3.6}$$

$$F_{zr} = m\,g\,l_f/(l_f + l_r)\,, \tag{3.7}$$

with J_r the combined inertia of the rear axle including wheels, r_r the radius of the rear wheels and F_{xr} the friction force between tire and road. The normal force F_{zr} depends on the total vehicle mass m, the gravitational acceleration g and the lever arm between the center of gravity (COG) of the vehicle and the rear axle. This term is given by the ratio of the distance between COG and front axle l_f and distance between front and rear axle $l_f + l_r$, where l_r is the distance between COG and rear axle, compare for example [83, pp. 11–13].

Remark 3. *For the proposed equations of motion, a vehicle with rear-wheel drive (RWD) is assumed. However, the method presented in the following sections is directly applicable for vehicles with front-wheel drive (FWD) as well, as this case follows analogously.*

The nonlinear tire force (3.6) is modeled using a variant of the Pacejka tire model [219], also known as "Magic Formula", due to its semi-empirical character. The tire force parameters B_r and C_r are typically adjusted to fit a set of measured tire force curves. Furthermore, the coefficient of friction between tire and road is denoted with μ and the wheel slip with λ_{xr}. In the literature, different definitions for the wheel slip exist. Most of these restrict the considered maneuvers for the TCS to specific cases, for example by excluding both the braking case and back ride [287] or just back ride [63], while some authors define wheel slip in terms of a differential equation rather than a static mapping [168]. A static formula that is applicable for accelerating and decelerating in both forward or backward directions, see for example [243], is

$$\lambda_{xr} = (r_r\omega_r - v_x)/v_{\text{norm},r} \tag{3.8}$$
$$v_{\text{norm},r} = \max(r_r|\omega_r|, |v_x|)\,. \tag{3.9}$$

Remark 4. *One common issue with the standard wheel slip definition as in (3.8) is, that for* $\omega_r = v_x = 0 \Rightarrow v_{\text{norm},r} = 0$*, so* λ_{xr} *is undefined at standstill. A possible solution to this problem is proposed in Section 3.2.2. For now we temporarily assume that* $v_{\text{norm},r} \neq 0$*.*

For "small" slip values $|\lambda_{xr}| \ll 1$, a linear approximation of the nonlinear force curve (3.6) can be obtained by linearization,

$$F_{xr} \approx c_{xr}\lambda_{xr} \tag{3.10a}$$
$$c_{xr} = \mathrm{d}F_{xr}/(\mathrm{d}\lambda_{xr})|_{\lambda_{xr}=0} = \mu F_{zr} B_r C_r\,. \tag{3.10b}$$

The longitudinal slip stiffness c_{xr} is defined as the slope of the friction curve (3.6) at the origin [46] and is an important characterizing tire property [32]. While the tire force F_{xr} can also be defined such that c_{xr} does not depend on μ, compare for example [218, p. 20], we use a variant here where c_{xr} depends on μ, cf. [95, 236]. Linear tire force approximations like (3.10a) are also used for control design and system analysis of TCSs [243] and ABSs [136]. The friction coefficient of the road μ is often defined in the interval $(0, 1]$, while coefficients larger than unity are possible and considered as well [203]. The actual value of μ depends on the driving surface and while the exact values for different road conditions vary in the literature it is common to assume for example $\mu \approx 0.3$ for snow, $\mu \approx 0.5$ for gravel and $\mu > 0.8$ for dry asphalt [95, 203]. Figure 3.1 shows three characteristic friction force curves (3.6) and their linearizations (3.10a) for different friction coefficients, each representing a different driving surface, computed by (3.6).

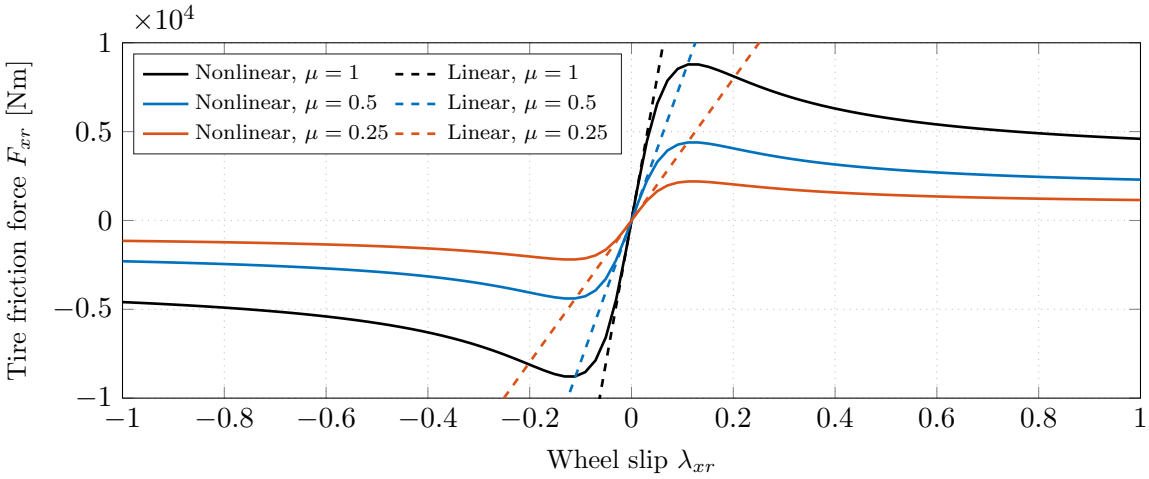

Figure 3.1: Tire friction force as a function of wheel slip λ_{xr} and friction coefficient μ [305].

.

The last quantity to complete the set of differential equations of the synthesis model for traction control of 2WD vehicles is the longitudinal velocity of the vehicle v_x, given by

$$\dot{v}_x = (F_{xr} - F_w)/m \tag{3.11}$$

$$F_w = (1/2)\rho c_w A_{st} v_x |v_x| \,. \tag{3.12}$$

Here, F_w is the aerodynamic drag force, which depends on the air density ρ, the aerodynamic drag coefficient c_w and the frontal area of the vehicle, denoted with A_{st}, see [83, pp. 97–100]. This completes the set of differential equations for the synthesis model in the 2WD case. Clearly, this model is built upon different simplifying assumptions of the underlying physics of the vehicle and drivetrain dynamics, where the most important ones are listed as follows.

1. Vehicle dynamics in lateral direction, cornering and μ-split is neglected.
2. Roll and pitch dynamics are neglected such that normal forces are static.
3. No road inclination is considered, the driving surface is assumed to be planar.
4. Actuator dynamics of the ICE are assumed to be a first order LTI system.
5. Additional resistance forces like rolling resistance are neglected.
6. The spring that models the torsional drivetrain dynamics is linear.
7. The gear is piecewise constant, shifting is not modeled explicitly.
8. Only the engine is controlled, actuators like brakes are not considered.

While these assumptions might look very limiting, they are valid for control design. This can be explained by looking at the model in a component-wise representation, as depicted in Figure 3.2, where single line borders denote linear and double line borders denote nonlinear blocks.

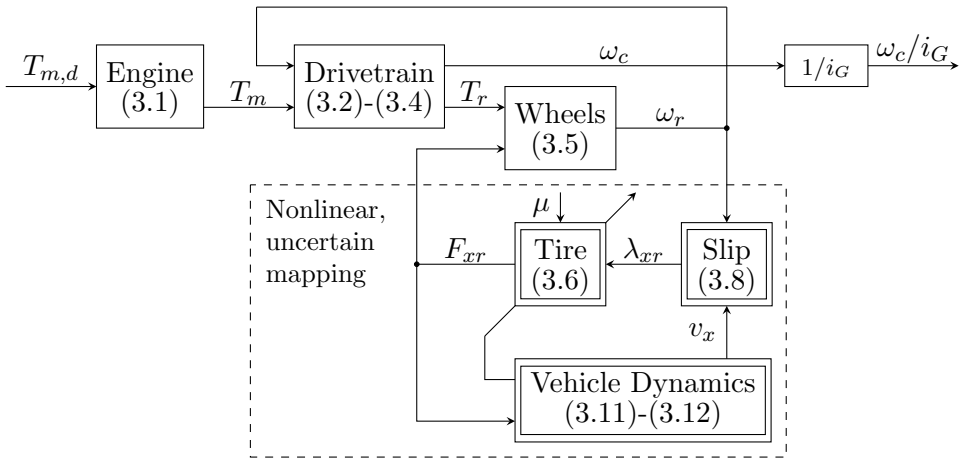

Figure 3.2: Component-wise representation of the nonlinear 2WD synthesis model [305].

The nonlinear, uncertain mapping from ω_r to F_{xr} depends on the tire model, the longitudinal vehicle dynamics and the time-varying friction coefficient. This mapping can be interpreted as a friction operator from ω_r to F_{xr} with internal dynamics $\dot{v}_x = (F_{xr} - F_w)/m$ from (3.11), to which F_{xr} acts as an input. From $V_v(v_x) = (m/2)v_x^2$ follows $\dot{V}_v(v_x) = v_x F_{xr} - c_a v_x^2 |v_x| \leq 0 \,, \forall v_x \in \mathbb{R} : |v_x| \geq \rho_v(|F_{xr}|) = \sqrt{|F_{xr}|/(c_a - c_a\theta)}$, with $c_a = (1/2)\rho c_w A_{st}$ and $\theta \in (0,1)$. Since ρ_v is a class $\mathcal{K}$ function and F_{xr} from (3.6) is bounded, the internal dynamics of the friction operator are ISS. The abstraction of a bounded (potentially dynamic) friction operator has been applied for example to funnel control of a two mass system with unknown load, compare [119] and [252]. While we pursue a different approach, the proposed TCSs will not require a model of the friction operator either. Considering Assumptions 1, 2 and 3, lateral dynamics due to cornering, pitch during acceleration or road inclination, as examples, are slowly time-varying compared to the wheel dynamics and hence are assumed as uncertainty of the tire model (3.6). In Figure 3.2, this is indicated with a diagonal arrow through the tire block. Hence, it is sufficient for the inner control loop on the ECU to track the target speed for different "deformed" friction curves.

As already discussed at the beginning of this section, Assumption 4 is valid during phases of active control, while additional resistance forces mentioned in Assumption 5, like rolling resistance, are typically small and can be considered as disturbance. Assumption 6 is valid, as it can be shown by measurements using torque sensors, that a linear spring models the torsional drivetrain dynamics with high accuracy [291, 307]. Assumption 7 is made as gear switching is not considered explicitly in this work. Assumption 8 is made as actuators like brakes are taken care of by other control systems not investigated in this work. Apart from these model-based assumptions, there are additional technical assumptions on the parameters and the friction coefficient of the road.

1a. All vehicle parameters are strictly positive, constant and finite.
2a. For the friction coefficient: $\mu \in (0, \mu_{\max})$ with $\mu_{\max}$ strictly positive and finite.
3a. For the Pacejka tire force shaping factor: $C_r \in (1, 2)$.
4a. For the Pacejka tire force stiffness factor: $B_r > \tan\big(\pi/(2C_r)\big)$.

The first two of these assumptions are required for different theoretical analyses later and can safely be considered true in practice.

Remark 5. *Vehicle parameters, from a strict viewpoint, are not constant. For example, the total vehicle mass decreases during driving due to fuel consumption, tire parameters are subject to mechanical wear and aerodynamic drag parameters, like density of air, depend on environmental conditions. However, such variations are usually orders of magnitude slower than the wheel dynamics relevant for TCSs and can therefore be neglected for control design.*

The third assumption is often assumed in literature, as together with Assumptions 1a. and 2a., it guarantees that λ_{xr} and F_{xr} always have the same sign, compare for example [219, p. 67]. Hence, a positive wheel slip has to generate an accelerating force and a negative wheel slip has to generate a decelerating force. This makes sense from a physical viewpoint and can readily be shown from the equation of the tire force (3.6) as follows.

Lemma 1. *Assume 1a.-3a. hold. Then,* $\lambda_{xr} F_{xr} > 0\,, \forall\, \lambda_{xr} \neq 0$.

Proof. For $C_r \in (1, 2)$ the $C_r \arctan(B_r \lambda_{xr})$ term in (3.6) is bounded to $(-\pi, \pi)$ and is zero if and only if $\lambda_{xr} = 0$ as by 1a. $B_r > 0$. Further, since the arc-tangent is monotone, it has the same sign as λ_{xr}. The sine function has a unique root in $(-\pi, \pi)$ at the origin and so $\lambda_{xr} F_{xr} > 0\,, \forall\, \lambda_{xr} \neq 0$ if $C_r \in (1, 2)$, cf. [305]. □

The fourth assumption ensures that the peaks of the force curve are attainable. It is not required for the main stability theorems of this work, but for some additional results. As in practice the tire force peaks are always attainable for some $\lambda_{xr} \in (-1, 1)$, it follows that B_r cannot be arbitrarily small as the wheel slip itself is bounded. While this is obvious from (3.8), it can be noted that in contrast to the commonly used one-directional slip definitions, a bi-directional definition (valid for forward and backward direction), ranges not only from $[-1, 1]$ but from $[-2, 2]$.

Lemma 2. *Assume 1a. holds and that either* $\omega_r \neq 0$ *or* $v_x \neq 0$. *Then, the wheel slip from Definition (3.8) is bounded to* $[-2, 2]$.

Proof. Assume without loss of generality that $|\omega_r r_r| \geq |v_x|$. Clearly, if either $\omega_r = 0$ or $v_x = 0$ then $|\lambda_{xr}| = 1$, so exclude those cases. Then, (3.8) reduces to

$$(\omega_r r_r - v_x)/|\omega_r r_r| = \operatorname{sign}(\omega_r r_r) - v_x/|\omega_r r_r|\,. \tag{3.13}$$

Since $|\omega_r r_r| \geq |v_x|$ by assumption, $v_x/|\omega_r r_r| \in [-1, 1]$, where the interval ends are attained for $v_x = \pm|\omega_r r_r|$. Therefore, λ_{xr} attains its maximum value of 2 for $\omega_r r_r > 0$ and $v_x = -\omega_r r_r$ and its minimum value of -2 for $v_x > 0$ and $\omega_r r_r = -v_x$. □

This also shows that ω_r and v_x must have different signs to result in wheel slip values larger than 1 or smaller than -1. Generally, however, the B_r parameter is chosen such, that the peak of the force curve is attained for $|\lambda_{xr}| < 1$.

Lemma 3. *Assume 1a.-4a. hold. Then, the extrema of (3.6) are attainable for wheel slip values* $\lambda_{xr} \in (-1, 1)$.

Proof. Since the sine function is bounded to $[-1, 1]$, the extrema of (3.6) are $\pm\mu F_z$. By 1a.-3a. and the proof of Lemma 1, the argument of the sine function is bounded to $(-\pi, \pi)$. Within this interval, the sine function evaluates to ± 1 if and only if its argument is $\pm\pi/2$, so the extrema are unique and attained at

$$\lambda^{+}_{xr,\text{peak}} = \tan\big(\pi/(2C_r)\big)/B_r \tag{3.14a}$$

$$\lambda^{-}_{xr,\text{peak}} = -\lambda^{+}_{xr,\text{peak}}\,. \tag{3.14b}$$

The $\tan\big(\pi/(2C_r)\big)$ term grows unbounded for $C_r \to 1^+$, but λ_{xr} is limited to $[-2, 2]$ by Definition (3.8), cf. Lemma 2. Therefore, if $B_r > \tan\big(\pi/(2C_r)\big)$, if follows that $\lambda^{+}_{xr,\text{peak}} \in (0, 1)$ and $\lambda^{-}_{xr,\text{peak}} \in (-1, 0)$. □

Remark 6. *The wheel slip from Definition 3.8 can take values from* $[-2, 2]$*, so mathematically* $B_r \geq \tan\big(\pi/(2C_r)\big)/2$ *would be sufficient to guarantee that the extrema of (3.6) are attainable. However, this is undesired since, in practice, the tire force peak is attained at wheel slip values well below unity, so peak values at* $|\lambda_{xr}| \geq 1$ *are not realistic.*

Remark 7. *Wheel slip values* $\lambda_{xr} \in [-2, -1)$ *correspond to maneuvers where the vehicle drives in forward direction, but the wheels turn backwards. Similarly,* $\lambda_{xr} \in (1, 2]$ *corresponds to the vehicle driving backwards, but the wheels turning in forward direction. While this can happen in practice (starting off uphill on an icy road, for example), it is intuitively clear that in such a case, the transmitted force would not be larger than for maneuvers where* v_x *and* ω_r *have the same sign. Hence, Assumption 4a. is plausible.*

An important property of the tire model is, that it is sector-bounded in the sector spanned by the linearized model resulting from a linearization at $\lambda_{xr} = 0$ as defined in (3.10a).

Lemma 4. *If 1a.-3a. hold then* $c_{xr}|\lambda_{xr}| > |F_{xr}|\,, \forall\, \lambda_{xr} \neq 0$ *and* $F_{xr} = c_{xr}\lambda_{xr} \iff \lambda_{xr} = 0$.

Proof. A proof is given in the Appendix A.3. □

This property will be important for the stability analysis of the zero dynamics of the proposed TCSs carried out in this chapter and also the passivity analysis presented in Chapter 4. Regarding the assumptions on the longitudinal vehicle model used for control design discussed above, it can also be noted that the available state of the art on TCSs and ABSs uses synthesis models that have more simplifying assumptions, by considering only a 2-state model with stiff drivetrain, see for example [36, 72, 113, 136] and the survey [129]. Various publications that consider torsional drivetrain dynamics for general analysis and control design exist, compare [251, pp. 1188–1291] and references therein. There also exist publications considering torsional drivetrain dynamics for TCS design and methods for AVC of drivetrain oscillations [10, 53, 91, 90, 181], see also Section 2.1.3. However, no work exists that uses such a model for an IOL based control design of 2WD and 4WD TCSs for the ECU based architecture discussed in Section 2.1.2, and that also includes a nonlinear stability analysis, except our recent work [300, 304, 305].

Following, we propose a new modified definition of the wheel slip, which avoids the singularity in the traditional wheel slip definition, see (3.8). Then the 2WD longitudinal model is extended to vehicles with on-demand 4WD torque bias systems and a control design based on the method of IOL is derived for these models. Thereafter, a stability analysis using a novel family of parametric, quadratic Lyapunov functions is presented and global, asymptotic stability of the zero dynamics resulting from the IOL control design is shown for all possible vehicle parameters.

3.2.2 Smooth Wheel Slip Approximation

As already mentioned in Remark 4, the standard wheel slip definitions like (3.8) have a singularity at $\omega_r = v_x = 0$. In the literature, there exist different approaches to deal with this issue. One possibility is to define the wheel slip in terms of a differential equation, rather than a static mapping [168]. The disadvantage of this method is that it increases the order of the system by adding another state. Furthermore, if arbitrary initial conditions must be assumed for a global stability analysis, implausible state combinations cannot be readily excluded. For example, considering an initial condition with $v_{x,0} = 10\,\mathrm{m/s}$, $\omega_{r,0} = (10/9)v_{x,0}/r_r\,\mathrm{rad/s}$ which, according to (3.8), corresponds to a wheel slip of $1/10 = 10\%$. In simulation, this can be taken into account by setting the wheel slip initial condition $\lambda_{xr,0} = 1/10$ accordingly. However, for global stability analysis, it is often necessary to consider the whole state space. So for example, $\lambda_{xr,0} = -1/10$ had to be considered here as well, or even $|\lambda_{xr,0}| > 2$, if one wants to avoid adding algebraic constraints to the dynamics, see also Remarks 6 and 7. This can complicate analysis significantly, while such state combinations cannot occur in practice.

Due to the aforementioned problems, a different direction is pursued in this work to deal with the singularity in (3.8). Another common approach in literature is to modify the denominator in the wheel slip definition, see [242, pp. 50–79] or [243], like

$$v_{\mathrm{norm},r} \approx v'_{\mathrm{norm},r} = \max(r_r|\omega_r|, |v_x|) + v_0\,, \tag{3.15}$$

with $v_0 > 0$. Since $\lim_{v_0 \to 0} v'_{\mathrm{norm},r} = v_{\mathrm{norm},r}$, choosing the value v_0 "small enough" approximates the normalization speed to an arbitrary accuracy. Furthermore, using (3.15) for the wheel slip calculation, if $\omega_r = v_x = 0 \Rightarrow \lambda_{xr} = 0 \Rightarrow F_{xr} = 0$, so no force is applied at standstill, which is plausible and gives the desired behavior. However, Equation (3.15) has the problem of not being differentiable everywhere. Therefore, a different approximation, as we previously published in [305], is derived here, using the identity

$$\max(a, b) = (a + b + |a - b|)/2\,. \tag{3.16}$$

A well known smooth approximation of the absolute value is

$$|a| \approx |a|_\epsilon = \sqrt{a^2 + \epsilon}\,, \tag{3.17}$$

with $\epsilon > 0$, so combining (3.16) and (3.17) results in the smoothed maximum function,

$$\max(a, b) \approx \max_\epsilon(a, b) = (a + b + |a - b|_\epsilon)/2\,. \tag{3.18}$$

This function is a variant of a specific instance from the Chen-Mangasarian family of smoothing functions [39], namely a variant of the Chen-Harker-Kanzow-Smale smoothing function [38, 145, 257]. These functions have been used, among others, for solving linear complementarity problems or constrained optimization problems [41]. In the context of vehicle dynamics, this technique has been used to smoothen constraints containing the max function in optimal control formulations for laptime minimization of race-cars [224].

Remark 8. *Definition (3.18) is called a "variant", as the Chen-Harker-Kanzow-Smale function usually defines a smoothed* min *function, cf. [41]. However, since* $\min(a, b) = (a + b - |a - b|)/2$ *and* $\min(a, b) = a - \max(0, a - b)$*, see [41], this can be readily adapted to the* max *function.*

While the Chen-Harker-Kanzow-Smale function has been already applied for different optimization tasks, its application to traction control by smoothly approximating the normalization speed (3.9) is new [305]. The modified normalization speed can then be defined as

$$v_{\mathrm{norm},r} \approx v_{nr} = \max_\epsilon(|r_r\omega_r|_\epsilon, |v_x|_\epsilon)\,, \tag{3.19}$$

which, like for Equation (3.15), gives $\lim_{\epsilon \to 0} v_{nr} = v_{\mathrm{norm},r}$ and hence approximates the standard normalization speed with an arbitrary accuracy as the smoothing parameter $\epsilon > 0$ approaches zero, with the additional advantage over (3.15) of being a smooth function.

A useful property of this definition is that $v_{nr} > 0$ for any $\epsilon > 0$, so no additional additive v_0 term is required to avoid the singularity in (3.8).

Lemma 5. *The smoothed normalization speed (3.19) has a unique, global minimum of* $v_0^* = 3\sqrt{\epsilon}/2 > 0$ *for* $\epsilon > 0$*, which is attained at* $\omega_r = v_x = 0$.

Proof. Define the intermediate function $v_\epsilon(\omega_r, v_x) = \left((|r_r\omega_r|_\epsilon - |v_x|_\epsilon)^2 + \epsilon\right)^{1/2}$ in order to write the components of the gradient of (3.19) as

$$\partial v_{nr}/(\partial\omega_r) = -r_r^2\omega_r\big(v_\epsilon(\omega_r, v_x) - (|r_r\omega_r|_\epsilon - |v_x|_\epsilon)\big)/\big(2\, v_\epsilon(\omega_r, v_x)|r_r\omega_r|_\epsilon\big) \tag{3.20a}$$

$$\partial v_{nr}/(\partial v_x) = v_x\big(v_\epsilon(\omega_r, v_x) - (|r_r\omega_r|_\epsilon - |v_x|_\epsilon)\big)/\big(2\, v_\epsilon(\omega_r, v_x)|v_x|_\epsilon\big)\,. \tag{3.20b}$$

Since $\epsilon > 0$ and so $v_\epsilon(\omega_r, v_x) > |r_r\omega_r|_\epsilon - |v_x|_\epsilon \geq 0$, the partial derivatives are well defined for any $(\omega_r, v_x) \in \mathbb{R}^2$ and equal to zero if and only if $\omega_r = v_x = 0$. The Hessian of v_{nr} at $(0,0)$ is positive definite as its eigenvalues are $1/(2\sqrt{\epsilon}) > 0$ and $r_r^2/(2\sqrt{\epsilon}) > 0$, so the unique, global minimum of v_{nr} is attained at the origin and evaluates to $3\sqrt{\epsilon}/2 > 0$, cf. [305]. □

Remark 9. *Comparing (3.19) with (3.9) or also (3.15) shows, that in the smoothed version, the tire radius* r_r *has been moved into the (smoothed) absolute value function. In the traditional definitions like (3.9) and (3.15), this makes no difference since* $r_r > 0$ *and so* $r_r|\omega_r| = |r_r\omega_r|\,, \forall\, \omega_r$. *For the smooth version, this is in general not the case, as for example if* $\omega_r = 0$*, this gives* $r_r|0|_\epsilon = r_r\sqrt{\epsilon} \neq |r_r\, 0|_\epsilon = \sqrt{\epsilon}$. *While for smoothing both variants would work, it is generally more plausible that* λ_{xr} *is independent of the tire radius* r_r *if* $\omega_r = 0$*, as it is the case for the traditional definitions as well. Hence,* r_r *is moved into the smoothed absolute value in (3.19).*

For the remainder of this work, if not stated otherwise explicitly, the smoothed version for the normalization speed v_{nr} from (3.19) is used to calculate the wheel slip by

$$\lambda_{xr} = (r_r\omega_r - v_x)/v_{nr}\,. \tag{3.21}$$

For small $\epsilon > 0$, which are required for a good approximation of (3.8), it can be noted that close to the standstill (3.21) becomes challenging for numerical ODE solvers, despite the proposed smoothing technique. The term standstill here refers to the case when both $v_x = 0$ and $\omega_r = 0$ such that $v_{nr} = v_0^*$ by Lemma 5. An analysis of this issue for the non-smooth approximation (3.15) was presented by Rill [243], with the advice stated in the conclusion to use an implicit solver for numerical simulation close to the standstill. In this work, no simulation close to the standstill is applied, so no further measures are taken in this direction. However, the smooth wheel slip approximation is also used in the stability analysis of the zero dynamics resulting from an IOL control design for the considered synthesis models. Regarding stability, global asymptotic stability of the zero dynamics will be shown for arbitrary small $\epsilon > 0$ later in this chapter, so from a theoretical viewpoint the smoothing parameter can be made as small as desired, without affecting the stability of the system. This is true for the both the 2WD TCS and the two control designs for the 4WD TCSs, as well as the passivity based stability results derived in Chapter 4.

Remark 10. *As discussed in Remark 9, the proposed definition guarantees that* v_{nr} *is independent of* r_r *if* $\omega_r = 0$ *and so also its global minimum* v_0^**, as derived in Lemma 5, does not depend on* r_r. *However, it is important to mention that the stability results derived later do not depend on this choice; in especially the arguments remain valid and follow analogously in case that* r_r *is not included in the smoothed absolute value function.*

We now continue by extending the proposed model for 2WD TCSs to vehicles with on-demand 4WD torque bias systems in the following section. Two different synthesis models suitable for traction control of vehicles with on-demand 4WD torque bias systems are presented, each with different advantages and disadvantages. Moreover, the state-space representations of the three synthesis models are stated there as well, which will thereafter be used for an analytic control design based on the method of IOL.

3.2.3 State Space Form and Extensions for Vehicles with 4WD

For control design of a TCS, it is desirable to express the dynamics of the longitudinal synthesis model (3.1)-(3.12) in a compact state space form. By defining the input $u_1 = T_{m,d}$, the output $y_1 = \omega_c / i_G$, and the state vector $\boldsymbol{x}^T = \begin{bmatrix} x_1 & x_2 & x_3 & x_4 & x_5 \end{bmatrix} = \begin{bmatrix} T_m & \Delta\phi_c & \omega_c & \omega_r & v_x \end{bmatrix}$, the dynamics of the 2WD longitudinal $\mathcal{M}_5$ model are given by

$$\mathcal{M}_5 : \begin{cases} \dot{\boldsymbol{x}} = \boldsymbol{f}(\boldsymbol{x}) + \boldsymbol{g} u_1 & \text{(3.22a)} \\ y_1 = h(\boldsymbol{x}) & \text{(3.22b)} \end{cases}$$

with

$$\boldsymbol{f}(\boldsymbol{x}) = \begin{bmatrix} -x_1/\tau_m \\ x_3/i_G - x_4 \\ (x_1 - 2\,T_r/i_G)/J_c \\ (2\,T_r - r_r F_{xr})/J_r \\ (F_{xr} - F_w)/m \end{bmatrix}, \; \boldsymbol{g} = \begin{bmatrix} 1/\tau_m \\ 0 \\ 0 \\ 0 \\ 0 \end{bmatrix}, \; h(\boldsymbol{x}) = x_3/i_G \,. \tag{3.23}$$

The notation $\mathcal{M}_5$ denotes the synthesis model with 5 states and is used to distinguish between this model and two other models for TCS design proposed in the following. While the $\mathcal{M}_5$ model is suitable for 2WD vehicles, two possible extensions for vehicles with on-demand 4WD torque bias systems are given. The modeling of such devices is discussed for example in [227, 229, 228]. An early work that analyzes the advantages of 4WD torque bias systems for maximizing traction and cornering performance is due to Torii *et al.* [270]. Figure 3.3 shows the schematic structure of the 2WD and the two 4WD models. While Figure 3.3a shows the already discussed 2WD configuration, Figure 3.3b extends this structure with a 4WD torque bias system, realized with an ETC, that can gradually couple the front axle with the rear axle by using a clutch which can be controlled with an electric motor. This model has 7 states and is named $\mathcal{M}_7$ model accordingly. Figure 3.3c shows a model with 9 states due to an additional torsion spring, referred to as $\mathcal{M}_9$ model. All springs in Figure 3.3 are virtual springs that represent the effective torsional dynamics and not the torsion at the specific component where they are indicated.

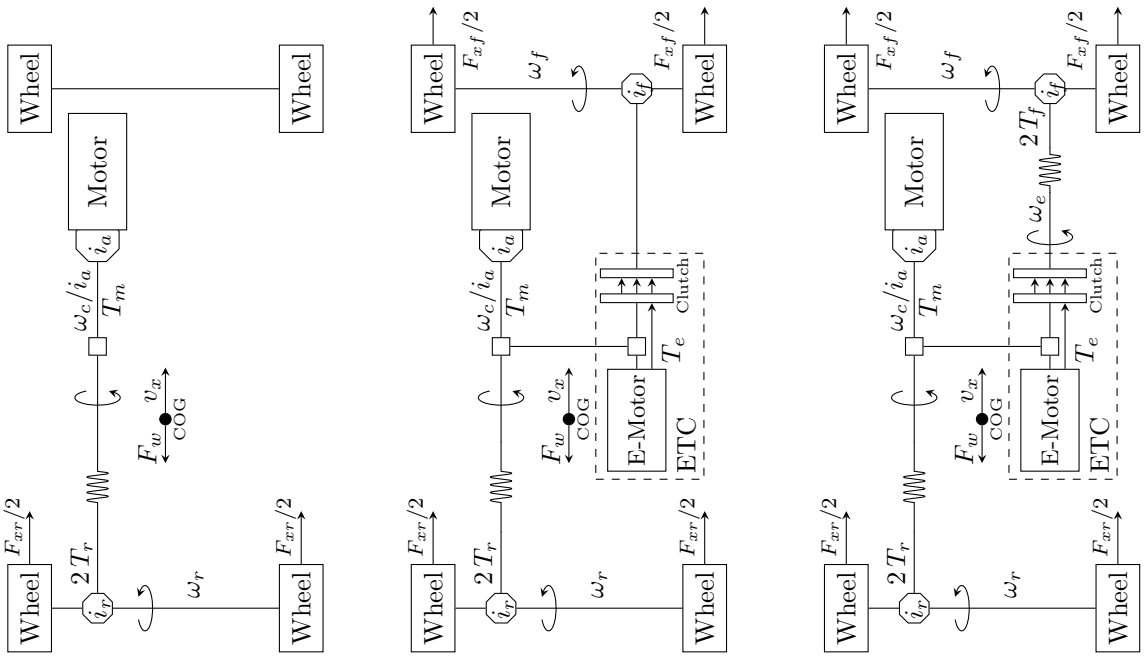

(a) 2WD model $\mathcal{M}_5$ with 5 states. **(b)** 4WD model $\mathcal{M}_7$ with 7 states. **(c)** 4WD model $\mathcal{M}_9$ with 9 states.

Figure 3.3: Structure of the longitudinal models for 2WD and 4WD TCS design, adapted from [300].

The actuator dynamics of the electric motor controlling the clutch can be described by a first order lag element with time constant τ_e, desired torque $T_{e,d}$ and actual torque T_e as

$$\dot{T}_e = (T_{e,d} - T_e)/\tau_e \,. \tag{3.24}$$

Remark 11. *Here, T_e denotes the torque of the electric motor applied to the clutch. The torque shifted to the front axle is $i_f T_e$, but only as long as the clutch is not locked and $0 \leq T_e/i_a \leq T_m$. These conditions are assumed for control design here. If these conditions are not satisfied, for example during drag torque control, then the actual drive torque on the front axle will deviate from T_e/i_a. While not considered in this work, the 4WD models and control laws can be extended to account for the sign of T_m as well. A model that takes the hybrid dynamics of the clutch into account for a numerical simulation study is presented in [297].*

As indicated in Figure 3.3b, the gear ratio of the automatic transmission is denoted with i_a, the gear ratios of the front and rear differential gears i_f and i_r, respectively. Furthermore, $i_G = i_a i_r$ and $i_E = i_a i_f$ are used for the total gear ratio from the main engine to the rear axle or rather the front axle. The equations for the front axle angular velocity ω_f can be described similarly to the rear axle (3.5)-(3.7), with

$$J_f \dot{\omega}_f = T_e i_f - r_f F_{xf} \tag{3.25}$$

$$F_{xf} = \mu F_{zf} \sin\big(C_f \arctan(B_f \lambda_{xf})\big) \tag{3.26}$$

$$F_{zf} = m\, g\, l_r/(l_f + l_r) \,. \tag{3.27}$$

Here, J_f is the moment of inertia of the front axle, r_f the wheel radius of the front wheels, F_{xf} the friction force generated by the front tires and F_{zf} the normal force, acting on the front axle. Moreover, C_f and B_f are Pacejka tire parameters, analogously to the rear axle, compare Section 3.2.1. The wheel slip on the front axle λ_{xf} and its normalization speed v_{nf} are

$$\lambda_{xf} = (r_f \omega_f - v_x)/v_{nf} \tag{3.28a}$$

$$v_{nf} = \max_\epsilon(|r_f \omega_f|_\epsilon, |v_x|_\epsilon) \,, \tag{3.28b}$$

like for the rear axle, cf. Section 3.2.2. Finally, the longitudinal acceleration of the vehicle (3.11) has to be adjusted in the 4WD case, to include the tire force on the front axle as well, by

$$\dot{v}_x = (F_{xr} + F_{xf} - F_w)/m \,. \tag{3.29}$$

Now, the 7-state 4WD synthesis model $\mathcal{M}_7$ from Figure 3.3b can be put in state space form by

$$\mathcal{M}_7 : \begin{cases} \dot{\boldsymbol{x}} = \boldsymbol{f}(\boldsymbol{x}) + \boldsymbol{G}\boldsymbol{u} & \text{(3.30a)} \\ \boldsymbol{y} = \boldsymbol{h}(\boldsymbol{x}) & \text{(3.30b)} \end{cases}$$

with the input $\boldsymbol{u}^T = \begin{bmatrix} u_1 & u_2 \end{bmatrix} = \begin{bmatrix} T_{m,d} & T_{e,d} \end{bmatrix}$, output $\boldsymbol{y}^T = \begin{bmatrix} y_1 & y_2 \end{bmatrix} = \begin{bmatrix} \omega_c/i_G & \omega_f \end{bmatrix}$ and state $\boldsymbol{x}^T = \begin{bmatrix} x_1 & x_2 & x_3 & x_4 & x_5 & x_6 & x_7 \end{bmatrix} = \begin{bmatrix} T_m & \Delta\phi_c & \omega_c & \omega_r & v_x & T_e & \omega_f \end{bmatrix}$, while

$$\boldsymbol{f}(\boldsymbol{x}) = \begin{bmatrix} -x_1/\tau_m \\ x_3/i_G - x_4 \\ (x_1 - x_6/i_a - 2\,T_r/i_G)/J_c \\ (2\,T_r - r_r F_{xr})/J_r \\ (F_{xr} + F_{xf} - F_w)/m \\ -x_6/\tau_e \\ (x_6 i_f - r_f F_{xf})/J_f \end{bmatrix}, \; \boldsymbol{G} = \begin{bmatrix} 1/\tau_m & 0 \\ 0 & 0 \\ 0 & 0 \\ 0 & 0 \\ 0 & 0 \\ 0 & 1/\tau_e \\ 0 & 0 \end{bmatrix}, \; \boldsymbol{h}(\boldsymbol{x}) = \begin{bmatrix} x_3/i_G \\ x_7 \end{bmatrix} . \tag{3.31}$$

Remark 12. *For a compact notation, symbols like $\boldsymbol{x}$, $\boldsymbol{u}$, $\boldsymbol{y}$, $\boldsymbol{f}$ and $\boldsymbol{h}$ are used for all three models. Since therefore their definition depends on the context, it is stated explicitly when required.*

As can be noted from Figure 3.3b, the $\mathcal{M}_7$ model assumes a stiff connection of the ETC to the front axle. A direct extension is therefore to include a substitute model of the drivetrain elasticity in form of a torsion spring for this axle as well, similar to the rear axle, cf. Section 3.2.1. This extended 4WD model is described next.

The ETC output speed ω_e and the twist angle between ETC and front axle $\Delta\phi_e$ satisfy

$$\Delta\dot{\phi}_e = \omega_e/i_f - \omega_f \tag{3.32}$$
$$J_e\dot{\omega}_e = T_e - 2\,T_f/i_f \tag{3.33}$$
$$T_f = k_e\Delta\phi_e + d_e(\omega_e/i_f - \omega_f)\,, \tag{3.34}$$

where J_e is the substitute moment of inertia for the ETC, $2\,T_f$ is the torque applied to the front axle and k_e, d_e are stiffness and damping factor of the torsion spring. Then, only the equation for the front axle speed has to be adjusted (the remaining equations stay the same), by

$$J_f\dot{\omega}_f = 2\,T_f - r_f F_{xf}\,. \tag{3.35}$$

Following, the $\mathcal{M}_9$ model can be put in state space form by

$$\mathcal{M}_9 : \begin{cases} \dot{\boldsymbol{x}} = \boldsymbol{f}(\boldsymbol{x}) + \boldsymbol{G}\boldsymbol{u} & \text{(3.36a)} \\ \boldsymbol{y} = \boldsymbol{h}(\boldsymbol{x}) & \text{(3.36b)} \end{cases}$$

with input $\boldsymbol{u}^T = \begin{bmatrix} u_1 & u_2 \end{bmatrix} = \begin{bmatrix} T_{m,d} & T_{e,d} \end{bmatrix}$, output $\boldsymbol{y}^T = \begin{bmatrix} y_1 & y_2 \end{bmatrix} = \begin{bmatrix} \omega_c/i_G & \omega_e/i_f \end{bmatrix}$, state $\boldsymbol{x}^T = \begin{bmatrix} x_1 & x_2 & x_3 & x_4 & x_5 & x_6 & x_7 & x_8 & x_9 \end{bmatrix} = \begin{bmatrix} T_m & \Delta\phi_c & \omega_c & \omega_r & v_x & T_e & \omega_f & \Delta\phi_e & \omega_e \end{bmatrix}$ and

$$\boldsymbol{f}(\boldsymbol{x}) = \begin{bmatrix} -x_1/\tau_m \\ x_3/i_G - x_4 \\ (x_1 - x_6/i_a - 2\,T_r/i_G)/J_c \\ (2\,T_r - r_r F_{xr})/J_r \\ (F_{xr} + F_{xf} - F_w)/m \\ -x_6/\tau_e \\ (2\,T_f - r_f F_{xf})/J_f \\ x_9/i_f - x_7 \\ (x_6 - 2\,T_f/i_f)/J_e \end{bmatrix}, \boldsymbol{G} = \begin{bmatrix} 1/\tau_m & 0 \\ 0 & 0 \\ 0 & 0 \\ 0 & 0 \\ 0 & 0 \\ 0 & 1/\tau_e \\ 0 & 0 \\ 0 & 0 \\ 0 & 0 \end{bmatrix}, \boldsymbol{h}(\boldsymbol{x}) = \begin{bmatrix} x_3/i_G \\ x_9/i_f \end{bmatrix}. \tag{3.37}$$

Table 3.1 lists the states, inputs and outputs and the models for which they are relevant. In the next section, the models are used for a control design based on IOL for TCSs. Also, the output definitions are discussed, for example why y_2 is different for the $\mathcal{M}_7$ model and the $\mathcal{M}_9$ model.

Table 3.1: Variable definitions of the three different synthesis models.

Variable	Symbol	Model	Description	Unit
u_1	$T_{m,d}$	$\mathcal{M}_5, \mathcal{M}_7, \mathcal{M}_9$	Desired motor torque	Nm
u_2	$T_{e,d}$	$\mathcal{M}_7, \mathcal{M}_9$	Desired ETC torque	Nm
y_1	ω_c/i_G	$\mathcal{M}_5, \mathcal{M}_7, \mathcal{M}_9$	Crankshaft angular velocity (wheel level)	rad/s
y_2	ω_f	$\mathcal{M}_7$	Front axle angular velocity	rad/s
y_2	ω_e/i_f	$\mathcal{M}_9$	ETC output angular velocity (wheel level)	rad/s
x_1	T_m	$\mathcal{M}_5, \mathcal{M}_7, \mathcal{M}_9$	Motor torque	Nm
x_2	$\Delta\phi_c$	$\mathcal{M}_5, \mathcal{M}_7, \mathcal{M}_9$	Twist angle of rear torsion spring	rad
x_3	ω_c	$\mathcal{M}_5, \mathcal{M}_7, \mathcal{M}_9$	Crankshaft angular velocity	rad/s
x_4	ω_r	$\mathcal{M}_5, \mathcal{M}_7, \mathcal{M}_9$	Rear axle angular velocity	rad/s
x_5	v_x	$\mathcal{M}_5, \mathcal{M}_7, \mathcal{M}_9$	Longitudinal vehicle velocity	m/s
x_6	T_e	$\mathcal{M}_7, \mathcal{M}_9$	ETC torque	Nm
x_7	ω_f	$\mathcal{M}_7, \mathcal{M}_9$	Front axle angular velocity	rad/s
x_8	$\Delta\phi_e$	$\mathcal{M}_9$	Twist angle of front torsion spring	rad
x_9	ω_e	$\mathcal{M}_9$	ETC output angular velocity	rad/s

3.3 Nonlinear Control Design

3.3.1 Derivation of the Control Laws and Zero Dynamics

Consider the three different cases for the control design based on the three longitudinal models from Section 3.2.3. The linearizing control laws, including the resulting zero dynamics in each case, are derived based on our previous work [300, 305]. Stability is then investigated in the subsequent sections.

3.3.1.1 The 5-State 2WD Case

The system output is given by the angular velocity of the crankshaft, scaled to wheel level by the total gear ratio from the engine to the rear axle,

$$y_1 = x_3/i_G\,. \tag{3.38}$$

The first derivative with respect to time of the output is given by

$$\dot{y}_1 = \dot{x}_3/i_G = (x_1 - 2\,T_r/i_G)/(i_G J_c) \tag{3.39}$$

where $T_r = k_c x_2 + d_c(x_3/i_G - x_4)$, compare (3.4). The second derivative with respect to time is given by

$$\ddot{y}_1 = \frac{1}{i_G J_c}\Big[\frac{1}{\tau_m}(u_1 - x_1) - \frac{2}{i_G}\Big(k_c\Big(x_3/i_G - x_4\Big) - d_c\Big(\dot{x}_3/i_G - \dot{x}_4\Big)\Big)\Big]\,. \tag{3.40}$$

Solving for the system input and defining $v_1 \overset{\text{def}}{=} \ddot{y}_1$ as the new input gives the linearizing control law in the 2WD case as

$$u_1 = x_1 + \tau_m\Big[v_1 J_c i_G + \frac{2}{i_G}\Big(k_c\Big(\frac{x_3}{i_G} - x_4\Big) + d_c\Big(\frac{\dot{x}_3}{i_G} - \dot{x}_4\Big)\Big)\Big]\,. \tag{3.41}$$

Remark 13. *The derivatives $\dot{x}_3$ and $\dot{x}_4$ are left in (3.41) for now and are not replaced by their differential equations. For the theoretical analysis, this keeps the notation compact, while practical advantages of this formulation are discussed in Section 3.4.*

To give a physical interpretation of (3.41), the control law can be separated into three basic terms, where each implicitly serves a different goal of the control objectives.

1. The x_1 term represents the resulting torque produced by the engine and accounts for the actuator dynamics of the engine. A useful side effect of this term is that it can be interpreted as a form of integral action as will be shown in Chapter 6. This term provides the first of two open loop integrators required for zero asymptotic tracking of a ramp-shaped reference trajectory during acceleration, see also Section 3.4.

2. The v_1 term, scaled with the gain $\tau_m i_G J_c$ for inertia compensation, represents the virtual control input to the linearized system and has the physical meaning of the rate of change of angular acceleration, or angular jerk.

3. The $x_3/i_G - x_4$ term denotes the speed difference between crankshaft angular velocity (scaled to wheel level) and rear axle angular velocity, which is passed to a PD controller with proportional gain $2\tau_m k_c/i_G$ and derivative gain $2\tau_m d_c/i_G$. Feedback of such a speed difference has been used for active damping as a separate part of the control design for TCSs before, see for example [17, 91, 291], as well as [90, pp. 85–99] and Section 2.1 for a literature overview. The proposed solution using input-output linearization provides a more uniform approach to traction control in combination with active vibration control for vehicles with 2WD, based on the nonlinear design model (3.22), as the damping terms naturally enter the control law (3.41).

Since the control law is obtained with the second derivative of the output, the relative degree of $\mathcal{M}_5$ is $\delta = 2$, resulting in an internal dynamic of order $n - \delta = 3$. In order to ensure stability of the overall control system using (3.41), it is necessary to show that the internal dynamics of the system are ISS. Using the following state transformation results in the Byrnes-Isidori normal form of the internal dynamics

$$\boldsymbol{\xi} = \begin{bmatrix} \xi_1 \\ \xi_2 \\ \xi_3 \\ \xi_4 \\ \xi_5 \end{bmatrix} = \boldsymbol{\phi}(\boldsymbol{x}) = \begin{bmatrix} \phi_1(\boldsymbol{x}) \\ \phi_2(\boldsymbol{x}) \\ \phi_3(\boldsymbol{x}) \\ \phi_4(\boldsymbol{x}) \\ \phi_5(\boldsymbol{x}) \end{bmatrix} = \begin{bmatrix} x_3/i_G \\ (i_G x_1 - 2\,T_r)/(J_c i_G^2) \\ x_2 \\ x_4 \\ x_5 \end{bmatrix}. \tag{3.42}$$

Note that T_r in $\boldsymbol{\xi}$-coordinates is $T_r = k_c\xi_3 + d_c(\xi_1 - \xi_4)$, so the inverse transformation from $\boldsymbol{\xi}$ to $\boldsymbol{x}$ is given by

$$\boldsymbol{x} = \begin{bmatrix} x_1 \\ x_2 \\ x_3 \\ x_4 \\ x_5 \end{bmatrix} = \boldsymbol{\phi}^{-1}(\boldsymbol{\xi}) = \begin{bmatrix} \phi_1^{-1}(\boldsymbol{\xi}) \\ \phi_2^{-1}(\boldsymbol{\xi}) \\ \phi_3^{-1}(\boldsymbol{\xi}) \\ \phi_4^{-1}(\boldsymbol{\xi}) \\ \phi_5^{-1}(\boldsymbol{\xi}) \end{bmatrix} = \begin{bmatrix} i_G J_c \xi_2 + 2\,T_r/i_G \\ \xi_3 \\ i_G\xi_1 \\ \xi_4 \\ \xi_5 \end{bmatrix}. \tag{3.43}$$

Lemma 6. *The state transformation $\boldsymbol{\phi} : \mathbb{R}^5 \to \mathbb{R}^5$ is a global diffeomorphism and decouples the internal dynamics from u_1.*

Proof. The Jacobian of $\boldsymbol{\phi}$ with respect to the state vector $\boldsymbol{x}$ is given by

$$\boldsymbol{J}_{\boldsymbol{\phi},\boldsymbol{x}}(\boldsymbol{x}) = \frac{\partial \boldsymbol{\phi}(\boldsymbol{x})}{\partial \boldsymbol{x}} = \begin{bmatrix} 0 & 0 & 1/i_G & 0 & 0 \\ 1/(i_G J_c) & -2k_c/(i_G^2 J_c) & -2d_c/(i_G^3 J_c) & 2d_c/(i_G^2 J_c) & 0 \\ 0 & 1 & 0 & 0 & 0 \\ 0 & 0 & 0 & 1 & 0 \\ 0 & 0 & 0 & 0 & 1 \end{bmatrix}. \tag{3.44}$$

The determinant of (3.44) is $\det\big(\boldsymbol{J}_{\boldsymbol{\phi},\boldsymbol{x}}(\boldsymbol{x})\big) = 1/(i_G^2 J_c) \neq 0\,, \forall \boldsymbol{x} \in \mathbb{R}^5$. Since $\boldsymbol{\phi}$ is also linear, it is a bijection and thus a global diffeomorphism. As the last $n-\delta = 3$ rows of $\boldsymbol{J}_{\boldsymbol{\phi},\boldsymbol{x}}(\boldsymbol{x})\boldsymbol{g}$ are zero, the state transformation $\boldsymbol{\phi}$ decouples the internal dynamics from the control input u_1, cf. [305]. □

Then, the system in Byrnes-Isidori normal form is given in $\boldsymbol{\xi}$-coordinates by

$$\dot{\boldsymbol{\xi}} = \begin{bmatrix} \dot{\xi}_1 \\ \dot{\xi}_2 \\ \dot{\xi}_3 \\ \dot{\xi}_4 \\ \dot{\xi}_5 \end{bmatrix} = \begin{bmatrix} \xi_2 \\ L_{\boldsymbol{f}}^2 h\big(\boldsymbol{\phi}^{-1}(\boldsymbol{\xi})\big) + L_{\boldsymbol{g}} L_{\boldsymbol{f}} h\big(\boldsymbol{\phi}^{-1}(\boldsymbol{\xi})\big) u_1 \\ \xi_1 - \xi_4 \\ \big(2d_c(\xi_1 - \xi_4) + 2k_c\xi_3 - r_r F_{xr}\big)/J_r \\ (F_{xr} - F_w)/m \end{bmatrix} \tag{3.45}$$

with the Lie-derivatives

$$L_{\boldsymbol{g}} L_{\boldsymbol{f}} h\big(\boldsymbol{\phi}^{-1}(\boldsymbol{\xi})\big) = 1/(i_G \tau_m J_c) \tag{3.46}$$

$$L_{\boldsymbol{f}}^2 h\big(\boldsymbol{\phi}^{-1}(\boldsymbol{\xi})\big) = \frac{q_1\xi_1 + q_2\xi_2 + q_3\xi_3 + q_4\xi_4 - 2\,\tau_m d_c r_r F_{xr}}{i_G^2 J_c \tau_m J_r}\,. \tag{3.47}$$

The parameters q_1, q_2, q_3 and q_4 in (3.47) are given by

$$q_1 = (4d_c^2 - 2J_r k_c)\tau_m - 2J_r d_c \tag{3.48a}$$

$$q_2 = -2J_r \tau_m d_c - i_G^2 J_c J_r \tag{3.48b}$$

$$q_3 = 4\tau_m d_c k_c - 2J_r k_c \tag{3.48c}$$

$$q_4 = (2J_r k_c - 4d_c^2)\tau_m + 2J_r d_c\,. \tag{3.48d}$$

A necessary condition for stability of the internal dynamics is that its zero dynamics are asymptotically stable. The zero dynamics describe the internal dynamics with linearizing control law applied such that the output of the system is identically zero. From (3.45), the zero dynamics can be derived by inserting the control law (3.41) for u_1 and setting $\xi_1 = \xi_2 = v_1 = 0$ as

$$\begin{bmatrix} \dot{\xi}_1 \\ \dot{\xi}_2 \\ \dot{\xi}_3 \\ \dot{\xi}_4 \\ \dot{\xi}_5 \end{bmatrix} = \begin{bmatrix} 0 \\ 0 \\ -\xi_4 \\ \big(2(k_c\xi_3 - d_c\xi_4) - r_r F_{xr}\big)/J_r \\ (F_{xr} - F_w)/m \end{bmatrix} . \tag{3.49}$$

Now, we can define $\boldsymbol{z}^T = \begin{bmatrix} z_1 & z_2 & z_3 \end{bmatrix} = \begin{bmatrix} \xi_3 & \xi_4 & \xi_5 \end{bmatrix}$ and write the zero dynamics of the $\mathcal{M}_5$ synthesis model for vehicles with 2WD as

$$\dot{\boldsymbol{z}} = \begin{bmatrix} \dot{z}_1 \\ \dot{z}_2 \\ \dot{z}_3 \end{bmatrix} = \begin{bmatrix} -z_2 \\ \big(2(k_c z_1 - d_c z_2) - r_r F_{xr}\big)/J_r \\ (F_{xr} - F_w)/m \end{bmatrix} . \tag{3.50}$$

For the linearizing control law (3.41) to be applicable in practice, it is necessary that the zero dynamics (3.50) are asymptotically stable. For now, the equilibria of (3.50) are determined, while stability is analyzed in detail in Section 3.3.2.

Lemma 7. *The zero dynamics (3.50) have a unique equilibrium* $\boldsymbol{z}_{eq}^T = \begin{bmatrix} 0 & 0 & 0 \end{bmatrix}$.

Proof. At equilibrium it is clear from (3.50) that $z_2 = 0$ holds. In this case, F_{xr} is a function of z_3 only, so the signs of F_{xr} and F_w can be readily inspected. Since $z_2 = 0$, if $z_3 > 0 \Rightarrow \lambda_x < 0 \Rightarrow F_{xr} < 0$. However, at the same time if $z_3 > 0 \Rightarrow F_w > 0$ so $\dot{z}_3 = (F_{xr} - F_w)/m < 0$. The case $z_3 < 0$ follows analogously and results in $\dot{z}_3 = (F_{xr} - F_w)/m > 0$. Therefore, $\dot{z}_3 = 0 \iff z_3 = 0$, so at equilibrium $F_{xr} = F_w = 0$. From this conclusion and the equation for $\dot{z}_2$ it follows that also $z_1 = 0$ must hold, so the origin is the only equilibrium of (3.50), cf. [305]. □

This equilibrium corresponds to the standstill with $v_x = z_3 = 0$, $\omega_r = z_2 = 0$ and the twist angle of the torsion spring that models the drivetrain torsional dynamics returned to zero twist with $\Delta\phi_c = z_1 = 0$ such that also the rear axle torque is zero.

Remark 14. *While the derivation of the control law and the zero dynamics was done assuming a vehicle with rear wheel drive, the derived equations can readily be used for vehicles with front wheel drive as well. This only requires to replace the corresponding drivetrain parameters of the rear wheel drive by parameters for front wheel drive. Also, the lever arm term in (3.7) has to be adjusted by exchanging l_f and l_r in the F_{zr} term. Therefore, both front wheel drive and rear wheel drive vehicles can be treated equally with the proposed approach.*

This concludes the first step of the control law derivation for the 2WD case. Further implementation details and how the control law is extended for tracking control in a TCS will be discussed in Section 3.4 and also later in Chapter 6. Before that, the control laws for the $\mathcal{M}_7$ and the $\mathcal{M}_9$ model are derived as well and stability is investigated.

In the following, the control law is extended to the MIMO system (3.30a) with 7 states, representing a vehicle with 4WD torque bias system and a stiff shaft connecting the ETC and the front axle. The internal dynamics and the zero dynamics of the 4WD control design are derived as well, analogously to the 2WD case. Also, the differences between the derivations of the 2WD case based on the $\mathcal{M}_5$ model and the 4WD case based on the $\mathcal{M}_7$ model are discussed. It is shown that the main difference, apart from the MIMO setting, results from the stiff connection of the ETC with the front axle in the $\mathcal{M}_7$ model. This leads to a nonlinear state transformation for the $\mathcal{M}_7$ model, in contrast to the linear transformation (3.42) for the $\mathcal{M}_5$ model.

3.3.1.2 The 7-State 4WD Case

Next, the linearizing control law is derived for the previously described 4WD model with 7 states. In this case, the first output of the system is again given by the angular velocity of the crankshaft scaled to the wheel by the total gear ratio, $y_1 = \omega_r / i_G = x_3 / i_G$. The second output is the angular velocity of the front axle, given by $y_2 = \omega_f = x_7$. The first and the second derivative with respect to time of y_2 is

$$\dot{y}_2 = (i_f x_6 - r_f F_{xf})/J_f \tag{3.51}$$

$$\ddot{y}_2 = \big(i_f(u_2 - x_6)/\tau_e - r_f \dot{F}_{xf}\big)/J_f \,. \tag{3.52}$$

Solving (3.52) for the second input u_2 and setting $v_2 \overset{\text{def}}{=} \ddot{y}_2$ gives

$$u_2 = x_6 + \tau_e(J_f v_2 + r_f \dot{F}_{xf})/i_f \,. \tag{3.53}$$

For y_1, the first and second derivative with respect to time is given by

$$\dot{y}_1 = \dot{x}_3/i_G = \big((x_1 - x_6/i_a) - 2\,T_r/i_G\big)/(i_G J_c) \tag{3.54}$$

$$\ddot{y}_1 = \frac{1}{i_G J_c}\Big(\frac{1}{\tau_m}(u_1 - x_1) - \frac{1}{\tau_e i_a}(u_2 - x_6) - \frac{2}{i_G}\dot{T}_r\Big) \,. \tag{3.55}$$

Next, solve (3.55) for the first input u_1, set $v_1 \overset{\text{def}}{=} \ddot{y}_1$ and insert (3.53) for u_2 to get

$$u_1 = x_1 + \tau_m\Big[v_1 J_c i_G + \frac{J_f v_2 + r_f \dot{F}_{xf}}{i_f i_a} + \frac{2}{i_G}\Big(k_c\Big(\frac{x_3}{i_G} - x_4\Big) + d_c\Big(\frac{\dot{x}_3}{i_G} - \dot{x}_4\Big)\Big)\Big] \,. \tag{3.56}$$

This control law for the rear axle is the same as in the 2WD case (3.41) with an additional $\tau_m(J_f v_2 + r_f \dot{F}_{xf})/(i_f i_a)$ term. This term is induced by the coupling between the rear axle and the front axle by the torque bias system, which shifts the portion generated by u_2 from the rear to the front axle. Therefore, the control laws u_1 and u_2 decouple the outputs y_1 and y_2 from each other by explicitly taking into account this effect.

Remark 15. *A potential difficulty for a real-world implementation of the control laws (3.53) and (3.56) is the $\dot{F}_{xf}$ term, since its computation would require tire parameters and the friction coefficient of the road. Online estimates of these quantities might not be available at the bandwidth of the controller on the ECU or on the ETC control unit. This issue will be further discussed later.*

Remark 16. *In contrast to the 2WD case, where no tire force term enters into the control law, the $\dot{F}_{xf}$ term appears here because the connection from the ETC to the front axle is modeled as stiff in the 7-state 4WD model (3.30). By modeling this connection as a torsion spring as well, the $\dot{F}_{xf}$ term can be avoided, as will be shown with the 9-state 4WD model later. The 7-state 4WD model can be useful in practice nevertheless and even preferable compared to the 9-state 4WD model, depending on the underlying conditions for the control design. Particularly, the above control law does not require a measurement of the ETC output speed, which might not be available. Following, the control laws and stability properties of both the 7-state and the 9-state 4WD model are derived.*

Here, the control law is obtained after differentiating both outputs y_1, y_2 twice. This results for the $\mathcal{M}_7$ model in a vector relative degree of $\begin{bmatrix}\delta_1 & \delta_2\end{bmatrix} = \begin{bmatrix}2 & 2\end{bmatrix}$, hence a total relative degree of $\delta = \delta_1 + \delta_2 = 4$ and an internal dynamic of order $n - \delta = 3$. Therefore, although the considered 7-state 4WD model has 2 more states than the 2WD model, the input-output linearization results in both cases in third order internal dynamics.

In order to analyze stability of the internal dynamics, we propose the following state transformation to Byrnes-Isidori normal form

$$\boldsymbol{\xi} = \begin{bmatrix}\xi_1\\ \xi_2\\ \xi_3\\ \xi_4\\ \xi_5\\ \xi_6\\ \xi_7\end{bmatrix} = \boldsymbol{\phi}(\boldsymbol{x}) = \begin{bmatrix}\phi_1(\boldsymbol{x})\\ \phi_2(\boldsymbol{x})\\ \phi_3(\boldsymbol{x})\\ \phi_4(\boldsymbol{x})\\ \phi_5(\boldsymbol{x})\\ \phi_6(\boldsymbol{x})\\ \phi_7(\boldsymbol{x})\end{bmatrix} = \begin{bmatrix} x_3/i_G \\ \big((i_G x_1 - 2\,T_r)i_a - i_G x_6\big)/(J_c i_a i_G^2) \\ x_2 \\ x_4 \\ x_5 \\ (i_f x_6 - r_f F_{xf})/J_f \\ x_7 \end{bmatrix}. \tag{3.57}$$

The inverse transformation, from $\boldsymbol{\xi}$ to $\boldsymbol{x}$, can then be defined, with $\phi_1^{-1}(\boldsymbol{\xi}) = i_G J_c \xi_2 + 2T_r/i_G + (J_f\xi_6 + r_f F_{xf})/(i_a i_f)$, as

$$\boldsymbol{x} = \begin{bmatrix}x_1\\ x_2\\ x_3\\ x_4\\ x_5\\ x_6\\ x_7\end{bmatrix} = \boldsymbol{\phi}^{-1}(\boldsymbol{\xi}) = \begin{bmatrix}\phi_1^{-1}(\boldsymbol{\xi})\\ \phi_2^{-1}(\boldsymbol{\xi})\\ \phi_3^{-1}(\boldsymbol{\xi})\\ \phi_4^{-1}(\boldsymbol{\xi})\\ \phi_5^{-1}(\boldsymbol{\xi})\\ \phi_6^{-1}(\boldsymbol{\xi})\\ \phi_7^{-1}(\boldsymbol{\xi})\end{bmatrix} = \begin{bmatrix} \phi_1^{-1}(\boldsymbol{\xi}) \\ \xi_3 \\ i_G\xi_1 \\ \xi_4 \\ \xi_5 \\ (J_f\xi_6 + r_f F_{xf})/i_f \\ \xi_7 \end{bmatrix}. \tag{3.58}$$

Lemma 8. *The state transformation $\boldsymbol{\phi}: \mathbb{R}^7 \to \mathbb{R}^7$ is a global diffeomorphism for constant μ and decouples the internal dynamics from $\boldsymbol{u}^T = \begin{bmatrix}u_1 & u_2\end{bmatrix}$.*

Proof. The Jacobian of (3.57), with respect to the system states $\boldsymbol{x}$ is $\boldsymbol{J}_{\boldsymbol{\phi},\boldsymbol{x}}(\boldsymbol{x}) = \partial\boldsymbol{\phi}(\boldsymbol{x})/(\partial\boldsymbol{x})$, with $J_{65}(\boldsymbol{x}) = -\partial(r_f F_{xf}/J_f)/(\partial x_5)$, $J_{67}(\boldsymbol{x}) = -\partial(r_f F_{xf}/J_f)/(\partial x_7)$ and

$$\boldsymbol{J}_{\boldsymbol{\phi},\boldsymbol{x}}(\boldsymbol{x}) = \begin{bmatrix} 0 & 0 & 1/i_G & 0 & 0 & 0 & 0 \\ 1/(J_c i_G) & -2k_c/(J_c i_G^2) & -2d_c/(J_c i_G^3) & 2d_c/(J_c i_G^2) & 0 & -1/(J_c i_G i_a) & 0 \\ 0 & 1 & 0 & 0 & 0 & 0 & 0 \\ 0 & 0 & 0 & 1 & 0 & 0 & 0 \\ 0 & 0 & 0 & 0 & 1 & 0 & 0 \\ 0 & 0 & 0 & 0 & J_{65}(\boldsymbol{x}) & i_f/J_f & J_{67}(\boldsymbol{x}) \\ 0 & 0 & 0 & 0 & 0 & 0 & 1 \end{bmatrix}. \tag{3.59}$$

The determinant of (3.59) is $\det\big(\boldsymbol{J}_{\boldsymbol{\phi},\boldsymbol{x}}(\boldsymbol{x})\big) = i_f/(i_G^2 J_c J_f) \neq 0\,, \forall \boldsymbol{x} \in \mathbb{R}^7$. Moreover, $\boldsymbol{\phi}$ is proper since $\lim_{\|\boldsymbol{x}\|\to\infty} \|\boldsymbol{\phi}(\boldsymbol{x})\| = \infty$. This can be seen as the nonlinearity F_{xf} is bounded and we can write $\boldsymbol{\phi}(\boldsymbol{x}) = \boldsymbol{\phi}_{\text{lin}}(\boldsymbol{x}) + \boldsymbol{\phi}_{\text{nlin}}(\boldsymbol{x})$ with $\boldsymbol{\phi}_{\text{nlin}}(\boldsymbol{x})^T = \begin{bmatrix}0 & 0 & 0 & 0 & 0 & -(r_f/i_f)F_{xf} & 0\end{bmatrix}$ and $\boldsymbol{\phi}_{\text{lin}}(\boldsymbol{x})$ given by (3.57) with F_{xf} set to zero. Since the determinant of the Jacobian of $\boldsymbol{\phi}_{\text{lin}}(\boldsymbol{x})$ is the same as the determinant of the Jacobian of $\boldsymbol{\phi}(\boldsymbol{x})$, by linearity of $\boldsymbol{\phi}_{\text{lin}}$ and boundedness of $\boldsymbol{\phi}_{\text{nlin}}$ it follows that $\boldsymbol{\phi}$ is proper. Since $\boldsymbol{\phi}$ is also C^2, it follows by Hadamard's global inverse function theorem, see [161, pp. 121–125] and [88], that $\boldsymbol{\phi}$ is a global bijection. Finally, the rows $\delta_1 + 1, \ldots, n - \delta_2$ (rows 3, 4 and 5) of $\boldsymbol{J}_{\boldsymbol{\phi},\boldsymbol{x}}(\boldsymbol{x})\boldsymbol{G}$ are zero, so the state transformation $\boldsymbol{\phi}$ also decouples the internal dynamics from the control input $\boldsymbol{u}$. □

Remark 17. *The state transformation (3.59) is non-standard, as y_2 and $\dot{y}_2$ are inserted in the last two rows instead directly after y_1 and $\dot{y}_1$ which are inserted in first two rows. The advantage of this formulation is that the first five state variables in (3.59), which also appear in the 2WD case, represent the same physical quantities in both cases.*

Showing that the state transformation (3.57) is a global diffeomorphism requires more steps compared to the 2WD case because (3.57) is nonlinear due to the F_{xf} term. Also, as stated in Lemma 8, for the derivation here we assume that μ is constant. Nevertheless, the 4WD TCS works for time-varying μ as well, compare for example the simulation study in [297].

The next steps follow analogously to the 2WD case. First, apply the state transformation (3.59) to derive the system in Byrnes-Isidori normal form,

$$\dot{\boldsymbol{\xi}} = \begin{bmatrix} \dot{\xi}_1 \\ \dot{\xi}_2 \\ \dot{\xi}_3 \\ \dot{\xi}_4 \\ \dot{\xi}_5 \\ \dot{\xi}_6 \\ \dot{\xi}_7 \end{bmatrix} = \begin{bmatrix} \xi_2 \\ L_{\boldsymbol{f}}^2 h_1\big(\boldsymbol{\phi}^{-1}(\boldsymbol{\xi})\big) + L_{\boldsymbol{g}_1} L_{\boldsymbol{f}} h_1\big(\boldsymbol{\phi}^{-1}(\boldsymbol{\xi})\big) u_1 + L_{\boldsymbol{g}_2} L_{\boldsymbol{f}} h_1\big(\boldsymbol{\phi}^{-1}(\boldsymbol{\xi})\big) u_2 \\ \xi_1 - \xi_4 \\ \big(2d_c(\xi_1 - \xi_4) + 2k_c\xi_3 - r_r F_{xr}\big)/J_r \\ (F_{xr} + F_{xf,0} - F_w)/m \\ (i_f u_2 - J_f \xi_6 - r_f F_{xf} - \tau_e r_f \dot{F}_{xf})/(\tau_e J_f) \\ \xi_6 \end{bmatrix} . \tag{3.60}$$

with $\boldsymbol{G}$ in the 7-state 4WD model equations (3.30a) partitioned as $\boldsymbol{G} = \begin{bmatrix} \boldsymbol{g}_1 & \boldsymbol{g}_2 \end{bmatrix}$, Lie-derivatives $L_{\boldsymbol{g}_1} L_{\boldsymbol{f}} h_1\big(\boldsymbol{\phi}^{-1}(\boldsymbol{\xi})\big) = 1/(\tau_m i_G J_c)$, $L_{\boldsymbol{g}_2} L_{\boldsymbol{f}} h_1\big(\boldsymbol{\phi}^{-1}(\boldsymbol{\xi})\big) = -1/(\tau_e i_a i_G J_c)$ and

$$L_{\boldsymbol{f}}^2 h_1\big(\boldsymbol{\phi}^{-1}(\boldsymbol{\xi})\big) = \frac{q_1\xi_1 + q_2\xi_2 + q_3\xi_3 + q_4\xi_4 + q_6\xi_6 + q_f F_{xf} + q_r F_{xr}}{\tau_m \tau_e i_G^2 i_E J_c J_r} . \tag{3.61}$$

The coefficients q_1, q_2, q_3, q_4, q_6, q_f and q_r in (3.61) are given by

$$q_1 = 4\tau_e\tau_m d_c^2 i_f i_a - 2J_r\tau_e\tau_m i_f i_a k_c - 2J_r\tau_e d_c i_E \tag{3.62a}$$
$$q_2 = -J_r J_c \tau_e i_E i_G^2 - 2\tau_e\tau_m J_r d_c i_E \tag{3.62b}$$
$$q_3 = 4\tau_e\tau_m d_c i_E k_c - 2\tau_e i_E k_c J_r \tag{3.62c}$$
$$q_4 = 2\tau_e\tau_m J_r i_E k_c - 4\tau_e\tau_m d_c^2 i_E + 2\tau_e J_r d_c i_E \tag{3.62d}$$
$$q_6 = \tau_m J_f J_r i_G - \tau_e J_f J_r i_G \tag{3.62e}$$
$$q_f = \tau_m J_r i_G r_f - \tau_e J_r i_G r_f \tag{3.62f}$$
$$q_r = -2\tau_e\tau_m d_c i_E r_r . \tag{3.62g}$$

Next, insert the control laws (3.56) and (3.53) for u_1 and u_2, set $\xi_1 = \xi_2 = \xi_6 = \xi_7 = v_1 = v_2 = 0$ and $\boldsymbol{z}^T = \begin{bmatrix} z_1 & z_2 & z_3 \end{bmatrix} = \begin{bmatrix} \xi_3 & \xi_4 & \xi_5 \end{bmatrix}$ to derive the zero dynamics as

$$\dot{\boldsymbol{z}} = \begin{bmatrix} \dot{z}_1 \\ \dot{z}_2 \\ \dot{z}_3 \end{bmatrix} = \begin{bmatrix} -z_2 \\ \big(2(k_c z_1 - d_c z_2) - r_r F_{xr}\big)/J_r \\ (F_{xr} + F_{xf,0} - F_w)/m \end{bmatrix} . \tag{3.63}$$

It can be noted that the 4WD zero dynamics (3.63) are the same as in the 2WD case (3.50) with an additional $F_{xf,0}$ term in the equation for $\dot{z}_3$. This term denotes the tire force generated at the front axle with $\omega_f = x_7 = \xi_7 = 0$ due to output zeroing:

$$F_{xf,0} = F_{xf}|_{x_7=0} \tag{3.64}$$

For $F_{xf,0} = 0$, the zero dynamics reduce to the 2WD case. However, since in the 4WD case $F_{xf,0} \neq 0$ in general, it is necessary to investigate stability for this case separately. Here, the equilibria of (3.63) are determined and stability is analyzed in detail in the next section.

Lemma 9. *The zero dynamics (3.63) have a unique equilibrium* $\boldsymbol{z}_{eq}^T = \begin{bmatrix} 0 & 0 & 0 \end{bmatrix}$.

Proof. At equilibrium $z_2 = 0$, so F_{xr}, the tire force generated at the rear axle, then depends like $F_{xf,0}$ only on z_3. For $z_3 > 0 \Rightarrow F_{xr} < 0$, $F_{xf,0} < 0$ and $F_w > 0$, so $\dot{z}_3 < 0$. Similarly, $z_3 < 0 \Rightarrow \dot{z}_3 > 0$, so $\dot{z}_3 = 0 \iff z_3 = 0$. Inserting $z_2 = z_3 = 0$ into (3.63) shows that $z_1 = 0$ must hold, so the origin is a unique equilibrium, cf. [300]. □

This concludes the derivation of the internal dynamics and the zero dynamics of the $\mathcal{M}_7$ model. While the derivation is similar to the 2WD case, some differences occurred as well. In particular, a nonlinear state transformation (3.57) is required for the 7-state 4WD model. This originates from the stiff connection between ETC and front axle of the $\mathcal{M}_7$ synthesis model. Following, it is shown that the $\mathcal{M}_9$ model avoids this by the inclusion of an additional torsion spring.

3.3.1.3 The 9-State 4WD Case

To complete the control design by input-output linearization for the three synthesis models, the 9-state 4WD case is considered. The first system output in this case is again $y_1 = \omega_r/i_G = x_3/i_G$. The second output is now defined as angular velocity of the shaft connecting the ETC with the front axle, scaled to wheel level, so $y_2 = \omega_e/i_f = x_9/i_f$. As in the 7-state 4WD case, the second output y_2 is differentiated twice with respect to time as

$$\dot{y}_2 = (x_6 - 2\,T_f/i_f)/(i_f J_e) \tag{3.65}$$

$$\ddot{y}_2 = \big((u_2 - x_6)/\tau_e - 2\,\dot{T}_f/i_f\big)/(i_f J_e)\,, \tag{3.66}$$

with $\dot{T}_f = k_e(x_9/i_f - x_7) + d_e(\dot{x}_9/i_f - \dot{x}_7)$. Define $v_2 = \ddot{y}_2$ and solve for u_2 to obtain

$$u_2 = x_6 + \tau_e(i_f J_e v_2 + 2\,\dot{T}_f/i_f)\,. \tag{3.67}$$

The first input y_1 follows analogously and results in

$$\dot{y}_1 = \big((x_1 - x_6/i_a) - 2\,T_r/i_G\big)/(i_G J_c) \tag{3.68}$$

$$\ddot{y}_1 = \frac{1}{i_G J_c}\Big(\frac{1}{\tau_m}(u_1 - x_1) - \frac{1}{\tau_e i_a}(u_2 - x_6) - \frac{2}{i_G}\dot{T}_r\Big)\,, \tag{3.69}$$

with $\dot{T}_r = k_c(x_3/i_G - x_4) + d_c(\dot{x}_3/i_G - \dot{x}_4)$, which is identical to the 7-state 4WD case, cf. (3.54)-(3.55). However, since the equation for u_2 (3.67) changed in comparison to the 7-state 4WD case (3.53) and u_2 also enters the equation for $\ddot{y}_1$ here, the resulting control law u_1 will also be different. Define $v_1 = \ddot{y}_1$, solve for u_1 and insert (3.67) for u_2, to obtain the control law for the 9-state 4WD case,

$$u_1 = x_1 + \tau_m\Big(v_1 J_c i_G + \frac{i_f}{i_a} J_e v_2 + \frac{2}{i_G}\dot{T}_r + \frac{2}{i_E}\dot{T}_f\Big)\,. \tag{3.70}$$

In comparison to the 7-state 4WD case, no derivative of the tire force appears in this control law. Instead, like for the rear axle, an additional damping term $\dot{T}_f$ is derived which can be interpreted as another PD controller (in addition to the $\dot{T}_r$ term, as described in the 2WD case) with the differential speed $x_9/i_f - x_7$ as input.

Remark 18. *The main advantage of the 9-state 4WD control laws (3.67) and (3.70) over the 7-state 4WD control laws (3.53) and (3.56) is, that the derivative of the front axle tire force disappears in the 9-state case. While the forces still enter into the $\dot{T}_r$, $\dot{T}_f$ terms through $\dot{x}_4$ and $\dot{x}_7$, these terms can be approximated efficiently in a real-world implementation using a filter to numerically calculate the derivative of the measured quantities x_4 and x_7. This basically implements the derivative parts of the PD controllers induced by $\dot{T}_r$ and $\dot{T}_f$.*

Again, the linearizing control laws are derived by differentiating y_1 and y_2 two times, so the $\mathcal{M}_9$ model has a vector relative degree of $\begin{bmatrix}\delta_1 & \delta_2\end{bmatrix} = \begin{bmatrix}2 & 2\end{bmatrix}$ and therefore, the total relative degree is $\delta = \delta_1 + \delta_2 = 4$ as in the 7-state 4WD case. However, the internal dynamics are now of order $n - \delta = 5$. Similarly to the 2WD and the 7-state 4WD case, the system is first transformed to Byrnes-Isidori normal form. We propose the following state transformation

$$\boldsymbol{\xi} = \begin{bmatrix}\xi_1\\ \xi_2\\ \xi_3\\ \xi_4\\ \xi_5\\ \xi_6\\ \xi_7\\ \xi_8\\ \xi_9\end{bmatrix} = \boldsymbol{\phi}(\boldsymbol{x}) = \begin{bmatrix}\phi_1(\boldsymbol{x})\\ \phi_2(\boldsymbol{x})\\ \phi_3(\boldsymbol{x})\\ \phi_4(\boldsymbol{x})\\ \phi_5(\boldsymbol{x})\\ \phi_6(\boldsymbol{x})\\ \phi_7(\boldsymbol{x})\\ \phi_8(\boldsymbol{x})\\ \phi_9(\boldsymbol{x})\end{bmatrix} = \begin{bmatrix} x_3/i_G \\ \big((i_G x_1 - 2\,T_r)i_a - i_G x_6\big)/(J_c i_a i_G^2) \\ x_2 \\ x_4 \\ x_5 \\ x_8 \\ x_7 \\ x_9/i_f \\ (i_f x_6 - 2\,T_f)/(i_f^2 J_e) \end{bmatrix}. \tag{3.71}$$

The inverse transformation, with T_r and T_f in $\boldsymbol{\xi}$-coordinates being defined as $T_r = k_c\xi_3 + d_c(\xi_1 - \xi_4)$ and $T_f = k_e\xi_6 + d_e(\xi_8 - \xi_7)$, is derived as

$$\boldsymbol{x} = \begin{bmatrix} x_1 \\ x_2 \\ x_3 \\ x_4 \\ x_5 \\ x_6 \\ x_7 \\ x_8 \\ x_9 \end{bmatrix} = \boldsymbol{\phi}^{-1}(\boldsymbol{\xi}) = \begin{bmatrix} \phi_1^{-1}(\boldsymbol{\xi}) \\ \phi_2^{-1}(\boldsymbol{\xi}) \\ \phi_3^{-1}(\boldsymbol{\xi}) \\ \phi_4^{-1}(\boldsymbol{\xi}) \\ \phi_5^{-1}(\boldsymbol{\xi}) \\ \phi_6^{-1}(\boldsymbol{\xi}) \\ \phi_7^{-1}(\boldsymbol{\xi}) \\ \phi_8^{-1}(\boldsymbol{\xi}) \\ \phi_9^{-1}(\boldsymbol{\xi}) \end{bmatrix} = \begin{bmatrix} \phi_1^{-1}(\boldsymbol{\xi}) \\ \xi_3 \\ i_G\xi_1 \\ \xi_4 \\ \xi_5 \\ (i_f^2 J_e\xi_9 + 2\,T_f)/i_f \\ \xi_7 \\ \xi_6 \\ i_f\xi_8 \end{bmatrix}, \tag{3.72}$$

with $\phi_1^{-1}(\boldsymbol{\xi}) = (i_a i_E i_G J_c\xi_2 + i_f i_E J_e\xi_9 + 2\,i_G T_f + 2\,i_G T_r)/(i_E i_G)$. First, it is ensured that (3.71) is globally invertible.

Lemma 10. *The state transformation $\boldsymbol{\phi} : \mathbb{R}^9 \to \mathbb{R}^9$ is a global diffeomorphism and decouples the internal dynamics from $\boldsymbol{u}^T = \begin{bmatrix} u_1 & u_2 \end{bmatrix}$.*

Proof. The Jacobian of (3.71), with $J_c' = 1/(J_c i_G)$ and $J_e' = 1/(J_e i_f)$, is derived as

$$\boldsymbol{J}_{\boldsymbol{\phi},\boldsymbol{x}}(\boldsymbol{x}) = \begin{bmatrix} 0 & 0 & 1/i_G & 0 & 0 & 0 & 0 & 0 & 0 \\ J_c' & -2k_cJ_c'/i_G & -2d_cJ_c'/i_G^2 & 2d_cJ_c'/i_G & 0 & -J_c'/i_a & 0 & 0 & 0 \\ 0 & 1 & 0 & 0 & 0 & 0 & 0 & 0 & 0 \\ 0 & 0 & 0 & 1 & 0 & 0 & 0 & 0 & 0 \\ 0 & 0 & 0 & 0 & 1 & 0 & 0 & 0 & 0 \\ 0 & 0 & 0 & 0 & 0 & 0 & 0 & 1 & 0 \\ 0 & 0 & 0 & 0 & 0 & 0 & 1 & 0 & 0 \\ 0 & 0 & 0 & 0 & 0 & 0 & 0 & 0 & 1/i_f \\ 0 & 0 & 0 & 0 & 0 & J_e' & 2d_eJ_e'/i_f & -2k_eJ_e'/i_f & -2d_eJ_e'/i_f^2 \end{bmatrix}. \tag{3.73}$$

The determinant of (3.73) is $\det\big(\boldsymbol{J}_{\boldsymbol{\phi},\boldsymbol{x}}(\boldsymbol{x})\big) = 1/(J_cJ_ei_f^2i_G^2) \neq 0\,, \forall \boldsymbol{x} \in \mathbb{R}^9$ and $\boldsymbol{\phi}$ is linear, thus a bijection and a global diffeomorphism. The rows $\delta_1 + 1, \ldots, n - \delta_2$ (rows 3 to 7) of $\boldsymbol{J}_{\boldsymbol{\phi},\boldsymbol{x}}(\boldsymbol{x})\boldsymbol{G}$ are zero, so the state transformation $\boldsymbol{\phi}$ decouples the internal dynamics from $\boldsymbol{u}$. □

Following, the full system equations in Byrnes-Isidori normal form are stated as well. It can be noted that here, like in the control law, the force derivative disappears, compared to the 7-state 4WD case, where the torsional dynamics of the connection between ETC and front axle are not modeled. The transformed system equations are

$$\dot{\boldsymbol{\xi}} = \begin{bmatrix} \dot{\xi}_1 \\ \dot{\xi}_2 \\ \dot{\xi}_3 \\ \dot{\xi}_4 \\ \dot{\xi}_5 \\ \dot{\xi}_6 \\ \dot{\xi}_7 \\ \dot{\xi}_8 \\ \dot{\xi}_9 \end{bmatrix} = \begin{bmatrix} \xi_2 \\ L_{\boldsymbol{f}}^2 h_1\big(\boldsymbol{\phi}^{-1}(\boldsymbol{\xi})\big) + L_{\boldsymbol{g}_1}L_{\boldsymbol{f}}h_1\big(\boldsymbol{\phi}^{-1}(\boldsymbol{\xi})\big)u_1 + L_{\boldsymbol{g}_2}L_{\boldsymbol{f}}h_1\big(\boldsymbol{\phi}^{-1}(\boldsymbol{\xi})\big)u_2 \\ \xi_1 - \xi_4 \\ \big(2d_c(\xi_1 - \xi_4) + 2k_c\xi_3 - r_rF_{xr}\big)/J_r \\ (F_{xr} + F_{xf} - F_w)/m \\ \xi_8 - \xi_7 \\ \big(2d_e(\xi_8 - \xi_7) + 2k_e\xi_6 - r_fF_{xf}\big)/J_f \\ \xi_9 \\ L_{\boldsymbol{f}}^2 h_2\big(\boldsymbol{\phi}^{-1}(\boldsymbol{\xi})\big) + L_{\boldsymbol{g}_2}L_{\boldsymbol{f}}h_2\big(\boldsymbol{\phi}^{-1}(\boldsymbol{\xi})\big)u_2 \end{bmatrix}, \tag{3.74}$$

with $\boldsymbol{G}$ from (3.36a) partitioned as $\boldsymbol{G} = \begin{bmatrix} \boldsymbol{g}_1 & \boldsymbol{g}_2 \end{bmatrix}$ like in the 7-state 4WD case and Lie-Derivatives $L_{\boldsymbol{g}_1}L_{\boldsymbol{f}}h_1\big(\boldsymbol{\phi}^{-1}(\boldsymbol{\xi})\big) = 1/(\tau_m i_G J_c)$, $L_{\boldsymbol{g}_2}L_{\boldsymbol{f}}h_1\big(\boldsymbol{\phi}^{-1}(\boldsymbol{\xi})\big) = -1/(\tau_e i_a i_G J_c)$ for the first output and $L_{\boldsymbol{g}_2}L_{\boldsymbol{f}}h_2\big(\boldsymbol{\phi}^{-1}(\boldsymbol{\xi})\big) = 1/(\tau_e i_f J_e)$ for the second output, with

$$L_{\boldsymbol{f}}^2 h_1\big(\boldsymbol{\phi}^{-1}(\boldsymbol{\xi})\big) = \frac{q_1\xi_1 + q_2\xi_2 + q_3\xi_3 + q_4\xi_4 + q_6\xi_6 + q_7\xi_7 + q_8\xi_8 + q_9\xi_9 + q_rF_{xr}}{\tau_e\tau_m i_a i_f i_G^2 J_c J_r} \tag{3.75}$$

$$L_{\boldsymbol{f}}^2 h_2\big(\boldsymbol{\phi}^{-1}(\boldsymbol{\xi})\big) = \frac{p_6\xi_6 + p_7\xi_7 + p_8\xi_8 + p_9\xi_9 + p_fF_{xf}}{\tau_e i_f^2 J_e J_f}\,. \tag{3.76}$$

The vehicle parameter dependent coefficients in (3.75) are given by

$$q_1 = -2i_E\tau_e((\tau_m k_c + d_c)J_r - 2d_c^2\tau_m) \tag{3.77a}$$
$$q_2 = -i_E J_r \tau_e(i_G^2 J_c + 2\tau_m d_c) \tag{3.77b}$$
$$q_3 = -2\tau_e i_E k_c(J_r - 2\tau_m d_c) \tag{3.77c}$$
$$q_4 = 2i_E\tau_e((\tau_m k_c + d_c)J_r - 2d_c^2\tau_m) \tag{3.77d}$$
$$q_6 = -2i_G J_r k_e(\tau_e - \tau_m) \tag{3.77e}$$
$$q_7 = 2i_G J_r d_e(\tau_e - \tau_m) \tag{3.77f}$$
$$q_8 = -2i_G J_r d_e(\tau_e - \tau_m) \tag{3.77g}$$
$$q_9 = -i_G i_f^2 J_e J_r(\tau_e - \tau_m) \tag{3.77h}$$
$$q_r = -2i_E\tau_e\tau_m d_c r_r\,, \tag{3.77i}$$

while the coefficients from (3.76) are

$$p_6 = -2k_e(J_f - 2\tau_e d_e) \tag{3.78a}$$
$$p_7 = 2(\tau_e k_e + d_e)J_f - 4d_e^2\tau_e \tag{3.78b}$$
$$p_8 = -2(\tau_e k_e + d_e)J_f + 4d_e^2\tau_e \tag{3.78c}$$
$$p_9 = -i_f^2 J_e J_f - 2J_f\tau_e d_e \tag{3.78d}$$
$$p_f = -2d_e r_f \tau_e\,. \tag{3.78e}$$

Following, insert (3.70) for u_1 and (3.67) for u_2, while setting $\xi_1 = \xi_2 = \xi_8 = \xi_9 = v_1 = v_2 = 0$. This enforces $\dot{\xi}_1 = \dot{\xi}_2 = \dot{\xi}_8 = \dot{\xi}_9 = 0$, so define $\boldsymbol{z}^T = \begin{bmatrix} z_1 & z_2 & z_3 & z_4 & z_5 \end{bmatrix} = \begin{bmatrix} \xi_3 & \xi_4 & \xi_5 & \xi_6 & \xi_7 \end{bmatrix}$ to derive the zero dynamics in the 9-state 4WD case as

$$\dot{\boldsymbol{z}} = \begin{bmatrix} \dot{z}_1 \\ \dot{z}_2 \\ \dot{z}_3 \\ \dot{z}_4 \\ \dot{z}_5 \end{bmatrix} = \begin{bmatrix} -z_2 \\ \big(2(k_r z_1 - d_r z_2\big) - r_r F_{xr})/J_r \\ (F_{xf} + F_{xr} - F_w)/m \\ -z_5 \\ \big(2(k_f z_4 - d_f z_5\big) - r_f F_{xf})/J_f \end{bmatrix}. \tag{3.79}$$

Again, the equilibria of the zero dynamics of the 4WD synthesis model are investigated.

Lemma 11. *The zero dynamics (3.79) have a unique equilibrium* $\boldsymbol{z}_{eq}^T = \begin{bmatrix} 0 & 0 & 0 & 0 & 0 \end{bmatrix}$.

Proof. Since at equilibrium $z_2 = z_5 = 0$, both tire forces F_{xf} and F_{xr} depend on z_3 only and so $z_3(F_{xf} + F_{xr}) < 0$ for $z_3 \neq 0$, so the same argument from the proof of Lemma 9 applies. □

Table 3.2 summarizes the findings of this section. These include the order of the nonlinear internal dynamics and their dependency on the external dynamics through the system outputs and the friction coefficient as external system input. Information on the state transformations is included and through which variables the tire force enters the corresponding control laws.

Table 3.2: Comparison of the IOL based control designs for the three synthesis models for TCSs.

	Control Law		**Internal Dynamics**		
Model	**TCS Type**	**Tire Force**	**Order**	**External Dependency**	$\boldsymbol{\phi(x)}$
$\mathcal{M}_5$	2WD, SISO	$\dot{x}_4$	3	$y_1 = x_3/i_G$ and μ	Linear
$\mathcal{M}_7$	4WD, MIMO	$\dot{x}_4$ and $\dot{F}_{xf}$	3	$y_1 = x_3/i_G$, $y_2 = x_7$ and μ	Nonlinear
$\mathcal{M}_9$	4WD, MIMO	$\dot{x}_4$ and $\dot{x}_7$	5	$y_1 = x_3/i_G$, $y_2 = x_9/i_f$ and μ	Linear

This concludes the derivation of the linearizing control laws and zero dynamics for the 5-state 2WD, the 7-state 4WD and the 9-state 4WD models for traction control. In the following section, stability of the nonlinear zero dynamics will be analyzed in detail for each of the three proposed traction control designs using a family of parametric, quadratic Lyapunov functions.

3.3.2 Stability Analysis using Parametric Lyapunov Functions

3.3.2.1 Stability Analysis of the 2WD Case

In this section, stability of the nonlinear zero dynamics is investigated. This is a necessary step in order to give a theoretical justification of the proposed control design. Since the parameters of the longitudinal model for traction control can vary in a wide range and might not be known exactly, the goal is to derive parameter independent stability statements. Stability is investigated for the 2WD model, first with the assumption of a constant friction coefficient. Thereafter, the results are extended to time-varying friction coefficients and to the 4WD case by considering vehicles with on-demand torque bias systems as well.

Beginning with the case of a 2WD vehicle, it is first demonstrated that the previously developed smooth approximation of the wheel slip quantity can be used to analyze and classify local stability properties of the zero dynamics. The Jacobian linearization of the zero dynamics at the origin, using $v_0^* = 3\sqrt{\epsilon}/2$ from Lemma 5, is given by

$$\dot{\boldsymbol{z}} \approx \boldsymbol{A}_{zd}\boldsymbol{z} = \begin{bmatrix} 0 & -1 & 0 \\ 2k_c/J_r & -(c_{xr}r_r^2/v_0^* + 2d_c) & c_{xr}r_r/(v_0^* J_r) \\ 0 & c_{xr}r_r/(v_0^* m) & -c_{xr}/(v_0^* m) \end{bmatrix} \boldsymbol{z}\,. \tag{3.80}$$

Remark 19. *Since λ_{xr} is a smooth function, computing the partial derivatives of the friction force F_{xr} at the origin is possible. Notice that the aerodynamic drag force (3.12) still contains the absolute value function, which is non-differentiable at the origin. This term could be replaced with the smooth approximation in (3.17) as well. However, here the fact is used that $\lim_{z_3\to 0} \partial F_w/(\partial z_3) = 0$, so $z_3 = 0$ is a removable singularity and thus the F_w term can be treated as zero for linearization about the origin.*

With (3.80) given, local stability can be analyzed using the Routh-Hurwitz criterion.

Lemma 12. *The zero dynamics (3.50) are locally asymptotically stable for all possible vehicle parameter combinations.*

Proof. The characteristic polynomial of $\boldsymbol{A}_{zd}$ is given by

$$p_c(s) = \det(s\boldsymbol{I}_3 - \boldsymbol{A}_{zd}) = s^3 + a_2 s^2 + a_1 s + a_0, \tag{3.81}$$

so a necessary condition is that $a_2, a_1, a_0 > 0$. Furthermore, its Hurwitz matrix is

$$\boldsymbol{H} = \begin{bmatrix} a_2 & a_0 & 0 \\ 1 & a_1 & 0 \\ 0 & a_2 & a_0 \end{bmatrix}, \tag{3.82}$$

from which the remaining conditions for necessity and sufficiency of local stability of the zero dynamics can be derived by computation of the three principal minors of $\boldsymbol{H}$. These are $\Delta_1 = a_2$, $\Delta_2 = a_1 a_2 - a_0$ and $\Delta_3 = -a_0^2 + a_1 a_2 a_0$. The coefficients a_0, a_1, a_2 and the principal minors Δ_1, Δ_2, Δ_3 can be found in Appendix A.1. Since all parameters in (A.1a)-(A.1c) and (A.2a)-(A.2c) are strictly positive, the zero dynamics (3.50) are locally asymptotically stable for all parameter combinations. □

In the following, the local stability result from Lemma 12, which also assumes a constant friction coefficient of the road μ, is shown to actually hold globally and for time-varying μ as well. A generalized version of the parametric Lyapunov function from our previously published work [305] is given by

$$V(\boldsymbol{z}) = \boldsymbol{z}^T \boldsymbol{P}\boldsymbol{z} = \boldsymbol{z}^T \begin{bmatrix} p_{11} & -1/2 & 0 \\ -1/2 & p_{22} & 0 \\ 0 & 0 & p_{33} \end{bmatrix} \boldsymbol{z} = p_{11}z_1^2 + p_{22}z_2^2 + p_{33}z_3^2 - z_1 z_2\,. \tag{3.83}$$

The coefficients of (3.83), with $\bar{c}_{xr} = \mu_{\max} F_{zr} B_r C_r$ are defined as

$$p_{11} = \frac{\gamma 12 J_r k_c \sqrt{\epsilon} + \bar{c}_{xr} d_c r_r^2 + 6 J_r k_c \sqrt{\epsilon} + 12 d_c^2 \sqrt{\epsilon}}{12 J_r d_c \sqrt{\epsilon}} \tag{3.84a}$$

$$p_{22} = \frac{\gamma 12 J_r k_c \sqrt{\epsilon} + \bar{c}_{xr} d_c r_r^2 + 6 J_r k_c \sqrt{\epsilon}}{24 k_c d_c \sqrt{\epsilon}} \tag{3.84b}$$

$$p_{33} = \frac{m}{J_r} p_{22}\,, \tag{3.84c}$$

where $\gamma > 0$ parametrizes a family of parametric Lyapunov functions for the zero dynamics of the TCS. First, it is shown that (3.83) qualifies as a Lyapunov function candidate.

Theorem 1. *Take $\gamma > 0$. Then, the function $V(\boldsymbol{z})$ is a Lyapunov function candidate for all possible vehicle parameters.*

Proof. From (3.83) it follows that $V(\boldsymbol{z})$ is a quadratic form. A necessary and sufficient condition for a real symmetric matrix $\boldsymbol{P} = \boldsymbol{P}^T$ to be positive definite is that all its leading principal minors are positive. These are given by $\Delta_1 = p_{11}$, $\Delta_2 = p_{11}p_{22} - 1/4$ and $\Delta_3 = p_{11}p_{22}p_{33} - p_{33}/4 = p_{33}\Delta_2$. Since the diagonal elements of $\boldsymbol{P}$ are strictly positive, it is sufficient to show that $\Delta_2 > 0$. Rearranging the resulting equation gives

$$\Delta_2 = \frac{\gamma}{2} + \gamma^2 \frac{k_c J_r}{2 d_c^2} + \gamma\Big(\frac{J_r k_c}{2 d_c^2} + \frac{\bar{c}_{xr} r_r^2}{12 d_c \sqrt{\epsilon}}\Big) + \frac{\bar{c}_{xr} d_c r_r^2}{24 J_r k_c \sqrt{\epsilon}} + \frac{J_r k_c}{8 d_c^2} + \frac{\bar{c}_{xr} r_r^2}{24 d_c \sqrt{\epsilon}} + \frac{\bar{c}_{xr}^2 r_r^4}{288 J_r k_c \epsilon}\,. \tag{3.85}$$

Then $\Delta_2 > \gamma/2 > 0$, so $\boldsymbol{P} \succ 0$ for all vehicle parameters. □

Remark 20. *The Lyapunov function we proposed in [305] is given by taking $\gamma = 7/2$ and can therefore be considered as a special case of the more general form (3.83).*

Remark 21. *Choosing $\gamma < 0$ would not necessarily make Δ_2 in (3.85) negative. However, its sign would then depend on the vehicle parameters and could be made negative by some parameter combinations. In order to prove parameter independent stability of the zero dynamics, we select $\gamma > 0$ without loss of generality. The case $\gamma = 0$ is excluded for the case of a time-varying friction coefficient, as will be discussed later.*

Remark 22. *Note that (3.83) was not obtained by solving the Lyapunov equation of the linearized zero dynamics. In particularly, such an approach would require the choice of an appropriate $\boldsymbol{Q}$ matrix, which has to be chosen such that the result is a global Lyapunov function for the nonlinear system, which is a non-trivial task. The standard choice $\boldsymbol{Q} = \boldsymbol{I}_3$ does not work here, because the resulting time derivative of this specific Lyapunov function candidate will not be globally negative definite for all vehicle parameters. Therefore, the Lyapunov function was constructed manually such that all the required inequalities are satisfied.*

Since (3.83) is a valid candidate Lyapunov function, we now show that $\dot{V}(\boldsymbol{z}) \prec 0$ holds for all vehicle parameters and that the zero dynamics are therefore globally asymptotically stable, which is one of the main stability results regarding TCSs.

Theorem 2. *The nonlinear zero dynamics of the TCS are globally asymptotically stable in the sense of Lyapunov for all vehicle parameter combinations.*

Proof. The time derivative of (3.83) can be partitioned by factoring out the tire force

$$\dot{V}(\boldsymbol{z}) = \dot{V}_1(\boldsymbol{z}) + \dot{V}_2(\boldsymbol{z}) \tag{3.86}$$

with the vehicle parameter dependent substitutions

$$\dot{V}_1(\boldsymbol{z}) = -\frac{2k_c}{J_r}z_1^2 - \Big(2\gamma + \frac{d_c\bar{c}_{xr}r_r^2}{6J_rk_c\sqrt{\epsilon}}\Big)z_2^2 - A_{st}\rho c_w\Big(\frac{\gamma}{2d_c} + \frac{1}{4d_c} + \frac{\bar{c}_{xr}r_r^2}{24J_rk_c\sqrt{\epsilon}}\Big)|z_3|z_3^2 \tag{3.87}$$

$$\dot{V}_2(\boldsymbol{z}) = F_{xr}\Big(\frac{\gamma z_3}{d_c} - \frac{\gamma r_r z_2}{d_c} - \frac{r_r z_2}{2d_c} + \frac{z_3}{2d_c} + \frac{r_r z_1}{J_r} - \frac{\bar{c}_{xr}r_r^3 z_2}{12J_rk_c\sqrt{\epsilon}} + \frac{\bar{c}_{xr}r_r^2 z_3}{12J_rk_c\sqrt{\epsilon}}\Big)\,. \tag{3.88}$$

Since the vehicle parameters are strictly positive and the mixed term z_1z_2 is canceled out, $V_1(\boldsymbol{z}) \prec 0$. It remains to show that $V_2(\boldsymbol{z})$ can not make (3.86) positive or zero for some $\boldsymbol{z}$, except at the origin. The idea is to rearrange the definition of the wheel slip as $r_rz_2 - z_3 = \lambda_{xr}v_{nr}$. Then, $\dot{V}_2(\boldsymbol{z})$ can be written as

$$\dot{V}_2(\boldsymbol{z}) = -\frac{\gamma v_{nr}}{d_c}\lambda_{xr}F_{xr} - \frac{v_{nr}}{2d_c}\lambda_{xr}F_{xr} - \frac{\bar{c}_{xr}v_{nr}r_r^2}{12J_rk_c\sqrt{\epsilon}}\lambda_{xr}F_{xr} + \frac{r_r}{J_r}z_1F_{xr}\,. \tag{3.89}$$

Both F_{xr} and λ_{xr} have the same sign by Lemma 1 and v_{nr} is strictly positive by Lemma 5, so the first three terms in (3.89) are never positive. It remains to show that the last term, $r_rJ_r^{-1}z_1F_{xr}$, cannot dominate the other terms. In the following, we assume without loss of generality, that $\lambda_{xr} \neq 0$. This is valid, because if $\lambda_{xr} = 0 \Rightarrow \dot{V}_2(\boldsymbol{z}) = 0$ and so (3.86) will be negative definite since then $\dot{V}(\boldsymbol{z}) = \dot{V}_1(\boldsymbol{z})$. Moreover we can assume that $z_1 \neq 0$, because if $z_1 = 0$, then $\dot{V}_2(\boldsymbol{z}) \leq 0$ since the remaining terms are non-positive. After these considerations, we can move the quadratic z_1 term from $\dot{V}_1$ to $\dot{V}_2$ to form

$$\dot{V}_3(\boldsymbol{z}) = \dot{V}_2(\boldsymbol{z}) - \frac{2k_c}{J_r}z_1^2\,. \tag{3.90}$$

Since $\lambda_{xr} \neq 0$, z_2 or z_3 will be non-zero and so the remaining terms in $\dot{V}_1$ will be non-positive. Therefore, if additionally $\dot{V}_3(\boldsymbol{z}) \prec 0$, then also $\dot{V}(\boldsymbol{z}) \prec 0$. Note that (3.90) is a quadratic equation in z_1, which is negative for $z_1 = 0$, $\lambda_{xr} \neq 0$. So if $\dot{V}_3(\boldsymbol{z})$ could be made positive, the quadratic equation $\dot{V}_3(\boldsymbol{z}) = 0$ would have real solutions. The discriminant of this equation, with respect to z_1, is given by

$$\mathrm{disc}_{z_1}(\dot{V}_3) = -\frac{8v_{nr}k_c\gamma}{J_rd_c}\lambda_{xr}F_{xr} - \frac{4k_cv_{nr}}{J_rd_c}\lambda_{xr}F_{xr} - \frac{2\bar{c}_{xr}r_r^2v_{nr}}{3J_r^2\sqrt{\epsilon}}\lambda_{xr}F_{xr} + \frac{r_r^2}{J_r^2}F_{xr}^2\,. \tag{3.91}$$

By Lemma 4, it holds that $|\bar{c}_{xr}\lambda_{xr}| \geq |F_{xr}|$ so we can bound (3.91) like

$$\mathrm{disc}_{z_1}(\dot{V}_3) \leq -\frac{8v_{nr}k_c\gamma}{J_rd_c}\lambda_{xr}F_{xr} - \frac{4k_cv_{nr}}{J_rd_c}\lambda_{xr}F_{xr} - \frac{2\bar{c}_{xr}r_r^2v_{nr}}{3J_r^2\sqrt{\epsilon}}\lambda_{xr}F_{xr} + \frac{r_r^2}{J_r^2}F_{xr}\bar{c}_{xr}\lambda_{xr}\,. \tag{3.92}$$

So if the right-hand side of (3.92) is always negative, then also $\mathrm{disc}_{z_1}(\dot{V}_3) < 0$. Since by assumption $\lambda_{xr} \neq 0$ and so $F_{xr} \neq 0$, the $\lambda_{xr}F_{xr}$ term is strictly positive and can be canceled out. Therefore, it remains to show that

$$-\frac{8v_{nr}k_c\gamma}{J_rd_c} - \frac{4k_cv_{nr}}{J_rd_c} - \frac{2\bar{c}_{xr}r_r^2v_{nr}}{3J_r^2\sqrt{\epsilon}} + \frac{r_r^2}{J_r^2}\bar{c}_{xr} < 0\,. \tag{3.93}$$

The v_{nr} term is strictly positive and a function of the state variables z_2 and z_3. However, it appears only in the negative terms in (3.93). So if v_{nr} attains its minimum value and the $r_r^2J_r^{-2}\bar{c}_{xr}$ term is still dominated, then (3.93) holds for all $\boldsymbol{z}$. By Lemma 5, the global minimum of v_{nr} is given by $3\sqrt{\epsilon}/2$, so

$$\mathrm{disc}_{z_1}(\dot{V}_3) \leq -\frac{(2\gamma+1)6k_c\sqrt{\epsilon}}{J_rd_c}\,. \tag{3.94}$$

From this follows, that if $\gamma > -1/2$ then $\mathrm{disc}_{z_1}(\dot{V}_3) < 0$. As discussed in the proof of Theorem 1 and Remark 21, the value of γ is restricted to $\gamma > 0$. Therefore, the discriminant (3.91) is strictly negative and so $\dot{V}_3(\boldsymbol{z}) = 0$ has no real solutions. Therefore, $\dot{V}(\boldsymbol{z}) \prec 0$ and the origin is globally asymptotically stable in the sense of Lyapunov for all vehicle parameters. □

The result above can be readily extended to the case that the friction coefficient of the road is time-varying, generalizing our result from [304] to the case $\gamma > 0$.

Corollary 1. *The zero dynamics (3.50) are globally asymptotically stable for all vehicle parameters and bounded positive time-varying friction coefficients* $\mu : \mathbb{R}_0^+ \to (0, \mu_{\max}]$.

Proof. The function $V(\boldsymbol{z})$ is bounded from below and above by $V(\boldsymbol{z})/\eta_1 \leq V(\boldsymbol{z}) \leq \eta_1 V(\boldsymbol{z})$ with $\eta_1 \geq 1$ as $V(\boldsymbol{z})$ does not depend on time explicitly. The time derivative of V is given, analogously to (3.86) by $\dot{V}(\boldsymbol{z},t) = \dot{V}_1(\boldsymbol{z}) + \dot{V}_2(\boldsymbol{z},t)$, since $F_{xr}(t)$ now is time-varying. At each time instant t we have $|F_{xr}(t)| \leq c_{xr}(t)|\lambda_{xr}| \leq \bar{c}_{xr}|\lambda_{xr}|$ with $c_{xr}(t) = \mu(t) C_r B_r F_{zr}$, so the argument used for Equation (3.92) still applies. Again we assume $\lambda_{xr} \neq 0$ because otherwise $\dot{V}(\boldsymbol{z},t) \leq \dot{V}_1(\boldsymbol{z})$, so in this case $\dot{V}(\boldsymbol{z},t)$ is trivially bounded by a negative definite function from above. If $\lambda_{xr} \neq 0$, an upper bound for $\dot{V}(\boldsymbol{z},t)$ is $\dot{V}_1(\boldsymbol{z}) + 2k_c J_r^{-1} z_1^2$, which is only negative semi-definite. However, note that in (3.90), we can as well move only a portion of the quadratic z_1 term from $\dot{V}_1(\boldsymbol{z})$ to construct the resulting quadratic equation

$$\dot{V}_3'(\boldsymbol{z},t) = \dot{V}_2(\boldsymbol{z},t) - \eta_2 \frac{2k_c}{J_r} z_1^2\,, \text{ with } \eta_2 = \frac{\bar{c}_{xr} d_c r_r^2}{\bar{c}_{xr} d_c r_r^2 + 6 J_r k_c \sqrt{\epsilon}}\,. \tag{3.95}$$

Since $\eta_2 \in (0,1)$, the portion $-(1-\eta_2) 2k_c J_r^{-1} z_1^2$ will remain in $\dot{V}_1(\boldsymbol{z})$. Repeating the procedure from Theorem 2 with the modified quadratic equation $\dot{V}_3'(\boldsymbol{z},t) = 0$ results in a new parametric bound for the discriminant, given by

$$\operatorname{disc}_{z_1}(\dot{V}_3') \leq -\eta_2 \frac{12\gamma k_c \sqrt{\epsilon}}{J_r d_c}\,. \tag{3.96}$$

Selecting $\gamma > 0$ guarantees that $\dot{V}_3'(\boldsymbol{z},t) \prec 0$ and $\dot{V}(\boldsymbol{z},t) \leq \dot{V}_1(\boldsymbol{z}) + \eta_2 2k_c J_r^{-1} z_1^2 \prec 0$. Therefore, the zero dynamics remain globally asymptotically stable for time-varying $\mu : \mathbb{R}_0^+ \to (0, \mu_{\max}]$. □

Remark 23. *By Theorem 2 and Corollary 1, it is shown that global stability holds for all possible parameter combinations and variations of the friction coefficient of the road. Furthermore, it also shows that stability holds for other tire friction models than (3.6), in especially for more complicated static tire models. As long as* $\lambda_{xr} F_{xr} > 0$ *for* $\lambda_{xr} \neq 0$, $F_{xr} = 0$ *for* $\lambda_{xr} = 0$ *and* $\bar{c}_{xr}|\lambda_{xr}| \geq |F_{xr}|$, *the friction curve can have an arbitrary, even time-varying, characteristic. This includes tire models which have a longitudinal slip stiffness that is not a function of* μ *and provides a strong robustness result on the global stability of the nonlinear zero dynamics.*

Remark 24. *The limitation that* $\mu > 0$ *is required in Corollary 1 can be relaxed since for* $\mu = 0$, *the time derivative (3.86) of the Lyapunov function (3.83) reduces to (3.87), which is a negative definite function that does not depend on time explicitly. In practice, the case of zero tire friction can realistically only occur if the rear axle lifts off (as then the normal force also becomes zero), a scenario that is not further pursued here. Nevertheless, asymptotic stability is preserved even for time-varying friction coefficients of the form* $\mu : \mathbb{R}_0^+ \to [0, \mu_{\max}]$, *so particularly including the case that* $\mu = 0\,, \forall t \in \mathbb{R}_0^+$. *However, a strictly positive lower bound for the friction coefficient is required for showing exponential stability, as will be discussed in Section 4.3.1.*

Remark 25. *In addition, since* ϵ *is a model parameter as well, it follows that stability also holds for arbitrary* $\epsilon > 0$. *Therefore, the normalization speed (3.9) can be approximated to an arbitrary accuracy, using the proposed smooth version (3.19).*

The classical approach proposed by Aizerman and Gantmacher is based on an application of the S-procedure [6]. In Theorem 2, symbolic discriminant analysis is used instead, which can be used in this case to prove stability independently of the vehicle parameters. This concludes the stability analysis of the zero dynamics of the $\mathcal{M}_5$ synthesis model for a 2WD TCS design based on the method of IOL. In the following, these results are extended to both the $\mathcal{M}_7$ and the $\mathcal{M}_9$ synthesis model, in order to prove global asymptotic stability for all vehicle parameters for the 4WD control designs based on IOL as well.

3.3.2.2 Generalization of Stability Results to the 4WD Cases

Following, the 4WD case is investigated, starting with the $\mathcal{M}_7$ model with the assumption of a stiff connection between the ETC and the front axle as described in Section 3.2.3. The zero dynamics in this case are identical to the 2WD case, with the exception of the last equation, where the additional $F_{xf,0}$ term enters (3.63). As demonstrated in our previously published work [300], the system remains globally asymptotically stable for all parameters. This can be shown by using the same Lyapunov function as for the 2WD case (3.83).

Theorem 3. *The nonlinear zero dynamics of the 4WD TCS with stiff connection between the ETC and the front axle are globally asymptotically stable in the sense of Lyapunov for all vehicle parameter combinations and time-varying friction coefficients* $\mu : \mathbb{R}_0^+ \to (0, \mu_{\max}]$.

Proof. Consider the Lyapunov function from (3.83). By Theorem 1, it is known that $V(\boldsymbol{z}) \succ 0$. The time derivative in the case of the 4WD drivetrain with stiff connection between the ETC and the front axle can be expressed in terms of the time derivative from the 2WD case and a separate term by

$$\dot{V}_{\mathcal{M}_7}(\boldsymbol{z}) = \dot{V}(\boldsymbol{z}) + \Big(\frac{\gamma}{d_c} + \frac{1}{2d_c} + \frac{\bar{c}_{xr} r_r^2}{12 J_r k_c \sqrt{\epsilon}}\Big) z_3 F_{xf,0}\,, \tag{3.97}$$

where $\dot{V}(\boldsymbol{z}) \prec 0$ is the time derivative of the 2WD case from Theorem 2. Since $\gamma > 0$, the factor in front of the $z_3 F_{xf,0}$ term is strictly positive. Therefore, if $z_3 F_{xf,0} \leq 0$, then automatically $\dot{V}_{\mathcal{M}_7}(\boldsymbol{z}) \prec 0$. Because $\omega_f = y_2 = 0$ by output zeroing and $F_{xf,0}$ is symmetric about the origin, it suffices to consider three cases for z_3 as shown in [300]:

(i) $z_3 > 0$ and $y_2 = 0 \Rightarrow \lambda_{xf} < 0 \Rightarrow F_{xf,0} < 0 \Rightarrow z_3 F_{xf,0} < 0$.
(ii) $z_3 < 0$ and $y_2 = 0 \Rightarrow \lambda_{xf} > 0 \Rightarrow F_{xf,0} > 0 \Rightarrow z_3 F_{xf,0} < 0$.
(iii) $z_3 = 0$ and $y_2 = 0 \Rightarrow \lambda_{xf} = 0 \Rightarrow F_{xf,0} = 0 \Rightarrow z_3 F_{xf,0} = 0$.

This shows that $z_3 F_{xf,0} \leq 0$, so $\dot{V}_{\mathcal{M}_7}(\boldsymbol{z}) \prec 0$ and by Corollary 1 it also follows immediately that $\dot{V}_{\mathcal{M}_7}(\boldsymbol{z}) \leq \dot{V}_1(\boldsymbol{z}) + \eta_2 2 k_c J_r^{-1} z_1^2$. Hence, the origin is globally asymptotically stable for all vehicle parameters and bounded positive time-varying $\mu(t)$. □

Remark 26. *Theorem 3 shows that the same Lyapunov function that could be used to prove stability of the zero dynamics in the 2WD case, can also be used in the 4WD case for the* $\mathcal{M}_7$ *model with a stiff connection between ETC and front axle. This is despite the fact that in this case the system model has* 7 *states instead of* 5*, because due to the MIMO control law, a vector relative degree of* $\begin{bmatrix} 2 & 2 \end{bmatrix}$ *results, instead of a scalar relative degree of* 2 *in the 2WD case. Therefore, the resulting zero dynamics have a dimension of 3 in both cases, which enables the use of the same Lyapunov function as in the 2WD case.*

In the following, the case of a vehicle with on-demand 4WD torque bias system and torsional dynamics between the ETC and the front axle, namely the $\mathcal{M}_9$ model, will be considered as well. In this case, as shown in Section 3.3.1.3, the resulting zero dynamics increase in dimension, leading to an overall dimension of 5. This means that the Lyapunov function from the 2WD case and the 7-state 4WD case is not directly applicable anymore. Nevertheless, in the following a method is proposed that shows how the Lyapunov function from these cases can be slightly modified in order to be applicable to the 5-dimensional zero dynamics of the $\mathcal{M}_9$ model as well. Recalling the 5-dimensional zero dynamics in the 4WD case from (3.79) gives

$$\dot{z}_1 = -z_2 \tag{3.98a}$$
$$\dot{z}_2 = \big(2(k_c z_1 - d_c z_2\big) - r_r F_{xr})/J_r \tag{3.98b}$$
$$\dot{z}_3 = (F_{xf} + F_{xr} - F_w)/m \tag{3.98c}$$
$$\dot{z}_4 = -z_5 \tag{3.98d}$$
$$\dot{z}_5 = \big(2(k_e z_4 - d_e z_5\big) - r_f F_{xf})/J_f\,. \tag{3.98e}$$

Looking at (3.98), if $F_{xf} = 0$ would hold then (3.98a)-(3.98c) would be independent of z_4, z_5 and describe exactly the 2WD case with rear drive, which was proven to be globally asymptotically stable by Theorem 2. On the other hand, if $F_{xr} = 0$ would hold, equations (3.98c)-(3.98e) would be independent of z_1, z_2 and describe the 2WD case with front drive, which is also covered by Theorem 2, as only the parameters change in this case and Theorem 2 guarantees parameter independent stability. So the two subsystems of (3.98) which are derived by setting the coupling term in (3.98c) to zero, are globally asymptotically stable by Theorem 2. The question now is whether the resulting coupled system is also stable and therefore, if a conclusion about stability of the overall system can be drawn from analyzing the uncoupled subsystems. Indeed this idea can be generalized to the case of n such subsystems as follows.

Given n globally asymptotically stable dynamical systems $\Sigma_1, \Sigma_2, \ldots, \Sigma_n$, each with unique equilibrium at the origin and radially unbounded Lyapunov functions $V_1, V_2, \ldots, V_n$ as

$$\Sigma_1 : \begin{cases} \dot{\boldsymbol{x}}_1 &= \boldsymbol{f}_1(\boldsymbol{x}_1, \boldsymbol{z}_1) \\ \dot{\boldsymbol{z}}_1 &= \boldsymbol{g}_1(\boldsymbol{x}_1, \boldsymbol{z}_1) \end{cases}, \text{ with } V_1(\boldsymbol{x}_1, \boldsymbol{z}_1) = W_1(\boldsymbol{x}_1) + U(\boldsymbol{z}_1)\,, \tag{3.99a}$$

$$\Sigma_2 : \begin{cases} \dot{\boldsymbol{x}}_2 &= \boldsymbol{f}_2(\boldsymbol{x}_2, \boldsymbol{z}_2) \\ \dot{\boldsymbol{z}}_2 &= \boldsymbol{g}_2(\boldsymbol{x}_2, \boldsymbol{z}_2) \end{cases}, \text{ with } V_2(\boldsymbol{x}_2, \boldsymbol{z}_2) = W_2(\boldsymbol{x}_2) + U(\boldsymbol{z}_2)\,, \tag{3.99b}$$

$$\vdots$$

$$\Sigma_n : \begin{cases} \dot{\boldsymbol{x}}_n &= \boldsymbol{f}_n(\boldsymbol{x}_n, \boldsymbol{z}_n) \\ \dot{\boldsymbol{z}}_n &= \boldsymbol{g}_n(\boldsymbol{x}_n, \boldsymbol{z}_n) \end{cases}, \text{ with } V_n(\boldsymbol{x}_n, \boldsymbol{z}_n) = W_n(\boldsymbol{x}_n) + U(\boldsymbol{z}_n)\,, \tag{3.99c}$$

with $\boldsymbol{x}_i \in \mathbb{R}^{n_i}$ and $\boldsymbol{z}_i \in \mathbb{R}^{n_z}, \forall i \in \{1, 2, \ldots, n\}$. Define the composite dynamical system Σ_c of dimension $n_c = n_z + \sum_{i=1}^{n} n_i$, coupled by the state vector $\boldsymbol{z} \in \mathbb{R}^{n_z}$, as

$$\Sigma_c : \begin{cases} \dot{\boldsymbol{x}}_1 &= \boldsymbol{f}_1(\boldsymbol{x}_1, \boldsymbol{z}) \\ \dot{\boldsymbol{x}}_2 &= \boldsymbol{f}_2(\boldsymbol{x}_2, \boldsymbol{z}) \\ \vdots & \\ \dot{\boldsymbol{x}}_n &= \boldsymbol{f}_n(\boldsymbol{x}_n, \boldsymbol{z}) \\ \dot{\boldsymbol{z}} &= \alpha_c\big(\boldsymbol{g}_1(\boldsymbol{x}_1, \boldsymbol{z}) + \boldsymbol{g}_2(\boldsymbol{x}_2, \boldsymbol{z}) + \cdots + \boldsymbol{g}_n(\boldsymbol{x}_n, \boldsymbol{z}) + \boldsymbol{d}(\boldsymbol{z})\big)\,, \end{cases} \tag{3.100}$$

with $\alpha_c > 0$. Then, the next fact is derived by combining the individual Lyapunov functions.

Lemma 13. *The system (3.100) is globally asymptotically stable if its subsystems are globally asymptotically and of the form (3.99) and* $\sum_{i=1}^{n} \dot{V}_i(\boldsymbol{x}_i, \boldsymbol{z_i}) + \boldsymbol{d}(\boldsymbol{z})\partial U(\boldsymbol{z})/(\partial \boldsymbol{z}) < 0\,, \forall \boldsymbol{z} \neq \boldsymbol{0}_{n_z}$. *The last condition is trivially satisfied for* $\boldsymbol{d}(\boldsymbol{z}) = \boldsymbol{0}_{n_z}$. *A Lyapunov function is given by*

$$V_c(\boldsymbol{x}_1, \boldsymbol{x}_2, \ldots, \boldsymbol{x}_n, \boldsymbol{z}) \overset{\text{def}}{=} (1/\alpha_c)U(\boldsymbol{z}) + \sum_{i=1}^{n} W_i(\boldsymbol{x}_i)\,. \tag{3.101}$$

Proof. Since U, scaled by $1/\alpha_c > 0$, is positive definite in $\boldsymbol{z}$ and W_i positive definite in $\boldsymbol{x}_i$, the sum (3.101) is positive definite in $\boldsymbol{\xi}^T = \begin{bmatrix} \boldsymbol{x}_1 & \boldsymbol{x}_2 & \ldots & \boldsymbol{x}_n & \boldsymbol{z} \end{bmatrix}$, so V_c is positive definite. Moreover,

$$\dot{V}_c(\boldsymbol{\xi}) = (1/\alpha_c)\frac{\partial U(\boldsymbol{z})}{\partial \boldsymbol{z}}\Big(\alpha_c \boldsymbol{d}(\boldsymbol{z}) + \sum_{i=1}^{n} \alpha_c \boldsymbol{g}_i(\boldsymbol{x}_i, \boldsymbol{z})\Big) + \sum_{i=1}^{n} \frac{\partial W_i(\boldsymbol{x}_i)}{\partial \boldsymbol{x}_i} \boldsymbol{f}(\boldsymbol{x}_i, \boldsymbol{z}) \tag{3.102}$$

$$= \frac{\partial U(\boldsymbol{z})}{\partial \boldsymbol{z}} \boldsymbol{d}(\boldsymbol{z}) + \sum_{i=1}^{n} \dot{V}_i(\boldsymbol{x}_i, \boldsymbol{z})\,. \tag{3.103}$$

The second term in (3.103) is the sum of individual derivatives and each is negative definite in $(\boldsymbol{x}_i, \boldsymbol{z})$ since each subsystem Σ_i is asymptotically stable, the sum is negative definite in $\boldsymbol{\xi}$. Since $\sum_{i=1}^{n} \dot{V}_i(\boldsymbol{x}_i, \boldsymbol{z_i}) + \boldsymbol{d}(\boldsymbol{z})\partial U(\boldsymbol{z})/(\partial \boldsymbol{z}) < 0\,, \forall \boldsymbol{z} \neq \boldsymbol{0}_{n_z}$, Σ_c is globally asymptotically stable. □

Theorem 4. *The zero dynamics (3.79) of the $\mathcal{M}_9$ model are globally asymptotically stable for all vehicle parameter combinations.*

Proof. Construct the two auxiliary dynamical systems Σ_1 and Σ_2 by

$$\Sigma_1 : \begin{cases} \dot{\boldsymbol{q}}_1 &= \boldsymbol{f}_1(\boldsymbol{q}_1, p_1) = \begin{bmatrix} -z_2 \\ \big(2(k_c z_1 - d_c z_2\big) - r_r F_{xr})/J_r \end{bmatrix} \\ \dot{p}_1 &= g_1(\boldsymbol{q}_1, p_1) = (F_{xr} - F_{wr})/m \end{cases} \tag{3.104a}$$

$$\Sigma_2 : \begin{cases} \dot{\boldsymbol{q}}_2 &= \boldsymbol{f}_2(\boldsymbol{q}_2, p_2) = \begin{bmatrix} -z_5 \\ \big(2(k_e z_4 - d_e z_5\big) - r_f F_{xf})/J_f \end{bmatrix} \\ \dot{p}_2 &= g_2(\boldsymbol{q}_2, p_2) = (F_{xf} - F_{wf})/m \end{cases} \tag{3.104b}$$

where $\boldsymbol{q}_1^T = \begin{bmatrix} z_1 & z_2 \end{bmatrix}$ and $\boldsymbol{q}_2^T = \begin{bmatrix} z_4 & z_5 \end{bmatrix}$. Here, $F_{wr} = F_w$ with F_w given by (3.12), where v_x is replaced by p_1. Analogously, $F_{wf} = F_w$ with F_w again given by (3.12), but v_x replaced with p_2. Furthermore, F_{xr} is given by (3.6) and (3.21) where ω_r is replaced by z_2 and v_x by p_1. Finally, F_{xf} is given by (3.26) and (3.28) where ω_f is replaced by z_5 and v_x by p_2.

The first system Σ_1 is identical to the zero dynamics of the 2WD case with RWD, see (3.50). The system Σ_2 represents the zero dynamics of the 2WD case with FWD. Global asymptotic stability of Σ_1 and Σ_2 follows from Theorem 2, as stability was shown there for all possible vehicle parameters. The corresponding Lyapunov functions for Σ_1 and Σ_2 are obtained as

$$V_1(\boldsymbol{q}_1, p_1) = W_1(\boldsymbol{q}_1) + U(p_1) = \boldsymbol{q}_1^T \boldsymbol{P}_1 \boldsymbol{q}_1 + p_1^2 \tag{3.105a}$$

$$V_2(\boldsymbol{q}_2, p_2) = W_2(\boldsymbol{q}_2) + U(p_2) = \boldsymbol{q}_2^T \boldsymbol{P}_2 \boldsymbol{q}_2 + p_2^2 \tag{3.105b}$$

where $\boldsymbol{P}_1$ and $\boldsymbol{P}_2$ are defined in the Appendix A.2. The composite system (3.100) is constructed with $\alpha_c = 1$ and $\boldsymbol{f}_1$, $\boldsymbol{f}_2$, g_1, g_2, $\boldsymbol{q}_1$, $\boldsymbol{q}_2$ from (3.104), $d(p) = (1/2)\rho c_w A_{st} p|p|/m$, $p = z_3$ and

$$\Sigma_c : \begin{cases} \dot{\boldsymbol{q}}_1 &= \boldsymbol{f}_1(\boldsymbol{q}_1, p) \\ \dot{\boldsymbol{q}}_2 &= \boldsymbol{f}_2(\boldsymbol{q}_2, p) \\ \dot{p} &= g_1(\boldsymbol{q}_1, p) + g_2(\boldsymbol{q}_2, p) + d(p)\,, \end{cases} \tag{3.106}$$

which is identical to the zero dynamics (3.98) of the $\mathcal{M}_9$ synthesis model. By (3.101), a Lyapunov function suitable for (3.106) can be constructed by $V_{\mathcal{M}_9}(\boldsymbol{q}_1, \boldsymbol{q}_2, p) = \boldsymbol{q}_1^T \boldsymbol{P}_1 \boldsymbol{q}_1 + \boldsymbol{q}_2^T \boldsymbol{P}_2 \boldsymbol{q}_2 + p^2$. Since $d(p) \neq 0$, this term must be examined as well. Since the derivative can be brought into the form $\dot{V}_{\mathcal{M}_9}(\boldsymbol{q}_1, \boldsymbol{q}_2, p) = \dot{\nu}_{\mathcal{M}_9}(\boldsymbol{q}_1, \boldsymbol{q}_2, p) + 2p\,d(p)$ where $\dot{\nu}_{\mathcal{M}_9}$ is negative definite in $(\boldsymbol{q}_1, \boldsymbol{q}_2, p)$ and compensates the $p\,d(p)$ term, it follows that $\dot{V}_{\mathcal{M}_9}(\boldsymbol{q}_1, \boldsymbol{q}_2, p) \prec 0$. This can be seen as $\dot{V}_{\mathcal{M}_9}$ can be expressed in terms of the derivatives of the 2WD Lyapunov functions for RWD and FWD as shown in Appendix A.2, so global asymptotic stability of (3.98) follows by Lemma 13. □

It can be noted that the zero dynamics of the $\mathcal{M}_9$ model (3.79) also arise for an IOL TCS design of an electric vehicle with four in-wheel motors, when considering only the longitudinal motion. A proof of global asymptotic stability for this case, assuming constant friction coefficients, is given by our colleague Lupberger *et al.* [183], using a variant of the parametric Lyapunov function (3.83), where the required inequalities are derived analogously to the proof of Theorem 2 and our original proof from [305] for the 2WD case. Lemma 13 and Theorem 4 generalize the approach from [183] to all composite nonlinear systems of the form (3.99)-(3.100). Time-varying friction coefficients in (3.79) are considered in Section 4.3.1.

This concludes the stability analysis of the zero dynamics resulting from an IOL based control design for the three synthesis models considered in this work. In the following section, some practical considerations for an implementation of the derived control laws are given. This includes the choice of the reference dynamics for the linearized substitute model resulting from the IOL design and considerations for tracking of ramp-shaped reference trajectories.

3.4 Reference Dynamics and Practical Considerations

After the stability analysis in the previous section, the design of reference dynamics and some practical considerations of the proposed TCS are given. First, we focus on the reference dynamics of the $\mathcal{M}_5$ 2WD synthesis model from (3.22). The control law (3.41) globally linearizes the input-output relation of the $\mathcal{M}_5$ model and since the relative degree is two, the resulting substitute model has the dynamics of a double integrator $\ddot{y}_1 = v_1$. However, it is possible to impose different linear dynamics on the system as well [256, pp. 116–118], by setting

$$v_1 \overset{\text{def}}{=} \ddot{y}_1 \overset{!}{=} -a_1\dot{y}_1 - a_0 y + b_0 w_1 \tag{3.107a}$$

$$y_1(t) \circ\!\!-\!\!\bullet\, Y_1(s) = \mathcal{R}_1(s) W_1(s) \tag{3.107b}$$

$$\mathcal{R}_1(s) = b_0/(s^2 + a_1 s + a_0)\,. \tag{3.107c}$$

Here, a_0, a_1 and b_0 are design parameters of the reference model $\mathcal{R}_1(s)$ in (3.107c). Taking for example $b_0 = 1$ and $a_0 = a_1 = 0$ results in the standard double integrator. We propose the following method for designing $\mathcal{R}_1(s)$: ideally, the behavior from u_1 to y_1 would be a first order lag element in series with an integrator. This accounts for first order actuator dynamics and the transfer from motor torque to the angular velocity of the crankshaft. This is the case for a rigid drivetrain, so that $\Delta\phi_c = \Delta\dot{\phi}_c = 0$ and under the assumption of linear, stationary tire forces such that $F_{xr} \approx c_{xr}\lambda_{xr} \approx$ constant. Clearly, then also $\omega_c/i_G = \omega_r$ and so $T_r = i_G T_m/2$. Note that while (3.4) would suggest $T_r = 0$ under these assumptions, this equation cannot be used for a rigid drivetrain as $k_c \to \infty$. The $\mathcal{M}_5$ model then simplifies to

$$\dot{x}_1 = (u_1 - x_1)/\tau_m \tag{3.108a}$$

$$\dot{x}_3/i_G = \dot{x}_4 = \big(i_G x_1 - \hat{d}(\lambda_{xr})\big)/J_r\,. \tag{3.108b}$$

Here, $\hat{d}(\lambda_{xr}) = r_r c_{xr}\lambda_{xr} \approx$ constant is an uncertain disturbance that encapsulates a range of wheel slip conditions at different longitudinal speeds. Following, (3.108a)-(3.108b) can be interpreted as a first order lag element in series with an integrator and an uncertain ramp-disturbance $d(\lambda_{xr}, t) = \hat{d}(\lambda_{xr})t/J_r$. Hence, a natural choice for the parameters of $\mathcal{R}_1(s)$, compare [305], is

$$a_0 = 0 \tag{3.109a}$$

$$a_1 = 1/\tau_m \tag{3.109b}$$

$$b_0 = i_G/(\tau_m J_r)\,. \tag{3.109c}$$

Remark 27. *These assumptions are only valid for linear, stationary driving conditions. While these conditions are not the use case of a TCS, the proposed reference model implements the desired behavior as it "corrects" only the nonlinearities, but does not modify the linear dynamics.*

Remark 28. *In the control laws (3.41), (3.56) and (3.70), the quantity $i_G = i_a i_r$ is used, where i_a is piecewise constant as it depends on the selected gear. In order to ensure a smooth transition during gear switching, i_a is lowpass filtered. For (3.109c) we use a constant i_G, corresponding to the second gear, in order keep the reference dynamics time-invariant.*

Hence, the linearized system behaves from w_1 to y_1 like the transfer function $i_G/\big(J_r s(\tau_m s+1)\big)$. Since this is a type 1 system and one task of the TCS is to track ramp-like reference trajectories during acceleration, an additional integrator is required in the forward path of the loop in order to achieve zero asymptotic tracking error, compare Table 2.1. This can be realized by a PID controller that is designed for the reference system $\mathcal{R}_1(s)$ and is given by

$$W_1(s) = C_{\text{PID}}(s) E_1(s) \tag{3.110a}$$

$$C_{\text{PID}}(s) = k_p + \frac{k_i}{s} + \frac{k_d s}{\tau_d s + 1}\,. \tag{3.110b}$$

Here, $W_1(s) \bullet\!\!-\!\!\circ\, w_1(t)$ and $E_1(s) \bullet\!\!-\!\!\circ\, e_1(t) \stackrel{\text{def}}{=} r_1(t) - y_1(t)$ where $e_1(t)$ is the error signal for the PID controller $C_{\text{PID}}(s)$, $r_1(t)$ is the reference trajectory, $y_1(t)$ the system output and $w_1(t)$ the input for the reference model (3.107a). Moreover, k_p, k_i and k_d are proportional, integral and derivative gain, τ_d is the derivative filter time constant. It can be noted that zero asymptotic tracking error would also be achieved by the original double integrator, since this is a type 2 system. However, the above formulation has the advantage that a standard PID controller can be used in combination with the IOL design, which is desirable from a parameter tuning perspective. Moreover, in order to take actuator limits into account, the integrator of the PID controller is implemented with the standard anti-windup method which depends on both control signal saturation and the sign of the error signal [66], using the following state-space representation for the PID controller with anti-windup,

$$\dot{x}_i = e_1(1 - \sigma_s) \tag{3.111a}$$

$$\dot{x}_d = (-1/\tau_d)x_d + e_1 \tag{3.111b}$$

$$w_1 = k_i x_i - (k_d/\tau_d^2)x_d + (k_p + k_d/\tau_d)e_1\,. \tag{3.111c}$$

Here, x_i is the integrator state and x_d the state of the derivative filter. The integrator depends on the boolean switching signal $\sigma_s \in \{0, 1\}$, indicating a control signal saturation by

$$\sigma_s = \begin{cases} 1\,, & (u_1 < u_{1,\min} \vee u_1 > u_{1,\max}) \wedge (e_1 u_1 \geq 0) \quad (3.112a) \\ 0\,, & \text{otherwise.} \quad (3.112b) \end{cases}$$

Doing so ensures that the integrator can still "integrate away" from the control limits $u_{1,\min}$ and $u_{1,\max}$ and is only put on hold if it would try to go beyond these bounds. This is preferable over the common method of just stopping the integration if the control signal is saturated, see [247] for a detailed investigation. The control signal itself is subject to the saturation by

$$\bar{u}_1 = \text{sat}(u_1, u_{1,\min}, u_{1,\max}) \stackrel{\text{def}}{=} \begin{cases} u_{1,\max}\,, & u_1 > u_{1,\max} \\ u_1\,, & u_{1,\min} \leq u_1 \leq u_{1,\max} \\ u_{1,\min}\,, & u_1 < u_{1,\min}\,. \end{cases} \tag{3.113}$$

An important aspect for practical implementation is that the control law (3.41) still contains the $\dot{x}_3$ and $\dot{x}_4$ terms. It is not desirable to insert the actual ODEs for these terms, as they contain quantities like tire parameters, the friction coefficient of the road and other uncertain variables. A more useful approach in practice is therefore to estimate these terms numerically with filters like $\dot{y}_1(t) \circ\!\!-\!\!\bullet\, sY_1(s) \approx F_{y_1}(s)Y_1(s)$, $\dot{x}_4(t) \circ\!\!-\!\!\bullet\, sX_4(s) \approx F_{x_4}(s)X_4(s)$, where $Y_1(s) \bullet\!\!-\!\!\circ\, y_1(t)$, $X_4(s) \bullet\!\!-\!\!\circ\, x_4(t)$ and

$$F_{y_1}(s) = F_{x_4}(s) = s/(\tau_d s + 1)\,. \tag{3.114}$$

This has the advantage that the control law does not depend directly on the nonlinear, uncertain, time-varying tire force, as it is implicitly included in the numerically calculated $\dot{x}_4$ term. Choosing a different mapping for the tire force in the design model would not change the control law itself. Similarly, it avoids the occurrence of the twist angle in the control law, which eliminates the need of an observer for this quantity. The actuator torque x_1 is not measured but calculated by (3.1).

Remark 29. *The stability analysis in Chapter 3 and Chapter 4 is based on an exact IOL, showing that such a design is feasible in theory. In practice, the IOL is achieved only approximately, due to parameter uncertainties, time delays, unmodeled dynamics, discretization, actuator limitations, measurement noise and the numerical approximation of x_1, $\dot{x}_3$ and $\dot{x}_4$. An experimental validation of the assumption that the errors introduced by these limitations are neglectable in practice is presented in Chapter 6, which shows the real world suitability of the proposed TCSs.*

Another aspect of the overall TCS is the reference generator which computes a target trajectory r_1 for the speed controller based on the driving situation. It is located on the DCU and transmits the reference trajectory r_1 for the system output $y_1 = x_3/i_G$ to the ECU, cf. Figure 2.3.

Generally, as the task is to maximize traction, the reference generator aims to generate a target speed that corresponds to a traction maximizing wheel slip. In the simplest case, this slip value can be obtained from Equation (3.14a), such that $\lambda_{xr,d} = \lambda^{+}_{xr,\text{peak}} = \tan\big(\pi/(2C_r)\big)/B_r$ where $\lambda_{xr,d}$ is the desired target wheel slip. This slip can then be converted to an angular velocity, assuming positive acceleration $r_r x_4 > x_5 > 0$, by solving (2.1c) for ω_r, by

$$r_1 = x_5/\big(r_r(1-\lambda_{xr,d})\big)\,. \tag{3.115}$$

In practice, the target wheel slip cannot be calculated a priori exactly, as its optimal value depends on various other variables like the friction coefficient of the road, tire wear, road slope or lateral acceleration during cornering, for example. Methods like online estimation of the tire force [129] or the friction coefficient [236, 286], as well as extremum seeking algorithms [8, 292] can be used to adapt the target slip value appropriately, see also [121, pp. 137–168]. In this work, we focus on achieving robust performance of the inner control loop for potentially non-optimal reference generation due to the mentioned uncertainties. The controller activation is implemented via

$$\sigma_a(k) = \begin{cases} 1 & e_1(k) < 0 & \text{(3.116a)} \\ 0 & e_1(k) \geq 0 \wedge T_{\text{driver}}(k) < \bar{u}_1(k) & \text{(3.116b)} \\ \sigma_a(k-1) & \text{otherwise} & \text{(3.116c)} \end{cases}$$

and $\sigma_a(0) = 0$. Here, $\sigma_a \in \{0, 1\}$ is the boolean controller activation signal. As long as $\sigma_a = 0$, the driver is the controller and the requested torque T_{driver} is realized. If the scaled engine speed y_1 exceeds the desired value r_1, the TCS takes over and ensures that excessive wheel slip is avoided. Optionally, the PID controller can be reset upon activation, while (3.116) can be debounced by the condition that once active, $\sigma_a(k) = 1$ must be maintained for a certain time in order to avoid repeated switching. The TCS is deactivated only if $y_1 \leq r_1$ and the requested torque of the driver is smaller than that of the controller. The final torque $\widetilde{u}_1$ is

$$\widetilde{u}_1(k) = \min\Big(T_{\text{driver}}(k),\, \bar{u}_1(k) + \hat{U}_1\big(1-\sigma_a(k)\big)\Big) \tag{3.117}$$

where $\hat{U}_1$ is chosen large enough that $\bar{u}_1 + \hat{U}_1 > T_{\text{driver}}$ for all $\bar{u}_1$ and T_{driver}, which implements a switch. As indicated by Equation (3.117), the controller is discretized for the digital microcontroller of the ECU, here by using the Tustin transformation. Figure 3.4 shows the proposed closed loop 2WD TCS based on IOL and the interconnection of the described components.

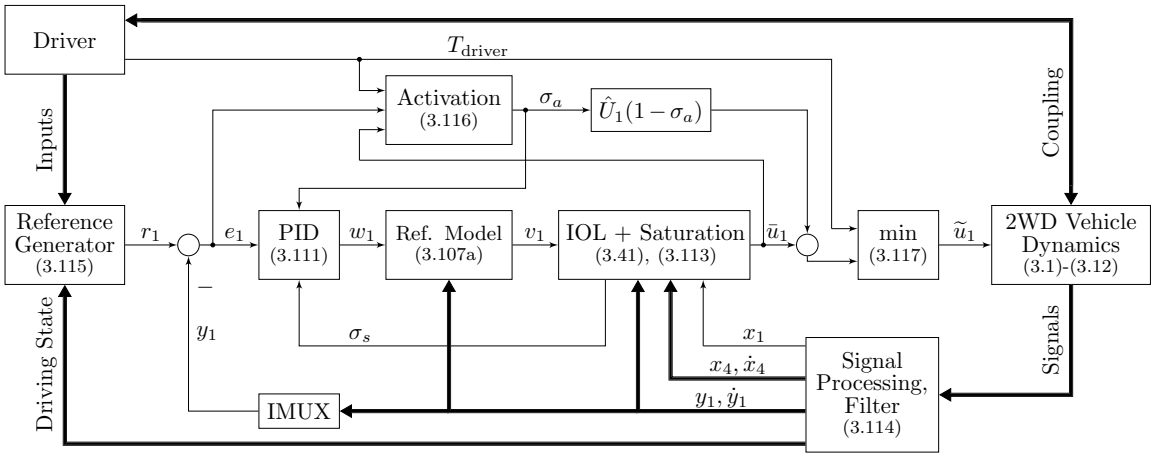

Figure 3.4: Closed loop control system for traction control using ECU-based IOL [305].

In the 4WD case, the implementation depends on the choice of the design model. For the $\mathcal{M}_9$ model, the control law (3.70) for the ETC has a structure similar to the 2WD case. Instead of one damping term, which takes into account the difference between scaled engine speed and rear axle speed, it has another damping term for the difference of the scaled ETC output speed and the front axle speed. This also shows the advantage of the proposed method to use torsion springs in the design model, as this leads to control laws that can readily be implemented by using filters to estimate the required angular accelerations. However, one disadvantage is that for each degree of freedom, two angular velocities are required: one "close" to the actuator and one at the location of the load torque, respectively the tire/axle.

However, not every 4WD vehicle configuration necessarily has a sensor for the ETC output speed. One possibility to overcome this issue is to design an observer for this quantity. In this work, a simplification is used instead resulting in a more compact control design, by using the control laws (3.53) and (3.56) based on the $\mathcal{M}_7$ model instead. Here, the connection between the ETC and the front axle is modeled as stiff, which leads to an $\dot{F}_{xf}$ term in both control laws and also a different second output y_2. Since during control, drivetrain oscillations on the rear axle are more dominant, this term is neglected by setting $\dot{F}_{xf} = 0$. This can be justified as it leads to an equivalent control law as for the $\mathcal{M}_9$ model, based on $y_2 = \omega_f$ instead of $y_2 = \omega_e/i_f$, while assuming the damping term from the IOL-induced PD controller for the front axle is neglected. The experimental evaluation in Section 6.3.3 demonstrates that despite this simplification, the proposed 4WD TCS achieves the desired performance and robustness.

Figure 3.5 shows the structure of the proposed 4WD TCS together with the three relevant control units. The DCU provides reference trajectories for the control law (3.56) on the ECU and for the control law (3.53) on the ETC. The omission of the $\dot{F}_{xf}$ term in the control laws is indicated by the dashed arrows for the y_2 signal in Figure 3.5. A remarkable aspect is the coupling of the MIMO control law by the v_2 term, which transmits information from the ETC to the ECU. This coupling term was implemented by an prototypical software bypass between both control units. The reference model on the ETC is $v_2 = b_{0,e}w_2 - a_{1,e}\dot{y}_2 - a_{0,e}y_2$ with $a_{0,e} = 0$ while the $b_{0,e}$ and $a_{1,e}$ terms started with a value of $b_{0,e} = i_f/(\tau_e J_f)$, $a_{1,e} = 1/\tau_e$ and were fine tuned experimentally. The implementation of the remaining components, like activation, anti-windup or filtering, was done analogously to the previously described 2WD case on the ECU. In the following section, the proposed TCSs are analyzed from a passivity viewpoint to gain further theoretical insights before the experimental evaluation.

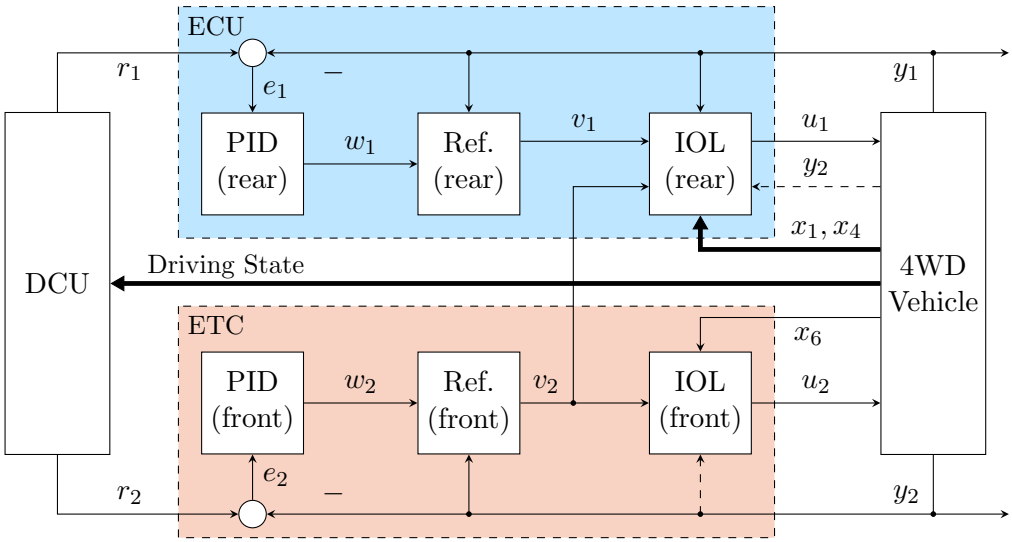

Figure 3.5: Proposed MIMO control structure for 4WD TCSs based on IOL, adapted from [300].

4 Passivity and Absolute Stability Analysis of the Zero Dynamics

Summary. *In this chapter, the zero dynamics resulting from the application of the input-output linearization technique to TCSs are analyzed from the viewpoint of passivity and absolute stability. The main contributions are:*

1. *A detailed analysis of two different formulations of the zero dynamics as a Lur'e system in the framework of absolute stability.*
2. *Proof of global, exponential, parameter-independent stability of the zero dynamics and input-to-state stability of the internal dynamics of the proposed TCSs.*
3. *Proposal and conjecture of a special case of the Markus-Yamabe conjecture, located on the frontier to the Kalman conjecture, resulting from the zero dynamics of the TCS.*

This chapter is partially based on our publications [304] and [306].

4.1 Sector-boundedness of the Tire Force

An interesting property of the zero dynamics (3.50) is that they depend on two memoryless nonlinearities, which are, when considered individually, sector bounded and passive, as defined in Section 2.2.2. These functions are the aerodynamic drag force F_w, which lies in the sector $[0, \infty]$ and the tire force F_{xr}, which lies in the sector $[\underline{c}_{xr}, \bar{c}_{xr}]$. Here, $\bar{c}_{xr} = \mu_{\max} F_{zr} B_r C_r > 0$ is the maximum longitudinal slip stiffness, which is positive and finite so F_{xr} is IFP. Furthermore,

$$\underline{c}_{xr} = (1/2)\mu_{\min} F_{zr} \sin\left(C_r \arctan(2\, B_r)\right) \tag{4.1}$$

can be derived as lower sector bound, taking into account that λ_{xr} is bounded by Lemma 2. Assuming now that the friction coefficient of the road is bounded from below by a positive number, such that $0 < \mu_{\min} \leq \mu(t) \leq \mu_{\max} < \infty$, then also $0 < \underline{c}_{xr}$ and F_{xr} is bounded like

$$(F_{xr} - \underline{c}_{xr}\lambda_{xr})(F_{xr} - \bar{c}_{xr}\lambda_{xr}) \leq 0\,, \tag{4.2}$$

with equality in (4.2) if and only if $\lambda_{xr} = F_{xr} = 0$. Hence, under the mentioned assumptions, F_{xr} is also OFP. Figure 4.1 shows both nonlinear functions embedded into their corresponding sectors (grey background color) and excess of passivity (blue background color). Figure 4.1a shows the tire force curves with $\mu = \mu_{\min}$ and $\mu = \mu_{\max}$ and the excess of passivity. It can be noted that the bound (4.1) holds mathematically, not only practically, due to the limited range of the wheel slip. It is therefore different to the common approach of limiting the input to the nonlinearity to a range of practical values, see for example [2, pp. 72–75], where this approach is applied to a saturation nonlinearity. Figure 4.1b shows the aerodynamic drag force F_w as a function of the longitudinal vehicle velocity v_x. Since $\lim_{v_x \to 0} \mathrm{d}F_w/(\mathrm{d}v_x) = 0$, (removable singularity at $v_x = 0$), F_w is not OFP, as its lower sector bound is the v_x–axis. It could be made IFP by assuming an upper bound on v_x, however, as we already showed global asymptotic stability of the zero dynamics in Theorem 2, this would add an artificial restriction, which is not necessary, as will be shown in the following. Also, since the goal is to strengthen the stability guarantees to exponential stability, the guaranteed decay rates would then also depend on such a bound.

This is undesirable, as the guaranteed decay rates of a globally exponentially stable system hold for the whole state space and so conclusions for all kind of vehicles with different maximum speeds can be drawn. However, without an upper bound, any line will be eventually intersected by F_w, which is effectively quadratic[1] in v_x, so the upper sector bound is the vertical axis at $v_x = 0$. Hence, F_w does not exhibit any excess of passivity, as indicated in Figure 4.1b.

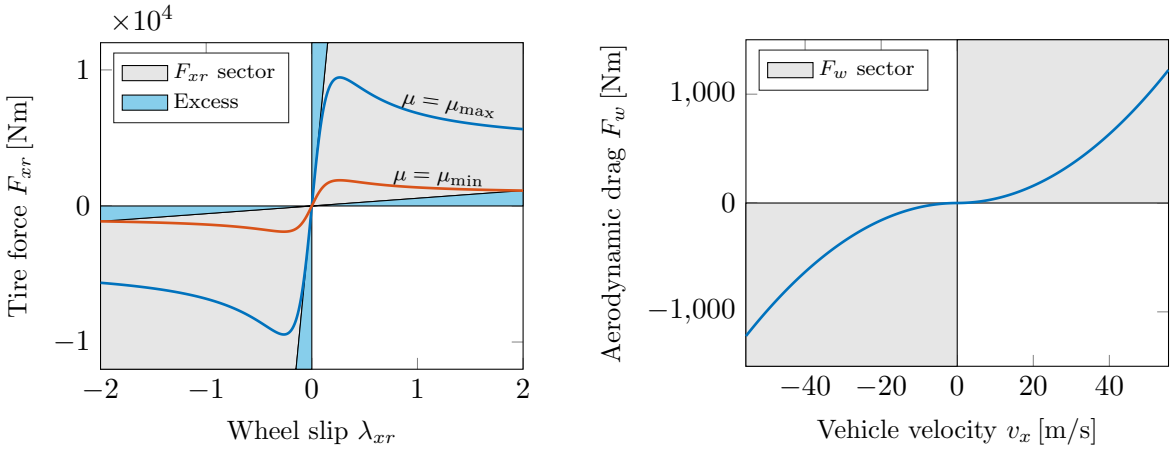

(a) Excess of passivity of the tire friction force.

(b) Passivity of the aerodynamic drag force.

Figure 4.1: Visualization of passivity properties of F_{xr} and F_w assuming a lower bound on μ.

Due to these passivity properties of both nonlinearities, a promising way to further investigate stability of the zero dynamics is the application of criteria for absolute stability or passivity based methods [233], as discussed in Section 2.2.2. The zero dynamics constitute a very general form of a Lur'e system [184] with multiple inputs, multiple outputs and multiple coupled, nonlinear, time-varying functions. However, several difficulties arise when trying to apply these approaches here. First, the discussed properties (with even an excess of passivity) of F_{xr}, were only shown for F_{xr} as a function of λ_{xr} so far. However, the wheel slip λ_{xr} itself is a nonlinear function of the state variables ω_r and v_x. This is the so-called unstructured case of a coupled, time-varying MIMO nonlinearity, which is a rather special case, considered only rarely in the literature [108, 248]. Traditional tools like the extended Popov criterion are not applicable to the unstructured case [222]. Safonov and Kulkarni showed that in the MIMO case, another standard tool like Zames-Falb multipliers requires that the nonlinearity is the gradient of a potential function to be applicable [248]. In addition, the nonlinearity is assumed to be incrementally positive, a MIMO generalization of monotonicity [248], which does not hold for the nonlinearities analyzed in Section 4.2, so this method is not applicable here. Considering Figure 4.1a this is no surprise, as F_{xr} is non-monotone even in the SISO case as a function of λ_{xr}.

Methods for the unstructured case have been proposed already [108], however, with the drawback, that they mainly rely on numerical LMI solvers, which only prove stability numerically and for a fixed set of parameters. This is typically also the case for analyses based on integral-quadratic constraints [140, 238]. The well-known circle criterion by Sandberg [250] and Zames [288] is suitable for the unstructured case, but requires a strictly positive real linear part [149, pp. 264–265] and like most methods, depends crucially on the system formulation. In the following, we provide two different formulations of the zero dynamics of the TCS and show, that for TCSs, this has a direct impact on the applicability of passivity based methods, even though both versions describe the same dynamics. Following, we start with a direct formulation of the problem.

[1] The term "effectively" quadratic is used here to denote a piecewise quadratic function with switching point at 0. Generally, we say that $f : \mathbb{R} \to \mathbb{R}$ with $f(x) = cx^{n-1}|x|$ is effectively of order n, where $c \in \mathbb{R} \setminus \{0\}$ and $n \in \mathbb{N}$. For example, $F_w = (1/2)\rho c_w A_{st} v_x |v_x|$, as defined in (3.12), is effectively quadratic in v_x.

4.2 Passivity and Absolute Stability Analysis

4.2.1 Direct Lur'e Formulation

In order to analyze a system with the methods of absolute stability, it has to be put in Lur'e form, if possible. Since in general such a formulation is not unique, a successful analysis can crucially depend on the right formulation. This is also true for TCSs as will be shown in the following. We start with a direct formulation of the TCS zero dynamics (3.50) in Lur'e form, cf. [304]. It is called direct Lur'e formulation here, because of the two states entering the nonlinearity corresponding directly to the outputs by $y_1 = z_2$ and $y_2 = z_3$. The direct Lur'e form of the zero dynamics is then given by an LTI system, in feedback with a nonlinear, sector bounded function with $\boldsymbol{z}^T = \begin{bmatrix} z_1 & z_2 & z_3 \end{bmatrix}$, $\boldsymbol{u}^T = \begin{bmatrix} u_1 & u_2 \end{bmatrix}$, $\boldsymbol{y}^T = \begin{bmatrix} y_1 & y_2 \end{bmatrix}$ and

$$\dot{\boldsymbol{z}} = \boldsymbol{A}\boldsymbol{z} + \boldsymbol{B}\boldsymbol{u} = \begin{bmatrix} 0 & -1 & 0 \\ 2k_c/J_r & -2d_c/J_r & 0 \\ 0 & 0 & -b_c \end{bmatrix} \boldsymbol{z} + \begin{bmatrix} 0 & 0 \\ r_r/J_r & 0 \\ -1/m & 1/m \end{bmatrix} \boldsymbol{u} \tag{4.3a}$$

$$\boldsymbol{y} = \boldsymbol{C}\boldsymbol{z} = \begin{bmatrix} 0 & r_r & 0 \\ 0 & 0 & 1 \end{bmatrix} \boldsymbol{z} \tag{4.3b}$$

$$\boldsymbol{u} = -\boldsymbol{\psi}(\boldsymbol{y}) = -\begin{bmatrix} \psi_1(y_1, y_2, t) \\ \psi_2(y_2) \end{bmatrix} = -\begin{bmatrix} F_{xr} \\ F_w - m b_c z_3 \end{bmatrix} . \tag{4.3c}$$

Since the wheel slip is by definition a nonlinear function of the angular velocity of the wheel and the vehicle velocity, it cannot be used directly as an output of the linear part of the Lur'e system. To keep linearity in the forward channel, a MIMO formulation is necessary. The artificial parameter $b_c \geq 0$ was introduced in order to be able to make $\boldsymbol{A}$ Hurwitz and is canceled out by the $m b_c z_3$ term in the input $\boldsymbol{u}$, so (4.3) represents the zero dynamics (3.50). For $b_c \neq 0$, this corresponds to a loop transformation, compare for example [149, pp. 227–259]. Before we continue, some preliminary results are derived for the Lur'e system (4.3a)-(4.3c).

Lemma 14. *The system matrix $\boldsymbol{A}$ in (4.3a) is Hurwitz if and only if $b_c > 0$.*

Proof. The eigenvalues of the system matrix $\boldsymbol{A}$, as functions of the vehicle parameters, are given by $\lambda_1 = -b_c$ and $\lambda_{2,3} = -(d_c \pm \sqrt{d_c^2 - 2J_r k_c})/J_r$. Since all vehicle parameters are assumed to be strictly positive, $d_c > \Re(\sqrt{d_c^2 - 2J_r k_c})$ will always hold and so all eigenvalues are guaranteed to have strictly negative real part. □

This is expected, since for $b_c = 0$ both the last row and column of the $\boldsymbol{A}$ matrix in (4.3a) are zero, so feedback of z_3 via the loop transformation is required in order to stabilize the linear part. However, the LTI system is not passive even if $b_c > 0$ such that $\boldsymbol{A}$ is Hurwitz.

Lemma 15. *The linear part (4.3a)-(4.3b) of the zero dynamics is not passive.*

Proof. By the Kalman-Yakubovich-Popov Lemma, compare (2.27) and Definition 32, a stable LTI system as in (4.3a)-(4.3b) is positive real if and only if there exists $\boldsymbol{P} = \boldsymbol{P}^T \succeq 0$ such that

$$\boldsymbol{A}^T\boldsymbol{P} + \boldsymbol{P}\boldsymbol{A} \preceq 0 \tag{4.4a}$$

$$\boldsymbol{P}\boldsymbol{B} = \boldsymbol{C}^T . \tag{4.4b}$$

Assuming an arbitrary symmetric $\boldsymbol{P}$, from (4.4b) it is immediate that $P_{13} = P_{31} = P_{23} = P_{32} = 0$ must hold. Fixing these values in $\boldsymbol{P}$ gives the equations $P_{33}/m = 1$ and $P_{33}/m = 0$, which have no common solution. Therefore, the linear part of the zero dynamics is not positive real and thus not passive, independently of b_c. □

It can be further noted that the loop transformation by output feedback of $y_2 = z_3$ relies on an excess of passivity in the second channel of the nonlinearity $\boldsymbol{\psi}$. However, as discussed previously and indicated in Figure 4.1b, the aerodynamic drag F_w has no such excess of passivity.

Therefore it is expected that the nonlinearity will also fail to be passive for $b_c \neq 0$, which would already prevent us from making $\boldsymbol{A}$ Hurwitz. However, a less expectable result is that even for $b_c = 0$, meaning that no loop transformation is applied, the nonlinearity is not passive.

Lemma 16. *The nonlinearity (4.3c) of the zero dynamics is not passive for $b_c \geq 0$.*

Proof. First, consider the case that $b_c > 0$. For passivity, $\boldsymbol{y}^T\boldsymbol{\psi}(\boldsymbol{y}) \geq 0$ must hold. Define $k_2 = (1/2)\rho c_w A_{st}$ and $k_3 = mb_c$, then $\boldsymbol{y}^T\boldsymbol{\psi}(\boldsymbol{y}) = r_r F_{xr} z_2 + k_2|z_3|z_3^2 - k_3 z_3^2$. Assume that $z_2 = 0$ and that $z_3 \neq 0$. Then, the equation

$$k_2|z_3|z_3^2 - k_3 z_3^2 = 0 \tag{4.5}$$

has the solutions $z_3 = \pm k_3/k_2$. Therefore, $z_2 = 0$ and $|z_3| < k_3/k_2$ will result in $\boldsymbol{y}^T\boldsymbol{\psi}(\boldsymbol{y}) < 0$, no matter how small $b_c > 0$ is made.

Now consider the case that $b_c = 0$ with k_1, k_2 defined as before and assume that $z_3 > r_r z_2 > 0$ such that $\lambda_{xr} < 0$. Then, since for negative λ_{xr} by (4.2) we have $\underline{c}_{xr}\lambda_{xr} \geq F_{xr}$, cf. also Figure 4.1a, it follows that

$$r_r \underline{c}_{xr}\lambda_{xr} z_2 + k_2|z_3|z_3^2 \geq r_r F_{xr} z_2 + k_2|z_3|z_3^2 = \boldsymbol{y}^T\boldsymbol{\psi}(\boldsymbol{y}) \geq 0 \tag{4.6}$$

must hold. Take $z_3 = 2r_r z_2 > r_r z_2 > 0$ and $\lambda_{xr} = (r_r z_2 - z_3)/v_{nr}$ with $v_{nr} > 0$ by Lemma 5, which results in the necessary equivalent conditions

$$r_r \underline{c}_{xr}\lambda_{xr} z_2 + k_2|z_3|z_3^2 \geq 0 \tag{4.7a}$$

$$r_r \underline{c}_{xr}(r_r z_2 - z_3) z_2 + k_2 v_{nr}|z_3|z_3^2 \geq 0 \tag{4.7b}$$

$$-r_r^2 \underline{c}_{xr} z_2^2 + 8r_r^3 k_2 \widetilde{v}_{nr}|z_2|z_2^2 \geq 0 \tag{4.7c}$$

where $\widetilde{v}_{nr} = \max_\epsilon(|r_r z_2|_\epsilon, |2r_r z_2|_\epsilon) > 0$. Assume now that $0 < z_2 < 1/(2r_r)$, then $\widetilde{v}_{nr}$ can be bounded by a constant like $0 < \widetilde{v}_{nr} \leq v_c = \max_\epsilon(|1|_\epsilon, |1|_\epsilon)$. So, after dividing both sides of (4.7c) by $z_2^2 > 0$, this means that

$$-r_r^2 \underline{c}_{xr} + 8r_r^3 k_2 v_c|z_2| \geq 0 \tag{4.8}$$

must hold. However, for $0 < z_2 < \min\{1/(2r_r), \underline{c}_{xr}/(8r_r k_2 v_c)\}$, this is impossible. Therefore, the nonlinearity (4.3c) is not passive for $b_c \geq 0$. □

This is interesting, because by looking at Figure 4.1, one would expect passivity of $\boldsymbol{\psi}$. In this specific formulation however, both subsystems are not passive. Since neither the linear part, nor the nonlinear function of the Lur'e system is passive, no conclusion of stability can be drawn from the absolute stability and passivity based methods here. Also a standard loop transformation could not resolve this issue.

It is also worth noting that the Kalman conjecture does not apply here. It is well known that the conjecture holds for systems of order $n \leq 3$, see [16], and is false in the general case $n > 3$, due to a counterexample by Fitts [68]. Here, the zero dynamics are of order $n = 3$, however, the Kalman conjecture is not applicable for three reasons. First, the conjecture, as stated by Kalman and investigated in the literature, does only cover SISO LTI systems in feedback with a scalar, memoryless nonlinearity. Here, the linear part is a MIMO LTI system, in feedback with a vector-valued nonlinearity. Second, it is only applicable to autonomous systems, while F_{xr} is generally time-varying. Third, a necessary assumption imposed by the Kalman conjecture is that the derivative of the nonlinearity with respect to its input is restricted to give a linear gain for which the linear system is stable at every operating point. This makes the Kalman conjecture a special case of the Markus-Yamabe conjecture (MYC), see [190]. It is known, by explicit counterexamples [44], that this conjecture is wrong for systems of order $n > 2$ and true only for $n \leq 2$, see [67, 86, 96]. Moreover, it generally considers autonomous systems only. Therefore, it is also not applicable to the zero dynamics (3.50). In addition, we show next that the necessary condition of the systems linearization being locally stable at every operating point does not hold, and so neither the Kalman conjecture nor the MYC is applicable here anyway.

Theorem 5. *For any set of vehicle parameters, there exist operating points such that the Jacobian linearization of the zero dynamics (3.50) at these points is locally unstable.*

Proof. Let $\boldsymbol{f}(\boldsymbol{z}) = \boldsymbol{A}\boldsymbol{z} - \boldsymbol{B}\boldsymbol{\psi}(\boldsymbol{C}\boldsymbol{z})$ with $\boldsymbol{A}$, $\boldsymbol{B}$, $\boldsymbol{C}$ and $\boldsymbol{\psi}$ from (4.3a). Its Jacobian is

$$\boldsymbol{J}_{\boldsymbol{f},\boldsymbol{z}}(\boldsymbol{z}) = \begin{bmatrix} 0 & -1 & 0 \\ 2k_c/J_r & -(1/J_r)\big(2d_c + r_r\partial F_{xr}/(\partial z_2)\big) & -(r_r/J_r)\partial F_{xr}/(\partial z_3) \\ 0 & (1/m)\partial F_{xr}/(\partial z_2) & (1/m)\partial(F_{xr} - F_w)/(\partial z_3) \end{bmatrix}, \tag{4.9}$$

with characteristic polynomial $p_c(s) = \det(s\boldsymbol{I}_3 - \boldsymbol{J}_{\boldsymbol{f},\boldsymbol{z}}(\boldsymbol{z})) = s^3 + p_2 s^2 + p_1 s + p_0$ and coefficients

$$p_2 = 2d_c/J_r - \mathcal{F}(\boldsymbol{z})/m + (r_r/J_r)\partial F_{xr}/(\partial z_2) \tag{4.10a}$$

$$p_1 = 2k_c/J_r - \big(2d_c\mathcal{F}(\boldsymbol{z}) + r_r(\partial F_{xr}/(\partial z_2))(\partial F_w/(\partial z_3))\big)/(mJ_r) \tag{4.10b}$$

$$p_0 = -2k_c\mathcal{F}(\boldsymbol{z})/(mJ_r)\,, \tag{4.10c}$$

where $\mathcal{F}(\boldsymbol{z}) = \partial(F_{xr} - F_w)/(\partial z_3)$. If (4.9) is globally Hurwitz, then $\mathcal{F}(\boldsymbol{z}) < 0\,, \forall \boldsymbol{z} \in \mathbb{R}^3$ so that the coefficients of $p_c(s)$ all have the same sign. As mentioned in Remark 19, $z_3 = 0$ is a removable singularity of $\partial F_w/(\partial z_3)$ since $\lim_{z_3 \to 0} \partial F_w/(\partial z_3) = 0$, so for linearization at $z_3 = 0$ this term can be replaced with zero. Hence, (4.10c) requires that $\mathcal{F}_0(z_2) = \partial F_{xr}/(\partial z_3)|_{z_3=0} < 0$, with

$$\mathcal{F}_0(z_2) = \frac{-\mu F_{zr} C_r B_r \cos(C_r \arctan(-B_r \lambda_{xr,0}))}{v_{nr,0}(1 + B_r^2 \lambda_{xr,0}^2)}\,. \tag{4.11}$$

Here, $\lambda_{xr,0}$ and $v_{nr,0}$ denote (3.21) and (3.19) respectively, with $z_3 = v_x = 0$. Now assume $z_2 \neq 0$ since (4.9) is Hurwitz at the origin by Lemma 12. As $C_r \in (1,2)$, $B_r > \tan\big(\pi/(2C_r)\big)$, $\mu F_{zr} > 0$, see Section 3.2.1, and $v_{nr,0} > 0\,, \forall z_2 \in \mathbb{R}$, $\mathcal{F}_0(z_2) < 0$ requires $\cos(C_r \arctan(B_r \lambda_{xr,0})) > 0$. Take z_2 such that $\lambda_{xr,0} = \lambda_{xr}^* = (\lambda_{xr,\text{peak}}^+ + 1)/2$ with $\lambda_{xr,\text{peak}}^+$ from (3.14a). This is always possible because $0 < \lambda_{xr}^* < 1$ by Lemma 3. As $\lambda_{xr,0} = 0$ if $z_2 = 0$ and $\lim_{z_2 \to \infty} \lambda_{xr,0} = 1$, it follows by continuity of $\lambda_{xr,0}$ that $\exists z_2^* \in \mathbb{R} : \lambda_{xr,0} = \lambda_{xr}^*$. At $z_2 = z_2^*, z_3 = 0$, $z_1 \in \mathbb{R}$, $p_0 < 0$ and so for any vehicle parameters there exist operating points where (4.9) is locally unstable. □

Remark 30. *We proved Theorem 5 in [306] based on formulation (4.12) from Section 4.2.2. Here, we use (4.3) instead. The result is the same as the Jacobian does not change.*

Remark 31. *Theorem 5 holds for all $\epsilon > 0$. This condition can be relaxed to the case $\epsilon = 0$, which corresponds to using the traditional wheel slip (3.8) instead of the smoothed version (3.21). For $z_2 > 0$, $z_3 = 0 \Rightarrow \lambda_{xr}^* = 1$ for $\epsilon = 0$ so $\cos(C_r \arctan(B_r \lambda_{xr,0})) > 0$ cannot be satisfied.*

A physical interpretation of Theorem 5 is that (4.9) becomes unstable for operating points located to the right of the positive peak or to the left of the negative peak of the tire force curve. This is known for the 2-state model for TCSs [243] and ABSs [136], but not for the zero dynamics of the $\mathcal{M}_5$ model. Theorem 5 shows that this property also holds for the zero dynamics (3.50), despite the additional dissipative torsion spring, compared to the 2-state model. Moreover, operating points can exist such that (4.9) is unstable even if F_{xr} is assumed to be strictly monotone like $F_{xr} = c_{xr}\lambda_{xr}$ with $c_{xr} > 0$ by (3.10b) and $\mu = 1$. For example, using the vehicle parameters from Table 6.1, $\epsilon = 10^{-6}$ and $z_2 = -z_3 = 1$ with (3.10a) for F_{xr} we still get $p_0 < 0$. This even is the case for the traditional 2-state model (2.1), which admits an unstable Jacobian for the vehicle parameters from Table 6.1, $\epsilon = 10^{-6}$ and $z_2 = 5$, $z_1 = -1$ with $\mu = 1$ and the monotone (3.10a) for F_{xr}. In both cases, this remains true even if $\epsilon = 0$, which is only seemingly in contradiction to [243], because there it is assumed that z_2 and z_3 have the same sign when selecting an operating point for linearization (and a different definition for v_{nr} is used). However, this assumption is not valid for the question whether the Jacobian is globally Hurwitz, which by Theorem 5 has a negative answer.

In the following, we propose a different Lur'e formulation for the zero dynamics, which in contrast to the direct formulation (4.3) allows a passivity based analysis (3.50). Thereafter, this formulation is used in Section 4.3.1 to extend the stability results from Theorem 2.

4.2.2 Sign-Preserving Lur'e Formulation

The direct formulation failed to separate the linear and nonlinear part of the zero dynamics such that passivity based methods could readily be applied. However, it is possible to use a different formulation [304], with $\dot{\boldsymbol{z}} = \boldsymbol{A}\boldsymbol{z} + \boldsymbol{B}\boldsymbol{u}$, $\boldsymbol{y} = \boldsymbol{C}\boldsymbol{z}$, $\boldsymbol{u} = -\boldsymbol{\psi}(\boldsymbol{y})$, where

$$\boldsymbol{A} = \begin{bmatrix} 0 & -1 & 0 \\ 2k_c/J_r & -2d_c/J_r & 0 \\ 0 & 0 & 0 \end{bmatrix}, \boldsymbol{B} = \begin{bmatrix} 0 & 0 \\ r_r/J_r & 0 \\ -1/m & 1/m \end{bmatrix}, \boldsymbol{C} = \begin{bmatrix} 0 & r_r & -1 \\ 0 & 0 & 1 \end{bmatrix} \text{ and} \tag{4.12a}$$

$$\boldsymbol{\psi}(\boldsymbol{y}, t) = \begin{bmatrix} \psi_1(y_1, y_2, t) \\ \psi_2(y_2) \end{bmatrix} = \begin{bmatrix} F_{xr} \\ F_w \end{bmatrix}. \tag{4.12b}$$

Here, the relevant difference to the direct formulation is the $\boldsymbol{C}$ matrix, which has now $C_{13} = -1$ instead of zero. With this new formulation, it is not possible anymore to directly replace z_2, z_3 with y_1, y_2 in the nonlinear functions F_{xr}, F_w. However, they can be rewritten as

$$F_{xr} = \mu F_{zr} \sin(C_r \arctan(B_r \lambda_{xr})) \tag{4.13a}$$

$$\lambda_{xr} = y_1 / v_{nr} \tag{4.13b}$$

$$v_{nr} = \max_\epsilon(|y_1 + y_2|_\epsilon, |y_2|_\epsilon) \tag{4.13c}$$

$$F_w = (1/2)\rho c_w A_{st} y_2 |y_2| \,. \tag{4.13d}$$

This slightly different formulation results in a passive nonlinearity.

Lemma 17. *The nonlinearity (4.12b) with formulation (4.12a) and (4.13a)-(4.13d) is passive.*

Proof. Again, for passivity, $\boldsymbol{y}^T \boldsymbol{\psi}(\boldsymbol{y}) \geq 0$ must hold, so $v_{nr} \lambda_{xr} F_{xr} + y_2 F_w \geq 0$. By Lemma 5, $v_{nr} > 0$ and by Lemma 1 $\lambda_{xr} F_{xr} \geq 0$. Finally, $y_2 F_w = (1/2)\rho c_w A_{st} y_2^2 |y_2| \geq 0$, so the inequality follows. Also, $\boldsymbol{y}^T \boldsymbol{\psi}(\boldsymbol{y}) = 0 \iff y_1 = y_2 = 0$, so $\boldsymbol{y}^T \boldsymbol{\psi}(\boldsymbol{y})$ is positive definite in $\boldsymbol{y}$. □

Here, the main idea is that v_{nr} can be reconstructed by the fact that $r_r z_2 = y_1 + y_2$ as in (4.13c). So, y_1 has always the same sign as F_{xr}. Hence, we call this a sign preserving formulation. Another advantage of this formulation is it resulting in a positive real/passive linear part [304].

Lemma 18. *The linear system $\dot{\boldsymbol{z}} = \boldsymbol{A}\boldsymbol{z} + \boldsymbol{B}\boldsymbol{u}$, $\boldsymbol{y} = \boldsymbol{C}\boldsymbol{z}$ with $\boldsymbol{A}, \boldsymbol{B}, \boldsymbol{C}$ from (4.12a) is passive.*

Proof. Using again the Kalman-Yakubovich-Popov Lemma it is immediate that (4.4a)-(4.4b), using $\boldsymbol{A}, \boldsymbol{B}, \boldsymbol{C}$ from (4.12a), admit the unique solution $\boldsymbol{P} = \operatorname{diag}(2k_c, J_r, m) \succ 0$. □

This can be used to directly show some stability properties of the zero dynamics.

Lemma 19. *The zero dynamics are Lyapunov stable and for constant μ, asymptotically stable.*

Proof. Let $V_s(\boldsymbol{z}) = (1/2)\boldsymbol{z}^T \boldsymbol{P} \boldsymbol{z} \succ 0$ with $\boldsymbol{P} = \operatorname{diag}(2k_c, J_r, m)$. The time derivative is $\dot{V}_s(\boldsymbol{z}) = -2d_c z_2^2 - z_3 F_w - (r_r z_2 - z_3) F_{xr} = -2d_c z_2^2 - z_3 F_w - v_{nr} \lambda_{xr} F_{xr} \preceq 0$, so Lyapunov stability follows. For a constant friction coefficient μ, asymptotic stability follows by LaSalle's invariance principle because $\dot{V}_s(\boldsymbol{z}) = 0 \iff z_2 = z_3 = 0$ and $\dot{z}_2 = (2k_c/J_r) z_1 \neq 0$ if $z_1 \neq 0$. Therefore, only the zero solution can remain in the set $\{\boldsymbol{z} \in \mathbb{R}^3 : \dot{V}_s(\boldsymbol{z}) = 0\}$ and asymptotic stability follows. □

The finding is not particularly new, as Theorem 2 and Corollary 1 already showed that the zero dynamics are globally asymptotically stable, even for time-varying μ. This conclusion cannot be reached by Lemma 19, as LaSalle's invariance principle is limited to autonomous systems and Barbalat's Lemma would require additional assumptions like uniform continuity of the time-varying function μ. Nevertheless, this result is interesting for three reasons. First, the proof itself is significantly shorter and the derived Lyapunov function is less complicated than the one used in Theorem 2. Second, it shows that the zero dynamics admit a formulation suitable for passivity analysis. Third, this formulation can be combined with Theorem 2 to derive the even stronger guarantee of global exponential stability, which is shown in the following.

4.3 Extended Stability Results

4.3.1 Exponential Stability of the Zero Dynamics

In this section, focus is set on investigating exponential stability of the zero dynamics (3.50). For this purpose, it is shown how the results from Section 3.3.2 can be combined with the passivity analysis from Section 4.2 in order to show exponential stability and, at the same time, keeping the relevant coefficients simple. This section generalizes the results from our publication [304] from the specific Lyapunov function with $\gamma = 7/2$ to the class of Lyapunov functions presented in Section 3.3.2. First, we rewrite the time derivative of the Lyapunov function from Corollary 1 as follows

$$\dot{V}(\boldsymbol{z},t) = \dot{V}_a(\boldsymbol{z}) + \dot{V}_b(\boldsymbol{z},t) \tag{4.14a}$$

$$\dot{V}_a(\boldsymbol{z}) = -q_1(1-\eta_2)z_1^2 - q_2 z_2^2 - q_3 z_3^2|z_3| \tag{4.14b}$$

$$\dot{V}_b(\boldsymbol{z},t) = -q_4 v_{nr}\lambda_{xr}F_{xr} + q_5 z_1 F_{xr} - q_1\eta_2 z_1^2\,, \tag{4.14c}$$

where $\dot{V}$ depends on time because μ and hence F_{xr} is assumed to depend on time. Furthermore, $\eta_2 \in (0,1)$ is defined in (3.95) and $q_1, q_2, q_3, q_4, q_5 > 0$ are given by

$$q_1 = 2k_c/J_r \tag{4.15a}$$

$$q_2 = 2\gamma + (\bar{c}_{xr} d_c r_r^2)/(6k_c J_r\sqrt{\epsilon}) \tag{4.15b}$$

$$q_3 = \rho c_w A_{st}\big(\gamma/(2d_c) + 1/(4d_c) + \bar{c}_{xr} r_r^2/(24k_c J_r\sqrt{\epsilon})\big) \tag{4.15c}$$

$$q_4 = \gamma/d_c + 1/(2d_c) + \bar{c}_{xr} r_r^2/(12k_c J_r\sqrt{\epsilon}) \tag{4.15d}$$

$$q_5 = r_r/J_r\,. \tag{4.15e}$$

The main difficulty for showing exponential stability of the zero dynamics is that (4.14a) is effectively cubic in z_3 due to the $q_3 z_3^2|z_3|$ term, while the Lyapunov function (3.83) itself is quadratic in z_3. As indicated in (2.13), this prevents the direct conclusion that the zero dynamics are exponentially stable. Instead, we first combine the Lyapunov function obtained with passivity based methods $V_s(\boldsymbol{z}) = (1/2)(2k_c z_1^2 + J_r z_2^2 + m z_3^2)$ from the proof of Lemma 19 with the Lyapunov function V from (3.83) like

$$\mathcal{V}(\boldsymbol{z}) = V(\boldsymbol{z}) + V_s(\boldsymbol{z})\,. \tag{4.16}$$

This function is positive definite because both V and V_s are positive definite, so it qualifies as a Lyapunov function candidate. After some rearrangements, its time derivative along solutions of (3.50) can be written as

$$\dot{\mathcal{V}}(\boldsymbol{z},t) = \dot{\mathcal{V}}_1(\boldsymbol{z},t) + \dot{\mathcal{V}}_2(\boldsymbol{z},t) \tag{4.17a}$$

$$\dot{\mathcal{V}}_1(\boldsymbol{z},t) = -\widetilde{q}_1 z_1^2 - \widetilde{q}_2 z_2^2 - \widetilde{q}_3 z_3^2|z_3| - v_{nr}\lambda_{xr}F_{xr} \tag{4.17b}$$

$$\dot{\mathcal{V}}_2(\boldsymbol{z},t) = -q_2 z_2^2 - q_3 z_3^2|z_3| + \dot{V}_b(\boldsymbol{z},t)\,, \tag{4.17c}$$

where $\widetilde{q}_1 = q_1(1-\eta_2)$, $\widetilde{q}_2 = 2d_c$, $\widetilde{q}_3 = (1/2)\rho c_w A_{st}$. By Theorem 2 and Corollary 1, $\dot{V}_b(\boldsymbol{z},t) \leq 0$ and hence $\dot{\mathcal{V}}_2(\boldsymbol{z},t) \leq 0$. Therefore, in order to show exponential stability it is sufficient to show $\dot{\mathcal{V}}_1(\boldsymbol{z},t) \leq -W(\boldsymbol{z}) \prec 0$ for some $W(\boldsymbol{z}) = \alpha_1 z_1^2 + \alpha_2 z_2^2 + \alpha_3 z_3^2$ with $\alpha_1, \alpha_2, \alpha_3 > 0$. It can be noted that a W of this form cannot exist for all $\boldsymbol{z} \in \mathbb{R}^n$ if the last term in (4.17b) is omitted. This is due to the $\widetilde{q}_3 z_3^2|z_3|$ term being (effectively) cubic in z_3 and therefore it vanishes faster for $z_3 \to 0$ than any quadratic term. However, in the following it is shown how the $v_{nr}\lambda_{xr}F_{xr}$ term in (4.17a) and therefore also $\mathcal{V}_1$ can be used to construct an appropriate upper bound $W(\boldsymbol{z})$. It is already hinted by (4.17) that the separation into (4.17b) and (4.17c) is advantageous for the analysis of $\mathcal{V}_1$, as it avoids the more complicated coefficients q_2, q_3, q_4 in $\mathcal{V}_1$. The next result shows the existence of an appropriate upper bound $W(\boldsymbol{z})$ and thereby global exponential stability, also generalizing our results from [304] to the case $\gamma > 0$. After that, $W(\boldsymbol{z})$ is constructed explicitly as well.

Theorem 6. *The zero dynamics (3.50) of the 2WD $\mathcal{M}_5$ model (3.22) are globally exponentially stable for all vehicle parameters and bounded positive time-varying friction coefficients $\mu(t)$.*

Proof. From (4.17) it follows that $\mathcal{V}_1$ is unchanged compared to the case $\gamma = 7/2$, so the case $\gamma > 0$ follows from (4.17) in combination with our proof from [304], which is restated here. Since the tire force is bounded like $\underline{c}_x|\lambda_x| \leq |F_x|$ by (4.2), it follows that $\dot{\mathcal{V}}_1(\boldsymbol{z}, t) \leq -\dot{U}_1(\boldsymbol{z})$ with

$$\dot{U}_1(\boldsymbol{z}) = \widetilde{q}_1 z_1^2 + \widetilde{q}_2 z_2^2 + \widetilde{q}_3 z_3^2|z_3| + \underline{c}_x(r_r z_2 - z_3)^2/v_{nr}\,. \tag{4.18}$$

As $\underline{c}_x$ as given in (4.1) is constant, the function $\dot{U}_1(\boldsymbol{z})$ does not depend on time explicitly and it suffices to show that

$$\dot{U}_1(\boldsymbol{z}) \geq W(\boldsymbol{z}) = \alpha_1 z_1^2 + \alpha_2 z_2^2 + \alpha_3 z_3^2\,, \tag{4.19}$$

so $\alpha_1 \leq \widetilde{q}_1$ and $\alpha_2 \leq \widetilde{q}_2$ is a necessary condition. First, consider $z_1 \in \mathbb{R}$ and $(z_2, z_3) \in \mathbb{R}^2 \backslash (-1, 1)^2$. However, if $|z_3| \geq 1$ then $\widetilde{q}_3 z_3^2|z_3| \geq \alpha_3 z_3^2$ with $\alpha_3 \leq \widetilde{q}_3$. If $|z_3| < 1$, $|z_2| \geq 1$, it is required that

$$\widetilde{q}_2 z_2^2 + \widetilde{q}_3 z_3^2|z_3| \geq \alpha_2 z_2^2 + \alpha_3 z_3^2\,, \text{ hence it is necessary that} \tag{4.20a}$$

$$\widetilde{q}_2 z_2^2 \geq \alpha_2 z_2^2 + \alpha_3 z_3^2\,, \text{ as } \widetilde{q}_3 z_3^2|z_3| < \alpha_3 z_3^2 \text{ for } z_3 \to 0. \text{ So,} \tag{4.20b}$$

$$(\widetilde{q}_2 - \alpha_2) z_2^2 \geq \alpha_3 z_3^2\,, \text{ by rearranging and} \tag{4.20c}$$

$$(\widetilde{q}_2 - \alpha_2) \geq \alpha_3\,, \text{ to cover the "worst case", } |z_2| = |z_3| = 1. \tag{4.20d}$$

The step from (4.20a) to (4.20b) is required because the quadratic term cannot be compensated by the (effectively) cubic term for small z_3, so we ensure the inequality holds even without the $\widetilde{q}_3 z_3^2|z_3|$ term. Inequality (4.20d) follows by minimizing over $|z_2| \geq 1$ and maximizing over $|z_3| \leq 1$. This shows that (4.19) is true for $z_1 \in \mathbb{R}$ and $(z_2, z_3) \in \mathbb{R}^2 \setminus [-1, 1]^2$ if $\alpha_1 \leq \widetilde{q}_1$, $\alpha_2 + \alpha_3 \leq \widetilde{q}_2$ and $\alpha_3 \leq \widetilde{q}_3$. Now, the portion of the state space where $z_1 \in \mathbb{R}$ and $(z_2, z_3) \in [-1, 1]^2$ is considered. With z_2, z_3 constrained to this domain, $v_{nr} \leq \widetilde{v}_{nr} =$ constant. This step is similar to the proof of Lemma 16, just that here the constant upper bound is given by

$$\widetilde{v}_{nr} = \max_\epsilon(|r_r|_\epsilon, |1|_\epsilon)\,. \tag{4.21}$$

Define $\widetilde{q}_4 = \underline{c}_x/\widetilde{v}_n > 0$, then for $(z_2, z_3) \in [-1, 1]^2$ clearly $\dot{U}_1(\boldsymbol{z}) \geq \dot{U}_2(\boldsymbol{z})$ with

$$\dot{U}_2(\boldsymbol{z}) = \widetilde{q}_1 z_1^2 + \widetilde{q}_2 z_2^2 + \widetilde{q}_3 z_3^2|z_3| + \widetilde{q}_4(r_r z_2 - z_3)^2\,. \tag{4.22}$$

Hence, (4.19) holds if $\dot{U}_2(\boldsymbol{z}) \geq W(\boldsymbol{z})$ holds. It remains to show that $\delta\dot{U}_2(\boldsymbol{z}) = \dot{U}_2(\boldsymbol{z}) - W(\boldsymbol{z}) \succeq 0$. Rewrite $\delta\dot{U}_2(\boldsymbol{z})$ as

$$\delta\dot{U}_2(\boldsymbol{z}) = (\widetilde{q}_1 - \alpha_1) z_1^2 + \begin{bmatrix} z_2 & z_3 \end{bmatrix} \boldsymbol{Q} \begin{bmatrix} z_2 \\ z_3 \end{bmatrix} + \widetilde{q}_3 z_3^2|z_3|\,, \tag{4.23a}$$

$$\boldsymbol{Q} = \begin{bmatrix} \widetilde{q}_4 r_r^2 + (\widetilde{q}_2 - \alpha_2) & -\widetilde{q}_4 r_r \\ -\widetilde{q}_4 r_r & (\widetilde{q}_4 - \alpha_3) \end{bmatrix}. \tag{4.23b}$$

First, this requires $\alpha_1 \leq \widetilde{q}_1$ which was derived earlier already. The requirement $\delta\dot{U}_2(\boldsymbol{z}) \succeq 0$ can be ensured by choosing $\alpha_2, \alpha_3 > 0$ such that $\boldsymbol{Q}$ is positive definite. This is guaranteed if the leading principle minors of $\boldsymbol{Q}$ are positive, specifically

$$\Delta_1 = \widetilde{q}_4 r_r^2 + \widetilde{q}_2 - \alpha_2 > 0 \tag{4.24a}$$

$$\Delta_2 = \widetilde{q}_2\widetilde{q}_4 + \alpha_2\alpha_3 - \widetilde{q}_4\alpha_2 - \widetilde{q}_2\alpha_3 - \widetilde{q}_4 r_r^2\alpha_3 > 0\,. \tag{4.24b}$$

Since the condition $\alpha_2 \leq \widetilde{q}_2$ is already required by (4.20d) since $\alpha_3 > 0$, it is clear this also makes inequality (4.24a) true as well because $\widetilde{q}_4 r_r^2 > 0$. The second condition (4.24b) can be made true by taking $\alpha_2, \alpha_3 > 0$ small enough, because this makes $\Delta_2 \approx \widetilde{q}_2\widetilde{q}_4 > 0$ up to an arbitrary accuracy. This shows that there must always exist $\alpha_1, \alpha_2, \alpha_3 > 0$ such that $\boldsymbol{Q} \succ 0$ and at the same time $\alpha_1 \leq \widetilde{q}_1$, $\alpha_2 + \alpha_3 \leq \widetilde{q}_2$ and $\alpha_3 \leq \widetilde{q}_3$, which is true for all $\gamma > 0$. Therefore, the origin of zero dynamics is globally exponentially stable for all possible vehicle parameters and bounded positive time-varying friction coefficients of the road. □

While Theorem 6 guarantees existence of an appropriate quadratic function $W(\boldsymbol{z})$ such that $\dot{\mathcal{V}}(\boldsymbol{z},t) \leq -W(\boldsymbol{z}), \forall \boldsymbol{z} \in \mathbb{R}^3$ and with that proves global exponential stability of (3.50), it is also possible to construct an explicit $W(\boldsymbol{z})$ based on the derived conditions.

Corollary 2. *Let $\eta_2 \in (0,1)$ be given by (3.95), $\widetilde{v}_{nr} > 0$ by (4.21) and $c \in (0,1)$. Let $\alpha_1, \alpha_2, \alpha_3 > 0$ be given by*

$$\alpha_1 = 2(1-\eta_2)k_c/J_r \tag{4.25a}$$

$$\alpha_2 = d_c \tag{4.25b}$$

$$\alpha_3 = \min\{d_c, (1/2)\rho c_w A_{st}, c\, d_c/(d_c\widetilde{v}_{nr} + r_r^2)\}\,. \tag{4.25c}$$

Then, $W(\boldsymbol{z}) = \alpha_1 z_1^2 + \alpha_2 z_2^2 + \alpha_3 z_3^2$ satisfies $\dot{U}_2(\boldsymbol{z}) \geq W(\boldsymbol{z})$ with $\dot{U}_2$ from (4.22) and therefore also $\dot{\mathcal{V}}(\boldsymbol{z},t) \leq -W(\boldsymbol{z}), \forall \boldsymbol{z} \in \mathbb{R}^3$.

Proof. Since by assumption all vehicle parameters are strictly positive, $0 < \eta_2 < 1$ and $\widetilde{v}_{nr} > 0$, the condition that $\alpha_1, \alpha_2, \alpha_3 > 0$ is satisfied. From Theorem 6, there are four more conditions that need to be satisfied. First, $\alpha_1 \leq \widetilde{q}_1$ which is trivially true because by (4.25a) we have $\alpha_1 = \widetilde{q}_1$. Second, $\alpha_2 \leq \widetilde{q}_2$ is true because $\alpha_2 = d_c$ by (4.25b) and $\widetilde{q}_2 = 2d_c$. It can be noted that this condition is redundant as it is contained in the next condition. Third, $\alpha_2 + \alpha_3 \leq \widetilde{q}_2$ which is true since by (4.25b) $\alpha_2 = d_c$ and by (4.25c) $\alpha_3 \leq d_c$ so $\alpha_2 + \alpha_3 \leq 2d_c = \widetilde{q}_2$. Fourth, the condition $\widetilde{q}_2\widetilde{q}_4 + \alpha_2\alpha_3 - \widetilde{q}_4\alpha_2 - \widetilde{q}_2\alpha_3 - \widetilde{q}_4 r_r^2 \alpha_3 > 0$ is required. After inserting $\alpha_2 = d_c$ from (4.25b) and solving for α_3, this gives

$$\alpha_3 < \frac{d_c}{d_c\widetilde{v}_{nr} + r_r^2}\,. \tag{4.26}$$

Since this inequality is satisfied for any $c \in (0,1)$ by (4.25c) it follows that $W(\boldsymbol{z})$ is a valid upper bound for (4.17a) for all possible vehicle parameters and the assertion is proven. □

These results can readily be generalized to both 4WD cases considered previously.

Corollary 3. *The zero dynamics (3.63) of the 4WD $\mathcal{M}_7$ model (3.30) are globally exponentially stable for all vehicle parameters and bounded positive time-varying $\mu(t)$.*

Proof. Use again (4.16) as Lyapunov function and observe that its time derivative along solutions of the zero dynamics (3.63) can be written as $\dot{\mathcal{V}}_{\mathcal{M}_7}(\boldsymbol{z},t) = \dot{\mathcal{V}}(\boldsymbol{z},t) + \dot{V}_{\mathcal{M}_7}(\boldsymbol{z},t) - \dot{V}(\boldsymbol{z},t) + z_3 F_{xf,0}$ with $\dot{V}_{\mathcal{M}_7}$ given by (3.97), $F_{xf,0}$ by (3.64), $\dot{V}$ by (4.14a) and $\dot{\mathcal{V}}$ by (4.17). By the proof of Theorem 3 $z_3 F_{xf,0} \leq 0$ and $\dot{V}_{\mathcal{M}_7}(\boldsymbol{z},t) \leq \dot{V}(\boldsymbol{z},t)$ so $\dot{\mathcal{V}}_{\mathcal{M}_7}(\boldsymbol{z},t) \leq \dot{\mathcal{V}}(\boldsymbol{z},t) \leq -W(\boldsymbol{z})$ by Theorem 6. □

Corollary 4. *The zero dynamics (3.79) of the 4WD $\mathcal{M}_9$ model (3.36) are globally exponentially stable for all vehicle parameters and bounded positive time-varying $\mu(t)$.*

Proof. This follows from Lemma 13 and Theorem 6. A proof is given in the Appendix A.3. □

This shows that the zero dynamics of the $\mathcal{M}_5$ 2WD model and of both the $\mathcal{M}_7$ and $\mathcal{M}_9$ 4WD models are globally exponentially stable. It can be noted that the expression for α_3 in (4.25c) is very general in order to construct a function W that is valid for any combination of vehicle parameters. For practical parameters, commonly $(1/2)\rho c_w A_{st} < 1 < d_c$ and $r_r < 1$ such that $\widetilde{v}_{nr} \approx 1$ and $r_r^2 \approx 0$. Since $c \in (0,1)$ can be chosen arbitrarily close to 1 in order to get a guaranteed bound, it follows under the mentioned assumptions that the third argument in (4.25c) is close to 1 and for practical vehicle parameters we have $\alpha_3 = (1/2)\rho c_w A_{st}$. However, Equation (4.25c) also covers cases where these assumptions do not apply and hence provides a general formula which is valid for arbitrary positive vehicle parameters.

This concludes the investigation of exponential stability of the zero dynamics of the TCSs considered in this work. However, as mentioned in Section 2.2.3, this still allows no conclusion of the global stability of the overall closed loop system. A sufficient condition for showing this (with the limitations mentioned in Remark 29) is, that the internal dynamics of the system are input-to-state stable. This condition is analyzed in the next section.

4.3.2 Input-to-State Stability of the Internal Dynamics

In this subsection, focus is set on analyzing the internal dynamics of the proposed TCSs. While the zero dynamics assume that the states of the external dynamics entering the internal dynamics are identically zero, this is not the case anymore in the upcoming analysis. Here, the system outputs are treated as inputs to the internal dynamics, so ISS is required, cf. Section 2.2.3 and Appendix A.4. These inputs are bounded by the stability of the external dynamics—which are stabilized by the reference model and the PID controller—and because the target speeds are saturated by the DCU when close to the maximum speed. The internal dynamics of the 2WD $\mathcal{M}_5$ model (3.22) can be derived from (3.45) by defining $\boldsymbol{z}^T = \begin{bmatrix} z_1 & z_2 & z_3 \end{bmatrix} = \begin{bmatrix} \xi_3 & \xi_4 & \xi_5 \end{bmatrix}$, $\zeta_1 = \xi_1$ and

$$\dot{\boldsymbol{z}} = \begin{bmatrix} \dot{z}_1 \\ \dot{z}_2 \\ \dot{z}_3 \end{bmatrix} = \begin{bmatrix} -z_2 \\ \big(2(k_c z_1 - d_c z_2) - r_r F_{xr}\big)/J_r \\ (F_{xr} - F_w)/m \end{bmatrix} + \begin{bmatrix} 1 \\ 2d_c/J_r \\ 0 \end{bmatrix} \zeta_1 \,. \tag{4.27}$$

For $\zeta_1 = 0$, Equation (4.27) reduces to the zero dynamics (3.50) as expected. For $\zeta_1 \neq 0$, stability can still be guaranteed for any piecewise continuous bounded ζ_1 by the following result.

Theorem 7. *The internal dynamics (4.27) of the 2WD $\mathcal{M}_5$ model (3.22) are input-to-state stable for all vehicle parameters and bounded positive time-varying friction coefficients $\mu(t)$.*

Proof. The time derivative of (4.16) along solutions of (4.27) can be written as

$$\dot{\mathcal{V}}(\boldsymbol{z}, t, \zeta_1) = \dot{\mathcal{V}}(\boldsymbol{z}, t) + \boldsymbol{z}^T \boldsymbol{\ell} \zeta_1 \tag{4.28}$$

with $\boldsymbol{\ell}^T = \begin{bmatrix} \ell_1 & \ell_2 & 0 \end{bmatrix}$, $\ell_1 = 2(k_c + p_{11} - d_c/J_r)$, $\ell_2 = 2d_c(1 + 2p_{22}) - 1$, where p_{11} and p_{22} are given by (3.84a) and (3.84b), respectively. By Theorem 6 we know that

$$\dot{\mathcal{V}}(\boldsymbol{z}, t) \leq -W(\boldsymbol{z}) \leq -\underline{\alpha} \|\boldsymbol{z}\|_2^2 \,, \tag{4.29}$$

where $\underline{\alpha} = \min\{\alpha_1, \alpha_2, \alpha_3\} > 0$ is the smallest of the coefficients (4.25a)-(4.25c) and the second inequality in (4.29) follows from basic properties of quadratic forms, see also Section 2.2.1. The mixed term in (4.28) can be bounded like

$$\begin{aligned} \boldsymbol{z}^T \boldsymbol{\ell} \xi_1 &\leq |\boldsymbol{z}^T \boldsymbol{\ell} \zeta_1| && && \text{(4.30a)} \\ &\leq \|\boldsymbol{z}\|_2 \, \|\boldsymbol{\ell} \zeta_1\|_2 && \text{(by the Cauchy-Schwarz inequality)} && \text{(4.30b)} \\ &= \|\boldsymbol{z}\|_2 \, \|\boldsymbol{\ell}\|_2 \, |\zeta_1| \,. && \text{(by homogeneity of the 2-norm)} && \text{(4.30c)} \end{aligned}$$

Let $-\underline{\alpha}\|\boldsymbol{z}\|_2^2 = -\theta\underline{\alpha}\|\boldsymbol{z}\|_2^2 - (1-\theta)\underline{\alpha}\|\boldsymbol{z}\|_2^2$, with $\theta \in (0, 1)$. Then,

$$\dot{\mathcal{V}}(\boldsymbol{z}, t, \zeta_1) \leq -\theta\underline{\alpha}\|\boldsymbol{z}\|_2^2 \,, \forall \boldsymbol{z} \in \mathbb{R}^3 : \|\boldsymbol{z}\|_2 \geq \rho_{\mathcal{M}_5}(|\zeta_1|) = \frac{\|\boldsymbol{\ell}\|_2}{\underline{\alpha}(1-\theta)} |\zeta_1| \,, \tag{4.31}$$

where $\rho_{\mathcal{M}_5}$ is a class $\mathcal{K}$ function, so input-to-state stability of (4.27) follows. □

Remark 32. *Due to the bound $\dot{\mathcal{V}}(\boldsymbol{z}, t, \zeta_1) \leq -\underline{\alpha}\|\boldsymbol{z}\|_2^2 + \boldsymbol{z}^T\boldsymbol{\ell}\zeta_1$ that is obtained by combining (4.28) and (4.29) from Theorem 6, another way to show ISS of (4.27) is by considering the LTI system $\dot{\boldsymbol{z}} = -\boldsymbol{z} + \boldsymbol{b}\zeta_1$ with $\boldsymbol{b}^T = \begin{bmatrix} b_1 & b_2 & 0 \end{bmatrix}$, $b_1 = 2(k_c/\underline{\alpha} - d_c/(J_r\underline{\alpha}) + 1)$ and $b_2 = (4/J_r + 2/\underline{\alpha})d_c - 1/\underline{\alpha}$. Take $\boldsymbol{P} = (\underline{\alpha}/2)\boldsymbol{I}_3$ to construct the Lyapunov function $\boldsymbol{z}^T\boldsymbol{P}\boldsymbol{z}$. Since $\boldsymbol{A} = -\boldsymbol{I}_3$ is Hurwitz, the Lyapunov equation (2.18) has a unique solution for $\boldsymbol{Q} = -\underline{\alpha}\boldsymbol{I}_3$, which results in the time derivative $-\underline{\alpha}\|\boldsymbol{z}\|_2^2 + \boldsymbol{z}^T\boldsymbol{\ell}\zeta_1$. Observe that this is exactly the bound previously derived for $\dot{\mathcal{V}}(\boldsymbol{z}, t, \zeta_1)$. Since LTI systems with Hurwitz $\boldsymbol{A}$ matrix are always ISS, compare [125, pp. 43–46, p. 391], it follows that the bound $\dot{\mathcal{V}}(\boldsymbol{z}, t, \zeta_1) \leq -\underline{\alpha}\|\boldsymbol{z}\|_2^2 + \boldsymbol{z}^T\boldsymbol{\ell}\zeta_1$ must also satisfy the ISS conditions.*

It can be stressed that both methods from Theorem 7 and Remark 32 are based on the bound on $\dot{\mathcal{V}}(\boldsymbol{z}, t)$ derived by Theorem 6. Both approaches are basically equivalent, since after constructing the bound (4.29), bounding the mixed term is analogous to the LTI case. The corresponding LTI system is explicitly constructed in Remark 32, while Theorem 7 focuses on a direct derivation of the desired inequality. As a result, it follows that the internal dynamics (4.27) are ISS.

Again, these results can readily be extended to the 4WD case. First, consider the Byrnes-Isidori normal form (3.60) of the $\mathcal{M}_7$ model (3.30). Let $\boldsymbol{z}^T = \begin{bmatrix} z_1 & z_2 & z_3 \end{bmatrix} = \begin{bmatrix} \xi_3 & \xi_4 & \xi_5 \end{bmatrix}$ and $\boldsymbol{\zeta}^T = \begin{bmatrix} \zeta_1 & \zeta_2 \end{bmatrix} = \begin{bmatrix} \xi_1 & \xi_7 \end{bmatrix}$, then the internal dynamics are given by

$$\dot{\boldsymbol{z}} = \begin{bmatrix} \dot{z}_1 \\ \dot{z}_2 \\ \dot{z}_3 \end{bmatrix} = \begin{bmatrix} -z_2 \\ \big(2(k_c z_1 - d_c z_2) - r_r F_{xr}\big)/J_r \\ (F_{xr} - F_w)/m \end{bmatrix} + \begin{bmatrix} 1 \\ 2d_c/J_r \\ 0 \end{bmatrix} \zeta_1 + \begin{bmatrix} 0 \\ 0 \\ 1/m \end{bmatrix} F_{xf}\,, \tag{4.32}$$

where F_{xf} is a function of ζ_2 and z_3 since by (3.26), (3.28) and the change of coordinates (3.57), it depends on $\lambda_{xf} = (r_f\zeta_2 - z_3)/v_{nf}$ with $v_{nf} = \max_\epsilon(|r_f\zeta_2|_\epsilon, |z_3|_\epsilon)$. Since for $\zeta_2 = 0$, $F_{xf} = F_{xf,0}$ as defined in (3.64), it follows that (4.32) reduces to the zero dynamics (3.63) of the $\mathcal{M}_7$ model (3.30) for $\boldsymbol{\zeta} = \boldsymbol{0}_2$, as expected. Now, we are ready to state the next result.

Corollary 5. *The internal dynamics (4.32) of the 4WD $\mathcal{M}_7$ model (3.30) are ISS for all vehicle parameters and bounded positive time-varying friction coefficients $\mu(t)$.*

Proof. Use again the Lyapunov function (4.16). Its derivative along solutions of (4.32) satisfies

$$\dot{\mathcal{V}}_{\mathcal{M}_7}(\boldsymbol{z}, \boldsymbol{\zeta}, t) = \dot{\mathcal{V}}(\boldsymbol{z}, t) + \dot{V}_{\mathcal{M}_7}(\boldsymbol{z}, t) - \dot{V}(\boldsymbol{z}, t) + z_3 F_{xf,0} + \boldsymbol{z}^T\boldsymbol{\ell}\zeta_1 + \widetilde{p} z_3(F_{xf} - F_{xf,0}) \tag{4.33a}$$

$$\leq -\underline{\alpha}\|\boldsymbol{z}\|_2^2 + \boldsymbol{z}^T\boldsymbol{\ell}\zeta_1 + z_3 F_{xf,0} + \widetilde{p} z_3(F_{xf} - F_{xf,0})\,, \text{ by Theorem 7,} \tag{4.33b}$$

$$\leq -\underline{\alpha}\|\boldsymbol{z}\|_2^2 + \boldsymbol{z}^T\boldsymbol{L}\boldsymbol{u}_a \text{ since } z_3 F_{xf,0} \leq 0\text{, compare Theorem 3.} \tag{4.33c}$$

Here, $\dot{\mathcal{V}}$ is given by by (4.17), $\dot{V}_{\mathcal{M}_7}$ by (3.97), $\dot{V}$ by (4.14a), $F_{xf,0}$ by (3.64), $\widetilde{p} = 2p_{33}/m + 1 > 0$ with p_{33} from (3.84c), $\underline{\alpha}$ as defined in the proof of Theorem 7. Moreover, $\boldsymbol{\ell}^T = \begin{bmatrix} \ell_1 & \ell_2 & 0 \end{bmatrix}$ with $\ell_1 = 2(k_c + p_{11} - d_c/J_r)$ and $\ell_2 = 2d_c(1 + 2p_{22}/J_r) - 1$. Note that the ℓ_1 is the same as in the proof of Theorem 7, but ℓ_2 is different due to the extra division by J_r. Finally, define $u_{a,1} = \zeta_1$ and $u_{a,2} = F_{xf} - F_{xf,0}$ as auxiliary inputs with $\boldsymbol{u}_a^T = \begin{bmatrix} u_{a,1} & u_{a,2} \end{bmatrix}$ and

$$\boldsymbol{L} = \begin{bmatrix} L_{11} & 0 \\ L_{21} & 0 \\ 0 & L_{32} \end{bmatrix} = \begin{bmatrix} \ell_1 & 0 \\ \ell_2 & 0 \\ 0 & \widetilde{p} \end{bmatrix} = \begin{bmatrix} 2(k_c + p_{11} - d_c/J_r) & 0 \\ 2d_c(1 + 2p_{22}/J_r) - 1 & 0 \\ 0 & 2p_{33}/m + 1 \end{bmatrix}, \tag{4.34}$$

so (4.33c) follows. The first input $u_{a,1} = \zeta_1$ is bounded as it is generated by the stable external dynamics. The second, auxiliary input $u_{a,2} = F_{xf} - F_{xf,0}$ is bounded as the tire force is bounded by definition, so $|u_{a,2}| \leq 2\mu_{\max} F_{zf}$. Since $\boldsymbol{z}^T\boldsymbol{L}\boldsymbol{u}_a \leq \|\boldsymbol{z}\|_2 \|\boldsymbol{L}\|_F \|\boldsymbol{u}_a\|_2$, with $\theta \in (0, 1)$, we get

$$\dot{\mathcal{V}}_{\mathcal{M}_7}(\boldsymbol{z}, \boldsymbol{\zeta}, t) \leq -\theta\underline{\alpha}\|\boldsymbol{z}\|_2^2\,, \forall \boldsymbol{z} \in \mathbb{R}^3 : \|\boldsymbol{z}\|_2 \geq \rho_{\mathcal{M}_7}(\|\boldsymbol{u}_a\|_2) = \frac{\|\boldsymbol{L}\|_F}{\underline{\alpha}(1-\theta)}\|\boldsymbol{u}_a\|_2 \tag{4.35}$$

where $\rho_{\mathcal{M}_7}$ is a class $\mathcal{K}$ function, so input-to-state stability of (4.32) follows. □

Finally, input-to-state stability can also be shown for the third synthesis model of this work.

Corollary 6. *The internal dynamics of the 4WD $\mathcal{M}_9$ model (3.36) are ISS.*

Proof. The proof is analogous to the proof of Theorem 7 and is included in the Appendix A.3. □

A proof for a similar system to the one considered in Corollary 6 has been proposed recently by our colleague Degel *et al.* [58]. In their work on a scalable TCS for an electric vehicle with four in-wheel motors, similar internal dynamics arise although the control laws are different compared to the control laws (3.67) and (3.70) of the 4WD torque bias systems from this work. The analysis in [58] is not based on the exponential stability of the zero dynamics, which was, for the zero dynamics of the $\mathcal{M}_9$ model, first shown in this work. Instead, they derive the required inequalities directly using a variant of the parametric Lyapunov function (3.83) from [305], however with an additional linear friction term in the synthesis model.

This concludes the stability analysis of the three synthesis models considered in this work. Following, it is shown how the stability analysis of the zero dynamics of the 2WD TCS leads to an interesting special case of the Markus-Yamabe conjecture and a new open problem.

4.4 A Special Case of the Markus-Yamabe Conjecture

4.4.1 Stability Conjectures by Aizerman, Kalman and Markus-Yamabe

In this section, which is mainly based on our work in [306], it is investigated how the zero dynamics of the proposed 2WD traction control system relate to some of the well known stability conjectures in the field: the Aizerman conjecture, the Kalman conjecture and the Markus-Yamabe conjecture. First, some historical background is given in this subsection. Thereafter, the relation to traction control is derived and how a given system can be analyzed efficiently with the framework of ridge functions and principal Hessian directions. The result of this analysis leads to a new stability conjecture, that is located on the frontier "between" the Kalman conjecture and the Markus-Yamabe conjecture.

Recalling the sector bounded nonlinearity from Figure 2.7a, it is visible that such a nonlinear function is bounded from above and below by linear functions. It is therefore natural to ask whether a Lur'e system with a sector bounded nonlinearity is always globally asymptotically stable if the system is stable for every linear gain in the sector. This would significantly simplify the analysis of such systems, as it would render the nonlinear stability problem into a family of linear stability problems that could then be approached with the Routh-Hurwitz criterion [246, 118] or the Nyquist criterion [213] for example. This question was first asked by Aizerman, who formulated the following conjecture. The notation used here is defined in Section 2.2.2.

Aizerman Conjecture [5]. *Given a Lur'e system (2.26) with $p = m = 1$ and $D = 0$, such that the linear system obtained by taking $\psi(y) = ky$ is stable for all $k \in [\underline{k}, \bar{k}]$. Then, the system is globally asymptotically stable for all time-invariant $\psi : \mathbb{R} \to \mathbb{R}$ with $\psi \in \sec[\underline{k}, \bar{k}]$.*

Initially, the conjecture was formulated for open intervals. Krasovskiy disproved this initial version of the conjecture with a planar ($n = 2$) counterexample, so the condition was strengthened to closed intervals. Early works considering the planar case are due to Krasovskiy, Yerugin and Malkin, compare [230, pp. 3–6] and [169, pp. 271–277], who showed that the conjecture with closed intervals is true for systems of order $n \leq 2$, see also [22, 33]. The conjecture was disproven for $n > 2$ by Pliss who also constructed an explicit third order counterexample [230], see also the remarks in [59]. It can be noted that the Aizerman conjecture is true if complex dynamics instead of dynamics of real-valued maps are considered [134]. However, in this work focus is set on dynamics of real-valued maps only.

Another well known stability conjecture is the Kalman conjecture. It is more restrictive than the Aizerman conjecture, as it requires the nonlinearity not only to be sector bounded, but also to be slope restricted, see also Definition 28. When looking at Figure 2.7a again, one can see that even if the nonlinearity is bounded between two linear gain functions, it might locally have a gain that is not contained in the sector. So locally the linearization might be unstable under the conditions of the Aizerman conjecture. The Kalman conjecture excludes this possibility.

Kalman Conjecture [143]. *Given a Lur'e system (2.26) with $p = m = 1$ and $D = 0$, such that the linear system obtained by taking $\psi(y) = ky$ is stable for all $k \in [0, \bar{k}]$. Then, the system is globally asymptotically stable for all time-invariant $\psi : \mathbb{R} \to \mathbb{R}$ with $\partial\psi \in \sec[0, \bar{k}]$.*

Barabanov showed that this conjecture is true for systems up to an order of $n = 3$, see [16]. However, it was disproven for $n \geq 4$ by Fitts, who constructed an explicit fourth order counterexample [68]. The idea to impose requirements on the local stability of a nonlinear system is not limited to Lur'e systems, but can be applied to general nonlinear systems with differentiable vector field. Therefore, the Kalman conjecture can be considered as a special case of the more general MYC. Although the original paper gave credit to Aizerman [5] for this question, it was first formulated explicitly by Markus and Yamabe in 1960, see also [197] for a historical overview and several example systems in the context of the conjecture.

The Markus-Yamabe conjecture on global asymptotic stability can be restated as follows.

Markus-Yamabe Conjecture [190]. *Given a C^1 vector field $\boldsymbol{f} : \mathbb{R}^n \to \mathbb{R}^n$ with $\boldsymbol{f}(\mathbf{0}_n) = \mathbf{0}_n$. Assume that its Jacobian at point $\boldsymbol{x}^*$, given by $\boldsymbol{J}_{\boldsymbol{f},\boldsymbol{x}}(\boldsymbol{x}^*)$, cf. (2.24), is Hurwitz for all $\boldsymbol{x}^* \in \mathbb{R}^n$. Then, the origin is a globally asymptotically stable equilibrium of the system $\dot{\boldsymbol{x}} = \boldsymbol{f}(\boldsymbol{x})$. A system that satisfies these conditions is also called a Markus-Yamabe system.*

The Markus-Yamabe conjecture is true for $n = 1$ as can be readily shown with the Lyapunov function $V(x) = (1/2)x^2$ as follows: a scalar system $\dot{x} = f(x)$ with $f : \mathbb{R} \to \mathbb{R}$, $f(0) = 0$ and $f \in C^1$ that satisfies these conditions must have a Jacobian $J_{f,x}(x) = \mathrm{d}f(x)/(\mathrm{d}x) < 0\,, \forall x \in \mathbb{R}$. Since $J_{f,x}(x)$ in the scalar case is just the derivative of $f(x)$, it follows that f must be strictly decreasing to satisfy the conditions of the Markus-Yamabe conjecture. Because $f(0) = 0$, it is clear that f cannot enter the first and third quadrant. Therefore, $xf(x) < 0$ for $x \neq 0$ and so $\dot{V}(x) = xf(x) \prec 0$. The proof for $n = 2$ is significantly more difficult. Nevertheless, the Markus-Yamabe conjecture was proven for $n = 2$ independently by Fessler [67], Gutiérrez [96] and Glutsuk [86]. For $n \geq 3$, the conjecture is false as Cima *et al.* [44] constructed a polynomial counterexample, which for $n = 3$ is given by

$$\dot{x}_1 = -x_1 + x_3(x_1 + x_2x_3)^2 \tag{4.36a}$$

$$\dot{x}_2 = -x_2 - (x_1 + x_2x_3)^2 \tag{4.36b}$$

$$\dot{x}_3 = -x_3\,. \tag{4.36c}$$

The Jacobian of (4.36) has all its three eigenvalues located at -1, for all operating points $\boldsymbol{x}^* \in \mathbb{R}^3$ and therefore satisfies the conditions of the Markus-Yamabe conjecture. However, it admits the exponentially diverging solution $x_1(t) = 18\exp(t)$, $x_2(t) = -12\exp(2t)$, $x_3(t) = \exp(-t)$, see [44]. For $n > 3$, it is sufficient to add as many equations of the form $\dot{x}_i = -x_i$, $i \geq 4$ as desired [44]. The system (4.36) is a special case of the more general family of polynomial counterexamples proposed by Cima *et al.* in [45]. More polynomial counterexamples were found subsequently by Castañeda and Guíñez [35, 92], as well as non-polynomial ones [87].

While the mentioned counterexamples demonstrate that neither of the three stability conjectures is true in the general case, they can still be used for systems up to the order of validity of each conjecture. An interesting aspect is that the Kalman conjecture, which can be considered as a special case of the Markus-Yamabe conjecture, is valid for $n \leq 3$, while the Markus-Yamabe conjecture itself is only valid for $n \leq 2$. This is not surprising, since the Kalman conjecture is more restrictive than the Markus-Yamabe conjecture, as the former requires the rather special Lur'e system structure (2.26) while the latter makes no such restriction. With respect to the system order, there is a clear boundary between applicability of each conjecture. However, if we restrict the considered system class to MIMO Lur'e systems, it is not so clear anymore which system classes of order $n = 3$ can still be covered by these conjectures. The Kalman conjecture covers the SISO case for $n = 3$ as shown in [16], but the proof methods based on multipliers can not be readily extended to a general MIMO setting as they require additional assumptions, cf. [248]. The counterexample (4.36) disproves the MIMO case with $n = 3$ and $p = m = 3$. For $n > 3$, the situation is clear because even the SISO case is known to be false in general, see for example [197]. For $n < 3$, the MIMO case is covered by the already mentioned proofs of the Markus-Yamabe conjecture for planar vector fields. For the case $n = 3$ and $p = m = 2$ however, it is not clear whether it is disproven by one of the existing counterexamples. This case is of particular interest since the zero dynamics of the proposed TCS can be described by a Lur'e system with $n = 3$ and $p = m = 2$, see (4.12).

It is not immediately obvious whether the counterexample (4.36) or other counterexamples can be reused to disprove this case as well and not only the case $n = p = m = 3$. In the following we show that the established theory of ridge functions and principal Hessian directions can be used to answer such questions conveniently.

4.4.2 Ridge Functions and Principal Hessian Directions

The term ridge function was first introduced by Logan and Shepp in their work on computed tomography [180]. Another earlier name for ridge functions is "plane waves", compare [225]. Ridge functions and their generalizations are defined as follows.

Definition 42. *(Generalized ridge function) [226, p. 1] Given a function $r : \mathbb{R}^n \to \mathbb{R}$ and assume there exists $\boldsymbol{C} \in \mathbb{R}^{m\times n}$ with $1 \leq m < n$ and a function $q : \mathbb{R}^m \to \mathbb{R}$ such that*

$$r(\boldsymbol{x}) = q(\boldsymbol{C}\boldsymbol{x}) \,, \forall \boldsymbol{x} \in \mathbb{R}^n \,. \tag{4.37}$$

If $m = 1$ then r is called ridge function. If $m > 1$, then r is called a generalized ridge function.

In this work, we use the term ridge functions for $m \geq 1$. Ridge functions are commonly used for function approximation, which can be achieved by linear combinations like

$$\hat{r}(\boldsymbol{x}) \approx r(\boldsymbol{x}) = \sum_{i=1}^{N} q_i(\boldsymbol{C}_i\boldsymbol{x}) \tag{4.38}$$

where $\hat{r}$ is the function to be approximated. For $m = 1$, this is also known as projection pursuit regression, which can reduce the dimension of the input space significantly. Other applications of ridge functions include artificial neural networks, hyperbolic partial differential equations with constant coefficients or multivariate Fourier series, see [225] and [226, pp. 1–5].

As can be seen from the Definition (4.37), ridge functions essentially have the same form as a time-invariant nonlinearity of a Lur'e system (2.26), assuming the feed-through matrix is zero. For the analysis here, it is of interest whether the counterexample (4.36) can be reformulated in a MIMO Lur'e form to disprove the case $n = 3$, $p = m = 2$. For $n = p = 3$, $m = 2$, this is trivially possible by $\boldsymbol{C} = \boldsymbol{I}_3$, $\boldsymbol{\psi}(\boldsymbol{y})^T = \begin{bmatrix}\psi_1(\boldsymbol{y}) & \psi_2(\boldsymbol{y})\end{bmatrix}$ with $\psi_1(\boldsymbol{y}) = -y_3(y_1+y_2y_3)^2$, $\psi_2(\boldsymbol{y}) = (y_1+y_2y_3)^2$ and

$$\boldsymbol{A} = \begin{bmatrix}-1 & 0 & 0\\ 0 & -1 & 0\\ 0 & 0 & -1\end{bmatrix}, \boldsymbol{B} = \begin{bmatrix}1 & 0\\ 0 & 1\\ 0 & 0\end{bmatrix} \,. \tag{4.39}$$

This is not a standard Lur'e system since $p \neq m$, so the transfer function of the linear part is non-square. However, it could be made square by partitioning a fraction of the third equation into the nonlinearity and modifying $\boldsymbol{A}$ and $\boldsymbol{B}$ accordingly. Hence, (4.36) disproves the Markus-Yamabe conjecture for MIMO Lur'e systems with $n \geq 3$, $n \geq p \geq 3$ and $m \geq 2$. However, it is not directly clear if it also covers the case $n = 3$, $p = m = 2$. If this would be the case, there would exist $\boldsymbol{C}' \in \mathbb{R}^{2\times 3}$ and $\boldsymbol{\varphi} : \mathbb{R}^2 \to \mathbb{R}^2$ such that $\boldsymbol{\psi}(\boldsymbol{x}) = \boldsymbol{\varphi}(\boldsymbol{C}'\boldsymbol{x}) \,, \forall \boldsymbol{x} \in \mathbb{R}^3$. Note that here $\boldsymbol{y} = \boldsymbol{C}\boldsymbol{x} = \boldsymbol{x}$. The problem of proving existence of such a $\boldsymbol{\varphi}$ and $\boldsymbol{C}'$ is known as the ridge recovery problem, which has been addressed for $m = 1$ by Buhmann and Pinkus [26] and for $m \geq 1$ by Pinkus, who also proposed two methods for the analysis [226, pp. 34–35]. We focus on the second method, which is based on the analysis of the Hessian of a function, an approach very similar to the so-called principal Hessian directions for dimension reduction by Li [175]. Given $r : \mathbb{R}^n \to \mathbb{R}$ with $r \in C^2$ and Hessian $\boldsymbol{H}_r$ evaluated at $\boldsymbol{x} \in \mathbb{R}^n$ by

$$\boldsymbol{H}_r(\boldsymbol{x}) \stackrel{\text{def}}{=} \begin{bmatrix}\partial^2 r(\boldsymbol{x})/(\partial x_1\partial x_1) & \partial^2 r(\boldsymbol{x})/(\partial x_1\partial x_2) & \dots & \partial^2 r(\boldsymbol{x})/(\partial x_1\partial x_n)\\ \partial^2 r(\boldsymbol{x})/(\partial x_2\partial x_1) & \partial^2 r(\boldsymbol{x})/(\partial x_2\partial x_2) & \dots & \partial^2 r(\boldsymbol{x})/(\partial x_2\partial x_n)\\ \vdots & \vdots & \ddots & \vdots\\ \partial^2 r(\boldsymbol{x})/(\partial x_n\partial x_1) & \partial^2 r(\boldsymbol{x})/(\partial x_n\partial x_2) & \dots & \partial^2 r(\boldsymbol{x})/(\partial x_n\partial x_n)\end{bmatrix} \,. \tag{4.40}$$

If $\exists \boldsymbol{x} \in \mathbb{R}^n$ such that $\det\left(\boldsymbol{H}_r(\boldsymbol{x})\right) \neq 0$ then there cannot exist $\boldsymbol{C} \in \mathbb{R}^{m\times n}$ with $m < n$ and $q : \mathbb{R}^m \to \mathbb{R}$ such that $r(\boldsymbol{x}) = q(\boldsymbol{C}\boldsymbol{x}) \,, \forall \boldsymbol{x} \in \mathbb{R}^n$. Pinkus also proposed a method for functions that are only C^1 [226, pp. 34–35], but as the functions analyzed in the following are C^2, we focus on the Hessian based method, which we use in the following to further analyze (4.36).

4.4.3 Results and a New Open Problem

The zero dynamics of the proposed TCS can be expressed as the Lur'e system (4.12), which has an order of $n = 3$ and two inputs and outputs, so $p = m = 2$. Although Theorem 5 showed that the zero dynamics generally do not satisfy the conditions of the Markus-Yamabe conjecture, it is still interesting if the existing counterexamples also cover the special case of a Lur'e system with $n = 3$ and $p = m = 2$. This is not obvious at first glance, since a reformulation of (4.36) into an appropriate Lur'e form might exist. However, using the framework of ridge functions, it can readily be shown that this is not possible and so the counterexample cannot be reused to disprove the Markus-Yamabe conjecture for Lur'e systems with $n = 3$ and $p = m = 2$. First, we show how the Hessian method can be used to derive a lower bound for the output dimension of a given Lur'e system. The following results are from our publication [306].

Theorem 8. *Let $\dot{\boldsymbol{x}} = \boldsymbol{f}(\boldsymbol{x})$ with $\boldsymbol{f} : \mathbb{R}^n \to \mathbb{R}^n$, $\boldsymbol{f}(\boldsymbol{0}_n) = \boldsymbol{0}_n$, $\boldsymbol{x} \in \mathbb{R}^n$ and $f_i \in C^2, \forall i = 1, \ldots, n$. Then, rewriting this system in Lur'e form requires at least p outputs where*

$$p \geq \max \quad \operatorname{rank}\big(\boldsymbol{H}_{f_i}(\boldsymbol{x}_o)\big) \tag{4.41a}$$

$$\text{over} \quad \boldsymbol{x}_o \in \mathbb{R}^n \text{ and } i \in \{1, \ldots, n\} \tag{4.41b}$$

and $\boldsymbol{H}_{f_i}(\boldsymbol{x}_o)$ denotes the Hessian matrix of f_i at $\boldsymbol{x}_o$ as defined in (4.40).

Proof. Since $\boldsymbol{f}$ must be of Lur'e form, $\boldsymbol{f}(\boldsymbol{x}) = \boldsymbol{A}\boldsymbol{x} - \boldsymbol{B}\boldsymbol{\psi}(\boldsymbol{C}\boldsymbol{x})$ must be satisfied with $\boldsymbol{A} \in \mathbb{R}^{n\times n}$, $\boldsymbol{B}^{n\times m}$ and $\boldsymbol{C} \in \mathbb{R}^{p\times n}$. Without loss of generality, assume $\boldsymbol{\psi} : \mathbb{R}^p \to \mathbb{R}^m$ contains no linear terms as these can be partitioned into the $\boldsymbol{A}\boldsymbol{x}$ term. Following, define $\boldsymbol{r}(\boldsymbol{x}) = \boldsymbol{B}\boldsymbol{\psi}(\boldsymbol{C}\boldsymbol{x})$ where $B_{ij} = 1$ if $f_i(\boldsymbol{x})$ is nonlinear with nonlinear part $-\psi_j(\boldsymbol{C}\boldsymbol{x})$, $B_{ij} = 0$ otherwise and $m \leq n$ the number of nonlinear $f_i(\boldsymbol{x})$. By the Hessian method, see [226, pp. 32–33] and [26, 175], it follows that $\exists \boldsymbol{x}_o \in \mathbb{R}^n : \operatorname{rank}\big(\boldsymbol{H}_{r_i}(\boldsymbol{x}_o)\big) = p_j$ if r_i is of the form (4.37). Adding linear terms to r_j does not change the Hessian [175], therefore $\operatorname{rank}\big(\boldsymbol{H}_{f_i}(\boldsymbol{x}_o)\big) = \operatorname{rank}\big(\boldsymbol{H}_{r_i}(\boldsymbol{x}_o)\big)$. Testing each $f_i(\boldsymbol{x})$ like this gives (4.41) as lower bound [306]. □

Remark 33. *In general, the lower bound (4.41) from Theorem 8 can be very conservative. For example, consider $\boldsymbol{f} : \mathbb{R}^n \to \mathbb{R}^n$ with $\boldsymbol{f}(\boldsymbol{x})^T = \begin{bmatrix} f_1(\boldsymbol{x}) & f_2(\boldsymbol{x}) & \ldots & f_n(\boldsymbol{x}) \end{bmatrix} = \begin{bmatrix} x_1^2 & x_2^2 & \ldots & x_n^2 \end{bmatrix}$. For $x_1, x_2, \ldots, x_n \neq 0$ we have $\operatorname{rank}\big(\boldsymbol{H}_{f_1}(\boldsymbol{x})\big) = \operatorname{rank}\big(\boldsymbol{H}_{f_2}(\boldsymbol{x})\big) = \cdots = \operatorname{rank}\big(\boldsymbol{H}_{f_n}(\boldsymbol{x})\big) = 1$. Following, $\operatorname{rank}\big(\boldsymbol{H}_{f_i}(\boldsymbol{x})\big) = 0 \iff x_i = 0$, so the maximum achievable rank over all $\boldsymbol{x} \in \mathbb{R}^n$ and over all $i \in \{1, \ldots, n\}$ is 1. Hence, by Theorem 8, a lower bound for the required number of outputs is $p \geq 1$. However, in this particular case the number of actually required outputs is of course $p = n$ because all x_i are required individually to construct the functions f_i. Generally, computing instead $\operatorname{rank}\big(\boldsymbol{H}_g(\boldsymbol{x})\big)$ with $g(\boldsymbol{x}) = \sum_{i=1}^n f_i(\boldsymbol{x})$ does not circumvent this limitation, as different terms could be canceled out when forming the sum of arbitrary $f_i(\boldsymbol{x})$.*

Although the difference between the lower bound (4.41) and the actual number of outputs can be maximal, namely up to $n - 1$ as mentioned in Remark 33, this limitation is not problematic here. This is because we are only interested in the question whether the number of outputs can be reduced from $n = 3$ to $n - 1 = 2$. For example, considering the family of counterexamples to the MYC by Cima *et al.* [45], given by

$$\dot{z}_1 = -cz_1 - bz_3^m(az_1z_3^\ell + bz_2z_3^m)^k \tag{4.42a}$$

$$\dot{z}_2 = -cz_2 + az_3^\ell(az_1z_3^\ell + bz_2z_3^m)^k \tag{4.42b}$$

$$\dot{z}_3 = -cz_3\,. \tag{4.42c}$$

Here, $c \in \mathbb{R}^+$, $a, b \in \mathbb{R} \setminus \{0\}$, k is even and $\ell, k, \ell - m \in \mathbb{N}$ unequal to zero, see also [92]. For $a = b = c = \ell = 1$, $k = 2$ and $m = 0$, the system (4.42) reduces to (4.36) after an application of the linear state transformation $z_1 = x_2$, $z_2 = x_1$, $z_3 = x_3$. Using Theorem 8, we can test whether the system (4.42) can be expressed in Lur'e form with $p = 2$ outputs.

Corollary 7. *The family of counterexamples (4.42) by Cima et al. [45] to the MYC cannot be rewritten as a Lur'e system with $p < 3$.*

Proof. If (4.42) could be written as a Lur'e system (2.26) with $p = 2$ then there exists $\varphi_1 : \mathbb{R}^2 \to \mathbb{R}$ and $\boldsymbol{C}' \in \mathbb{R}^{2\times 3}$ such that $\psi_1(\boldsymbol{z}) = -bz_3^m(az_1z_3^\ell + bz_2z_3^m)^k = \varphi_1(\boldsymbol{C}'\boldsymbol{z})\,, \forall \boldsymbol{z} \in \mathbb{R}^3$. At the operating point $\boldsymbol{z}_o^T = \begin{bmatrix}1 & 0 & 1\end{bmatrix}$ however we have

$$\det\left(\boldsymbol{H}_{\psi_1}(\boldsymbol{z}_o)\right) = a^{3k-2}b^5k^3(\ell-m)^2(k-1)\,. \tag{4.43}$$

Since $ab \neq 0$, $k \geq 2$ and $\ell - m > 0$ by assumption, the determinant is different from zero at $\boldsymbol{z}_o$ and so the result follows for all instances of (4.42) by Theorem 8, cf. [306]. □

As can be seen from the proof of Corollary 7, the analysis based on ridge functions can answer questions regarding the required output dimension of a given Lur'e system. Given an arbitrary Lur'e system, it might be challenging to analyze the rank of the Hessian matrix as finding a suitable operating point might be difficult. In such cases, a numerical search by drawing random operating points and numerically evaluating the resulting Hessian matrix might be useful. For the system (4.42) this was not required. While Theorem 8 provides a tool for analyzing the output dimension of a given Lur'e system, we also propose a method for analyzing the input dimension with the following result.

Theorem 9. *Given a Lur'e system (2.26) with m inputs, reducible at most to $m' < m \leq n$. Then, $\boldsymbol{B}\boldsymbol{\psi}(\boldsymbol{y}) = \boldsymbol{B}'\boldsymbol{\varphi}(\boldsymbol{y})$ can be tested by solving a system of $N = (n-m')m'$ linear equations.*

Proof. If $m' < m$ is possible there exist functions $\varphi_i : \mathbb{R}^{m'} \to \mathbb{R}$, $i \in \{1, \ldots, m'\}$ and $\boldsymbol{B}' \in \mathbb{R}^{n\times m'}$ such that

$$\boldsymbol{B}'\boldsymbol{\varphi}(\boldsymbol{y}) = \boldsymbol{r}(\boldsymbol{y})\,, \forall \boldsymbol{y} \in \mathbb{R}^p \text{ with } \boldsymbol{r}(\boldsymbol{y}) = \boldsymbol{B}\boldsymbol{\psi}(\boldsymbol{y})\,. \tag{4.44}$$

Construct $\boldsymbol{B}_1' \in \mathbb{R}^{m'\times m'}$ from linear independent rows and $\boldsymbol{B}_2' \in \mathbb{R}^{n-m'\times m'}$ from the remaining rows of $\boldsymbol{B}'$ (so $\boldsymbol{B}'$ has full column rank, otherwise m' can be reduced further). Let $\boldsymbol{r}_1 : \mathbb{R}^p \to \mathbb{R}^{m'}$ and $\boldsymbol{r}_2 : \mathbb{R}^p \to \mathbb{R}^{n-m'}$ be the associated functions from $\boldsymbol{r}$. Let $\boldsymbol{B}_1' = \boldsymbol{I}_{m'}$ so $\boldsymbol{\varphi}(\boldsymbol{y}) = \boldsymbol{r}_1(\boldsymbol{y})$ as $\boldsymbol{r}_2$ are linear combinations of $\boldsymbol{r}_1$. From this construct $N = (n-m')m'$ equations with $\boldsymbol{\Psi}_1\boldsymbol{B}_{\text{eq}} = \boldsymbol{\Psi}_2$, $\boldsymbol{\Psi}_1^T = [\boldsymbol{r}_1(\boldsymbol{y}_1)\ldots\boldsymbol{r}_1(\boldsymbol{y}_{m'})]$ and $\boldsymbol{\Psi}_2^T = [\boldsymbol{r}_2(\boldsymbol{y}_1)\ldots\boldsymbol{r}_2(\boldsymbol{y}_{m'})]$, where $\boldsymbol{y}_j \in \mathbb{R}^p$ with $j \in \{1, \ldots, m'\}$ are m' points chosen such that $\boldsymbol{\Psi}_1^{-1}$ exists. Then $\bar{\boldsymbol{B}}^T = \begin{bmatrix}\boldsymbol{I}_{m'} & \boldsymbol{B}_{\text{eq}}\end{bmatrix}$, $\boldsymbol{B}_{\text{eq}} = \boldsymbol{\Psi}_1^{-1}\boldsymbol{\Psi}_2$ and $\boldsymbol{B}' = \boldsymbol{P}_p\bar{\boldsymbol{B}}$, where $\boldsymbol{P}_p$ is an $n \times n$ permutation matrix such that $\boldsymbol{P}_p\begin{bmatrix}\boldsymbol{r}_1(\boldsymbol{y})^T & \boldsymbol{r}_2(\boldsymbol{y})^T\end{bmatrix}^T = \boldsymbol{r}(\boldsymbol{y})$, cf. [306]. □

The approach is best illustrated with an example which also demonstrates its limitations. Consider $\boldsymbol{B} = \boldsymbol{I}_4$ such that $\boldsymbol{B}\boldsymbol{\psi}(\boldsymbol{y}) = \boldsymbol{r}(\boldsymbol{y})$ with $\boldsymbol{r} : \mathbb{R}^4 \to \mathbb{R}^4$ and

$$\boldsymbol{r}(\boldsymbol{y})^T = \begin{bmatrix}y_1^2 + y_2^3/2 & -3y_1^2y_2^2 - 6y_2 & (y_1^2 + y_2)(y_2^2 + 2) & \sin(y_3 + y_4)\end{bmatrix}\,. \tag{4.45}$$

Since $\boldsymbol{B}$ has 4 columns, a Lur'e system with such a nonlinearity $\boldsymbol{r}(\boldsymbol{y})$ would have 4 inputs. The question is whether the number of inputs can be reduced to 3. Hence we have $n = m = 4$ and $m' = 3$, so $N = 3$. By the proof of Theorem 9, we construct the system of linear equations $\boldsymbol{\Psi}_1\boldsymbol{B}_{\text{eq}} = \boldsymbol{\Psi}_2$ to find $\boldsymbol{B}_{\text{eq}}^T = \begin{bmatrix}B_{\text{eq},1} & B_{\text{eq},2} & B_{\text{eq},3}\end{bmatrix}$ and partition $\boldsymbol{r}(\boldsymbol{y})$ as

$$\boldsymbol{r}_1(\boldsymbol{y}) = \begin{bmatrix}y_1^2 + y_2^3/2 \\ -3y_1^2y_2^2 - 6y_2 \\ \sin(y_3 + y_4)\end{bmatrix} \text{ and } r_2(\boldsymbol{y}) = (y_1^2 + y_2)(y_2^2 + 2)\,. \tag{4.46}$$

Let $\boldsymbol{y}_1^T = \begin{bmatrix}1 & 1 & 1 & 1\end{bmatrix}$, $\boldsymbol{y}_2^T = \begin{bmatrix}2 & 2 & 2 & 2\end{bmatrix}$ and $\boldsymbol{y}_3^T = \begin{bmatrix}3 & 3 & 3 & 3\end{bmatrix}$. Then, from (4.46) results

$$\begin{bmatrix}3/2 & -9 & \sin(2) \\ 8 & -60 & \sin(4) \\ 45/2 & -261 & \sin(6)\end{bmatrix}\begin{bmatrix}B_{\text{eq},1} \\ B_{\text{eq},2} \\ B_{\text{eq},3}\end{bmatrix} = \begin{bmatrix}6 \\ 36 \\ 132\end{bmatrix} \implies \boldsymbol{B}_{\text{eq}} = \begin{bmatrix}B_{\text{eq},1} \\ B_{\text{eq},2} \\ B_{\text{eq},3}\end{bmatrix} = \begin{bmatrix}2 \\ -1/3 \\ 0\end{bmatrix}\,. \tag{4.47}$$

Now let $\boldsymbol{B}_1' = \boldsymbol{I}_3$, which is possible if the functions in $\boldsymbol{r}_1$ are linearly independent of each other and the functions in $\boldsymbol{r}_2$ are linear combinations of the functions in $\boldsymbol{r}_1$, so $\boldsymbol{\varphi}(\boldsymbol{y}) = \boldsymbol{r}_1(\boldsymbol{y})$.

Following, define $\bar{\boldsymbol{B}}^T = \begin{bmatrix}\boldsymbol{B}_1' & \boldsymbol{B}_2'\end{bmatrix} = \begin{bmatrix}\boldsymbol{I}_3 & \boldsymbol{B}_{\text{eq}}\end{bmatrix}$. The matrix $\bar{\boldsymbol{B}}$ represents the new input matrix $\boldsymbol{B}'$ up to a change of rows, depending on the partitioning of $\boldsymbol{r}$ into $\boldsymbol{r}_1$ and $\boldsymbol{r}_2$. Here,

$$\boldsymbol{P}_p = \begin{bmatrix}1 & 0 & 0 & 0\\ 0 & 1 & 0 & 0\\ 0 & 0 & 0 & 1\\ 0 & 0 & 1 & 0\end{bmatrix} \text{ since then } \boldsymbol{P}_p \begin{bmatrix}\boldsymbol{r}_1(\boldsymbol{y})\\ \boldsymbol{r}_2(\boldsymbol{y})\end{bmatrix} = \boldsymbol{r}(\boldsymbol{y}), \text{ so } \boldsymbol{B}' = \boldsymbol{P}_p\bar{\boldsymbol{B}} = \begin{bmatrix}1 & 0 & 0\\ 0 & 1 & 0\\ 2 & -1/3 & 0\\ 0 & 0 & 1\end{bmatrix}. \tag{4.48}$$

The first two rows of $\boldsymbol{r}$ are the first two rows of $\bar{\boldsymbol{r}}(\boldsymbol{y})^T = \begin{bmatrix}\boldsymbol{r}_1(\boldsymbol{y})^T & \boldsymbol{r}_2(\boldsymbol{y})^T\end{bmatrix}$, so the first two rows of $\bar{\boldsymbol{B}}$ remain unchanged. However, the third element of $\boldsymbol{r}$ is the fourth element of $\bar{\boldsymbol{r}}$, so the third and the fourth row of $\bar{\boldsymbol{B}}$ have to be swapped such that

$$\boldsymbol{r}(\boldsymbol{y}) = \boldsymbol{B}'\boldsymbol{\varphi}(\boldsymbol{y}), \text{ which is } \begin{bmatrix}y_1^2 + y_2^3/2\\ -3y_1^2y_2^2 - 6y_2\\ (y_1^2 + y_2)(y_2^2 + 2)\\ \sin(y_3 + y_4)\end{bmatrix} = \begin{bmatrix}1 & 0 & 0\\ 0 & 1 & 0\\ 2 & -1/3 & 0\\ 0 & 0 & 1\end{bmatrix} \begin{bmatrix}y_1^2 + y_2^3/2\\ -3y_1^2y_2^2 - 6y_2\\ \sin(y_3 + y_4)\end{bmatrix}. \tag{4.49}$$

From this, it can be seen that a Lur'e system with $n = 4$ and the example nonlinearity (4.45) in the feedback path does not necessarily require 4 inputs but can be rewritten with 3 inputs, using the new input matrix $\boldsymbol{B}'$ calculated in (4.48).

Two steps in this approach require a further explanation. The first step is the partitioning of $\boldsymbol{r}$ into $\boldsymbol{r}_1$ and $\boldsymbol{r}_2$, which implicitly already requires the knowledge which functions of $\boldsymbol{r}$ are linear combinations of the remaining functions of $\boldsymbol{r}$. In the above example, a valid combination is assumed to be known. Indeed, the combination $\boldsymbol{r}_1$ works because there exist $\boldsymbol{y}_1$, $\boldsymbol{y}_2$, $\boldsymbol{y}_3$ such that $\boldsymbol{\Psi}_1^{-1}$ exists. If we choose for example $\boldsymbol{r}_1(\boldsymbol{y})^T = \begin{bmatrix}y_1^2 + y_2^3/2 & -3y_1^2y_2^2 - 6y_2 & (y_2^2 + 2)(y_1^2 + y_2)\end{bmatrix}$ then $\det(\boldsymbol{\Psi}_1) = 0$ for any $\boldsymbol{y}_1, \boldsymbol{y}_2, \boldsymbol{y}_3 \in \mathbb{R}^3$. Here this is obvious, because a finite linear combination of polynomials cannot be identical to a trigonometric function like $\sin(y_3 + y_4)$. However, in more complicated cases it might not be obvious which combination is the correct one, assuming one exists. In such a case, one option is to enumerate all possible combinations and test each combination individually. Since the order of functions within $\boldsymbol{r}_1(\boldsymbol{y})$ does not matter, the total number of such combinations is given by the binomial coefficient

$$N_c = \binom{n}{m'} = \frac{n!}{m'!(n - m')!} \tag{4.50}$$

where $n!$ denotes the factorial of n. Each combination can be tested by solving a system of $N = (n - m')m'$ linear equations, assuming the m' test points are given. From the four possible combinations to form $\boldsymbol{r}_1(\boldsymbol{y})$, given by

$$\begin{bmatrix}y_1^2 + y_2^3/2\\ -3y_1^2y_2^2 - 6y_2\\ (y_2^2 + 2)(y_1^2 + y_2)\end{bmatrix}, \begin{bmatrix}y_1^2 + y_2^3/2\\ -3y_1^2y_2^2 - 6y_2\\ \sin(y_3 + y_4)\end{bmatrix}, \begin{bmatrix}y_1^2 + y_2^3/2\\ (y_2^2 + 2)(y_1^2 + y_2)\\ \sin(y_3 + y_4)\end{bmatrix}, \begin{bmatrix}-3y_1^2y_2^2 - 6y_2\\ (y_2^2 + 2)(y_1^2 + y_2)\\ \sin(y_3 + y_4)\end{bmatrix}, \tag{4.51}$$

only the first does not work because $\det(\boldsymbol{\Psi}_1) = 0$ for any $\boldsymbol{y}_1, \boldsymbol{y}_2, \boldsymbol{y}_3 \in \mathbb{R}^3$. The remaining three combinations admit nonzero determinants, for example the matrix from (4.47) has $\det(\boldsymbol{\Psi}_1) = 189\sin(4) - 738\sin(2) - 18\sin(6) \neq 0$ at the above defined $\boldsymbol{y}_1, \boldsymbol{y}_2, \boldsymbol{y}_3$. This leads to the potentially challenging second step from the approach, namely the choice of the test points $\boldsymbol{y}_j \in \mathbb{R}^p$ with $j \in \{1, \ldots, m'\}$. While the problem of constructing $\boldsymbol{r}_1$ can in principle be solved by trying all possible combinations, for the test points this is not possible as they can be chosen from a continuum. Therefore, this step might be challenging when analyzing an arbitrary Lur'e system. A numerical search by drawing random test points might be useful in such cases. In the above example, this was not required as it is assumed that suitable test points can readily be chosen by inspection of the nonlinearity $\boldsymbol{r}(\boldsymbol{y}) = \boldsymbol{B}\boldsymbol{\psi}(\boldsymbol{y})$. Finally, it can be noted that even if test points are available such that $\boldsymbol{\Psi}_1^{-1}$ exists, the equation $\boldsymbol{r}(\boldsymbol{y}) = \boldsymbol{B}'\boldsymbol{\varphi}(\boldsymbol{y})$ has to be tested after constructing $\boldsymbol{B}'$ and $\boldsymbol{\varphi}(\boldsymbol{y})$, as done in (4.49), as equality at the test points is only necessary, not sufficient.

A family of counterexamples to the MYC by Castañeda and Guíñez [35] provides an application for Theorem 9. The system in Lur'e form is $\dot{\boldsymbol{x}} = \boldsymbol{A}\boldsymbol{x} - \boldsymbol{B}\boldsymbol{\psi}(\boldsymbol{y})$, $\boldsymbol{y} = \boldsymbol{C}\boldsymbol{x}$, with

$$\boldsymbol{A} = \begin{bmatrix} -a-c & 1 & 0 \\ -a^2 & a-c & 1 \\ 0 & 0 & -c \end{bmatrix}, \boldsymbol{C} = \begin{bmatrix} 1 & 0 & 0 \\ 0 & 1 & 0 \end{bmatrix} \tag{4.52}$$

and $\boldsymbol{B} = \boldsymbol{I}_3$, $\boldsymbol{\psi}(\boldsymbol{y})^T = \begin{bmatrix} \psi_1(\boldsymbol{y}) & \psi_2(\boldsymbol{y}) & \psi_3(\boldsymbol{y}) \end{bmatrix}$, where

$$\psi_1(\boldsymbol{y}) = by_1^2 \tag{4.53a}$$
$$\psi_2(\boldsymbol{y}) = by_1(2by_1^2 + 3ay_1 - 2y_2) \tag{4.53b}$$
$$\psi_3(\boldsymbol{y}) = b(by_1^2 + ay_1 - y_2)^2 \tag{4.53c}$$

with $c \in \mathbb{R}^+$ and $b \neq 0$. Here, $p = 2$ is possible as $\boldsymbol{\psi}$ depends only on $y_1 = x_1$ and $y_2 = x_2$. The question is if the $m = 3$ inputs can be reduced to $m' = 2$, which has a negative answer.

Corollary 8. *The family of counterexamples (4.52) from [35] to the Markus-Yamabe conjecture cannot be expressed in Lur'e form with $m < 3$.*

Proof. The result can be shown by using Theorem 9. Here, $N = 2$ and $N_c = 3$. The three possible combinations to construct $\boldsymbol{r}_1(\boldsymbol{y})$ and $\boldsymbol{r}_2(\boldsymbol{y})$ from $\boldsymbol{r}(\boldsymbol{y}) = \boldsymbol{B}\boldsymbol{\psi}(\boldsymbol{y})$ with $\boldsymbol{B} = \boldsymbol{I}_3$ and $\boldsymbol{\psi}(\boldsymbol{y})$ from (4.53), denoted by $\boldsymbol{r}_{1,k}$ and $r_{2,k}$ with $k \in \{1, \ldots, N_c\} = \{1, 2, 3\}$, are given by

$$\boldsymbol{r}_{1,1}(\boldsymbol{y})^T = \begin{bmatrix} by_1^2 & by_1(2by_1^2 + 3ay_1 - 2y_2) \end{bmatrix}, r_{2,1}(\boldsymbol{y}) = b(by_1^2 + ay_1 - y_2)^2 \tag{4.54a}$$
$$\boldsymbol{r}_{1,2}(\boldsymbol{y})^T = \begin{bmatrix} by_1^2 & b(by_1^2 + ay_1 - y_2)^2 \end{bmatrix}, r_{2,2}(\boldsymbol{y}) = by_1(2by_1^2 + 3ay_1 - 2y_2) \tag{4.54b}$$
$$\boldsymbol{r}_{1,3}(\boldsymbol{y})^T = \begin{bmatrix} by_1(2by_1^2 + 3ay_1 - 2y_2) & b(by_1^2 + ay_1 - y_2)^2 \end{bmatrix}, r_{2,3}(\boldsymbol{y}) = by_1^2 . \tag{4.54c}$$

Let $\boldsymbol{y}_1^T = \begin{bmatrix} 1 & 1 \end{bmatrix}$ and $\boldsymbol{y}_2^T = \begin{bmatrix} 2 & 2 \end{bmatrix}$ be the test points. Then, the $\boldsymbol{\Psi}_{1,k}$ corresponding to (4.54) are

$$\boldsymbol{\Psi}_{1,1} = \begin{bmatrix} b & b(3a+2b-2) \\ 4b & 2b(6a+8b-4) \end{bmatrix} \implies \det(\boldsymbol{\Psi}_{1,1}) = 8b^3 \tag{4.55a}$$
$$\boldsymbol{\Psi}_{1,2} = \begin{bmatrix} b & b(a+b-1)^2 \\ 4b & b(2a+4b-2)^2 \end{bmatrix} \implies \det(\boldsymbol{\Psi}_{1,2}) = 4b^3(2a+3b-2) \tag{4.55b}$$
$$\boldsymbol{\Psi}_{1,3} = \begin{bmatrix} b(3a+2b-2) & b(a+b-1)^2 \\ 2b(6a+8b-4) & b(2a+4b-2)^2 \end{bmatrix} \implies \det(\boldsymbol{\Psi}_{1,3}) = 4b^3 d(a,b) , \tag{4.55c}$$

with $d(a,b) = 4a^2 + 9ab - 6a + 4b^2 - 6b + 2$. Moreover, $\boldsymbol{\Psi}_{2,1}^T = \begin{bmatrix} b(3a+2b-2) & b(a+b-1)^2 \end{bmatrix}$, $\boldsymbol{\Psi}_{2,2}^T = \begin{bmatrix} b & b(a+b-1)^2 \end{bmatrix}$ and $\boldsymbol{\Psi}_{2,3}^T = \begin{bmatrix} b & b(3a+2b-2) \end{bmatrix}$. Following, $\boldsymbol{B}_{\mathrm{eq},k} = \boldsymbol{\Psi}_{1,k}^{-1}\boldsymbol{\Psi}_{2,k}$ results in the necessary condition that $\boldsymbol{B}_{\mathrm{eq},k}\boldsymbol{r}_{1,k}(\boldsymbol{y}) = \boldsymbol{r}_{2,k}(\boldsymbol{y}) , \forall \boldsymbol{y} \in \mathbb{R}^2$ for at least one $k \in \{1, 2, 3\}$. Evaluating these equations at $\boldsymbol{y}_3^T = \begin{bmatrix} 0 & 1 \end{bmatrix}$ gives after some rearrangements

$$b = 0 \text{ for } k = 1 , \tag{4.56a}$$
$$2b/(2a+3b-2) = 0 \text{ for } k = 2 , \tag{4.56b}$$
$$2b/d(a,b) = 0 \text{ for } k = 3 . \tag{4.56c}$$

These equations require $b = 0$, which contradicts the initial assumption that $b \neq 0$. Repeating the procedure with $m' = 1$ and the same test points leads to conditions which require $b = 0$ as well, leading to a contradiction. Therefore, $m = 3$ is the smallest possible number of inputs. □

Remark 34. *Testing only $m' = 2$ in Corollary 8 would not be sufficient to rule out the possibility that the number of inputs can be reduced to 2. Indeed, if $m' = 1$ would be possible then also $m' = 2$ inputs could be realized, but the test with $m' = 2$ would always fail because $\boldsymbol{\Psi}_1^{-1}$ could never exist. This is why Theorem 9 assumes that m can be at most reduced to m'. For algorithmic tests, this can be solved by testing all smaller input dimensions as well, as done in Corollary 8.*

While this procedure can be readily automated, the same conclusion can be reached here by keeping the input matrix in symbolic form and comparing coefficients in the resulting equations. The following alternative proof of Corollary 8 from our previous work [306] illustrates this approach. The method based on Theorem 9 outlined above can be seen as a systematic extension of this method, which in contrast to the following method avoids the symbolic matrix inversion but instead requires a suitable choice of test points. It can further be noted that both methods are limited in practice for higher order systems, as the number of combinations (4.50) can become impractically large or, due to the symbolic matrix inversion. For the analysis here this is not relevant, as the special case of the MYC considered in this work requires $n = 3$. The following alternative method to test whether the input dimension of a Lur'e system can be reduced confirms the findings from Corollary 8.

Alternative proof of Corollary 8. If $m = 2$ would be possible, then the solutions of the first and the third equation of (4.44) would be

$$\varphi_1(\boldsymbol{y}) = \big(B'_{32}\psi_1(\boldsymbol{y}) - B'_{12}\psi_3(\boldsymbol{y})\big)/\Delta \tag{4.57a}$$

$$\varphi_2(\boldsymbol{y}) = \big(B'_{11}\psi_3(\boldsymbol{y}) - B'_{31}\psi_1(\boldsymbol{y})\big)/\Delta\,, \tag{4.57b}$$

where $\Delta = B'_{11}B'_{32} - B'_{12}B'_{31}$. For the denominator, $\Delta \neq 0$ because otherwise there would exist $k \neq 0$ such that $\psi_1(\boldsymbol{y}) = k\psi_3(\boldsymbol{y})\,, \forall \boldsymbol{y} \in \mathbb{R}^2$, which cannot be the case since for $b \neq 0$, ψ_3 depends only on y_2 while ψ_1 depends on both y_1 and y_2. Following, insert (4.57a)-(4.57b) into the second equation of (4.44) and compare the coefficients of the result with the coefficients of (4.53b). This results in

$$2ab^2(B'_{11}B'_{22} - B'_{12}B'_{21})/\Delta = 2b^2 \text{ for the } y_1^3 \text{ term}, \tag{4.58a}$$

$$-2b^2(B'_{11}B'_{22} - B'_{12}B'_{21})/\Delta = 0 \text{ for the } y_1^2y_2 \text{ term}, \tag{4.58b}$$

which is a contradiction since $b \neq 0$ is required by assumption as for $b = 0$, the system (4.52) reduces to an LTI system. Therefore, the system of equations (4.44) has no solution and it is not possible to rewrite (4.52) as a Lur'e system with less than 3 inputs [306]. □

The question remains if either p or m must be at least 3 to construct a valid counterexample to the Markus-Yamabe conjecture, if the system type is constrained to be a Lur'e system. We leave this question as an open problem, see also [306].

Problem. *Does there exist a counterexample to the Markus-Yamabe conjecture that can be expressed in Lur'e form (2.26) with $n = 3$ and $p = m = 2$?*

This question can also be interpreted as asking to which extent the Kalman conjecture can be generalized to a MIMO Lur'e setting. Clearly, it can be generalized for $n = p = m = 2$, due to the proofs of the more general Markus-Yamabe conjecture by Fessler, Gutiérrez and Glutsuk for $n = 2$. However, it cannot be applied for $n \geq 3$ if either $m \geq 2$, $p \geq 3$ or $m \geq 3$, $p \geq 2$, due to the above counterexamples which we reformulated as Lur'e systems with non-square transfer function matrix. This leaves a gap for the "next simplest" case $n = 3$, $p = m = 2$, which we propose as an open problem for the control community.

The previous two chapters were mainly focused on the control design based on IOL and a detailed stability and passivity analysis of the zero dynamics of the proposed TCSs. Before we proceed to a theoretical analysis in the frequency domain and an experimental evaluation of these control systems in different test vehicles, a heuristic optimization method for Lyapunov function identification based on genetic programming is presented in the following chapter. A novel heuristic for the evaluation of the conditions imposed on a Lyapunov function in the form of a fitness function suitable for GP is proposed. The method is tested on two benchmark systems from the literature, where the first requires a non-polynomial Lyapunov function and the second a fourth order polynomial Lyapunov function for showing global asymptotic stability. Additionally, the method is applied to the nonlinear zero dynamics of the proposed 2WD TCS.

5 Lyapunov Function Identification using Genetic Programming

Summary. *This chapter describes a new approach for Lyapunov function identification for nonlinear systems based on the heuristic optimization method of GP. The main contributions are:*

1. *A new fitness function formulation and a corresponding algorithm suitable for Lyapunov function identification by GP.*
2. *A validation of the algorithm on two nonlinear benchmark systems from the literature, including a discussion of the limitations of the approach.*
3. *An application of the algorithm to the stability analysis of the zero dynamics of the 2WD TCS from Chapter 3.*

This chapter builds upon and extends some ideas of our work in [301, 302] and [303].

5.1 Preliminary Remarks on Lyapunov Function Synthesis

A major obstacle for stability proofs based on the second method of Lyapunov, from a practical viewpoint, is that the method is not constructive. While for LTI systems, a Lyapunov function can be computed by solving the associated Lyapunov equation (2.18), the situation is more difficult for nonlinear systems [99, pp. 104–105] and in the general case still an open problem. Methods for Lyapunov function construction exist for specific classes of nonlinear systems like Lur'e systems, as discussed in Chapter 4. Other traditional methods for finding Lyapunov functions can be found in the survey [94]. More recent approaches include sum-of-squares programming [234], which can be applied to systems with polynomial vector fields, methods based on linear programming [23] or LMIs [137]. More details on state of the art computational methods for Lyapunov function identification can be found in the survey paper [81].

In this work we focus on Lyapunov function synthesis by the means of GP. The heuristic GP algorithm has been applied to the problem of finding Lyapunov functions before [15, 89, 194, 260]. Here we propose a novel fitness function and demonstrate that the method can be applied to the zero dynamics of the 2WD TCS. The fitness function is based on sampling of the state space and uses several heuristic measures to identify promising candidate functions. An important part of the fitness function is the estimation of a subset of the DOA obtained via the level curves of the candidate functions. Various methods already exist to obtain an estimate of the DOA, or a subset of it. An analytic method to compute the DOA is available by the solution of the Zubov equation [296], see also [99, pp. 161–165]. However, since this is a nonlinear partial differential equation, it is often practically impossible to derive an analytic solution. Also, it requires the choice of a suitable positive definite auxiliary function. Because of these difficulties, a range of different approaches for estimating the DOA of a nonlinear system exist. An early review paper on this topic is given by Genesio et al. [78]. Recent approaches include LMIs [42, 170, 191, 268], sum-of-squares programming [84, 139] and methods based on interval arithmetic [192, 279], linear programming [98], mesh-free collocation [80], linear programming combined with satisfiability modulo theories solvers [146] and sampling methods [19, 204].

In the following, a fitness function suitable for Lyapunov function synthesis by a GP algorithm is presented. One part of this fitness function is the estimation of a subset of the DOA by sampling, with the goal of identifying functions that maximize the volume of this set.

5.2 A Sampling Algorithm for Rating Lyapunov Functions

The herein proposed sampling algorithm has the goal to quantify how close a given real valued function is to being a Lyapunov function for a given continuous, autonomous, nonlinear dynamical system $\dot{\boldsymbol{x}} = \boldsymbol{f}(\boldsymbol{x})$ with $\boldsymbol{f}(\mathbf{0}_n) = \mathbf{0}_n$. This algorithm is used by a GP algorithm to search for Lyapunov functions by maximizing the estimated DOA. This can be formulated as a bi-level optimization problem over a function space:

$$
\begin{aligned}
&\text{supremum} && \Lambda(\Omega_0) && (5.1a)\\
&\text{over} && V \in \mathcal{F}_{\mathcal{G}}(\mathbb{R}^n, \mathbb{R}) && (5.1b)\\
&\text{subject to} && \Omega = \{\boldsymbol{x} \in \mathbb{R}^n : V(\boldsymbol{x}) > 0, \dot{V}(\boldsymbol{x}) \leq 0\} \cup \{\mathbf{0}_n\} && (5.1c)\\
& && \Omega_0 \subseteq \Omega_c = \{\boldsymbol{x} \in \Omega : V(\boldsymbol{x}) < c^*\} && (5.1d)\\
& && c^* = \text{infimum} \quad V(\boldsymbol{x}) && (5.1e)\\
& && \qquad \text{over} \quad \boldsymbol{x} \in \Omega \setminus \{\mathbf{0}_n\} && \\
& && \qquad \text{subject to} \quad \dot{V}(\boldsymbol{x}) = 0 && \\
& && V(\mathbf{0}_n) = 0 \text{ and } \lim_{\|\boldsymbol{x}\| \to \infty} V(\boldsymbol{x}) = \infty \text{ when } c^* = \infty\,. && (5.1f)
\end{aligned}
$$

Here, $\Lambda(\Omega_0)$ denotes the Lebesgue measure (hypervolume) of Ω_0, which is the maximal connected component of Ω_c that contains the origin, while Ω_c is required to be either bounded or the whole $\mathbb{R}^n$, see also (2.10). Moreover, $\mathcal{F}_{\mathcal{G}}(\mathbb{R}^n, \mathbb{R})$ is the space of C^1 functions $V : \mathbb{R}^n \to \mathbb{R}$ that can be generated by a GP algorithm using the BNF grammar $\mathcal{G}$, cf. Section 2.3.2. Following, Ω is the set of points satisfying the Lyapunov conditions and Ω_c is the subset of Ω bounded by the level set $V(\boldsymbol{x}) = c^*$. The inner optimization problem is used in the literature for estimating a subset of the DOA of a given positive definite Lyapunov function by finding the smallest level set $V(\boldsymbol{x}) = c^*$ such that $\dot{V}(\boldsymbol{x}) = 0$ when $\boldsymbol{x} \neq \mathbf{0}_n$, see for example [42]. If $\Omega = \mathbb{R}^n$ but no c^* with $V(\boldsymbol{x}) = c^*$ exists such that $\dot{V}(\boldsymbol{x}) = 0$, then $c^* = \infty$. The last constraint of (5.1) requires that V is radially unbounded when $c^* = \infty$ and that it vanishes at the origin.

Even the inner optimization problem alone, which deals with finding c^* given a positive definite function V is a challenging problem, depending on the dynamical system under consideration. Therefore, we approach (5.1) with the heuristic GP optimization algorithm. As mentioned in Section 5.1, there exist different methods for estimating a subset of the DOA. We successfully used a modified version of the sampling based algorithm by [204] in our previous work [302, 303] for controller synthesis. The sampling algorithm is depicted in Table 5.1. However, it cannot be applied directly to (5.1) as will be discussed in the following.

Table 5.1: Heuristic state of the art DOA size estimation for positive definite functions.

Algorithm 1 Domain of attraction estimation, used in [302, 303], based on [204].

```
1: function DOASize(V)
2:     Initialization: c* ← ∞, k_mc ← 0, v_mc ← 0_{N_x}        ▷ Initialize local variables.
3:     for k ← 1 to N_x do                                      ▷ Monte Carlo search with N_x samples.
4:         Pick random state x_k                                ▷ Draw from a uniform distribution.
5:         v_mc,k ← V(x_k)                                      ▷ Store V(x_k) in k-th row of the vector v_mc.
6:         if V(x_k) < c* and V̇(x_k) ≥ 0 then c* ← V(x_k)       ▷ Update the level curve.
7:     for k ← 1 to N_x do                                      ▷ Estimate the size of the DOA.
8:         if v_mc,k < c* then k_mc ← k_mc + 1                  ▷ Count the samples inside the level curve.
9:     return k_mc/N_x                                          ▷ Return the normalized size of the DOA estimate.
```

The sampling algorithm from Table 5.1 assumes that V is a positive definite function. However, a function generated by GP might be only locally positive definite, negative definite or indefinite, but should still be assigned a suitable fitness value. We propose a solution on how to update the level curve when there exist $\boldsymbol{x}$ such that $V(\boldsymbol{x})$ is negative, illustrated in Figure 5.1.

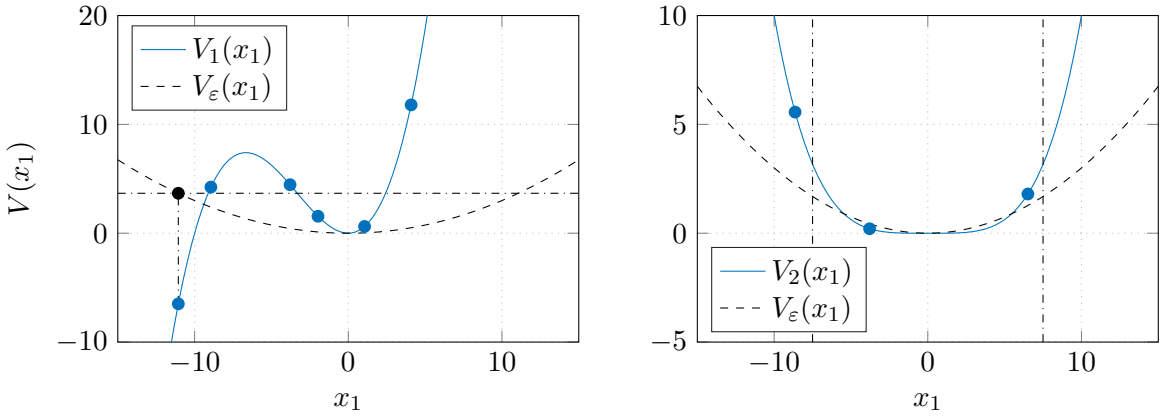

(a) Level curve adaptation at negative values.

(b) Inner and outer segments for evaluation.

Figure 5.1: Illustration of specific cases of the proposed heuristic fitness evaluation method.

Figure 5.1a shows the example function $V_1(x_1) = x_1^3/20 + x_1^2/2$ and $N_x = 6$ different sampling points. Assume we want to evaluate this function with the globally exponentially stable system $\dot{x}_1 = -x_1$. Using Algorithm 1, assuming the sample points from Figure 5.1a, that would result in $c^* \approx -6.5$ because $\dot{V}(x_1) = -3x_1^3/20 - x_1^2$ is positive at the leftmost sample point. This is invalid however, because c^* must be non-negative. Setting c^* to zero in such a case would be too restrictive, because in a neighborhood of the origin, V_1 has the shape of a Lyapunov function. Updating c^* only at samples where V_1 is positive would ignore the information provided by the remaining samples. A possible solution is to define a lower bound for the function under consideration by defining

$$V_\varepsilon(\boldsymbol{x}) = \varepsilon \boldsymbol{x}^T \boldsymbol{x}\,. \tag{5.2}$$

Here, $\varepsilon > 0$ is a design parameter that has to be chosen before the analysis. Figure 5.1a also shows V_ε computed with $\varepsilon = 0.03$. This value was selected for better illustration, typically ε is chosen smaller. This lower bound can now be used to handle negative samples: whenever $V(\boldsymbol{x}) \leq 0$ for $\boldsymbol{x} \neq \mathbf{0}_n$ then c^* is updated to $V_\varepsilon(\boldsymbol{x})$ as shown in Figure 5.1a, leading in this example to $c^* \approx 3.67$. Counting then only the points with $0 < V(\boldsymbol{x}) < c^*$ and $\dot{V}(\boldsymbol{x}) \leq 0$ results in $k_{\mathrm{mc}} = 2$, such that $k_{\mathrm{mc}}/N_x = 1/3$ of the samples (the two samples closest to the origin) would be the estimated, normalized size of the DOA.

This is not an exact but a heuristic approach, as the third sample at $x_1 \approx -3.79$ in Figure 5.1a is excluded although $\dot{V}_1(x_1) = 0$ for $x_1 = -20/3 \approx -6.67$. So the exact bound in this example is $c^* = V_1(-20/3) = 200/27 \approx 7.41 > 3.67$. However, this method can be automatized efficiently and also handles cases like $V_3(x_1) = x_1^3$ appropriately, which satisfies $\dot{V}_3(x_1) = 0$ only at the origin. Ignoring samples where $V_3(x_1) < 0$ would here result in $c^* = \infty$, which is wrong since V_3 becomes negative arbitrarily close to the origin. The method from Figure 5.1a will correctly shrink the level set of V_3 as the number of samples increases. Also, it biases the GP algorithm towards preferring functions that are positive definite on all sample points over locally positive definite functions. This property is not required for every system, for example when the DOA is only a subset of $\mathbb{R}^n$ that is fully contained in the sampling region. However, it is considered useful here as we are interested in global stability and although positive definiteness within the bounded sampling region is not sufficient, it is a necessary property of a global Lyapunov function.

The discussed measures are not yet enough to bias the GP algorithm towards generating valid Lyapunov function candidates. For example, consider the globally exponentially stable system $\dot{x}_1 = -x_1$, $\dot{x}_2 = -x_2$ with an example function $V_4(\boldsymbol{x}) = (1/2)x_1^2$. Then $\dot{V}_4(\boldsymbol{x}) = -x_1^2$, which is negative semi-definite. With uniform random sampling, it is very unlikely to hit a sample exactly at $x_1 = 0$ and $x_2 \neq 0$, so for the sampling algorithm, V_4 will appear positive definite although it is only positive semi-definite. Explicit sampling on the axis $x_i = 0$, $i \in \{1, \ldots, n\}$ does not fully avoid this problem, because the algorithm might for example still generate functions like $V_5(\boldsymbol{x}) = (c_1 x_1 - c_2 x_2)^2$ with $c_1, c_2 > 0$. Therefore, two different heuristic measures to counter this issue are used, first using a lower bound and second using the Hessian of V.

The first method is illustrated in Figure 5.1b and is a modified version of the approach used frequently in sum-of-squares programming, compare [234], which requires that $V(\boldsymbol{x}) \geq V_\varepsilon(\boldsymbol{x})$ with V_ε from (5.2). However, this approach has the disadvantage that it does not admit functions like for example $V_6(\boldsymbol{x}) = \sum_{i=1}^{n} x_i^4$, as close to the origin such a function vanishes faster than any quadratic function. Also, (5.2) does not account for the shape of the level set in a vicinity about the origin. To address the latter, when the Jacobian linearization of the system at the origin is exponentially stable we use

$$V_\varepsilon(\boldsymbol{x}) = \varepsilon \boldsymbol{x}^T \boldsymbol{P} \boldsymbol{x} \tag{5.3}$$

instead of (5.2), where $\boldsymbol{P}$ is the solution to the Lyapunov equation (2.18) with $\boldsymbol{A} = \boldsymbol{J}_{\boldsymbol{f},\boldsymbol{x}}(\boldsymbol{0}_n)$ and $\boldsymbol{Q} = \boldsymbol{I}_n$, see also (2.24). Only for systems like $\dot{x}_1 = -x_1^3$, which do not admit an exponentially stable linearization, (5.2) is used. Moreover, the sampling space is divided into an inner and an outer region, as shown in Figure 5.1b. In the inner region, $V(\boldsymbol{x}) > 0$ is required, while in the outer region $V(\boldsymbol{x}) > V_\varepsilon(\boldsymbol{x})$ is required. In both regions, the level curve is updated to $V_\varepsilon(\boldsymbol{x})$ in case the corresponding condition fails. Figure 5.1b shows the example function $V_2(x_1) = x_1^4/1000$ and the same V_ε as in Figure 5.1a. The second sample at $x_1 \approx -3.8$ is below V_ε but is valid, as it is in the inner region. In the outer region, V_ε can be used as lower bound to ensure a certain amount of growth of V_2. Table 5.2 shows the algorithm used to initialize the state space samples, stored in the $(2N_xN_s) \times n$ matrix $\boldsymbol{X}_s$. Here, N_s is the number of stages. Each stage has N_x samples for the inner and N_x samples for the outer region and n is the system order.

Table 5.2: Initialization of inner and outer state space samples with rejection sampling.

Algorithm 2 State space sample initialization, called once before the actual optimization.

function InitializeSamples($\boldsymbol{x}_{\text{int}}$, $\boldsymbol{a}_{\text{int}}$)
  Initialization: $\boldsymbol{X}_s \leftarrow \boldsymbol{0}_{(2N_xN_s)\times n}$, $\boldsymbol{x}_s \leftarrow \boldsymbol{0}_n$ ▷ Initialize sample matrix and vector.
  for $i \leftarrow 1$ **to** N_s **do** ▷ Iteration for stages.
    for $k \leftarrow 1$ **to** N_x **do** ▷ Iteration for inner samples.
      for $j \leftarrow 1$ **to** n **do** ▷ Iteration for state vector.
        $x_{s,j} \sim \mathcal{U}(-a_{\text{int},j} x_{\text{int},j}, a_{\text{int},j} x_{\text{int},j})$ ▷ Draw random inner sample.
        if $i < n$ **then** $x_{s,i} \leftarrow 0$ ▷ Ensure first n samples have one zero component.
      $\ell \leftarrow 2N_x(i-1) + k$ and $X_{s,\ell j} \leftarrow x_{s,j}\,, \forall j \in \{1, \ldots, n\}$ ▷ Fill next row of $\boldsymbol{X}_s$.
    for $k \leftarrow N_x + 1$ **to** $2N_x$ **do** ▷ Iteration for outer samples.
      for $j \leftarrow 1$ **to** n **do** ▷ Iteration for state vector.
        while true **do** ▷ Loop for rejection sampling.
          $x_{s,j} \sim \mathcal{U}(-x_{\text{int},j}, x_{\text{int},j})$ ▷ Draw random sample.
          if $|x_{s,j}| > a_{\text{int},j} x_{\text{int},j}$ **then break** ▷ If outer sample, leave while loop.
      $\ell \leftarrow 2N_x(i-1) + k$ and $X_{s,\ell j} \leftarrow x_{s,j}\,, \forall j \in \{1, \ldots, n\}$ ▷ Fill next row of $\boldsymbol{X}_s$.
  return $\boldsymbol{X}_s$ ▷ Return the matrix of random state space samples.

Algorithm 2 uses the intervals $\boldsymbol{x}_{\text{int}}^T = \begin{bmatrix} x_{\text{int},1} & x_{\text{int},2} & \dots & x_{\text{int},n} \end{bmatrix}$ which specify the whole sampling region in the state space by $-x_{\text{int},i} \leq x_{s,i} \leq x_{\text{int},i}\,, \forall i \in \{1, \dots, n\}$. The user also has to define the vector $\boldsymbol{a}^T = \begin{bmatrix} a_1 & a_2 & \dots & a_n \end{bmatrix}$ with $0 < a_i < 1$ which is used to draw samples in the inner region from a uniform continuous distribution with support $x_{s,i} \in [-a_i x_{\text{int},i}, a_i x_{\text{int},i}]$. The outer region is initialized with rejection sampling such that $x_{s,i} \in [-x_{\text{int},i}, x_{\text{int},i}] \setminus [-a_i x_{\text{int},i}, a_i x_{\text{int},i}]$. Before the concept of stages is detailed, the fitness function used in conjunction with the GP algorithm is listed in Table 5.3, which is a wrapper for the stage-wise fitness computation.

Table 5.3: Fitness function wrapper with preliminary steps for the fitness computation.

Algorithm 3 Fitness Function Wrapper, called by the GP optimization algorithm.

1: **function** FitnessWrapper(V_{GP})
2: **if** nodes(V_{GP}) $> N_{\text{node}}$ **then** $V_{\text{GP}} \leftarrow V_q$ ▷ Limit complexity of V_{GP}, see also (5.5).
3: **if** $V_{\text{GP}}(\mathbf{0}_n) \neq 0$ **then** $V_0(\boldsymbol{x}) \leftarrow V_{\text{GP}}(\boldsymbol{x}) - V_{\text{GP}}(\mathbf{0}_n)$ ▷ Shift to the origin if required.
4: **else** $V_0(\boldsymbol{x}) \leftarrow V_{\text{GP}}(\boldsymbol{x})$ ▷ No shifting required, avoid unnecessary nodes.
5: **if** $|V_q(\varepsilon_{\text{norm}}\mathbf{1}_n)/V_0(\varepsilon_{\text{norm}}\mathbf{1}_n)| > h_{\text{norm}}$ **then return** 1 ▷ Check normalization factor.
6: $V(\boldsymbol{x}) \leftarrow V_0(\boldsymbol{x})V_q(\varepsilon_{\text{norm}}\mathbf{1}_n)/V_0(\varepsilon_{\text{norm}}\mathbf{1}_n)$ ▷ Normalize V_0 to obtain V.
7: **return** ComputeFitnessStages(V) ▷ Compute fitness using Algorithm 4.

The first step of Algorithm 3 is to limit the complexity of the function V_{GP}, generated by the GP algorithm in order to avoid the so-called expression bloat, which describes the generation of overly complicated expressions without significant fitness improvement [231, pp. 101–108]. Here, nodes(V_{GP}) denotes the number of nodes of V_{GP} for a user-defined grammar. Whenever this number exceeds N_{node}, we replace V_{GP} with V_q, which is defined similarly to V_ε by

$$V_q(\boldsymbol{x}) = \begin{cases} \boldsymbol{x}^T \boldsymbol{P} \boldsymbol{x} & \boldsymbol{J}_{\boldsymbol{f},\boldsymbol{x}}(\mathbf{0}_n) \text{ is Hurwitz} \\ \boldsymbol{x}^T \boldsymbol{x} & \text{otherwise.} \end{cases} \tag{5.4}$$

where $\boldsymbol{P}$ is again the solution of the Lyapunov equation using $\boldsymbol{Q} = \boldsymbol{I}_n$, so also $V_\varepsilon(\boldsymbol{x}) = \varepsilon V_q(\boldsymbol{x})$. This mechanism limits the maximum number of expression nodes by replacing expressions with too many nodes with a quadratic form, which in case that $\boldsymbol{J}_{\boldsymbol{f},\boldsymbol{x}}(\mathbf{0}_n)$ is Hurwitz is at least locally a valid Lyapunov function for the original system. This approach raises the question how N_{node} should be chosen. We propose the following formula for the maximum number of nodes

$$N_{\text{node}} = k_{\text{node}}\big(3n(n+1) - 1\big)\,, \tag{5.5}$$

where $k_{\text{node}} \geq 2$ is an integer and n is the order of the considered system. The rational behind (5.5) is to construct a reasonable estimate of the smallest possible solution which is then scaled up by k_{node}. The general idea of this approach is taken from [231, pp. 104–105], while the formula itself is based on the thought that the GP algorithm should at least be able to construct solutions of the size required to construct a quadratic form, as this already covers stable linear systems. The assumption made here is that the grammar provided by the user admits addition and multiplication as binary non-terminals and constants and state variables as terminals. Then, each summand of a general quadratic form can be expressed by two multiplication nodes, two variable nodes and 1 constant node. This gives 5 nodes per $n(n+1)/2$ individual summands, plus $n(n+1)/2 - 1$ nodes for the summation itself, resulting in $3n(n+1) - 1$ nodes in total. The next step of Algorithm 3 is to shift the function to the origin if required, as proposed by [15], and then to normalize by multiplying V_0 with $V_q(\varepsilon_{\text{norm}}\mathbf{1}_n)/V_0(\varepsilon_{\text{norm}}\mathbf{1}_n)$, where $\mathbf{1}_n$ is an n-dimensional vector of ones and $\varepsilon_{\text{norm}}$ a small constant. This last step is a heuristic to scale V_0 such that its range is similar to the range of V_q near the origin. After these preparatory steps, the algorithm returns the result of the stage-wise fitness computation of the shifted and normalized function. The stage-wise fitness computation performed by Algorithm 4 is listed in Table 5.4.

Table 5.4: Successive fitness refinement by a stage-wise fitness computation.

Algorithm 4 Fitness Computation by Stages, called by Algorithm 3. Proposed by [15].

1: **function** ComputeFitnessStages(V)
2: Initialization: $F_\ell \leftarrow 0$, $F_u \leftarrow 1$, $F_m \leftarrow 1/2$ ▷ Initialize fitness intervals.
3: $F \leftarrow$ ComputeFitness($V, 1$) ▷ Compute fitness at Stage 1 using Algorithm 5.
4: **for** $n_{\text{stage}} \leftarrow 2$ **to** N_s **do** ▷ Loop over all stages for the fitness evaluation.
5: **if** $F \leq F_m$ **then break** ▷ Leave the loop if fitness value not small enough.
6: $F_c \leftarrow$ ComputeFitness(V, n_{stage}) ▷ Compute fitness using Algorithm 5.
7: $F \leftarrow \min\{F, F_c\}$ ▷ Update fitness value taking into account the previous stage.
8: $F_\ell \leftarrow F_m$, $F_m \leftarrow (F_\ell + F_u)/2$ ▷ Update fitness intervals.
9: **return** $1 - F$ ▷ Return the final fitness value corresponding to the function V.

Algorithm 4 implements the stage-wise fitness computation proposed by Banks [15]. The idea is to evaluate individuals on a relatively small number of samples in the first stage. Only individuals with good enough fitness are passed to the next stage for a more detailed evaluation, otherwise the current fitness is returned. This is repeated for N_s stages, where N_s is a parameter provided by the user. This is a heuristic based on interval nesting which avoids wasting evaluations, as only promising individuals are evaluated on the full set of samples.

Remark 35. *All algorithms discussed in this section except Algorithm 2 require some additional sanity checks to work in practice. For example, it must be ensured that all function evaluations like $V(\boldsymbol{x}_s)$ are finite and exist and do not evaluate to not-a-number or infinity when using floating point arithmetic. In such cases, the evaluation of the individual is stopped and the worst possible fitness value is returned. These checks are not explicitly displayed here for the sake of clarity.*

The core of the fitness evaluation is Algorithm 5, displayed in Table 5.5, which is called during the stage-wise fitness computation by Algorithm 4. First, it is ensured that V satisfies the necessary condition for a local minimum at the origin, that its gradient vanishes at $\mathbf{0}_n$. All derivatives are computed symbolically using the automatic differentiation technique, see for example [237]. Moreover, V is limited to not exceed a threshold V_L at $h_L \mathbf{1}_n$, which is outside of the sample region of Algorithm 2, so $h_L > \max_i x_{\text{int},i}$. This is a heuristic to reduce the occurrence of terms that only become significant outside of the sample region. The actual fitness value is comprised of five different quantities. The algorithm loops first over the inner, then over the outer sample region and counts the points where V is positive enough and where $\dot{V}$ is negative or zero in the variables c_V and $c_{\dot{V}}$. These quantities are commonly used for Lyapunov function identification using GP, cf. [15, 89]. We additionally use the cumulative ratios r_V and $r_{\dot{V}}$, compare Line 6–7 and Line 16–17 of Algorithm 5, in order to add some continuity to the fitness value.

Moreover, we use the aforementioned Hessian of V, denoted by $\boldsymbol{H}_V(\boldsymbol{x})$, to incorporate some information about the curvature of V into the fitness value. In contrast to for example [20], we do not require $\boldsymbol{H}_V(\mathbf{0}_n)$ to be positive definite, as this would exclude functions like $V_6(\boldsymbol{x}) = \sum_{i=1}^n x_i^4$, similarly to the lower bound, see also the discussion above Equation (5.3). Instead, we only require a certain portion $k_H \in (0, 1)$ of samples in the inner sampling region to admit a positive definite $\boldsymbol{H}_V(\boldsymbol{x})$. The heuristic here is that at least at some points in the inner region, V should curve upwards. By excluding the outer region from this, it is at least in principle possible to also allow functions like $V_7(x_1) = \log(x_1^2 + 1)$, which has positive curvature only for $|x_1| < 1$ and negative curvature for $|x_1| > 1$, despite being positive definite on the whole $\mathbb{R}$. However, this is also dependent on the sampling region and its segmentation into inner and outer region, so it is only an additional heuristic measure. For an inner region sample point to satisfy the Hessian condition, we require that at this point, all eigenvalues of $\boldsymbol{H}_V$ are larger than some $\varepsilon_H > 0$. The value $h_{\max} > 0$ in Line 10 is used to limit the absolute magnitude of the eigenvalues of $\boldsymbol{H}_V$.

The Hessian evaluation solves the issue with functions of the form $V_5(\boldsymbol{x}) = (c_1 x_1 - c_2 x_2)^2$ discussed before, as its Hessian has a zero eigenvalue and hence the check in Line 9 will fail at every sample point, leading to $c_H = 0$. Since the symbolic computation of $\boldsymbol{H}_V$ is computationally expensive, it is not evaluated at the first stage, but only for $n_{\text{stage}} > 1$.

The overall fitness value is computed by Algorithm 5 from F_1, F_2, F_3, F_4 and F_5. Here, F_1 is the normalized number of samples that satisfy the condition that V is positive and $\dot{V}$ is negative or zero, while F_2 denotes the normalized number of samples contained in the estimated subset of the DOA and F_3 quantifies the Hessian condition, compare Line 26. Moreover, F_4 and F_5 denote one minus the normalized, accumulated ratios computed in Line 6–7 and Line 16–17. Hence, $F_i \in [0,1], \forall i \in \{1,\dots,5\}$ where $F_i = 1$ is the best possible and $F_i = 0$ the worst possible value of F_i in terms of fitness. The overall fitness is the weighted sum of these values, cf. Line 28. This weighting is chosen such that the number of points within the DOA and the Hessian condition are the dominant terms of the overall fitness $F \in [0,1]$ at a given stage. Finally, Algorithm 4 returns $1 - F$ instead of F as the GP algorithm was implemented to perform minimization.

Table 5.5: Fitness computation based on Monte-Carlo sampling and Hessian evaluation.

Algorithm 5 Fitness Computation, called by Algorithm 4.

1: **function** ComputeFitness(V, n_{stage})
2: Initialize: $r_V \leftarrow 0$, $r_{\dot{V}} \leftarrow 0$, $c_V \leftarrow 0$, $c_{\dot{V}} \leftarrow 0$, $k_{\text{mc}} \leftarrow 0$, $c^* \leftarrow \infty$ ▷ Local variables.
3: Let $\boldsymbol{x}_k^T$ denote the $\big(2N_x(n_{\text{stage}}-1)+k\big)$-th row of $\boldsymbol{X}_s$ ▷ Notation, see also Algorithm 2.
4: **if** $\text{grad}(V)|_{\boldsymbol{x}=\boldsymbol{0}_n} \neq \boldsymbol{0}_n^T$ or $V(h_L \boldsymbol{1}_n) \notin (0, V_L]$ **then return** 0 ▷ Check gradient and range.
5: **for** $k \leftarrow 1$ **to** N_x **do** ▷ Loop for inner region.
6: $r_V \leftarrow r_V + \max\{0, -V(\boldsymbol{x}_k)\}/(\max\{0, -V(\boldsymbol{x}_k)\} + 1)$ ▷ Update r_V based on $V(\boldsymbol{x}_k)$.
7: $r_{\dot{V}} \leftarrow r_{\dot{V}} + \max\{0, \dot{V}(\boldsymbol{x}_k)\}/(\max\{0, \dot{V}(\boldsymbol{x}_k)\} + 1)$ ▷ Update $r_{\dot{V}}$ based on $\dot{V}(\boldsymbol{x}_k)$.
8: **if** $n_{\text{stage}} > 1$ **then** ▷ Do not evaluate Hessian in first stage.
9: **if** $\min_{i\in\{1,\dots,n\}} \lambda_i\big(\boldsymbol{H}_V(\boldsymbol{x}_k)\big) > \varepsilon_H$ **then** $c_H \leftarrow c_H + 1$ ▷ Evaluate Hessian.
10: **if** $\exists i \in \{1,\dots,n\} : |\lambda_i\big(\boldsymbol{H}_V(\boldsymbol{x}_k)\big)| > h_{\max}$ **then return** 0 ▷ Limit curvature.
11: **if** $V(\boldsymbol{x}_k) > 0$ **then** $c_V \leftarrow c_V + 1$ ▷ Count points where V is positive.
12: **if** $\dot{V}(\boldsymbol{x}_k) \leq 0$ **then** $c_{\dot{V}} \leftarrow c_{\dot{V}} + 1$ ▷ Count points where $\dot{V}$ negative or zero.
13: **if** $0 < V(\boldsymbol{x}_k) < c^*$ and $\dot{V}(\boldsymbol{x}_k) \geq 0$ **then** $c^* \leftarrow V(\boldsymbol{x}_k)$ ▷ Update level curve.
14: **if** $V(\boldsymbol{x}_k) \leq 0$ **then** $c^* \leftarrow V_\varepsilon(\boldsymbol{x}_k)$ ▷ Ensure $c^* > 0$. See also (5.3).
15: **for** $k \leftarrow N_x + 1$ **to** $2N_x$ **do** ▷ Loop for outer region.
16: $r_V \leftarrow r_V + \max\{0, -V(\boldsymbol{x}_k)\}/(\max\{0, -V(\boldsymbol{x}_k)\} + 1)$ ▷ Update r_V based on $V(\boldsymbol{x}_k)$.
17: $r_{\dot{V}} \leftarrow r_{\dot{V}} + \max\{0, \dot{V}(\boldsymbol{x}_k)\}/(\max\{0, \dot{V}(\boldsymbol{x}_k)\} + 1)$ ▷ Update $r_{\dot{V}}$ based on $\dot{V}(\boldsymbol{x}_k)$.
18: **if** $V(\boldsymbol{x}_k) > V_\varepsilon(\boldsymbol{x}_k)$ **then** $c_V \leftarrow c_V + 1$ ▷ Count points where V is positive enough.
19: **if** $\dot{V}(\boldsymbol{x}_k) \leq 0$ **then** $c_{\dot{V}} \leftarrow c_{\dot{V}} + 1$ ▷ Count points where $\dot{V}$ is negative or zero.
20: **if** $V_\varepsilon(\boldsymbol{x}_k) < V(\boldsymbol{x}_k) < c^*$ and $\dot{V}(\boldsymbol{x}_k) \geq 0$ **then** $c^* \leftarrow V(\boldsymbol{x}_k)$ ▷ Update level curve.
21: **if** $V(\boldsymbol{x}_k) \leq V_\varepsilon(\boldsymbol{x}_k)$ **then** $c^* \leftarrow V_\varepsilon(\boldsymbol{x}_k)$ ▷ Ensure c^* is large enough.
22: **for** $k \leftarrow 1$ to $2N_x$ **do** ▷ Loop for inner and outer region.
23: **if** $k \leq N_x$ **then** $c_\ell \leftarrow 0$ **else** $c_\ell \leftarrow V_\varepsilon(\boldsymbol{x}_k)$ ▷ Assign lower bound for V.
24: **if** $c_\ell < V(\boldsymbol{x}_k) < c^*$ and $\dot{V}(\boldsymbol{x}_k) \leq 0$ **then** $k_{\text{mc}} \leftarrow k_{\text{mc}} + 1$ ▷ Estimate DOA size.
25: **if** $n_{\text{stage}} = 1$ or $c_H/N_x \geq k_H$ **then** $c_H \leftarrow N_x$ ▷ Adjust Hessian evaluation.
26: $F_1 \leftarrow (c_V + c_{\dot{V}})/(4N_x)$, $F_2 \leftarrow k_{\text{mc}}/(2N_x)$, $F_3 \leftarrow c_H/N_x$ ▷ Discontinuous fitness portion.
27: $F_4 \leftarrow 1 - r_V/(2N_x)$, $F_5 \leftarrow 1 - r_{\dot{V}}/(2N_x)$ ▷ Continuous fitness portion.
28: **return** $(F_1 + N_x F_2 + N_x F_3 + F_4 + F_5)/(2N_x + 3)$ ▷ Return overall fitness F.

The general optimization options for the GP algorithm are displayed in Table 5.6. These are applied to all considered GP based optimization problems in this work.

Table 5.6: General optimization parameters used for the GP algorithm.

Parameter	**Value**	**Parameter**	**Value**
Population size	100	Selection	Rank selection
Number of generations	10000	Recombination	Subtree crossover
Selection pressure	1.5	Initialization	Ramped half-and-half
Point mutation rate	0.05	Subtree mutation rate	0.02
Node mutation rate	0.3	Crossover rate	0.5
Elitism rate	0.03	Random rate	0.05
Maximum tree depth (grow)	10	Maximum tree depth (full)	5

For selection, the standard rank selection mechanism with selection pressure is used, compare Section 2.3.1. Recombination is performed by subtree crossover, where the crossover points for the selected individuals are drawn from a discrete uniform distribution. The crossover rate of 0.5 means that 50% of non-elite, non-random individuals are replaced with offspring at each generation. The elitism rate of 0.03 means the 3 fittest of the 100 individuals are copied into the next generation, while the random rate of 0.05 means that 5 random individuals are inserted into the population at each generation.

Initialization is done using the ramped half-and-half initialization technique, see Section 2.3.2, so 50 individuals are initialized using the "grow" technique with a maximum tree depth of 10 and 50 individuals using the "full" initialization technique with a maximum (fixed) tree depth of 5. Also, the 5 random individuals are created at each generation using this techniques, 3 with the grow and 2 with the full initialization technique.

Mutation is performed with a certain probability for every new individual, except for the 5 randomly generated individuals, such that only individuals formed by recombination are mutated. First, point mutation is performed, where the probability for point mutation is set to 5%. Thereafter, subtree mutation is performed in 2% of the cases, where a random node (drawn from a discrete uniform distribution) is replaced by a randomly generated subtree. The random subtree is generated using the grow technique with a maximum tree depth of 10. When point mutation happens, each expression node of the individual is point-mutated with a certain probability, in this work with a chance of 30%, denoted by node mutation rate. Point mutation of non-terminals and variables is performed by drawing the new non-terminal/variable from a discrete uniform distribution. Constants are point-mutated by adding a random value which is either zero or uniformly drawn from one of the intervals $[-0.1, 0.1]$, $[-1, 1]$ or $[-10, 10]$. Which of these four cases is applied is randomly determined using a discrete uniform distribution. Additionally, when mutation happens at a specific variable or constant node, there is a 50% chance that a constant node is changed to a variable node, where the variable is chosen from a discrete uniform distribution. Similarly, a variable node has a 50% chance to be mutated to a constant node, where the value is uniformly drawn from the interval $[-5, 5]$.

Constants for creation of random individuals (both for initialization and for insertion during the optimization) are drawn uniformly from the interval $[-1, 1]$. Moreover, we use $N_x = 100$ samples for Algorithm 2 and $N_s = 10$ stages for Algorithm 4 while N_{node} is computed by (5.5) with $k_{\text{node}} = 2$. Furthermore, $k_H = 0.3$, $\varepsilon = 10^{-6}$, $\varepsilon_H = 10^{-5}$, $\varepsilon_{\text{norm}} = 10^{-6}$, $h_{\text{norm}} = 10^6$, $h_L = 1000$, $V_L = 3 \times 10^{15}$ and $h_{\max} = 10^{15}$ is used. Equality for a zero gradient in Line 4 of Algorithm 5 is determined using a tolerance of 10^{-12}.

Following, the proposed GP based algorithm for Lyapunov function identification is evaluated on two benchmark systems and on the zero dynamics of the 2WD TCS from Chapter 3.

5.3 Evaluation and Results

5.3.1 Nonlinear System with Non-Polynomial Lyapunov Function

The first considered benchmark system is a nonlinear planar system with polynomial vector field proposed by Ahmadi *et al.* [4] which is given by

$$\dot{x}_1 = -x_1 + x_1 x_2 \,, \dot{x}_2 = -x_2 \,. \tag{5.6}$$

This system is used by Ahmadi *et al.* [4] as an example of a system with polynomial vector field that is globally asymptotically stable but does not admit a polynomial Lyapunov function which proves this. Instead, global asymptotic stability is demonstrated in [4] using the Lyapunov function

$$V(\boldsymbol{x}) = \log(x_1^2 + 1) + x_2^2 \,, \tag{5.7}$$

which is positive definite on the whole $\mathbb{R}^2$, radially unbounded and its time derivative satisfies $\dot{V}(\boldsymbol{x}) = -\big(x_1^2 + 2x_2^2 + x_1^2 x_2^2 + (x_1 - x_1 x_2)^2\big)/(1 + x_1^2) \prec 0$, compare [4]. Here, log denotes the natural logarithm. Following, we apply the GP based Lyapunov identification method proposed in Section 5.2 to find a Lyapunov function for the system (5.6), which here serves as a benchmark test. For the general GP settings, the parameters from Table 5.6 are used, see also the end of Section 5.2. Moreover, we use $\boldsymbol{x}_{\text{int}}^T = \begin{bmatrix} x_{\text{int},1} & x_{\text{int},2} \end{bmatrix} = \begin{bmatrix} 50 & 50 \end{bmatrix}$ and $\boldsymbol{a}^T = \begin{bmatrix} a_1 & a_2 \end{bmatrix} = \begin{bmatrix} 0.01 & 0.01 \end{bmatrix}$ for the generation of state space samples by Algorithm 2. The context free grammar used for representation of solutions is defined in BNF as $\mathcal{G} = (\mathcal{N}, \Sigma, \mathcal{P}, \mathcal{S})$ with $\mathcal{N} = \{\langle e\rangle, \langle o\rangle, \langle u\rangle, \langle v\rangle, \langle c\rangle\}$, $\Sigma = \{+, -, \times, \text{square}, \log, \text{id}, x_1, x_2, C, (,), \,,\}$ and $\mathcal{S} = \langle e\rangle$, where $\text{square}(x_1) = x_1^2$, log is the natural logarithm and $\text{id}(x_1) = x_1$ the identity function. The identity function is included so that nesting of unary functions can be reduced by point mutation. The production rules $\mathcal{P}$ are given by $\langle e\rangle \mapsto \langle o\rangle(\langle e\rangle, \langle e\rangle) \mid \langle u\rangle(\langle e\rangle) \mid \langle v\rangle \mid \langle c\rangle$, $\langle o\rangle \mapsto + \mid - \mid \times$, $\langle u\rangle \mapsto \text{square} \mid \log \mid \text{id}$, $\langle v\rangle \mapsto x_1 \mid x_2$ and $\langle c\rangle \mapsto C$ where C is the ephemeral constant, cf. Section 2.3.2.

The GP algorithm is executed 100 times, resulting in different results due to the randomness of the method. In all 100 runs, the GP algorithm finds a solution with the best possible fitness $F = 1$. An example solution identified by the GP algorithm is given by

$$V(\boldsymbol{x}) = 0.39998 \log(1.5x_1^2 + 1) + 0.39998 x_2^2 = k_1\big(\log(k_2 x_1^2 + 1) + x_2^2\big) \,, \tag{5.8}$$

with $k_1 = 0.39998$, $k_2 = 1.5$. Moreover, it follows that $V(\boldsymbol{x}) \succ 0$ for all $k_1 > 0$, $k_2 > 0$ and

$$\dot{V}(\boldsymbol{x}) = -\frac{k_1}{k_2 x_1^2 + 1} \boldsymbol{m}(\boldsymbol{x})^T \boldsymbol{Q} \boldsymbol{m}(\boldsymbol{x}) \text{ with } \boldsymbol{m}(\boldsymbol{x}) = \begin{bmatrix} x_1 \\ x_2 \\ x_1 x_2 \end{bmatrix} \text{ and } \boldsymbol{Q} = \begin{bmatrix} 2k_2 & 0 & -k_2 \\ 0 & 2 & 0 \\ -k_2 & 0 & 2k_2 \end{bmatrix} . \tag{5.9}$$

The leading principal minors of $\boldsymbol{Q}$ are $\Delta_1 = 2k_2$, $\Delta_2 = 4k_2$ and $\Delta_3 = 6k_2^2$, so if $k_2 > 0$ then $\boldsymbol{Q} \succ 0$ and for $k_1 > 0$ it follows that $\dot{V}(\boldsymbol{x}) \prec 0$. This demonstrates that the proposed GP algorithm is able to identify a valid Lyapunov function for (5.6), despite the limited sampling region and amount of samples.

It can be noted that although the GP algorithm found a solution with highest possible fitness in all 100 runs, not all of these are suitable for showing global asymptotic stability. In total, 11 out of 100 cases resulted in solutions involving the natural logarithm, while 89 cases were polynomial solutions. The latter cannot be used to show global asymptotic stability, as showed by Ahmadi *et al.* [4], but the GP algorithm could not identify this issue in these cases due to the limited sampling region and number of samples. Another identified function is for example $V(\boldsymbol{x}) = 7.2 \times 10^{-6} x_1^2 \log(3.7x_1^2 + 0.24x_2^2 + 6.96)^2 + x_2^2$, which despite the logarithm has a positive time derivative at $x_1 = 100$, $x_2 = 2$. Finally, choosing a suitable grammar and region in the state space for sampling can be challenging. Here, we included the logarithm in the grammar, but whether this is required is generally not known beforehand. Nevertheless, the results demonstrate that with a suitable grammar, the proposed method is able to find a Lyapunov function for (5.6). Following, we apply the method to another benchmark system for further evaluation.

5.3.2 Nonlinear System with Polynomial Lyapunov Function of Fourth Degree

The second considered benchmark system is a nonlinear planar system with polynomial vector field taken from Parrilo and Lall [223] which is given by

$$\dot{x}_1 = -x_1 + (1 + x_1)x_2\,, \dot{x}_2 = -(1 + x_1)x_1\,. \tag{5.10}$$

They show that this system is globally asymptotically stable as it admits the Lyapunov function

$$V(\boldsymbol{x}) = 6x_1^2 - 2x_1x_2 + 8x_2^2 - 2x_2^3 + 3x_1^4 + 6x_1^2x_2^2 + 3x_2^4\,, \tag{5.11}$$

which can be written as a sum of squares with $V(\boldsymbol{x}) = 3x_1^4 + 6x_1^2x_2^2 + (p_1x_1 + p_2x_2 + p_3x_2^2)^2 + (p_2x_1 + p_4x_2 + p_5x_2^2)^2 + (p_3x_1 + p_5x_2 + p_6x_2^2)^2$ where $p_1 \approx -2.442$, $p_2 \approx 0.19071$, $p_3 \approx 0.010137$, $p_4 \approx -2.8133$, $p_5 \approx 0.22112$, $p_6 \approx -1.7178$ and $V(\boldsymbol{x}) \succ 0$. They also show that $-\dot{V}(\boldsymbol{x})$ can be written as a (positive definite) sum of squares, compare [223]. Since (5.11) is radially unbounded, global asymptotic stability follows.

Next, we apply GP to search for a Lyapunov function for system (5.10). The general GP settings used here are listed in Table 5.6 and at the end of Section 5.2. As previously, we use $\boldsymbol{x}_{\text{int}}^T = \begin{bmatrix} x_{\text{int},1} & x_{\text{int},2} \end{bmatrix} = \begin{bmatrix} 50 & 50 \end{bmatrix}$ and $\boldsymbol{a}^T = \begin{bmatrix} a_1 & a_2 \end{bmatrix} = \begin{bmatrix} 0.01 & 0.01 \end{bmatrix}$ for Algorithm 2. The context free grammar in BNF is defined as $\mathcal{G} = (\mathcal{N}, \Sigma, \mathcal{P}, \mathcal{S})$ with $\mathcal{N} = \{\langle e\rangle, \langle o\rangle, \langle u\rangle, \langle v\rangle, \langle c\rangle\}$, $\Sigma = \{+, -, \times, \text{square}, \text{id}, x_1, x_2, C, (,), ,\}$, $\mathcal{S} = \langle e\rangle$ and production rules $\mathcal{P}$, given by $\langle e\rangle \mapsto \langle o\rangle(\langle e\rangle, \langle e\rangle) \mid \langle u\rangle(\langle e\rangle) \mid \langle v\rangle \mid \langle c\rangle$, $\langle o\rangle \mapsto + \mid - \mid \times$, $\langle u\rangle \mapsto \text{square} \mid \text{id}$, $\langle v\rangle \mapsto x_1 \mid x_2$ and $\langle c\rangle \mapsto C$ where C is the ephemeral random constant, see also Section 5.3.1. The GP algorithm is again executed 100 times. In all 100 independent runs, the GP algorithm identified a solution with the best possible fitness of $F = 1$. An example solution found by GP (after scaling) is

$$V(\boldsymbol{x}) = 6x_1^2 - 3x_1x_2 + 3x_2^2 + 3x_1^4 + 6x_1^2x_2^2 + 3x_2^4\,. \tag{5.12}$$

Using the SOSTOOLS toolbox [234], we can show that (5.12) and its time derivative admit sum of square decompositions, rounded to three decimal places as

$$V(\boldsymbol{x}) = \boldsymbol{m}_1(\boldsymbol{x})^T \boldsymbol{P} \boldsymbol{m}_1(\boldsymbol{x}) = \begin{bmatrix} x_1 \\ x_2 \\ x_1^2 \\ x_1x_2 \\ x_2^2 \end{bmatrix}^T \begin{bmatrix} 6 & -1.5 & 0 & 0 & 0 \\ -1.5 & 3 & 0 & 0 & 0 \\ 0 & 0 & 3 & 0 & 0 \\ 0 & 0 & 0 & 6 & 0 \\ 0 & 0 & 0 & 0 & 3 \end{bmatrix} \begin{bmatrix} x_1 \\ x_2 \\ x_1^2 \\ x_1x_2 \\ x_2^2 \end{bmatrix} \tag{5.13a}$$

$$-\dot{V}(\boldsymbol{x}) = \boldsymbol{m}_2(\boldsymbol{x})^T \boldsymbol{Q} \boldsymbol{m}_2(\boldsymbol{x}) = \begin{bmatrix} x_1 \\ x_2 \\ x_1^2 \\ x_1x_2 \end{bmatrix}^T \begin{bmatrix} 9 & -4.5 & -1.5 & -3.156 \\ -4.5 & 3 & 0.156 & 1.5 \\ -1.5 & 0.156 & 12 & 0 \\ -3.156 & 1.5 & 0 & 12 \end{bmatrix} \begin{bmatrix} x_1 \\ x_2 \\ x_1^2 \\ x_1x_2 \end{bmatrix}. \tag{5.13b}$$

Since $\boldsymbol{P} \succ 0$ and $\boldsymbol{Q} \succ 0$ in (5.13), it follows that the GP algorithm identified with (5.12) a valid Lyapunov function for showing global asymptotic stability of (5.10). Another solution found by the GP algorithm is for example $V(\boldsymbol{x}) = 6x_1^2 - 0.0018132477x_1x_2 + 6x_2^2$, which is locally a valid Lyapunov function for (5.10). However, its time derivative becomes positive for x_1 large enough, so with this Lyapunov function only local stability can be concluded. This limitation is due to the fact that the sampling algorithm can only cover a bounded region of the state space using a limited amount of function evaluations of both V and its time derivative. Nevertheless, the GP algorithm succeeded in finding a valid Lyapunov function for showing global asymptotic stability for both benchmark systems considered in this analysis. Therefore, it can be a useful heuristic if standard methods fail, at least for systems of relatively low order.

Following, the method is applied to the third order zero dynamics of the 2WD TCS derived in Chapter 3. While global asymptotic stability of this system is already proven by Theorem 2, it provides an interesting problem of a real-world system for the proposed method.

5.3.3 Application to Traction Control

The third considered system is given by the zero dynamics of the 2WD TCS of the $\mathcal{M}_5$ synthesis model, derived in Section 3.3.1.1. The ODEs are restated here as

$$\dot{\boldsymbol{z}} = \begin{bmatrix} \dot{z}_1 \\ \dot{z}_2 \\ \dot{z}_3 \end{bmatrix} = \begin{bmatrix} -z_2 \\ \big(2(k_c z_1 - d_c z_2) - r_r F_{xr}\big)/J_r \\ (F_{xr} - F_w)/m \end{bmatrix} . \tag{5.14}$$

The parameters used are listed in Table 6.1 with $\epsilon = 10^{-6}$ for the computation of (3.19), while $\boldsymbol{z}_{\text{int}}^T = \begin{bmatrix} z_{\text{int},1} & z_{\text{int},2} & z_{\text{int},3} \end{bmatrix} = \begin{bmatrix} 50 & 50 & 50 \end{bmatrix}$ and $\boldsymbol{a}^T = \begin{bmatrix} a_1 & a_2 & a_3 \end{bmatrix} = \begin{bmatrix} 0.01 & 0.01 & 0.01 \end{bmatrix}$ is used for Algorithm 2. The context free grammar in BNF is $\mathcal{G} = (\mathcal{N}, \Sigma, \mathcal{P}, \mathcal{S})$ with $\mathcal{N} = \{\langle e\rangle, \langle o\rangle, \langle u\rangle, \langle v\rangle, \langle c\rangle\}$, $\Sigma = \{+, -, \times, \text{square}, \text{id}, z_1, z_2, z_3, C, (,), ,\}$, $\mathcal{S} = \langle e\rangle$ and production rules $\mathcal{P}$, which are given by $\langle e\rangle \mapsto \langle o\rangle(\langle e\rangle, \langle e\rangle) \mid \langle u\rangle(\langle e\rangle) \mid \langle v\rangle \mid \langle c\rangle$, $\langle o\rangle \mapsto + \mid - \mid \times$, $\langle u\rangle \mapsto \text{square} \mid \text{id}$, $\langle v\rangle \mapsto z_1 \mid z_2 \mid z_3$ and $\langle c\rangle \mapsto C$ where C is the ephemeral random constant. The GP algorithm is again executed 100 times. For this system, the success rate of the algorithm drops significantly, compared to the two previously considered benchmark examples. While for the benchmark examples from Section 5.3.1 and Section 5.3.2, in each run the GP algorithm identified a solution with the best possible fitness, it achieves this for the zero dynamics of the 2WD TCS only in 9 out of 100 runs. One example solution identified by the GP algorithm (after scaling, coefficients rounded to four decimal places) is given by

$$V(\boldsymbol{z}) = 5300 z_1^2 + 1.5021 z_2^2 + 975.1 z_3^2 . \tag{5.15}$$

The Lyapunov function obtained by an application of the Kalman-Yakubovich-Popov Lemma to the sign-preserving Lur'e formulation of the zero dynamics of the 2WD TCS from Section 4.2.2 is, for the vehicle parameters from Table 6.1, given by

$$V(\boldsymbol{z}) = 5300 z_1^2 + 1.5 z_2^2 + 975 z_3^2 . \tag{5.16}$$

So in this optimization run, the GP algorithm approximated the analytic solution obtained by the passivity analysis in Section 4.2.2. It can be noted that despite the similarity, (5.15) is not suitable as an actual Lyapunov function as its derivative along solutions of (5.14) is positive at $z_1 = 0.79$, $z_2 = 0.3651$, $z_3 = 0.1204$, for example. The GP algorithm did not identify this due to the limited number of sample points, so increasing the number of state space samples might lead to a better approximation of the actual solution. Another solution with the maximum fitness value identified by the GP algorithm (after scaling, coefficients rounded to two decimal places) is

$$V(\boldsymbol{z}) = 517975.41 z_1^2 + 145.18 z_2^2 + 92614.15 z_3^2 - 2.47 z_1 z_2 . \tag{5.17}$$

The Lyapunov function from (3.83), used in the proof of Theorem 2 to show global asymptotic stability of the zero dynamics (5.14), assuming here $\epsilon = 10^{-6}$, $\gamma = 7/2$ and the vehicle parameters from Table 6.1, with coefficients rounded to two decimal places, is given by

$$V(\boldsymbol{z}) = 517975.41 z_1^2 + 146.60 z_2^2 + 95287.01 z_3^2 - z_1 z_2 . \tag{5.18}$$

In this optimization run, the GP algorithm evidently approximated a numerical instance of the class of parametric Lyapunov functions used for the stability analysis in Section 3.3.2. It can be noted that (5.17) is not suitable as an actual Lyapunov function for showing global asymptotic stability, as its time derivative is positive for example at $z_1 = -0.064$, $z_2 = 0.199$, $z_3 = 0.066$, in contrast to (5.18), which is (except for the rounded coefficients) a Lyapunov function for (5.14) by Theorem 1 and Theorem 2. Like for the previous example solution (5.15), this can be explained by the limited number of sample points available for computing the fitness value. While the GP algorithm with the proposed fitness function was able to identify exact solutions for the first two considered benchmark problems, the algorithm identified some approximate solutions for the zero dynamics of the TCS. In the following, a review of the proposed heuristic method for Lyapunov function identification is given and some possible extensions of the method are discussed.

5.4 Discussion and Potential Extensions

In summary, the GP algorithm succeeds in finding a valid Lyapunov function for the first two systems and delivers an approximation of a valid solution for the zero dynamics of the 2WD TCS. The latter example highlights the limitations of the method: besides the lower success rate of identifying a solution with the best possible fitness, also the runtime of the algorithm increases for the third example. The system from Section 5.3.1 required 7.1 minutes, while the system from Section 5.3.2 required 31.3 minutes for 100 optimization runs. The zero dynamics of the 2WD TCS required 23.93 hours for 100 optimization runs. All GP experiments are conducted on a computer with Intel® Core i7 processor with 2.6 Gigahertz and 32 Gigabyte random access memory, using Microsoft® Windows 10 Enterprise as operating system. The GP algorithm is implemented in C++ and compiled as a 64 bit application using Microsoft® Visual Studio Professional 2015. The fitness evaluation of the individuals at each generation is parallelized using the Microsoft® Parallel Patterns Library.

Considering the results for the zero dynamics of the 2WD TCS, the GP algorithm approximated in some runs the Lyapunov function obtained from the sign-preserving Lur'e formulation from Section 4.2.2, compare (5.15). This is interesting, because by Lemma 19, the time derivative of this Lyapunov function is only negative semi-definite. Therefore, the inner optimization problem (5.1e) for finding the level curve in the original problem (5.1) results for such a function always in $c^* = 0$ because $\dot{V}(\boldsymbol{z}) = 0$ arbitrarily close to the origin and hence $\Omega_0 = \emptyset$. The reason why the GP algorithm nevertheless identified this function here with the best possible fitness is due to the sampling of the state space, since $\dot{V}(\boldsymbol{z})$ in this case is only zero for $z_2 = z_3 = 0$, which is unlikely to occur using random samples from a uniform continuous distribution. Although the algorithm for generating the state space samples demands for the first n samples one zero component, compare Line 7 in Algorithm 2, this does not exclude a negative semi-definite $\dot{V}$ here because the remaining components of the samples are still drawn randomly.

In general, the method used for estimating a subset of the DOA in the proposed fitness function is only a heuristic as indicated in Figure 5.1 and discussed in Section 5.2. For example, Algorithm 5 does not ensure that the computed subset is connected or that the level curve $V(\boldsymbol{z}) = c^*$ does not intersect the boundary of the user-defined sampling region that is spanned by $[-x_{\text{int},1}, x_{\text{int},1}] \times [-x_{\text{int},2}, x_{\text{int},2}] \times \cdots \times [-x_{\text{int},n}, x_{\text{int},n}]$. Therefore, the computed subset will generally deviate from Ω_0 as defined in (5.1). One possible extension of the proposed fitness function is therefore to use a different method for the DOA estimation. For example, Giesl *et al.* [82] propose a method to compute connected sublevel sets by triangulation of the considered subset of the state space, which would provide a solution for the above mentioned limitations of the fitness function. A combination of the GP algorithm with this approach would therefore be interesting and warrants further research. However, it can also be noted that despite the mentioned limitations, the proposed heuristic method succeeded in identifying a valid Lyapunov function for the first two considered benchmark examples and generated different approximate solutions for the zero dynamics of the 2WD TCS. Therefore, it can be a useful heuristic when searching for Lyapunov functions for nonlinear dynamical systems.

As already mentioned in Section 2.3.2, symbolic optimization can be applied to various other control related problems as well. Apart from the GP based Lyapunov function identification approach proposed here, we also considered synthesis of feedback controllers, see [301, 302, 303] and supervised a work on the synthesis of feedforward controllers [298] and on a method for rating dynamic drifting maneuvers in real-time [299]. These methods were based on grammatical evolution [217], an optimization method similar to GP.

This concludes the analysis of the proposed method for Lyapunov function identification by GP. In the following, a theoretical analysis of the 2WD TCS and an experimental evaluation of the 2WD and the 4WD TCSs is presented with different test vehicles.

6 Experiments

Summary. *In this chapter, a detailed analysis of the proposed TCSs, for both vehicles with 2WD and on-demand 4WD torque bias systems is carried out. The main contributions are:*

1. *Validation of the longitudinal model by comparing the simulation results with measurements from experiments with a test vehicle.*
2. *LTI reformulation of the proposed control design, comparison with PID control and analysis in the frequency domain.*
3. *Experimental evaluation of the TCSs on different challenging maneuvers, comparison with DCU based traction control and other control methods.*

This chapter is partially based on our publications [302], [307] [300] and [304].

6.1 Validation of the Longitudinal Model

Before the proposed TCSs are evaluated in detail in a test vehicle, a validation of the longitudinal model is presented. For this purpose, the control structure shown in Figure 3.4 is implemented in MATLAB® Simulink®, where the $\mathcal{M}_5$ model (3.22) with an additional actuator delay of 10 ms is used to model the vehicle. Numerical simulation is performed for the continuous dynamics of the $\mathcal{M}_5$ model with a Runge-Kutta-4 solver using a simulation step time of 1 ms. The TCS is executed with a fixed, discrete sample time of 10 ms, where all dynamic parts of the controller where discretized using the Tustin transformation and zero order hold elements are used for the interface of the discrete controller with the continuous $\mathcal{M}_5$ model.

The TCS in the test vehicle is implemented on a dSPACE® MicroAutoBox II embedded real-time system for rapid control prototyping (RCP), where the signals transmitted to the ECU are bypassed and modified during runtime in order to realize the controller. The test vehicle used for the model validation is equipped with a twin-turbocharged spark ignition engine with direct injection and six in-line cylinders.

The maneuver for the validation of the model is a longitudinal acceleration with a sudden change of the friction coefficient. At the start of the maneuver, the vehicle is accelerating on dry asphalt with $\mu \approx 1$, then the friction coefficient drops down to $\mu \approx 0.1$, which is comparable to polished ice. In the experiment, this is realized with wet glass tiles, which have a comparable friction coefficient to ice. In this situation, the controller has to reduce the requested torque quickly in order to stabilize the wheel dynamics. Figure 6.1 shows the trajectories of $x_4 = \omega_r$, $y_1 = x_3/i_G = \omega_c/i_G$ and the setpoint $r_1 = \omega_{c,d}$, which is generated according to (3.115). The target slip $\lambda_{xr,d}$ is generated on the DCU and determined experimentally such that it is located close to the optimal, traction maximizing value. Figure 6.1a shows the results of the simulation, while Figure 6.1b shows the experimental results for the described maneuver. As mentioned in Section 3.2.1, the first order lag element (3.1) does not model the whole operating range of an ICE, as it does not include the dynamics of the turbocharger, for example. Hence, the actuator model from [290] is used here to reach the initial wheel speed of $\omega_r \approx 40\,\mathrm{rad/s}$. During torque reduction, this model reduces to (3.1), with the above mentioned actuator delay of 10 ms. The $\mathcal{M}_5$ model is able to reproduce the experimental results with sufficient accuracy as both the amplitude and the frequency of the drivetrain oscillation of the simulation match the experimental results well. Also, it can be seen that the controller successfully stabilizes the nonlinear wheel dynamics and is able to track the setpoint while damping drivetrain oscillations.

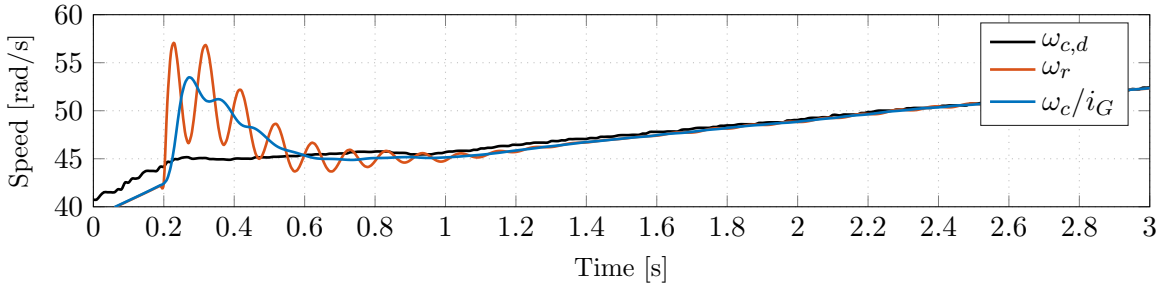

(a) Controlled rear axle and crankshaft speed (simulation).

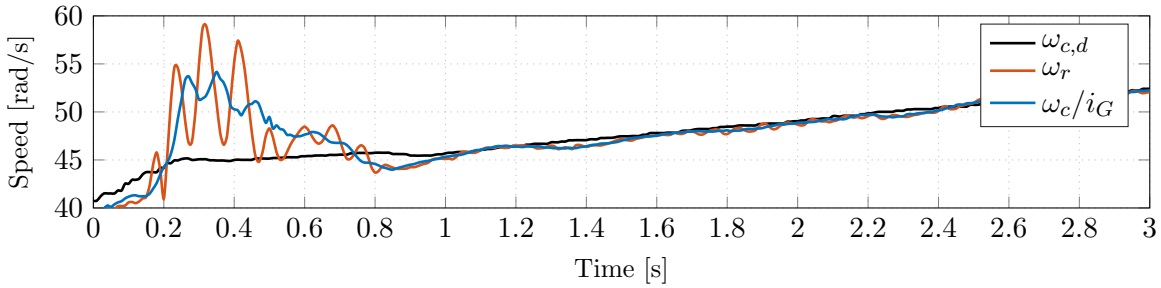

(b) Controlled rear axle and crankshaft speed (measurement).

Figure 6.1: Comparison between simulation and experiment.

The vehicle parameters used for the simulation are given in Table 6.1, with $\epsilon = 10^{-6}$ in (3.19). Further validation of the longitudinal model used in this work can be found in [307]. The parameters of the $\mathcal{M}_7$ model can be found in the Appendix A.5, see Table A.1 and Table A.2. For details on the tire parameter identification see also [297]. We proceed with a theoretical analysis of the proposed 2WD TCS. For this purpose, a standard PID controller is designed as a benchmark, which is then compared to the proposed controller based on IOL.

Table 6.1: Parameters of the $\mathcal{M}_5$ model [305].

Name	Description	Value	Unit
τ_m	Motor time constant	0.02	s
J_c	Aggregated inertia of the drive side	0.23	$\mathrm{kg\,m^2}$
J_r	Rear axle inertia	3	$\mathrm{kg\,m^2}$
r_r	Radius of the rear wheels	0.33	m
m	Vehicle mass	1950	kg
k_c	Aggregated drivetrain torsional stiffness	5300	$\mathrm{N\,m/rad}$
d_c	Aggregated drivetrain damping constant	15	$\mathrm{N\,m\,s/rad}$
ρ	Air density	1.1	$\mathrm{kg/m^3}$
A_{st}	Vehicle frontal area	2.37	$\mathrm{m^2}$
c_w	Aerodynamic drag coefficient	0.3	–
g	Gravitational acceleration	9.81	$\mathrm{m/s^2}$
i_G	Total gear ratio (2. gear)	8.98	–
l_f	Distance front axle to COG	1.3	m
l_r	Distance rear axle to COG	1.4	m
B_r	Pacejka stiffness factor of the rear tires	10.3	–
C_r	Pacejka shape factor of the rear tires	1.8	–

6.2 Theoretical Evaluation

6.2.1 Linear Control Law Representation

For a frequency domain analysis of both the proposed TCS and the PID-only control approach, the plant dynamics are linearized using Jacobian linearization. For that purpose, the common assumption is used that the longitudinal vehicle speed changes significantly slower than the other state variables of the $\mathcal{M}_5$ model from (3.22). Then, $\dot{x}_5 \approx 0$ and so $x_5 = x_{5,0}$ can be assumed to be constant over the considered time interval. This reduces the dynamics to four state equations, given by $\dot{\boldsymbol{x}} = \boldsymbol{F}(\boldsymbol{x}, u_1, \mu) = \boldsymbol{f}(\boldsymbol{x}, \mu) + \boldsymbol{b}u_1$, $\boldsymbol{y} = \boldsymbol{h}(\boldsymbol{x})$ with

$$\boldsymbol{f}(\boldsymbol{x}, \mu) = \begin{bmatrix} -x_1/\tau_m \\ x_3/i_G - x_4 \\ (x_1 - 2\,T_r/i_G)/J_c \\ (2\,T_r - r_r F_{xr})/J_r \end{bmatrix}, \; \boldsymbol{b} = \begin{bmatrix} 1/\tau_m \\ 0 \\ 0 \\ 0 \end{bmatrix}, \; \boldsymbol{h}(\boldsymbol{x}) = \begin{bmatrix} x_3/i_G \\ x_4 \end{bmatrix} \tag{6.1}$$

and $\boldsymbol{x}^T = \begin{bmatrix} x_1 & x_2 & x_3 & x_4 \end{bmatrix} = \begin{bmatrix} T_m & \Delta\phi_c & \omega_c & \omega_r \end{bmatrix}$, $u_1 = T_{m,d}$, $\boldsymbol{y}^T = \begin{bmatrix} y_1 & y_2 \end{bmatrix} = \begin{bmatrix} \omega_c/i_G & \omega_r \end{bmatrix}$ where T_r, F_{xr} are given by (3.22), but with $x_5 = x_{5,0} = v_{x,0}$ constant, see also (3.6) and (3.4). In contrast to the $\mathcal{M}_5$ model (3.22), the friction coefficient μ and the state x_4 are defined explicitly as (disturbance) input and output, respectively. This will be advantageous for the analysis. The system (6.1) has an equilibrium at $\boldsymbol{x}_0^T = \begin{bmatrix} x_{1,0} & x_{2,0} & x_{3,0} & x_{4,0} \end{bmatrix}$, $u_{1,0}$, μ_0, where

$$x_{1,0} = 2k_c x_{2,0}/i_G \tag{6.2a}$$
$$x_{2,0} = r_r F_{xr,0}/(2k_c) \tag{6.2b}$$
$$x_{3,0} = i_G x_{4,0} \tag{6.2c}$$
$$x_{4,0} = v_{x,0}/\big(r_r(1 - \lambda_{xr,0})\big) \tag{6.2d}$$

and $u_{1,0} = x_{1,0}$. Following, $F_{xr,0}$ denotes F_{xr} evaluated at $\lambda_{xr} = \lambda_{xr,0} = (r_r x_{4,0} - v_{x,0})/(r_r x_{4,0})$ and $\mu = \mu_0$, see (3.6). Note that (6.2) assumes acceleration in forward direction with $v_{x,0} > 0$ and $\lambda_{xr,0} \geq 0$, such that no numerical regularization of $\lambda_{xr,0}$ is required. The equilibrium $(\boldsymbol{x}_0, u_{1,0}, \mu_0)$ is parameterized by the free variables $\lambda_{xr,0}$, $v_{x,0}$, μ_0 and (6.2). Then, after defining $\delta\boldsymbol{x} = \boldsymbol{x} - \boldsymbol{x}_0$, $\delta\boldsymbol{y} = \boldsymbol{y} - \boldsymbol{h}(\boldsymbol{x}_0)$, $\delta u_1 = u_1 - u_{1,0}$ and $\delta\mu = \mu - \mu_0$, the linearized dynamics of (6.1) are given by

$$\delta\dot{\boldsymbol{x}} = \boldsymbol{A}\delta\boldsymbol{x} + \boldsymbol{b}\delta u_1 + \boldsymbol{b}_d\delta\mu \tag{6.3a}$$
$$\delta\boldsymbol{y} = \boldsymbol{C}\delta\boldsymbol{x} \tag{6.3b}$$

with system matrix $\boldsymbol{A} = \boldsymbol{J}_{\boldsymbol{F},\boldsymbol{x}}(\boldsymbol{x}_0, u_{1,0}, \mu_0)$, input vector $\boldsymbol{b} = \boldsymbol{J}_{\boldsymbol{F},u_1}(\boldsymbol{x}_0, u_{1,0}, \mu_0)$, disturbance input vector $\boldsymbol{b}_d = \boldsymbol{J}_{\boldsymbol{F},\mu}(\boldsymbol{x}_0, u_{1,0}, \mu_0)$ and measurement matrix $\boldsymbol{C} = \boldsymbol{J}_{\boldsymbol{h},\boldsymbol{x}}(\boldsymbol{x}_0, u_{1,0}, \mu_0)$. Here, for example, $\boldsymbol{J}_{\boldsymbol{F},\boldsymbol{x}}(\boldsymbol{x}_0, u_{1,0}, \mu_0)$ denotes the Jacobian of $\boldsymbol{F}$ with respect to $\boldsymbol{x}$, evaluated at $\boldsymbol{x} = \boldsymbol{x}_0$, $u_1 = u_{1,0}$ and $\mu = \mu_0$, analogously to (2.24). More explicitly, this procedure gives $\boldsymbol{b}$ as in (6.1), $\boldsymbol{b}_d^T = \begin{bmatrix} 0 & 0 & 0 & -(r_r/J_r)\partial F_{xr}/(\partial\mu)|_{x_4=x_{4,0},\mu=\mu_0} \end{bmatrix}$ and

$$\boldsymbol{A} = \begin{bmatrix} -1/\tau_m & 0 & 0 & 0 \\ 0 & 0 & 1/i_G & -1 \\ 1/J_c & -2k_c/(i_G J_c) & -2d_c/(i_G^2 J_c) & 2d_c/(i_G J_c) \\ 0 & 2k_c/J_r & 2d_c/(i_G J_r) & -\big(2d_c + r_r \partial F_{xr}/(\partial x_4)|_{x_4=x_{4,0},\mu=\mu_0}\big)/J_r \end{bmatrix} \tag{6.4a}$$

$$\boldsymbol{C} = \begin{bmatrix} 0 & 0 & 1/i_G & 0 \\ 0 & 0 & 0 & 1 \end{bmatrix} \tag{6.4b}$$

with

$$\partial F_{xr}/(\partial x_4)|_{x_4=x_{4,0},\mu=\mu_0} = \frac{\mu_0\, F_{zr}\, C_r\, B_r\, v_{x,0} \cos\big(C_r \arctan(B_r\lambda_{xr,0})\big)}{r_r x_{4,0}^2 (B_r^2\lambda_{xr,0}^2 + 1)} \tag{6.5a}$$

$$\partial F_{xr}/(\partial\mu)|_{x_4=x_{4,0},\mu=\mu_0} = F_{zr} \sin\big(C_r \arctan(B_r\lambda_{xr,0})\big)\,. \tag{6.5b}$$

From this linear state space representation, the transfer function matrix of the linearized plant can be derived by

$$\boldsymbol{P}(s) = \begin{bmatrix} P_{11}(s) & P_{12}(s) \\ P_{21}(s) & P_{22}(s) \end{bmatrix} = \boldsymbol{C}(s\boldsymbol{I}_4 - \boldsymbol{A})^{-1}\boldsymbol{B} \tag{6.6}$$

with $\boldsymbol{B} = \begin{bmatrix} \boldsymbol{b} & \boldsymbol{b}_d \end{bmatrix}$. If derivatives in the control law (3.41) and the reference dynamics (3.107) are approximated by linear filters as discussed in Section 3.4, then the controller can be represented in an LTI structure as shown in Figure 6.2.

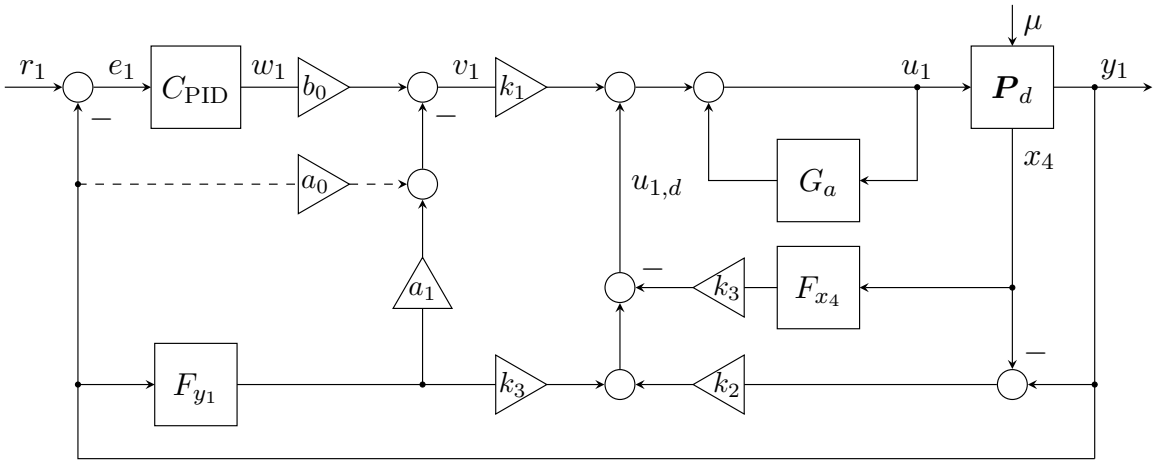

Figure 6.2: LTI representation of the proposed TCS based on IOL with linearized plant.

Here, $a_0 = 0$, $a_1 = 1/\tau_{s,e}$ and $b_0 = i_{G,e}/(\tau_{m,e} J_{r,e})$ as in (3.109). The dashed line indicates that $a_0 = 0$ as in (3.109a) and hence that connection is only included for illustration. Moreover, $k_1 = \tau_{m,e} J_{c,e} i_{G,e}$, $k_2 = 2\tau_{m,e} k_{c,e}/i_{G,e}$, $k_3 = 2\tau_{m,e} d_{c,e}/i_{G,e}$ where $\tau_{m,e}$, $\tau_{s,e}$, $k_{c,e}$, $d_{c,e}$, $J_{c,e}$, $J_{r,e}$, $i_{G,e}$ are controller parameters and estimates of the actual plant parameters $\tau_m, k_c, d_c, J_c, J_r, i_G$. In the continuous, delay-free case, $\tau_{s,e} = \tau_{m,e}$ can be chosen to approximate τ_m. The distinction is made to account for the effect of the delay and discretization by taking $\tau_{s,e} > \tau_{m,e} \approx \tau_m$ as additional tuning parameter. The $C_{\mathrm{PID}}(s)$ controller is defined in (3.110b), the filters $F_{y_1}(s)$ and $F_{x_4}(s)$ in (3.114) and the actuator model by $G_a(s) = 1/(\tau_{s,e} s + 1)$. Finally, a time delay $\tau_{m,d}$ is included in the first input channel of the plant model (6.6) such that

$$\boldsymbol{P}_d(s) = \begin{bmatrix} P_{d,11}(s) & P_{d,12}(s) \\ P_{d,21}(s) & P_{d,22}(s) \end{bmatrix} = \begin{bmatrix} P_{11}(s)\exp(-\tau_{m,d}s) & P_{12}(s) \\ P_{21}(s)\exp(-\tau_{m,d}s) & P_{22}(s) \end{bmatrix} . \tag{6.7}$$

Following, the discretized version $\boldsymbol{P}_d(z)$ is obtained by zero order hold discretization using a sample time of $\tau_s = 0.01\,\mathrm{s}$. Then, the time delay can be absorbed into the plant transfer function such that $\boldsymbol{P}_d(z)$ is a rational function in the discrete z-domain. The dynamic parts of the proposed controller are discretized using the Tustin transformation with the same sample time to obtain $C_{\mathrm{PID}}(z)$, $F_{y_1}(z)$, $F_{x_4}(z)$ and $G_a(z)$. Then, from Figure 6.2 we get

$$U_1(z) = C_{r_1}(z)R_1(z) + C_{y_1}(z)Y_1(z) + C_{\mu}(z)M(z) \tag{6.8a}$$

$$C_{r_1}(z) = \frac{b_0 k_1 C_{\mathrm{PID}}(z)}{1 + k_2 P_{d,21}(z) + F_{x_4}(z)P_{d,21}(z) - G_a(z)} \tag{6.8b}$$

$$C_{y_1}(z) = \frac{k_2 + k_3 F_{y_1}(z) - k_1(a_0 + b_0 C_{\mathrm{PID}}(z) + a_1 F_{y_1}(z))}{1 + k_2 P_{d,21}(z) + F_{x_4}(z)P_{d,21}(z) - G_a(z)} \tag{6.8c}$$

$$C_{\mu}(z) = -\frac{k_2 P_{d,22}(z) + k_3 F_{x_4}(z) P_{d,22}(z)}{1 + k_2 P_{d,21}(z) + F_{x_4}(z)P_{d,21}(z) - G_a(z)} . \tag{6.8d}$$

Here, $R_1(z)$, $U_1(z)$, $Y_1(z)$ and $M(z)$ represent the z-domain versions of their corresponding time-domain functions $r_1(t)$, $u_1(t)$, $y_1(t)$ and $\mu(t)$, respectively. From (6.8), the transfer function from reference input $r_1(t)$ to the system output $y_1(t)$ can be derived as

$$T(z) = \frac{Y_1(z)}{R_1(z)} = \frac{P_{d,11}(z)C_{r_1}(z)}{1 - P_{d,11}(z)C_{y_1}(z)} \,. \tag{6.9}$$

Similarly, the transfer function function from $\mu(t)$ to the system output $y_1(t)$ is given by

$$S_\mu(z) = \frac{Y_1(z)}{M(z)} = \frac{P_{d,12}(z) + P_{d,11}(z)C_{y_1}(z)}{1 - P_{d,11}(z)C_{y_1}(z)} \,, \tag{6.10}$$

while the sensitivity function is $S(z) = 1 - T(z)$. For analysis of tracking a ramp reference input $r_1(t)$, an integrator can be used as pre-filter $F_r(z)$ from the auxiliary reference input $r_{1,a}(t)$ to $r_1(t)$, in the z-domain given by

$$F_r(z) = \frac{R_1(z)}{R_{1,a}(z)} = \frac{\tau_s}{z-1} \,. \tag{6.11}$$

The transfer function from $r_{1,a}(t)$ to $e_1(t)$ is then given by $S_r(z) = F_r(z)S(z)$. For example, using the nominal vehicle parameters from Table 6.1, the controller parameters $k_p = 5$, $k_i = 40$, $k_d = 0.2$, $\tau_d = 0.02\,\mathrm{s}$, $\tau_{m,e} = \tau_m$, $\tau_{s,e} = 5\tau_{m,e}$, $k_{c,e} = k_c$, $d_{c,e} = d_c$, $J_{c,e} = J_c$, $J_{r,e} = J_r$ and $i_{G,e} = i_G$, a sample time of $\tau_s = 0.01\,\mathrm{s}$, a time delay of $\tau_{m,d} = \tau_s$ and the operating point $v_{x,0} = 50\,\mathrm{km/h} = (50/3.6)\,\mathrm{m/s}$, $\mu_0 = 1$, $\lambda_{xr,0} = \lambda^+_{xr,\mathrm{peak}}/2$, with $\lambda^+_{xr,\mathrm{peak}}$ from (3.14a), results in the following transfer functions in minimal realization,

$$T(z) \approx \frac{0.087483(z+0.8424)(z-0.7935)(z-0.9048)(z-0.217)(z^2-1.812z+0.8242)}{(z-0.2219)(z+0.1001)(z^2-1.934z+0.9367)(z^2-1.618z+0.6781)(z^2-1.477z+0.6654)} \tag{6.12a}$$

$$S(z) \approx \frac{(z-1)^2(z-0.232)(z-0.001109)(z^2-1.124z+0.3294)(z^2-1.794z+0.8313)}{(z-0.2219)(z+0.1001)(z^2-1.934z+0.9367)(z^2-1.618z+0.6781)(z^2-1.477z+0.6654)} \tag{6.12b}$$

$$S_\mu(z) \approx \frac{-0.091854(z+1.731)(z+0.6433)(z-0.6385)(z-1)^2(z^2-1.598z+0.7813)}{(z-0.2219)(z+0.1001)(z^2-1.934z+0.9367)(z^2-1.618z+0.6781)(z^2-1.477z+0.6654)} \tag{6.12c}$$

$$S_r(z) \approx \frac{0.01(z-1)(z-0.232)(z-0.001109)(z^2-1.124z+0.3294)(z^2-1.794z+0.8313)}{(z-0.2219)(z+0.1001)(z^2-1.934z+0.9367)(z^2-1.618z+0.6781)(z^2-1.477z+0.6654)} \,. \tag{6.12d}$$

It can be noted that the computation of the transfer function using the equations (6.8), (6.9) and (6.10) is numerically very sensitive. Therefore it is recommended to use the state space representation of the involved transfer functions in order to compute $T(z)$, $S(z)$, $S_\mu(z)$, and $S_r(z)$. The state space representation is included in Appendix A.6. Also, the coefficients of the transfer functions in (6.12) are rounded and only included for an approximate reference. The following analysis in the frequency domain is performed using the numerically more accurate state space representations only.

The above IOL design is compared to a PID-only control design, for which the four considered sensitivity functions are given by $\widetilde{S}(z) = 1 - \widetilde{T}(z)$, $\widetilde{S}_r(z) = F_r(z)\widetilde{S}(z)$ and

$$\widetilde{T}(z) = \frac{P_{d,11}(z)\widetilde{C}_{\mathrm{PID}}(z)}{1 + P_{d,11}(z)\widetilde{C}_{\mathrm{PID}}(z)} \,, \widetilde{S}_\mu(z) = \frac{P_{d,12}(z)}{1 + P_{d,11}(z)\widetilde{C}_{\mathrm{PID}}(z)} \,. \tag{6.13}$$

The tilde is used here to distinguish the transfer functions of the PID-only control design from the transfer functions of the IOL based control design. The PID controller $\widetilde{C}_{\mathrm{PID}}(z)$ is obtained by a Tustin transformation with $\tau_s = 0.01\,\mathrm{s}$ of

$$\widetilde{C}_{\mathrm{PID}}(s) = \widetilde{k}_p + \frac{\widetilde{k}_i}{s} + \frac{\widetilde{k}_d s}{\widetilde{\tau}_d s + 1} \,, \tag{6.14}$$

analogously to the IOL based control design. Here, $\widetilde{k}_p$, $\widetilde{k}_i$, $\widetilde{k}_d$ and $\widetilde{\tau}_d$ are the PID parameters of the PID-only control design. In the following, both control designs are compared with each other in the frequency domain. Focus is set on analyzing how the additional components of the IOL based control design, like the actuator model and the usage of the x_4 measurement influence the closed loop dynamics, compared to the traditional PID-only control structure.

6.2.2 Evaluation and Comparison with PID Control in the Frequency Domain

The first considered structural difference between the IOL based TCS and the PID-only design is the actuator model $G_a(z)$, depicted in Figure 6.2. In order to compare the tracking performance of both controllers for ramp inputs, the Bode magnitude plots of $S_r(z)$ and $\widetilde{S}_r(z)$ for three operating points are shown in Figure 6.3. The dash-dotted line at 50 Hz marks the Nyquist frequency.

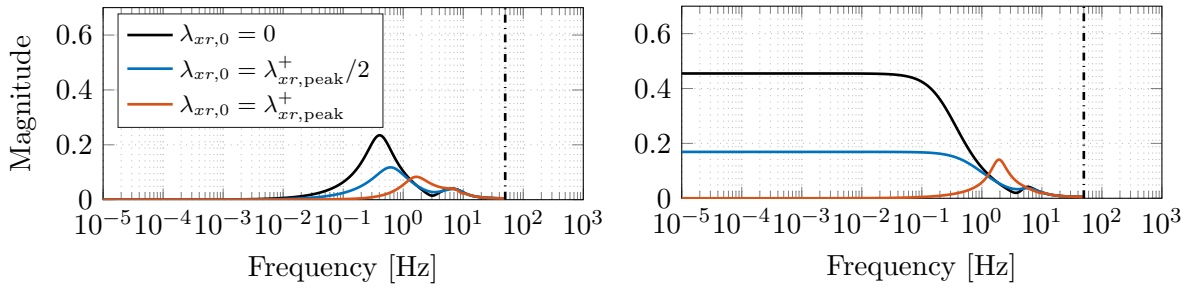

(a) Bode magnitude plots of $S_r(z)$.

(b) Bode magnitude plots of $\widetilde{S}_r(z)$.

Figure 6.3: Bode plots of the IOL based TCS (left) and PID-only TCS (right) at three operating points.

The plot is created with $v_{x,0} = (50/3.6)\,\text{m/s}$, $\mu_0 = 1$, the vehicle parameters from Table 6.1, actuator delay, discretization and IOL controller parameters as described below Equation (6.11). The PID-only parameters are $\widetilde{k}_p = 27.2$, $\widetilde{k}_i = 328$, $\widetilde{k}_d = 0.527$, $\widetilde{\tau}_d = 0.02\,\text{s}$, which were identified in our previous work as a reasonable compromise between performance and robustness [305]. The feedback of the first order actuator model acts as an additional integrator in the forward channel, resulting together with the PID controller of the IOL control design in a type 2 open loop control system. This is required for tracking ramp signals with zero asymptotic error. Figure 6.3a confirms that the IOL design achieves this, independently of the operating point on the tire force curve. Figure 6.3b shows that the PID-only design requires $\lambda_{xr,0} = \lambda^+_{xr,\text{peak}}$, because there the constant term of the denominator polynomial of $P_{11}(s)$ vanishes and hence the plant provides the required integrating behavior. This also provides a theoretical argument that PID-only control can achieve reasonable asymptotic tracking errors, as the goal of a TCS is usually to operate at $\lambda_{xr,0} \approx \lambda^+_{xr,\text{peak}}$, such that the velocity error constant becomes small. The IOL based control design does not have this limitation, as the feedback of the actuator model in conjunction with the PID controller ensures double integrating behavior.

The second considered structural difference between the IOL based TCS and the PID-only design is the implicit PD action on the speed difference between the scaled crankshaft angular velocity y_1 and the rear axle angular velocity x_4, which can be extracted from Figure 6.2 as $U_{1,d}(z) = k_2(Y_1(z) - X_4(z)) + k_3\big[F_{y_1}(z)Y_1(z) - F_{x_4}(z)X_4(z)\big]$, where $U_{1,d}(z)$, $Y_1(z)$ and $X_4(z)$ are the z-domain versions of their corresponding time-domain functions $u_{1,d}(t)$, $y_1(t)$ and $x_4(t)$, while $F_{y_1}(z)$ and $F_{x_4}(z)$ are filters to approximate the time derivatives of $y_1(t)$ and $x_4(t)$. If $F_{y_1} = F_{x_4}$ like in this analysis, then $u_{1,d}(t)$ is generated by a standard PD controller. In order to analyze the effect of the $u_{1,d}(t)$ term on the closed loop system, we use the FRM, given by

$$M_F \overset{\text{def}}{=} \sup_{\omega} \big|F\big(\exp(j\omega\tau_s)\big)\big| \tag{6.15}$$

for a discrete transfer function $F(z)$, where τ_s is the sample time and j the imaginary unit. In the following, the FRM is approximated numerically by evaluating (6.15) at 1000 values for $\omega = 2\pi f$ where f is spaced logarithmically (to base 10) between 10^{-5} Hz and 50 Hz. The maximum of these values is then used as FRM. Using $v_{x,0} = (50/3.6)\,\text{m/s}$, $\lambda_{xr,0} = \lambda^+_{xr,\text{peak}}$ and $\mu_0 = 1$ as an example operating point with the plant and controller parameters from above, we obtain for example $M_{S_\mu} = 8.78$ (the IOL based design) and $M_{\widetilde{S}_\mu} = 20.60$ (the PID-only design).

Let furthermore $S_{\mu,0}$ denote (6.10) computed with the same parameters and operating point, but with $k_{c,e} = d_{c,e} = 0$ such that $k_2 = k_3 = 0$ and hence (6.15) is inactive as then $u_{1,d} = 0$. The FRM in this case evaluates to $M_{S_{\mu,0}} = 18.27$. So using the extra information from the rear axle speed measurement explicitly in the control law leads in this case to a significantly smaller FRM. This shows that the $u_{1,d}$ term can reduce sensitivity of the closed loop system compared to a PID-only design if parameterized correctly.

Since the PID-only control design was not explicitly tuned for a small FRM of $\widetilde{S}_\mu$, a more detailed analysis to confirm these findings is presented in the following. First, let

$$M_{F_1,F_2,F_3} \stackrel{\text{def}}{=} \frac{1}{3}\big(M_{F_1} + M_{F_2} + M_{F_3}\big) \tag{6.16}$$

be a shorthand for the average FRM of three different discrete transfer functions. Since a TCS has to cover a wide range of operating points, we consider different operating points collected in the three vectors $\boldsymbol{\mu}_{\text{op}} \in \mathbb{R}^{n_\mu}$, $\boldsymbol{\lambda}_{\text{op}} \in \mathbb{R}^{n_\lambda}$, $\boldsymbol{v}_{\text{op}} \in \mathbb{R}^{n_v}$ with $n_\mu = 2$, $n_\lambda = n_v = 3$ and

$$\boldsymbol{\mu}_{\text{op}}^T = \begin{bmatrix}\mu_{\text{op},1} & \mu_{\text{op},2}\end{bmatrix} = \begin{bmatrix}0.1 & 1\end{bmatrix} \tag{6.17a}$$

$$\boldsymbol{\lambda}_{\text{op}}^T = \begin{bmatrix}\lambda_{\text{op},1} & \lambda_{\text{op},2} & \lambda_{\text{op},3}\end{bmatrix} = \lambda^+_{xr,\text{peak}} \begin{bmatrix}0.1 & 0.5 & 1\end{bmatrix} \approx \begin{bmatrix}0.01 & 0.06 & 0.12\end{bmatrix} \tag{6.17b}$$

$$\boldsymbol{v}_{\text{op}}^T = \begin{bmatrix}v_{\text{op},1} & v_{\text{op},2} & v_{\text{op},3}\end{bmatrix} = (1/3.6) \begin{bmatrix}10 & 50 & 70\end{bmatrix} \text{m/s} \approx \begin{bmatrix}2.8 & 13.9 & 19.4\end{bmatrix} \text{m/s}\,, \tag{6.17c}$$

which result in a total of $2 \times 3 \times 3 = 18$ different operating points. With (6.16) and (6.17), we can define a cost value for the IOL based design and the PID-only design, given by

$$J_{\text{IOL}} \stackrel{\text{def}}{=} \frac{1}{n_\mu n_\lambda n_v} \sum_{i=1}^{n_\mu} \sum_{j=1}^{n_\lambda} \sum_{k=1}^{n_v} M_{T,S,S_\mu}\,, \text{ with } \mu_0 = \mu_{\text{op},i}, \lambda_{xr,0} = \lambda_{\text{op},j}, v_{x,0} = v_{\text{op},k}\,, \tag{6.18a}$$

$$J_{\text{PID}} \stackrel{\text{def}}{=} \frac{1}{n_\mu n_\lambda n_v} \sum_{i=1}^{n_\mu} \sum_{j=1}^{n_\lambda} \sum_{k=1}^{n_v} M_{\widetilde{T},\widetilde{S},\widetilde{S}_\mu}\,, \text{ with } \mu_0 = \mu_{\text{op},i}, \lambda_{xr,0} = \lambda_{\text{op},j}, v_{x,0} = v_{\text{op},k}\,. \tag{6.18b}$$

The value J_{IOL} describes the average FRM of the three sensitivity functions $T(z)$, $S(z)$, $S_\mu(z)$ (J_{PID} for $\widetilde{T}(z)$, $\widetilde{S}(z)$, $\widetilde{S}_\mu(z)$, respectively), averaged over the operating points from (6.17) as each sensitivity function depends on the operating points. This dependency is not written out explicitly here in favor of a more compact notation. The functions $S_r(z)$ and $\widetilde{S}_r(z)$ are not used here, since the PID-only design cannot remove the steady-state error for operating points with $\lambda_{xr,0} \neq \lambda^+_{xr,\text{peak}}$ when tracking ramp inputs as discussed before. The cost value (6.18b) can then be used in an optimization problem to identify the PID parameters of the PID-only control design which minimize (6.18b). The optimization problem is formulated as

$$J^*_{\text{PID}} = \min \quad J_{\text{PID}} \tag{6.19a}$$

$$\text{over} \quad (\widetilde{k}_p, \widetilde{k}_i, \widetilde{k}_d) \in \mathbb{R}^3 \tag{6.19b}$$

$$\text{subject to} \quad \widetilde{T}(z)\,, \widetilde{S}(z)\,, \widetilde{S}_\mu(z) \text{ stable}, \tag{6.19c}$$

$$|1 - \widetilde{T}(1)| \leq M_0\,, |\widetilde{S}(1)| \leq M_0\,, |\widetilde{S}_\mu(1)| \leq M_0\,. \tag{6.19d}$$

The constraint (6.19c) requires stability of the sensitivity functions, while (6.19d) constrains their steady state values to deviate from the desired values by at most M_0. Here, we choose $M_0 = 0.01$ and require that $\widetilde{T}(1) \approx 1$, $\widetilde{S}(1) \approx 0$ and $\widetilde{S}_\mu(1) \approx 0$. Since an exact solution to (6.19) is out of the scope of this analysis, we limit the search space in the first step to a finite, equidistant grid with $\widetilde{k}_p \in [0, 100]$, $\widetilde{k}_i \in [0, 1000]$, $\widetilde{k}_d \in [0, 2]$ and 100 values for each decision variable, resulting in a total of $100 \times 100 \times 100 = 10^6$ evaluated parameter combinations. The parameter combination with the best cost value is then, in a second step, used as start point for an optimization with the Nelder-Mead simplex method [208], using the MATLAB® `fminsearch` function, whose implementation is based on the publication by Lagarias *et al.* [165]. For the stopping criteria, the termination tolerance for both the function value `TolFun` and the current point `TolX` is set to 10^{-12}.

The results of the analysis are listed in Table 6.2. Also, the FRMs for each operating point and the considered sensitivity functions are listed there individually. The first six columns contain information regarding each operating point. The columns seven to nine contain the FRMs of the PID-only control design with parameters $\widetilde{k}_p = 27.2$, $\widetilde{k}_i = 328$ and $\widetilde{k}_p = 0.527$. Columns ten to twelve contain the FRMs of the optimized PID-only control design according to (6.19) with the identified parameters $\widetilde{k}_p^* = 29.1$, $\widetilde{k}_i^* = 2.13$ and $\widetilde{k}_d^* = 0.25$. The asterisk is used to distinguish the sensitivity optimized PID-only design from the PID-only design proposed in [305]. Finally, the last three columns contain the FRMs of the IOL based control design. The last row contains the cost values of the three control designs.

Looking at the cost values, we obtain $J_{\mathrm{PID}} = 4.24$ for the PID-only design from [305], $J_{\mathrm{PID}}^* = 3.07$ for the PID-only design optimized according to (6.19) and $J_{\mathrm{IOL}} = 2.53$ for the IOL based control design. This demonstrates that the IOL based design can achieve a significantly smaller overall sensitivity compared to the PID-only control design, even when the latter is explicitly optimized for this specification. Especially for $\lambda_{xr,0} = \lambda_{xr,\mathrm{peak}}^+$, the sensitivity to variations of the friction coefficient of the IOL based TCS is significantly lower compared to both PID-only control designs. This is also the case if only a single $v_{x,0}$ is used from (6.17c) and the optimization is performed individually for each $v_{\mathrm{op},k}$ with $k \in \{1, 2, 3\}$. Therefore, even a gain-scheduled PID-only control design which uses the vehicle speed as scheduling variable cannot achieve the same performance according to (6.18) as the IOL based TCS. Using μ_0 or $\lambda_{xr,0}$ as scheduling variables poses challenges as these are highly dynamic and in the case of μ_0 require additional estimation mechanisms. The IOL based TCS achieves relatively low sensitivity compared to the PID only control design without these limitations. In the following, a prototypical implementation of the proposed TCS based on IOL is evaluated in different test vehicles.

Table 6.2: Comparison of frequency response magnitudes of PID-only and IOL based TCSs.

Operating Point						PID-only TCS						IOL based TCS		
i	j	k	μ_0	$\lambda_{xr,0}$	$v_{x,0}$	$M_{\widetilde{T}}$	$M_{\widetilde{S}}$	$M_{\widetilde{S}_\mu}$	$M_{\widetilde{T}^*}$	$M_{\widetilde{S}^*}$	$M_{\widetilde{S}_\mu^*}$	M_T	M_S	M_{S_μ}
1	1	1	0.1	0.01	2.8	1.00	1.50	0.95	1.00	1.42	0.87	1.19	1.81	0.61
1	1	2	0.1	0.01	13.9	1.16	1.32	2.29	1.00	1.27	1.66	1.22	1.72	1.36
1	1	3	0.1	0.01	19.4	1.31	1.29	2.65	1.00	1.24	1.84	1.28	1.70	1.47
1	2	1	0.1	0.06	2.8	1.00	1.39	6.12	1.00	1.33	4.91	1.16	1.76	4.11
1	2	2	0.1	0.06	13.9	1.55	1.41	12.51	1.00	1.25	8.06	1.37	1.68	6.32
1	2	3	0.1	0.06	19.4	1.66	1.50	13.52	1.00	1.26	8.44	1.41	1.69	6.56
1	3	1	0.1	0.12	2.8	2.05	1.81	20.60	1.01	1.30	14.39	1.53	1.73	8.78
1	3	2	0.1	0.12	13.9	2.05	1.81	20.60	1.01	1.30	14.39	1.53	1.73	8.78
1	3	3	0.1	0.12	19.4	2.05	1.81	20.60	1.01	1.30	14.39	1.53	1.73	8.78
2	1	1	1.0	0.01	2.8	1.35	1.72	0.18	1.15	1.58	0.16	1.25	1.85	0.09
2	1	2	1.0	0.01	13.9	1.01	1.59	0.64	1.00	1.49	0.59	1.23	1.83	0.36
2	1	3	1.0	0.01	19.4	1.00	1.55	0.79	1.00	1.46	0.72	1.21	1.82	0.47
2	2	1	1.0	0.06	2.8	1.19	1.66	1.54	1.02	1.54	1.40	1.26	1.84	0.80
2	2	2	1.0	0.06	13.9	1.00	1.47	4.16	1.00	1.40	3.78	1.17	1.80	2.80
2	2	3	1.0	0.06	19.4	1.00	1.43	4.92	1.00	1.36	4.32	1.16	1.78	3.43
2	3	1	1.0	0.12	2.8	2.05	1.81	20.60	1.01	1.30	14.39	1.53	1.73	8.78
2	3	2	1.0	0.12	13.9	2.05	1.81	20.60	1.01	1.30	14.39	1.53	1.73	8.78
2	3	3	1.0	0.12	19.4	2.05	1.81	20.60	1.01	1.30	14.39	1.53	1.73	8.78
Cost Value						$J_{\mathrm{PID}} = 4.24$			$J_{\mathrm{PID}}^* = 3.07$			$J_{\mathrm{IOL}} = 2.53$		

6.3 Experimental Evaluation with Test Vehicles

6.3.1 Comparison of ECU based and DCU based Traction Control

In this section, an experimental evaluation of the proposed ECU based TCS and a comparison to a traditional DCU based TCS, as well as a comparison with a different ECU based control design is presented. Plots that contain data which has been published in our previous work [300, 304] are indicated with a corresponding label in their caption. The setup of the used test vehicles in this work is described in Section 6.1. The maneuver considered here is a longitudinal acceleration, starting on dry asphalt with $\mu \approx 1$, which changes abruptly to $\mu \approx 0.1$ on a watered metal plate and finally changes back to dry asphalt again. These changes of the friction coefficient are depicted in the following figures by vertical dashed lines. Figure 6.4 shows the results of the proposed IOL controller, parameterized experimentally using the Ziegler-Nichols tuning rules for this maneuver, cf. [216, pp. 568–577]. Figure 6.4a shows that the system output y_1 successfully tracks the reference trajectory r_1, after an overshoot of 5.97 rad/s at $t \approx 2.66$ s. Figure 6.4b shows how the controller reduces the requested torque from the driver in order to prevent the wheels from spinning. Figure 6.4c shows the target wheel slip $\lambda_{xr,d}$ and the actual wheel slip λ_{xr} of the rear axle. The slip calculated from the crankshaft speed (scaled to wheel level) instead of the wheel speed by

$$\lambda_{xr,c} = (r_r y_1 - v_x) / \max(|r_r y_1|, |v_x|) \tag{6.20}$$

with $y_1 = \omega_c / i_G$ is included for reference. At $t \approx 11$ s, the offset between r_1 and y_1 is due to rate limitations of the actuator. Hence, the TCS increases the drive torque as fast as possible as the friction coefficient increases abruptly. During the maneuver, drivetrain oscillations are damped such that driving comfort is not negatively affected by the intervention of the TCS.

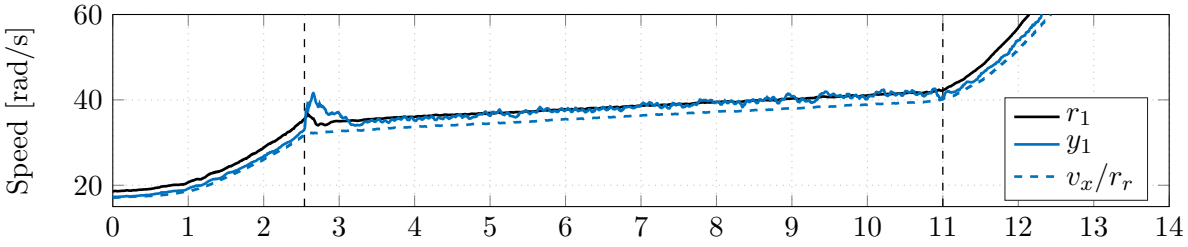

(a) Target and actual speed of the crankshaft and longitudinal vehicle speed [304].

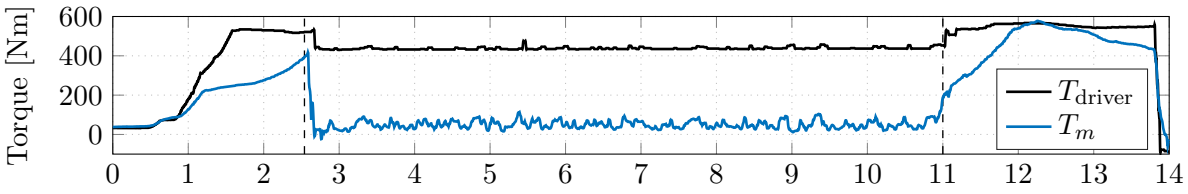

(b) Requested torque by the driver and actual drive torque of the engine.

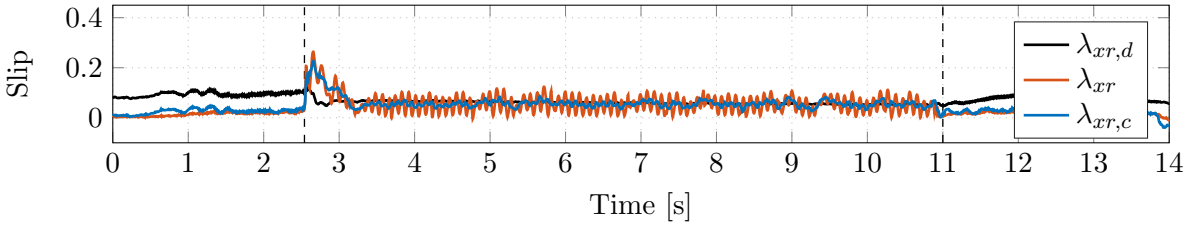

(c) Target slip, average slip of the rear wheels and the slip based on the crankshaft speed.

Figure 6.4: Experimental evaluation of the proposed ECU based TCS using IOL.

Next, the performance of a benchmark ECU based TCS is evaluated on the same maneuver. This analysis is carried out to demonstrate the advantages of the control design based on IOL in comparison to traditional control design techniques which are more commonly used in the industry. The benchmark implementation uses a PI controller in combination with a DOB. Figure 6.5 shows the results of the benchmark TCS on the previously described maneuver. Figure 6.5a depicts the reference trajectory and the system output, as well as the longitudinal speed of the vehicle. The overshoot is 7.6 rad/s and hence larger compared to the control design based on IOL. While the benchmark TCS also achieves asymptotic tracking of the reference speed, a significant undershoot can be observed between $t \approx 2.8\,\mathrm{s}$ and $t \approx 3.8\,\mathrm{s}$. This is not ideal from a performance perspective as the wheel slip, and with that the transmitted tire force, is below potential. The undershoot can also be seen in Figure 6.5c, where the wheel slip decreases to approximately 1.5% during this time interval.

Another issue of the benchmark TCS can be seen at $t \approx 10\,\mathrm{s}$, as the friction coefficient changes from $\mu \approx 0.1$ to $\mu \approx 1$. There, the drivetrain starts to oscillate severely such that the maneuver even has to be interrupted at $t \approx 11.5\,\mathrm{s}$, due to a lack of robustness of this control design with respect to time-varying friction coefficients. In comparison, the IOL based control design does not display such problems and accelerates smoothly after the abrupt increase of the friction coefficient. Figure 6.5b shows the requested torque of the driver and the engine torque. It can be noted that the torque produced by the benchmark controller is smoother than the torque of the IOL control design. This is also due to the benchmark controller computing the torque based on the system output $y_1 = \omega_c / i_G$ only, while the IOL based control design also takes into account the measurement of the wheel speeds, resulting in an active damping mechanism. This experiment also shows the difficulties of finding a robust parameterization for the benchmark controller, while the IOL based control design combines performance, robustness and easy parameterization.

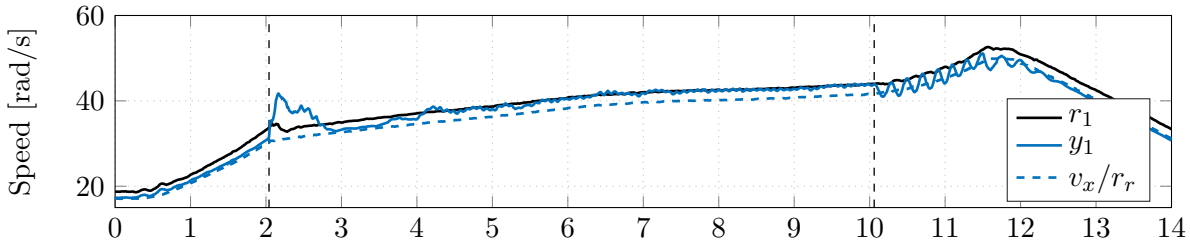

(a) Target and actual speed of the crankshaft and longitudinal vehicle speed [304].

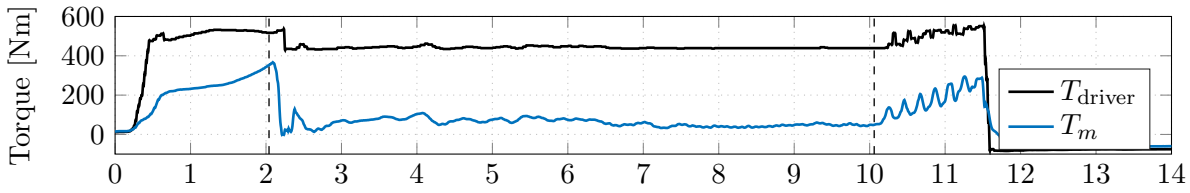

(b) Requested torque by the driver and actual drive torque of the engine.

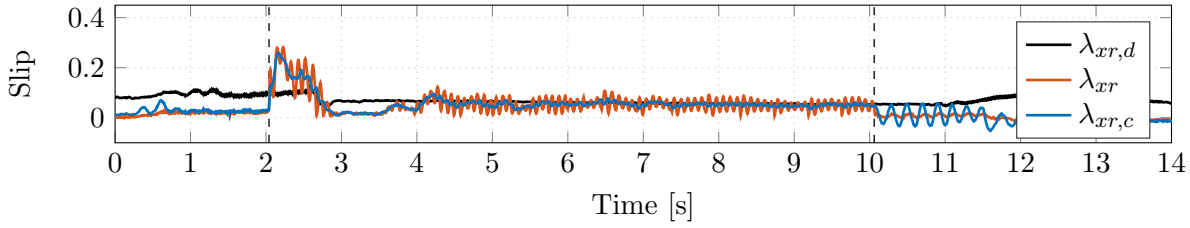

(c) Target slip, average slip of the rear wheels and the slip based on the crankshaft speed.

Figure 6.5: Experimental evaluation of the benchmark ECU based TCS.

Finally, the performance of the traditional DCU based TCS is evaluated on the same maneuver. This analysis is carried out to demonstrate the advantages of the ECU based control architecture over the DCU based control architecture. Figure 6.6 shows the results of the DCU based TCS on the previously described maneuver. Figure 6.6a depicts the estimated reference trajectory (see also the footnote below) and the system output, as well as the longitudinal speed of the vehicle. The overshoot to the estimated reference trajectory is 21.6 rad/s and hence significantly larger than for the two ECU based TCSs analyzed before. Also, it can be seen that the DCU based TCS does not achieve asymptotic tracking but exhibits low frequency oscillations which negatively affect driving comfort. Figure 6.6b depicts the requested torque of the driver and the engine torque. Figure 6.6c shows the estimated target wheel slip, as well as the actual wheel slip and the slip calculated from the scaled crankshaft angular velocity. There it can be seen that the DCU based TCS reaches the optimal target slip only during relatively short time intervals but is not able to maintain this operating point.

The experiments demonstrate the advantages of the ECU based control architecture compared to the traditional DCU based control architecture. The higher bandwidth of the inner control loop of the former achieves a significant overshoot reduction on a longitudinal acceleration maneuver with abruptly varying friction coefficient. However, with traditional control designs it can be challenging to achieve robustness of the closed loop control system, as indicated by the analysis of the benchmark ECU based TCS. The control design based on the method of IOL results in an ECU based TCS that achieves performance and robustness while damping drivetrain oscillations.

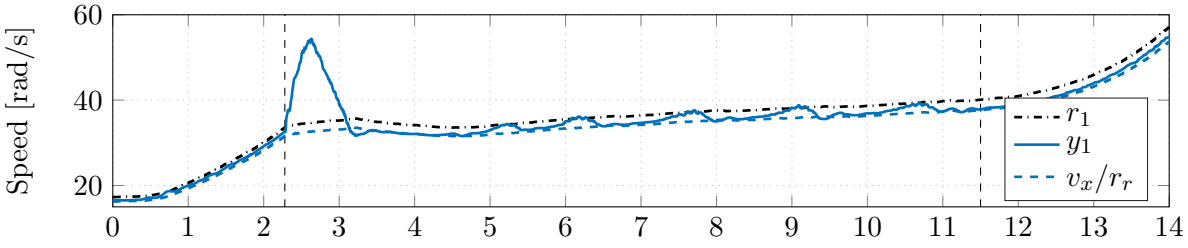

(a) Target[1] and actual speed of the crankshaft and longitudinal vehicle speed [304].

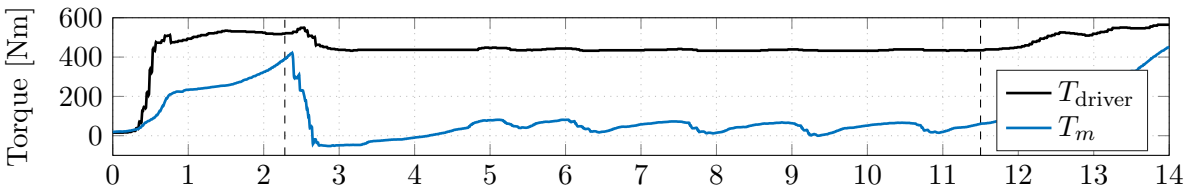

(b) Requested torque by the driver and actual drive torque of the engine.

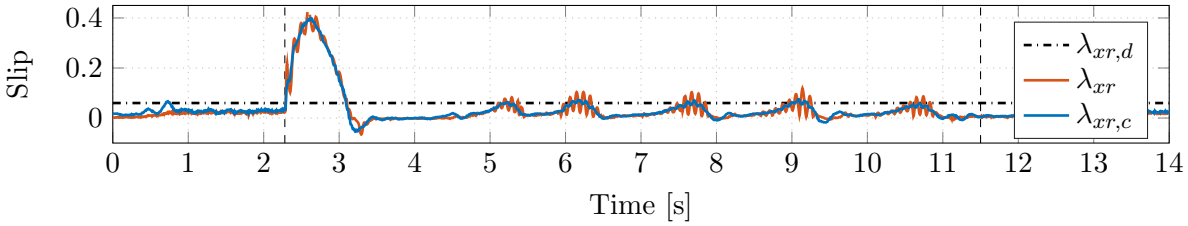

(c) Target slip[1], average slip of the rear wheels and the slip based on the crankshaft speed.

Figure 6.6: Experimental evaluation of the traditional DCU based TCS.

[1]The target values r_1 and $\lambda_{xr,d}$ in Figure 6.6 are estimated by $\lambda_{xr,d} = 6\%$, indicated by a dashed-dotted line, as the DCU based TCS is available as a blackbox only. This is assumed to give a slightly more accurate estimation of the real target values than in [304], where the estimated target speed was drawn only manually for reference.

6.3.2 Evaluation on Driving Maneuvers with Lateral Acceleration

Following, we evaluate the TCS on a drifting maneuver on snow with varying longitudinal and lateral acceleration. The friction coefficient is $\mu \approx 0.3$ throughout the maneuver, where the driver ensures by steering that the vehicle motion follows the desired path. The results for this maneuver are depicted in Figure 6.7. Here, the phases of active control are indicated with blue background color. The target and actual angular velocity of the crankshaft, scaled to wheel level and the longitudinal vehicle speed (divided by the rear wheel radius) are shown in Figure 6.7a. The TCS successfully prevents excessive wheel slip while the system output tracks the target speed without visible drivetrain oscillations. The longitudinal and lateral acceleration during the maneuver are shown in Figure 6.7b. Despite the changing acceleration throughout the drifting maneuver, tracking performance of the TCS is not negatively affected. This can also be observed in Figure 6.7c, where the target and actual wheel slip signals are depicted. During the three displayed phases of active control, the mean wheel slip deviation from the target value is approximately 0.0041, the standard deviation 0.0213. Finally, the driving torque requested by the driver and the observed engine torque are depicted in Figure 6.7d. There it can be seen how the TCS reduces the requested driving torque in order to track the target speed and by that assists the driver in stabilizing the vehicle. In order to further evaluate the performance of the 2WD TCS, a track with a higher friction coefficient is chosen for the next experiment.

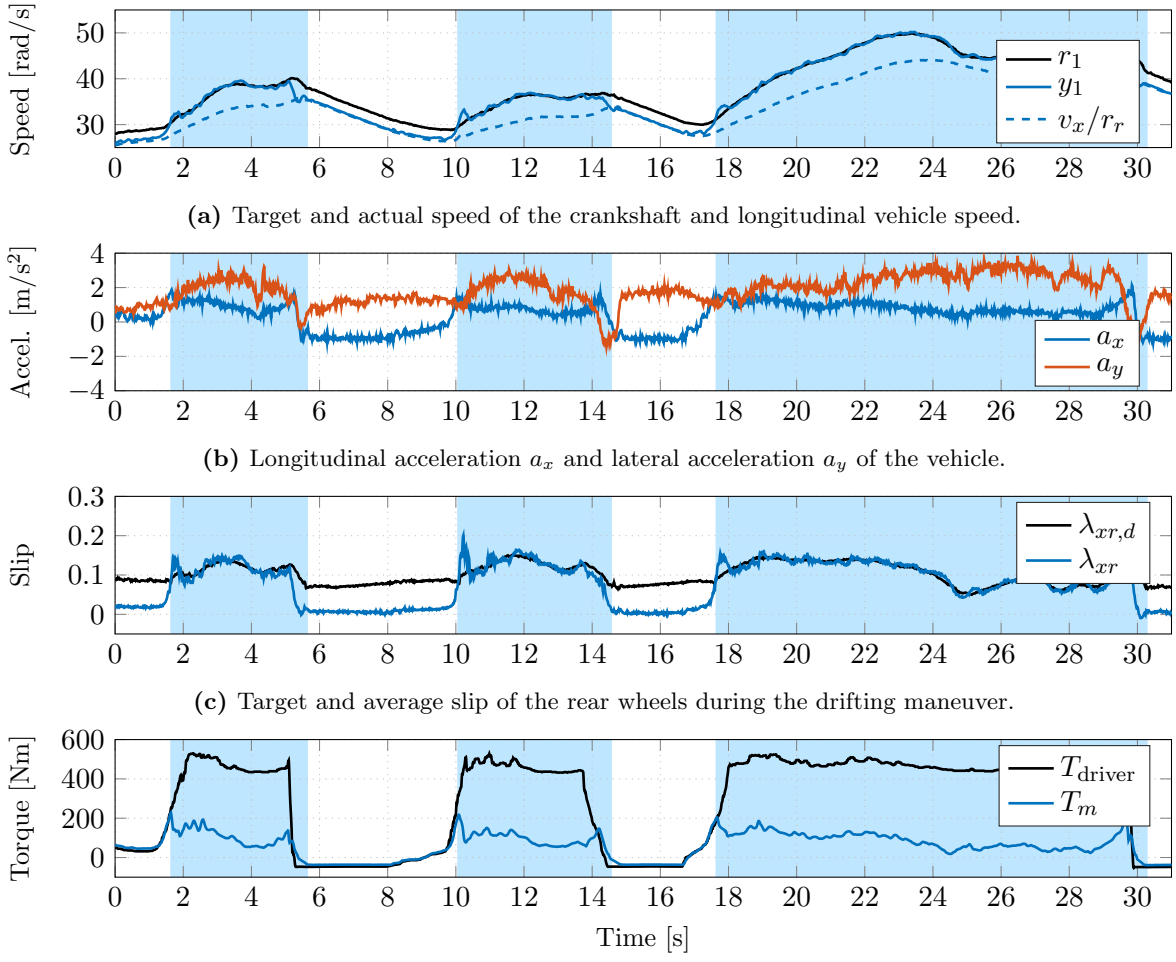

(a) Target and actual speed of the crankshaft and longitudinal vehicle speed.

(b) Longitudinal acceleration a_x and lateral acceleration a_y of the vehicle.

(c) Target and average slip of the rear wheels during the drifting maneuver.

(d) Requested torque by the driver and actual drive torque of the engine.

Figure 6.7: Controlled drifting maneuver on snow with $\mu \approx 0.3$.

The next considered maneuver is driving on wet asphalt through a section of a handling course with a friction coefficient of $\mu \approx 0.7$. During the maneuver, the driver ensures by steering that the vehicle stays on the track. The results for this maneuver are depicted in Figure 6.8. The phases of active control of the TCS are indicated with blue background color. The target and actual angular velocity of the crankshaft, scaled to wheel level and the longitudinal vehicle speed, divided by the rear wheel radius, are shown in Figure 6.8a. Similarly to the drifting maneuver on snow from Figure 6.7, the TCS prevents excessive wheel slip on wet asphalt as well, while the system output tracks the target speed without significant drivetrain oscillations. The longitudinal and lateral acceleration of this maneuver are shown in Figure 6.8b, while the target and actual wheel slip are depicted in Figure 6.8c. During the two displayed phases of active control, the mean wheel slip deviation from the target value is approximately 0.0050, with standard deviation 0.0209, while the average lateral acceleration is approximately $5.05\,\mathrm{m/s^2}$ with standard deviation $1.45\,\mathrm{m/s^2}$. Finally, the driving torque requested by the driver and the observed engine torque are depicted in Figure 6.8d. There it can be seen how the TCS reduces the requested torque in order to limit the wheel slip and thereby assists the driver in stabilizing the vehicle motion. This also demonstrates that the proposed TCS is suitable for limiting the wheel slip during maneuvers with lateral acceleration and concludes the experimental evaluation of the proposed 2WD TCS based on IOL. In the following, the proposed 4WD TCS based on IOL is evaluated in a test vehicle as well and a comparison to a PID controller is presented.

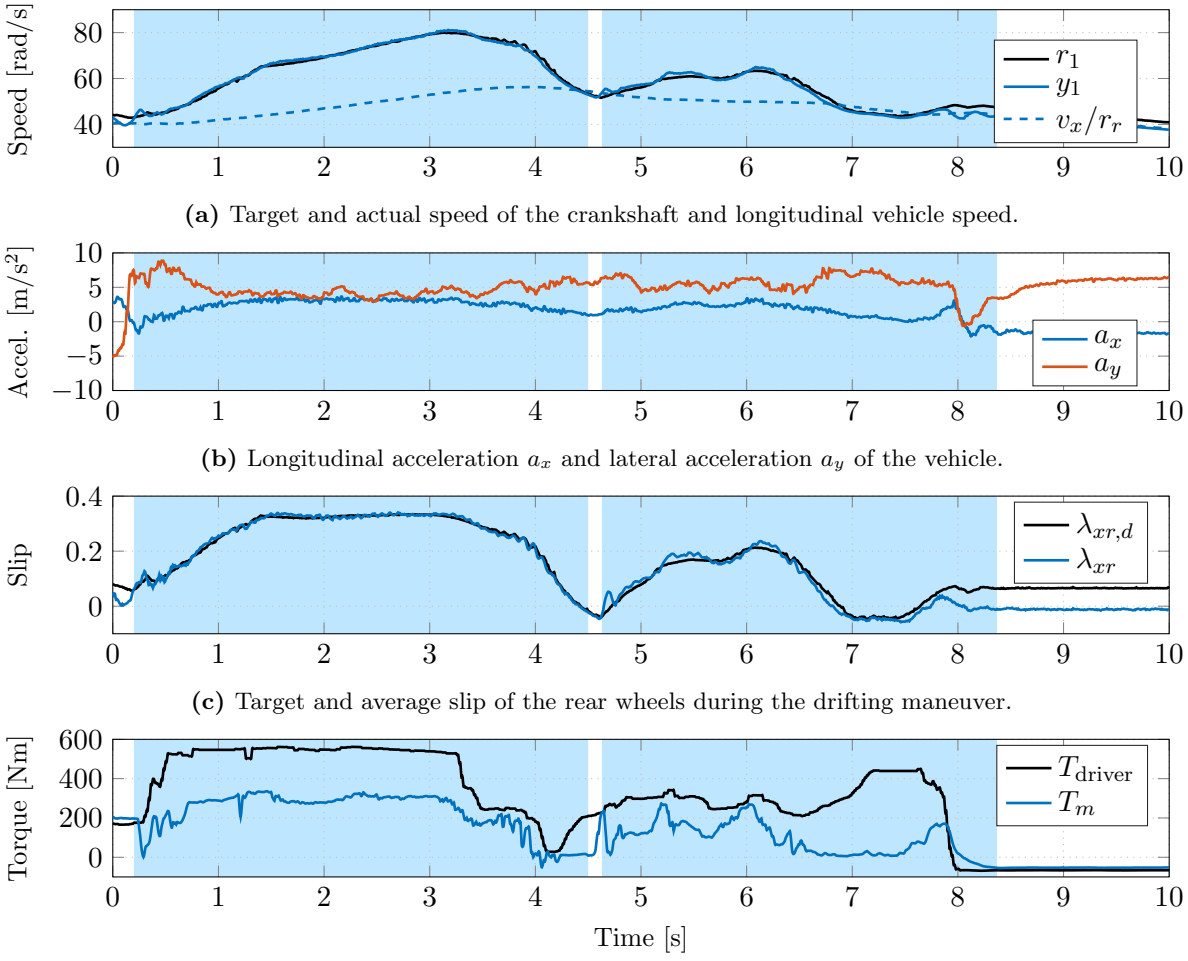

(a) Target and actual speed of the crankshaft and longitudinal vehicle speed.

(b) Longitudinal acceleration a_x and lateral acceleration a_y of the vehicle.

(c) Target and average slip of the rear wheels during the drifting maneuver.

(d) Requested torque by the driver and actual drive torque of the engine.

Figure 6.8: Controlled drifting maneuver on wet asphalt with $\mu \approx 0.7$.

6.3.3 Evaluation of the 4WD Traction Control System

After evaluating the 2WD TCS, the scalable MIMO 4WD TCS is evaluated, first considering the maneuver of drifting a circle on wet asphalt with $\mu \approx 0.7$. The lateral acceleration between $t = 1\,\mathrm{s}$ to $t = 3.5\,\mathrm{s}$ is almost constant and on average $2.63\,\mathrm{m/s^2}$. It increases to $5.43\,\mathrm{m/s^2}$ at $t = 5\,\mathrm{s}$, then decreases to $2.89\,\mathrm{m/s^2}$ at $t = 6\,\mathrm{s}$ and increases to $5.47\,\mathrm{m/s^2}$ at $t = 7.5\mathrm{m/s^2}$. Figure 6.9 depicts the results obtained from this experiment. Figure 6.9a shows the two system outputs $y_1 = \omega_c/i_G$ and $y_2 = \omega_f$ and their target speeds r_1 and r_2, acting as speed limiters in upper and lower direction. The scalability of the TCS can be observed in the figure. At $t = 3.67\,\mathrm{s}$, the ECU based controller reduces the requested torque of the driver in order to let y_1 track r_1, indicated with blue background color. At $t = 4.01\,\mathrm{s}$, the controller for the ETC is activated as well, in order to let y_2 track r_2, indicated with green background color. At $t \approx 5.9\,\mathrm{s}$, the driver requests few enough drive torque so the controller for y_1 is deactivated, while the controller for y_2 remains active until $t = 7.5\,\mathrm{s}$, indicated with red background color. The requested torque of the driver and the torques of the main engine and the ETC are shown in Figure 6.9b. The term T_e/i_a is an estimate of the front axle torque, scaled to engine level, with the limitations mentioned in Remark 11. Figure 6.9c shows the target and actual rear wheel slip.

The results demonstrate the scalability of the 4WD TCS, as the control system transitions smoothly and on demand between the three different control modes. Also, the system outputs y_1 and y_2 are successfully forced by the coupled MIMO control law to remain within the range spanned by r_1 and r_2. Throughout the maneuver, no visible drivetrain oscillations occur, while the wheel slip is stabilized and tracks the target value. Following, the proposed TCS is compared against a benchmark PID controller on the control mode of controlling the front axle only.

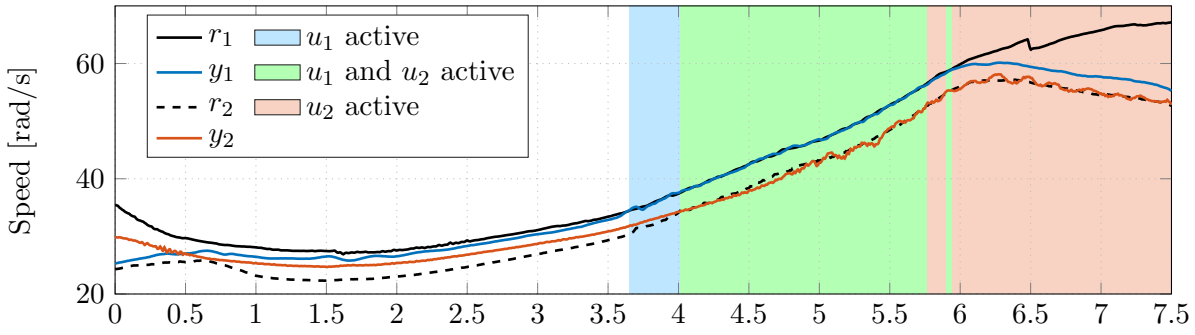

(a) Simultaneous control of front axle speed and the crankshaft speed by the TCS [300].

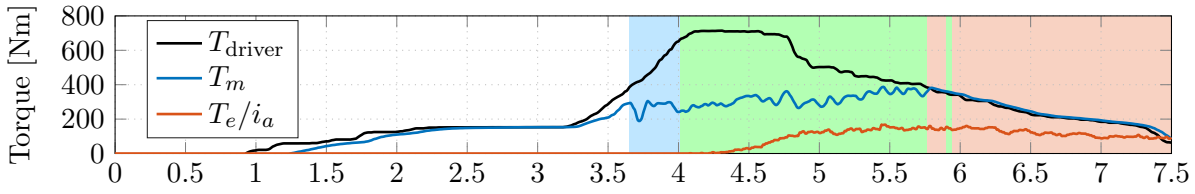

(b) Requested drive torque, main engine torque and ETC torque scaled to the engine.

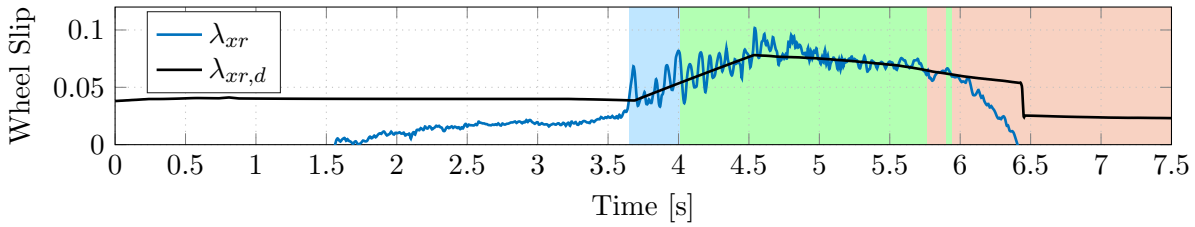

(c) Target and average slip of the rear wheels, stabilized by the TCS [300].

Figure 6.9: Drift maneuver on wet asphalt of the proposed 4WD TCS with coupled MIMO control law.

The previous experiments demonstrated that the proposed TCS works well when controlling the crankshaft speed in the 2WD case and also when dynamically switching as required between different modes of operations in the 4WD case. In the following, the case that only the front axle is controlled by the TCS is considered as well. This allows in principle arbitrary wheel slip on the rear axle, which is controlled by the driver only, but forces the front axle to follow the rear axle angular velocity with a certain configurable speed offset. The proposed TCS is compared on a drifting maneuver on snow to a benchmark implementation of a TCS which uses a traditional PID controller on the ETC control unit for this task. Here, the TCSs operate in conjunction with a standard feed-forward controller located on the DCU.

Figure 6.10 shows the results of the proposed 4WD TCS on this maneuver, using only the ETC for controlling the front axle speed, where phases of active control are indicated by red background color. Figure 6.10a depicts the second system output $y_2 = \omega_f$, the rear axle speed $x_4 = \omega_r$ and the target speed r_2 for the front axle. The output y_1 and the target speed r_1 are not displayed since the u_1 control law is deactivated here, such that the driver alone is responsible for controlling y_1. The proposed TCS successfully tracks the target speed and ensures that y_2 does not fall below r_2. The maneuver is started in the third gear, at $t \approx 5\,\mathrm{s}$ the automatic transmission switches to second gear and at $t \approx 7.4\,\mathrm{s}$ back to the third gear. Throughout the phases of active control, the average lateral acceleration is approximately $1.7\,\mathrm{m/s^2}$ with a standard deviation of approximately $0.49\,\mathrm{m/s^2}$. Figure 6.10b depicts the requested torque of the driver, the main engine torque and the ETC torque scaled to engine level, see also Remark 11. Figure 6.10c shows the control error signal $e_2 = r_2 - y_2$ and its constant target value $e_{2,d} = 0$. The mean absolute value of the control error e_2 of the proposed TCS during the maneuver is approximately $0.46\,\mathrm{rad/s}$. This value is computed by taking into account only segments where the u_2 control law is active.

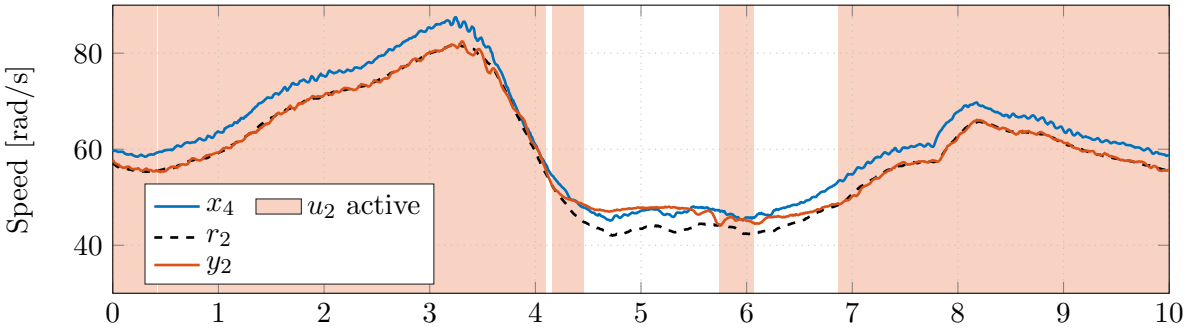

(a) Front axle speed, rear axle speed and target speed for the front axle [300].

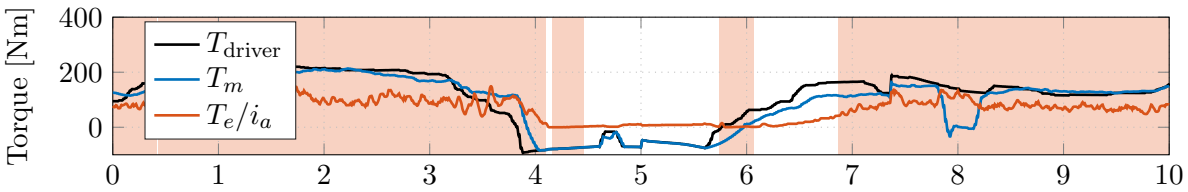

(b) Requested drive torque, main engine torque and ETC torque scaled to the engine.

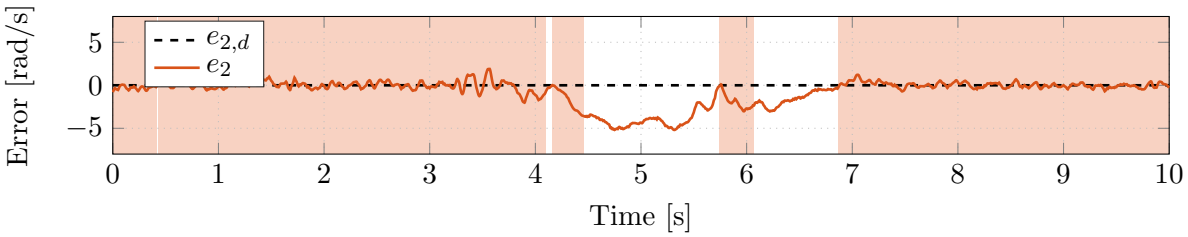

(c) Target and actual control error for the front axle angular velocity.

Figure 6.10: Drift maneuver on snow of the proposed 4WD TCS using the ETC for control only.

Following, a benchmark PID controller is used for a drift maneuver on the same track for comparison. The results of this experiment are depicted in Figure 6.11, where again the phases of active control are indicated by red background color. At $t \approx 0.8\,\mathrm{s}$ the automatic transmission switches from third to second gear and at $t \approx 4.8\,\mathrm{s}$ back to third gear. During the phases of active control, the average lateral acceleration is approximately $1.58\,\mathrm{m/s^2}$ with a standard deviation of approximately $0.51\,\mathrm{m/s^2}$. Figure 6.11a shows the angular velocity of the front axle $y_2 = \omega_f$, the target speed for the front axle r_2 and the angular velocity of the rear axle $x_4 = \omega_r$. The PID controller is also capable of stabilizing the wheel slip of the front wheels and tracking the reference speed. Figure 6.11b depicts the corresponding requested torque of the driver, the main engine torque and the ETC torque scaled to engine level. Figure 6.11c shows the target and actual control error, where the mean absolute value of e_2 is approximately $0.70\,\mathrm{rad/s}$, which is significantly higher compared to the IOL based controller. This value is again computed by only considering the segments where the TCS is operating and the PID controller is active. Apart from the better tracking performance, the actuator signal of the ETC shows less oscillations for the IOL design in Figure 6.10b, compared to the PID controller in Figure 6.11b. This is advantageous in terms of reducing control effort and increasing tracking performance while improving driving comfort at the same time.

The results demonstrate that the proposed TCS is also capable of outperforming a fine tuned benchmark implementation of a traditional PID controller on a drift maneuver on snow. This analysis completes the experimental evaluations of this work. In the following, a summary of the findings of this dissertation is given and complemented by a discussion. Also, an outlook for future research is given and possible extensions of this work are proposed.

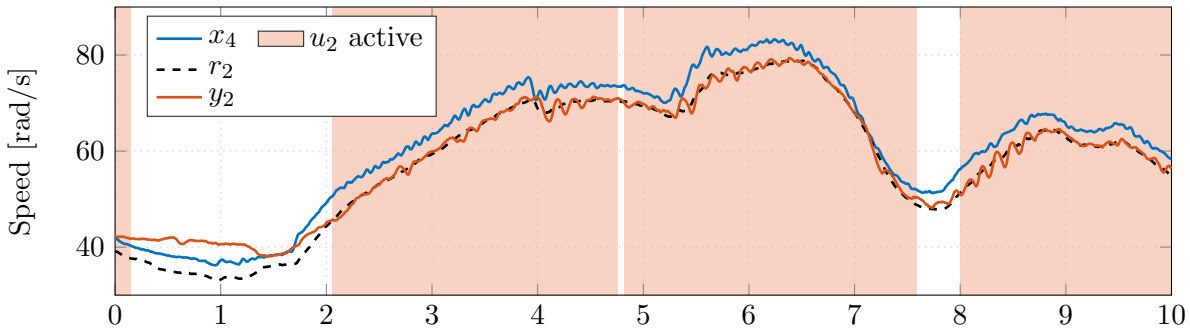

(a) Front axle speed, rear axle speed and target speed for the front axle [300].

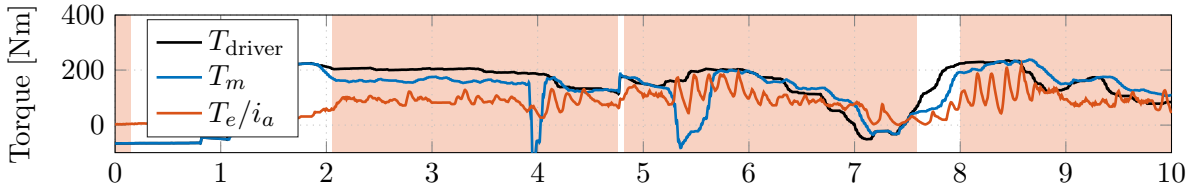

(b) Requested drive torque, main engine torque and ETC torque scaled to the engine.

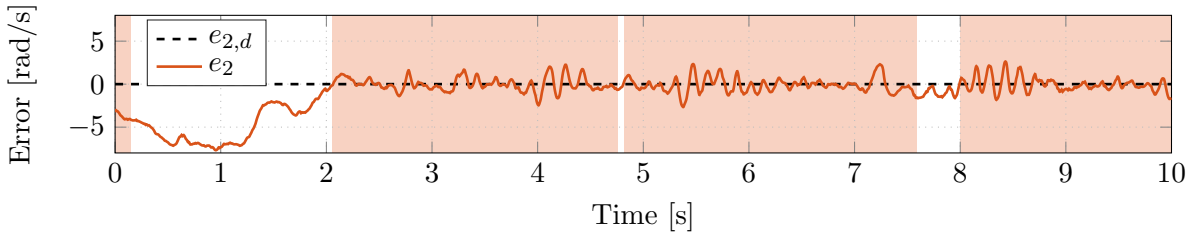

(c) Target and actual control error for the front axle angular velocity.

Figure 6.11: Drift maneuver on snow of a PID based 4WD TCS using the ETC for control only.

7 Conclusion and Outlook

7.1 Summary and Discussion

Traction control systems contribute to driving stability, performance and comfort. In this work, three different traction control designs based on IOL are proposed. The first is based on a design model for 2WD vehicles, the second and third are proposed for vehicles with on-demand 4WD torque bias systems. All three design models include the relevant torsional dynamics of the drivetrain, leading to explicit terms for active damping of drivetrain oscillations in the derived control laws. A stability analysis is presented for the three designs, based on novel classes of parametric Lyapunov functions. The results in this work and our corresponding publications show for the first time absolute stability and global exponential stability, for all possible vehicle parameters and time-varying friction coefficients, of the zero dynamics of TCSs with torsional drivetrain dynamics, assuming an exact IOL. Moreover, input-to-state stability of the internal dynamics is shown. A reformulation of the zero dynamics of the 2WD TCS as Lur'e system is proposed and used for a passivity based analysis. In addition, a method for the parameterization of the reference dynamics of the TCSs is proposed.

While the IOL of a nonlinear system typically results in a nonlinear control law, the numerical approximation of the wheel and crankshaft angular accelerations admits an LTI controller formulation, as derived in Chapter 6. This is advantageous in practice, as in this form only drivetrain parameters are required for an implementation of the 2WD TCS, which can be identified with sufficient accuracy, in contrast to tire parameters, for example. This advantage depends on the modeling of the torsional dynamics of the drivetrain. In the 4WD case, this can be seen by looking at the two different design models proposed in Chapter 3. The reduced model (with 7 states) assumes a stiff connection between the ETC and the front axle, which leads to a term that includes the time derivative of the tire force in the control law. The second proposed 4WD design model (with 9 states) does not have this issue, as it models both the connections to the rear and the front axle as torsion springs. However, it also requires more information, namely the ETC output speed which might not be directly available as a measurement signal in the target vehicle. The main difference between the simplified control law of the 7-state model—omitting the time derivative of the tire force as discussed in Chapter 3—and the control law of the 9-state model is an extra damping term for the front axle. In practice, this term can be omitted as shown in Chapter 6, as the oscillations on the front axle are not as pronounced as on the rear axle in the considered test vehicle.

Moreover, a novel heuristic method for Lyapunov function identification based on GP is proposed and applied to two nonlinear benchmark systems and the zero dynamics of the 2WD TCS. It is shown that the method is able to identify valid Lyapunov functions for the two benchmark systems and that it can approximate a numerical instance of the parametric Lyapunov function resulting from a Lur'e formulation of the 2WD TCS in Chapter 4. Due to the heuristic nature of GP, the method is not guaranteed to always find a valid Lyapunov function for an arbitrary nonlinear dynamical system. Also, as the identified Lyapunov function only is an approximate instance for a specific set of vehicle parameters, it cannot be used to derive the more general results obtained by the handcrafted parametric Lyapunov function presented in Chapter 3. Nevertheless, the results of Chapter 5 demonstrate that GP can indeed be useful for Lyapunov function approximation not only for abstract benchmark systems, but also for systems arising from real-world applications like the considered 2WD TCS.

The passivity analysis in Chapter 4 leads to a third order Lur'e system formulation of the zero dynamics of the 2WD TCS with two inputs and two outputs. This system class is analyzed in the context of the Kalman conjecture and the MYC. Two methods are presented for testing whether the input dimension, respectively output dimension, of a Lur'e system can be reduced. Applied to existing counterexamples of the MYC, this analysis leads to the open question whether the MYC is true for third order Lur'e systems with two inputs and two outputs, or to which extent the Kalman conjecture can be generalized to a MIMO Lur'e setting.

Finally, an experimental evaluation of the IOL based TCSs for both vehicles with 2WD and 4WD is presented in Chapter 6, after a validation of the design model and an analysis of the 2WD TCS using frequency domain methods. A comparison of a traditional DCU based with an ECU based TCS architecture demonstrates the advantages of the latter while the benefits of the IOL based design are shown by a comparison with a benchmark implementation. The performance of the 2WD TCS is also evaluated on two driving maneuvers with lateral acceleration and with different friction coefficients. Following, the performance of the MIMO 4WD TCS is tested during a drift maneuver, and a comparison with a PID controller is carried out. The results of this experimental study demonstrate that an ECU based TCS, designed with the method of IOL, is not only feasible in practice but can achieve a significant improvement compared to traditional designs in terms of tracking performance, robustness with respect to disturbances like time-varying friction coefficients and damping of drivetrain oscillations.

7.2 Directions for Future Work

The findings of this work can be extended in several directions. For example, the control design model could be extended to include dynamic wheel loads. This would not change the derived control law, as the numerical approximation of the angular accelerations takes such variations into account. However, the order of the zero dynamics then increases by one per driven axle, assuming first order tire dynamics. Hence the question arises, whether the class of parametric Lyapunov functions from Chapter 3 can be extended to this case as well. Corollary 1 cannot be used directly in this case, although variations of the normal force can be subsumed by a time-varying friction coefficient. However, the condition used in Theorem 2, that tire force and wheel slip have the same sign, is then not applicable for some initial conditions. An explicit parametric Lyapunov function for this case would be interesting.

The control design derived for the 9-state 4WD design model could be evaluated experimentally, either using an additional sensor or an observer for the required output speed of the ETC. A direct comparison to the control design based on the 7-state 4WD model, which is evaluated in a test vehicle in this work, would be interesting. Another direction for future work is the reference speed computation. This is especially interesting in the 4WD case, as vehicle speed estimation can be challenging when all four wheels operate with significant wheel slip. Also, variations of tire parameters and the friction coefficient, among other, have an impact on the optimal reference speed. For this purpose, adaptive control approaches like extremum seeking control and online estimation of tire forces might be an option.

The question whether the Markus-Yamabe conjecture is true for third order Lur'e systems with two inputs and two outputs, motivated by the passivity analysis of the zero dynamics of the 2WD TCS, remains open as well. Using ridge regression to approximate existing counterexamples might lead to counterexamples with two inputs and two outputs.

Recent works have extended some of the methods of this dissertation and applied them to traction control with electronic limited slip differentials [57], electric vehicles with four in-wheel motors [58], regenerative and hybrid anti-lock braking [183] and control allocation [182], leading to new challenges. With the development of modern engines and control architectures, traction control still offers various directions for future research.

A Appendix

A.1 Coefficients and Principle Minors for Local Stability

The parameters of the characteristic polynomial in Lemma 12 are

$$a_0 = (2c_{xr}k_c)/(J_r m v_0^*) \tag{A.1a}$$
$$a_1 = (2c_{xr}d_c + 2k_c m v_0^*)/(J_r m v_0^*) \tag{A.1b}$$
$$a_2 = (c_{xr}mr_r^2 + J_r c_{xr} + 2d_c m v_0^*)/(J_r m v_0^*)\,. \tag{A.1c}$$

The three leading principal minors of $\boldsymbol{H}$ in (3.82), as a function of the vehicle parameters, are

$$\Delta_1 = (c_{xr}mr_r^2 + J_r c_{xr} + 2d_c m v_0^*)/(J_r m v_0^*) \tag{A.2a}$$
$$\Delta_2 = \big(2c_{xr}^2 d_c m r_r^2 + 2J_r c_{xr}^2 d_c + 4c_{xr}d_c^2 m v_0^* + 2k_c c_{xr} m^2 r_r^2 v_0^* + \ldots \tag{A.2b}$$
$$\ldots 4k_c d_c m^2 (v_0^*)^2\big)/\big(J_r^2 m^2 (v_0^*)^2\big)$$
$$\Delta_3 = \Big(4c_{xr}k_c\big(c_{xr}^2 d_c m r_r^2 + J_r c_{xr}^2 d_c + 2c_{xr}d_c^2 m v_0^* + k_c c_{xr} m^2 r_r^2 v_0^* + \ldots \tag{A.2c}$$
$$\ldots 2k_c d_c m^2 (v_0^*)^2\big)\Big)/\big(J_r^3 m^3 (v_0^*)^3\big)\,.$$

Since the vehicle parameters are strictly positive and (A.1a)-(A.1c) as well as (A.2a)-(A.2c) consist only of addition, multiplication and division operations, it is clear that $a_0, a_1, a_2, \Delta_1, \Delta_2, \Delta_3 > 0$.

A.2 Supplementary Analysis of the 9-State 4WD Case

The matrices $\boldsymbol{P}_1$ and $\boldsymbol{P}_2$ used in the proof of Theorem 4 are given by

$$\boldsymbol{P}_1 = \frac{1}{s_r - m/2}\begin{bmatrix} P_{1,11} & -1/2 \\ -1/2 & P_{1,22}\end{bmatrix} \text{ and } \boldsymbol{P}_2 = \frac{1}{s_f - m/2}\begin{bmatrix} P_{2,11} & -1/2 \\ -1/2 & P_{2,22}\end{bmatrix} \tag{A.3}$$

with s_r, s_f taken from (A.11), $P_{1,11} = p_{11}$ from (3.84a), $P_{1,22} = p_{22}$ from (3.84b) and

$$P_{2,11} = \big(\gamma 12 J_f k_e\sqrt{\epsilon} + \bar{c}_{xf} d_e r_f^2 + 6J_f k_e\sqrt{\epsilon} + 12 d_e^2\sqrt{\epsilon}\big)/(12 J_f d_e\sqrt{\epsilon}) \tag{A.4a}$$
$$P_{2,22} = \big(\gamma 12 J_f k_e\sqrt{\epsilon} + \bar{c}_{xf} d_e r_f^2 + 6J_f k_e\sqrt{\epsilon}\big)/(24 k_e d_e\sqrt{\epsilon})\,. \tag{A.4b}$$

From (A.11) it can be seen that $s_r > m/2$ and $s_f > m/2$, so $\boldsymbol{P}_1$ is the upper left 2×2 submatrix of $\boldsymbol{P}$ from (3.83), scaled by a positive constant, so $\boldsymbol{P}_1 \succ 0$ by Theorem 1. Moreover, also $\boldsymbol{P}_2 \succ 0$ analogously, as it is like $\boldsymbol{P}_1$ only with FWD instead of RWD parameters. The time derivative of the Lyapunov function constructed in Theorem 4 along solutions of (3.79) is given by $\dot{V}_{\mathcal{M}_9}(\boldsymbol{q}_1, \boldsymbol{q}_2, p) = \dot{\nu}_{\mathcal{M}_9}(\boldsymbol{q}_1, \boldsymbol{q}_2, p) + p\,d(p)$ with $d(p) = (1/2)\rho c_w A_{st} p|p|/m$ and

$$\dot{\nu}_{\mathcal{M}_9}(\boldsymbol{q}_1, \boldsymbol{q}_2, p) = \dot{\nu}_r(\boldsymbol{q}_1, p) + \dot{\nu}_f(\boldsymbol{q}_2, p) \tag{A.5}$$

where $\dot{\nu}_r(\boldsymbol{q}_1, p) = \dot{V}(\boldsymbol{z}_r)/(s_r - m/2)$ using $\boldsymbol{z_r}^T = \begin{bmatrix}\boldsymbol{q}_1^T & p\end{bmatrix} = \begin{bmatrix} z_1 & z_2 & z_3\end{bmatrix}$ and $\dot{V}$ from (3.86). Following, $\dot{\nu}_f(\boldsymbol{q}_2, p) = \dot{V}|_{\text{FWD}}(\boldsymbol{z}_f)/(s_f - m/2)$ using $\boldsymbol{z_f}^T = \begin{bmatrix}\boldsymbol{q}_2^T & p\end{bmatrix} = \begin{bmatrix} z_4 & z_5 & z_3\end{bmatrix}$. Here, $\dot{V}|_{\text{FWD}}$ denotes $\dot{V}$ from (3.86) but with FWD instead of RWD parameters, hence replacing r_r, J_r, k_c, d_c, $\bar{c}_{xr}$ with r_f, J_f, k_e, d_e, $\bar{c}_{xf}$ where $\bar{c}_{xf} = \mu_{\max} F_{zf} B_f C_f$. Now observe that both $\dot{\nu}_r(\boldsymbol{q}_1, p)$ and $\dot{\nu}_f(\boldsymbol{q}_2, p)$ contain the term $-p\,d(p)$, so they compensate the $p\,d(p)$ term in $\dot{V}_{\mathcal{M}_9}$. From the proof of Theorem 2 it follows that $\dot{\nu}_r(\boldsymbol{q}_1, p) + p\,d(p)/2$ and $\dot{\nu}_f(\boldsymbol{q}_2, p) + p\,d(p)/2$ remain negative definite, hence compensating the $p\,d(p)$ term in $\dot{V}_{\mathcal{M}_9}(\boldsymbol{q}_1, \boldsymbol{q}_2, p)$ such that $\dot{V}_{\mathcal{M}_9}(\boldsymbol{q}_1, \boldsymbol{q}_2, p) \prec 0$.

A.3 Additional Proofs

Proof of Lemma 4. Without loss of generality, assume $\lambda_{xr} \geq 0$ by symmetry of (3.6) and (3.10a). Clearly, $c_{xr}|\lambda_{xr}| > |F_{xr}|$ for $\lambda_{xr} \to \infty$ as the sine function is bounded. While λ_{xr}, by Definition (3.8) can only take values from $[-2, 2]$ (cf. also Remark 7), this means that if $|F_{xr}|$ could be larger than $c_{xr}|\lambda_{xr}|$ for some λ_{xr}, that the equation

$$F_\Delta = c_{xr}\lambda_{xr} - \mu F_{zr} \sin\big(C_r \arctan(B_r\lambda_{xr})\big) = 0 \tag{A.6}$$

would be solved by some $\lambda_{xr} > 0$. The first derivative of F_Δ in (A.6) with respect to λ_{xr} is used to find the minimum of this difference (for $\lambda_{xr} \geq 0$), by setting

$$\frac{\mathrm{d}}{\mathrm{d}\lambda_{xr}} F_\Delta = c_{xr}\left(1 - \frac{\cos\big(C_r \arctan(B_r\lambda_{xr})\big)}{(B_r\lambda_{xr})^2 + 1}\right) = 0\,, \tag{A.7}$$

which can hold if and only if

$$\cos\big(C_r \arctan(B_r\lambda_{xr})\big) = (B_r\lambda_{xr})^2 + 1\,. \tag{A.8}$$

The cosine function has range $[-1, 1]$ and the right-hand side of (A.8) is strictly larger than 1 for $\lambda_{xr} > 0$. The case $\lambda_{xr} \leq 0$ follows analogously. Hence, $c_{xr}|\lambda_{xr}| \geq |F_{xr}|$ with equality if and only if $\lambda_{xr} = 0$, where the linear tire model is equal to the nonlinear tire model [305]. □

Proof of Corollary 4. The proof mainly resembles the proofs of Theorem 6 and Corollary 2 and is included here for the sake of completeness. Define the Lyapunov function for the zero dynamics of the $\mathcal{M}_9$ model (3.36) as

$$\begin{aligned}\mathcal{V}_{\mathcal{M}_9}(\boldsymbol{z}) =& \frac{1}{s_r}\Big(\begin{bmatrix} z_1 \\ z_2 \end{bmatrix}^T \begin{bmatrix} p_{r,11} & -1/2 \\ -1/2 & p_{r,22} \end{bmatrix} \begin{bmatrix} z_1 \\ z_2 \end{bmatrix} + \frac{1}{2}(2k_c z_1^2 + J_r z_2^2 + m z_3^2)\Big) + \dots \\ \dots & \frac{1}{s_f}\Big(\begin{bmatrix} z_4 \\ z_5 \end{bmatrix}^T \begin{bmatrix} p_{f,11} & -1/2 \\ -1/2 & p_{f,22} \end{bmatrix} \begin{bmatrix} z_4 \\ z_5 \end{bmatrix} + \frac{1}{2}(2k_e z_4^2 + J_f z_5^2 + m z_3^2)\Big) + z_3^2\,,\end{aligned} \tag{A.9}$$

where $p_{r,11} = p_{11}$ taken from (3.84a) and $p_{r,22} = p_{22}$ taken from (3.84b). The quantities for the front axle are defined analogously by

$$p_{f,11} = \frac{\gamma 12 J_f k_e\sqrt{\epsilon} + \bar{c}_{xf} d_e r_f^2 + 6 J_f k_e \sqrt{\epsilon} + 12 d_e^2 \sqrt{\epsilon}}{12 J_f d_e \sqrt{\epsilon}} \tag{A.10a}$$

$$p_{f,22} = \frac{\gamma 12 J_f k_e\sqrt{\epsilon} + \bar{c}_{xf} d_e r_f^2 + 6 J_f k_e \sqrt{\epsilon}}{24 k_e d_e \sqrt{\epsilon}} \tag{A.10b}$$

Moreover, the values used for scaling in (A.9) are given by

$$s_r = \frac{m}{2} + \frac{m(6k_c J_r\sqrt{\epsilon} + \bar{c}_{xr} d_c r_r^2 + 12\gamma k_c J_r \sqrt{\epsilon})}{24 J_r d_c k_c \sqrt{\epsilon}} \tag{A.11a}$$

$$s_f = \frac{m}{2} + \frac{m(6k_e J_f\sqrt{\epsilon} + \bar{c}_{xf} d_e r_f^2 + 12\gamma k_e J_f \sqrt{\epsilon})}{24 J_f d_e k_e \sqrt{\epsilon}} \tag{A.11b}$$

with $s_r > 0$ and $s_f > 0$ due to $\gamma > 0$ and the positivity of the vehicle parameters. The Lyapunov function is positive definite, as the matrices in (A.9) are positive definite. This can be seen from the proof of Theorem 1, as its argument applies here analogously: the leading principal minors of the first matrix are

$$\Delta_{r,1} = (12 d_c^2\sqrt{\epsilon} + 6k_c J_r\sqrt{\epsilon} + \bar{c}_{xr} d_c r_r^2 + 12\gamma k_c J_r\sqrt{\epsilon})/(12 d_c J_r \sqrt{\epsilon}) \tag{A.12a}$$

$$\begin{aligned}\Delta_{r,2} =& (36 J_r^2 \epsilon k_c^2 + \bar{c}_{xr}^2 d_c^2 r_r^4 + 12\bar{c}_{xr} d_c^3\sqrt{\epsilon} r_r^2 + 144\gamma J_r^2 \epsilon k_c^2 + 144\gamma^2 J_r^2 \epsilon k_c^2 + \dots \\ & \dots 144\gamma J_r d_c^2 \epsilon k_c + 12 J_r \bar{c}_{xr} d_c \sqrt{\epsilon} k_c r_r^2 + 24\gamma J_r \bar{c}_{xr} d_c \sqrt{\epsilon} k_c r_r^2)/(288 J_r d_c^2 \epsilon k_c)\,,\end{aligned} \tag{A.12b}$$

while the leading principal minors of the second matrix in (A.9) are

$$\Delta_{f,1} = (12d_e^2\sqrt{\epsilon} + 6k_eJ_f\sqrt{\epsilon} + \bar{c}_{xf}d_er_f^2 + 12\gamma k_eJ_f\sqrt{\epsilon})/(12d_eJ_f\sqrt{\epsilon}) \tag{A.13a}$$

$$\Delta_{f,2} = (36J_f^2\epsilon k_e^2 + \bar{c}_{xr}^2d_e^2r_f^4 + 12\bar{c}_{xf}d_e^3\sqrt{\epsilon}r_f^2 + 144\gamma J_f^2\epsilon k_e^2 + 144\gamma^2J_f^2\epsilon k_e^2 + \dots \tag{A.13b}$$
$$\dots 144\gamma J_fd_e^2\epsilon k_e + 12J_f\bar{c}_{xf}d_e\sqrt{\epsilon}k_er_f^2 + 24\gamma J_f\bar{c}_{xf}d_e\sqrt{\epsilon}k_er_f^2)/(288J_fd_e^2\epsilon k_e)\,.$$

Since (A.12) and (A.13) consist only of addition, multiplication and division operations of strictly positive quantities, it follows that $\Delta_{r,1}, \Delta_{r,2}, \Delta_{f,1}, \Delta_{f,2} > 0$ and hence $\mathcal{V}_{\mathcal{M}_9}(\boldsymbol{z}) \succ 0$. The time derivative of (A.9) along solutions of (3.79) can after some rearrangements be written as

$$\dot{\mathcal{V}}_{\mathcal{M}_9}(\boldsymbol{z},t) = (1/s_r)\dot{\mathcal{V}}_r(\boldsymbol{z},t) + (1/s_f)\dot{\mathcal{V}}_f(\boldsymbol{z},t) \tag{A.14a}$$

$$\dot{\mathcal{V}}_r(\boldsymbol{z},t) = -q_{r,1}z_1^2 - q_{r,2}z_2^2 - q_{r,3}z_3^2|z_3| - v_{nr}\lambda_{xr}F_{xr} - q_{r,4}z_2^2 - q_{r,5}z_3^2|z_3| + \dot{V}_{r,b}(\boldsymbol{z},t) \tag{A.14b}$$

$$\dot{\mathcal{V}}_f(\boldsymbol{z},t) = -q_{f,1}z_4^2 - q_{f,2}z_5^2 - q_{f,3}z_3^2|z_3| - v_{nf}\lambda_{xf}F_{xf} - q_{f,4}z_5^2 - q_{f,5}z_3^2|z_3| + \dot{V}_{f,b}(\boldsymbol{z},t)\,. \tag{A.14c}$$

The coefficients are $q_{r,1} = 2k_c(1-\eta_r)/J_r$, $q_{r,2} = 2d_c$, $q_{r,3} = A_{st}c_w\rho/4$, $q_{r,4} = 2\gamma + \bar{c}_{xr}d_cr_r^2/(6J_rk_c\sqrt{\epsilon})$, $q_{r,5} = (A_{st}c_w\rho(6J_r\sqrt{\epsilon}k_c + \bar{c}_{xr}d_cr_r^2 + 12\gamma k_cJ_r\sqrt{\epsilon}))/(48k_cd_cJ_r\sqrt{\epsilon})$ and $q_{f,1} = 2k_e(1-\eta_f)/J_f$, $q_{f,2} = 2d_e$, $q_{f,3} = A_{st}c_w\rho/4$, $q_{f,4} = 2\gamma + \bar{c}_{xf}d_er_f^2/(6J_fk_e\sqrt{\epsilon})$, $q_{f,5} = (A_{st}c_w\rho(6J_f\sqrt{\epsilon}k_e + \bar{c}_{xf}d_er_f^2 + 12\gamma k_eJ_f\sqrt{\epsilon}))/(48k_ed_eJ_f\sqrt{\epsilon})$, which are all strictly positive as $\gamma > 0$ and $\eta_r = \bar{c}_{xr}d_cr_r^2/(\bar{c}_{xr}d_cr_r^2 + 6J_rk_c\sqrt{\epsilon}) \in (0,1)$ and $\eta_f = \bar{c}_{xf}d_er_f^2/(\bar{c}_{xf}d_er_f^2 + 6J_fk_e\sqrt{\epsilon}) \in (0,1)$ by definition, compare also the proof of Corollary 1. Moreover, the remaining functions in (A.14b) and (A.14c) are given by

$$\dot{V}_{r,b}(\boldsymbol{z},t) = -\widetilde{q}_{r,1}z_1^2 + \widetilde{q}_{r,2}z_1F_{xr} - \widetilde{q}_{r,3}v_{nr}\lambda_{xr}F_{xr} \tag{A.15a}$$

$$\dot{V}_{f,b}(\boldsymbol{z},t) = -\widetilde{q}_{f,1}z_4^2 + \widetilde{q}_{f,2}z_4F_{xf} - \widetilde{q}_{f,3}v_{nf}\lambda_{xf}F_{xf} \tag{A.15b}$$

with $v_{nr} > 0$, $v_{nf} > 0$ and $\widetilde{q}_{r,1} = 2\eta_rk_c/J_r$, $\widetilde{q}_{r,2} = r_r/J_r$, $\widetilde{q}_{r,3} = \gamma/d_c + 1/(2d_c) + \bar{c}_{xr}r_r^2/(12k_cJ_r\sqrt{\epsilon})$, $\widetilde{q}_{f,1} = 2\eta_fk_e/J_f$, $\widetilde{q}_{f,2} = r_f/J_f$ and $\widetilde{q}_{f,3} = \gamma/d_e + 1/(2d_e) + (\bar{c}_{xf}r_f^2)/(12k_eJ_f\sqrt{\epsilon})$. Then, $\dot{V}_{r,b}(\boldsymbol{z},t) = 0$ and $\dot{V}_{f,b}(\boldsymbol{z},t) = 0$ are quadratic equations in z_1, respectively z_4 with discriminants

$$\mathrm{disc}_{z_1}(\dot{V}_{r,b}) = -4\widetilde{q}_{r,1}\widetilde{q}_{r,3}v_{nr}\lambda_{xr}F_{xr} + \widetilde{q}_{r,2}F_{xr}^2 \leq -4\widetilde{q}_{r,1}\widetilde{q}_{r,3}v_{nr}\lambda_{xr}F_{xr} + \widetilde{q}_{r,2}F_{xr}\bar{c}_{xr}\lambda_{xr} \tag{A.16a}$$

$$\mathrm{disc}_{z_4}(\dot{V}_{f,b}) = -4\widetilde{q}_{f,1}\widetilde{q}_{f,3}v_{nf}\lambda_{xf}F_{xf} + \widetilde{q}_{f,2}F_{xf}^2 \leq -4\widetilde{q}_{f,1}\widetilde{q}_{f,3}v_{nf}\lambda_{xf}F_{xf} + \widetilde{q}_{f,2}F_{xf}\bar{c}_{xf}\lambda_{xf} \tag{A.16b}$$

as $F_{xr} \leq \bar{c}_{xr}|\lambda_{xr}|$ and $F_{xf} \leq \bar{c}_{xf}|\lambda_{xf}|$, compare Lemma 4. Since $v_{nr} \geq 3\sqrt{\epsilon}/2$ and $v_{nf} \geq 3\sqrt{\epsilon}/2$ by Lemma 5, it follows that $\mathrm{disc}_{z_1}(\dot{V}_{r,b}) \leq -12\gamma\bar{c}_{xr}k_cr_r^2\sqrt{\epsilon}/(6k_cJ_r^2\sqrt{\epsilon} + d_cr_r^2J_r\bar{c}_{xr}) < 0$ and $\mathrm{disc}_{z_4}(\dot{V}_{f,b}) \leq -12\gamma\bar{c}_{xf}k_er_f^2\sqrt{\epsilon}/(6k_eJ_f^2\sqrt{\epsilon} + d_er_f^2J_f\bar{c}_{xf}) < 0$, analogously to the proof of Theorem 2. Hence, $\dot{V}_{r,b}(\boldsymbol{z},t) \leq 0$ and $\dot{V}_{f,b}(\boldsymbol{z},t) \leq 0$. The implicit assumption $\lambda_{xr}F_{xr} \neq 0$ is without loss of generality since for $\lambda_{xr}F_{xr} = 0$ still $\dot{V}_{r,b}(\boldsymbol{z},t) \leq 0$ (the same holds for $\dot{V}_{f,b}$). Thus,

$$\dot{\mathcal{V}}_r(\boldsymbol{z},t) \leq -q_{r,1}z_1^2 - q_{r,2}z_2^2 - q_{r,3}z_3^2|z_3| - v_{nr}\lambda_{xr}F_{xr} \stackrel{\text{def}}{=} \dot{U}_r(\boldsymbol{z},t) \tag{A.17a}$$

$$\dot{\mathcal{V}}_f(\boldsymbol{z},t) \leq -q_{f,1}z_4^2 - q_{f,2}z_5^2 - q_{f,3}z_3^2|z_3| - v_{nf}\lambda_{xf}F_{xf} \stackrel{\text{def}}{=} \dot{U}_f(\boldsymbol{z},t)\,. \tag{A.17b}$$

This confirms the results from Theorem 4, as it shows that the zero dynamics (3.79) are globally asymptotically stable for time-varying friction coefficients, since $\dot{\mathcal{V}}_{\mathcal{M}_9}(\boldsymbol{z},t)$ is bounded from above by a negative definite function that does not depend on time explicitly because for the time-varying terms we have $-v_{nr}\lambda_{xr}F_{xr} \leq 0$ and $-v_{nf}\lambda_{xf}F_{xf} \leq 0$. Scaling (A.14a) with $2/m > 0$ we get $(2/m)\dot{\mathcal{V}}_{\mathcal{M}_9}(\boldsymbol{z},t) \leq \dot{\mathcal{V}}_r(\boldsymbol{z},t) + \dot{\mathcal{V}}_f(\boldsymbol{z},t)$ since $2/(s_rm) > 1$ and $2/(s_fm) > 1$. Finally, observe that $\dot{U}_r(\boldsymbol{z},t) + \dot{U}_f(\boldsymbol{z},t) = \dot{\mathcal{V}}_1(\boldsymbol{z},t) - q_{f,1}z_4^2 - q_{f,2}z_5^2 - v_{nf}\lambda_{xf}F_{xf} \leq \dot{\mathcal{V}}_1(\boldsymbol{z},t) - q_{f,1}z_4^2 - q_{f,2}z_5^2$ where $\dot{\mathcal{V}}_1(\boldsymbol{z},t)$ from (4.17a) is negative definite in (z_1,z_2,z_3) by Theorem 6 and Corollary 2, so for $\mu(t) \in [\mu_{\min}, \mu_{\max}]$, we have $\dot{\mathcal{V}}_{\mathcal{M}_9}(\boldsymbol{z},t) \leq -\underline{\alpha}\|\boldsymbol{z}\|_2^2$ with

$$\underline{\alpha} = (m/2)\min\{\alpha_1, \alpha_2, \alpha_3, \alpha_4, \alpha_5\} \tag{A.18}$$

and $\alpha_1 = 2(1-\eta_r)k_c/J_r > 0$, $\alpha_2 = d_c > 0$, $\alpha_3 = \min\{d_c, (1/2)\rho c_wA_{st}, cd_c/(d_c\widetilde{v}_{nr} + r_r^2)\} > 0$, $\alpha_4 = 2(1-\eta_f)k_e/J_f > 0$, $\alpha_5 = d_e > 0$, $c \in (0,1)$ and $\widetilde{v}_{nr} > 0$ from (4.21). Hence, $\underline{\alpha} > 0$ and so the zero dynamics (3.79) are globally exponentially stable for all vehicle parameters. □

Proof of Corollary 6. The internal dynamics of the $\mathcal{M}_9$ model (3.36), resulting from the control laws (3.67) and (3.70), are given by $\dot{\boldsymbol{z}} = \boldsymbol{f}(\boldsymbol{z}) + \boldsymbol{L}\boldsymbol{\zeta}$ with

$$\dot{\boldsymbol{z}} = \begin{bmatrix} \dot{z}_1 \\ \dot{z}_2 \\ \dot{z}_3 \\ \dot{z}_4 \\ \dot{z}_5 \end{bmatrix} = \begin{bmatrix} -z_2 \\ \big(2(k_r z_1 - d_r z_2) - r_r F_{xr}\big)/J_r \\ (F_{xf} + F_{xr} - F_w)/m \\ -z_5 \\ \big(2(k_f z_4 - d_f z_5) - r_f F_{xf}\big)/J_f \end{bmatrix} + \begin{bmatrix} 1 & 0 \\ 2d_c/J_r & 0 \\ 0 & 0 \\ 0 & 1 \\ 0 & 2d_e/J_f \end{bmatrix} \boldsymbol{\zeta} \tag{A.19}$$

where $\boldsymbol{\zeta}^T = \begin{bmatrix} \zeta_1 & \zeta_2 \end{bmatrix} = \begin{bmatrix} y_1 & y_2 \end{bmatrix} = \begin{bmatrix} \omega_c/i_G & \omega_e/i_f \end{bmatrix}$ is the bounded input resulting from the external dynamics. Furthermore, $\boldsymbol{z}^T = \begin{bmatrix} z_1 & z_2 & z_3 & z_4 & z_5 \end{bmatrix} = \begin{bmatrix} \Delta\phi_c & \omega_r & v_x & \Delta\phi_e & \omega_f \end{bmatrix}$, while F_{xr}, F_{xf} and F_w are given by (3.6), (3.26) and (3.29), respectively. By Corollary 4

$$\dot{\mathcal{V}}_{\mathcal{M}_9}(\boldsymbol{z}, \boldsymbol{\zeta}, t) = \dot{\mathcal{V}}_{\mathcal{M}_9}(\boldsymbol{z}, t) + \boldsymbol{z}^T \boldsymbol{L}\boldsymbol{\zeta} \leq -\underline{\alpha}\|\boldsymbol{z}\|_2^2 + \boldsymbol{z}^T \boldsymbol{L}\boldsymbol{\zeta}\,, \tag{A.20}$$

where $\dot{\mathcal{V}}_{\mathcal{M}_9}(\boldsymbol{z}, t)$ is given by (A.14a) and $\underline{\alpha}$ by (A.18). As $\boldsymbol{z}^T \boldsymbol{L}\boldsymbol{\zeta} \leq \|\boldsymbol{z}\|_2 \, \|\boldsymbol{L}\|_F \, \|\boldsymbol{\zeta}\|_2$, with $\theta \in (0, 1)$, we have

$$\dot{\mathcal{V}}_{\mathcal{M}_9}(\boldsymbol{z}, \boldsymbol{\zeta}, t) \leq -\theta\underline{\alpha}\|\boldsymbol{z}\|_2^2, \forall \boldsymbol{z} \in \mathbb{R}^5 : \|\boldsymbol{z}\|_2 \geq \rho_{\mathcal{M}_9}(\|\boldsymbol{\zeta}\|_2) = \frac{\|\boldsymbol{L}\|_F}{\underline{\alpha}(1-\theta)}\|\boldsymbol{\zeta}\|_2 \tag{A.21}$$

where $\rho_{\mathcal{M}_9}$ is a class $\mathcal{K}$ function, so input-to-state stability of (A.19) follows. □

A.4 Example of Globally but not Strongly Minimum Phase System

It is well known that global exponential stability of the zero dynamics is not sufficient for global stability of the overall closed loop system, see for example [149, pp. 532–533]. A very descriptive example of such a system can be obtained by slight modification of the system proposed by Cima *et al.* [45]. Adding an input and an auxiliary function yields

$$\dot{x}_1 = f(x_1) + u_1 \tag{A.22a}$$

$$\dot{x}_2 = -x_2 + x_1^2(x_3 x_1^2 + x_2 x_1)^2 \tag{A.22b}$$

$$\dot{x}_3 = -x_3 - x_1(x_3 x_1^2 + x_2 x_1)^2\,, \tag{A.22c}$$

with output $y_1 = x_1$ and $f : \mathbb{R} \to \mathbb{R}$ an arbitrary C^1 function. The system is already in normal form with a relative degree of $\delta_1 = 1$ since $\dot{y}_1 = f(x_1) + u_1$ depends on the input u_1 directly, resulting in second order internal dynamics. The control law $u_1 = -f(x_1) - x_1$ linearizes the first equation of the system and produces the closed loop dynamics

$$\dot{x}_1 = -x_1 \tag{A.23a}$$

$$\dot{x}_2 = -x_2 + x_1^2(x_3 x_1^2 + x_2 x_1)^2 \tag{A.23b}$$

$$\dot{x}_3 = -x_3 - x_1(x_3 x_1^2 + x_2 x_1)^2\,, \tag{A.23c}$$

where the external dynamics (A.23a) are globally exponentially stable. The zero dynamics of the system are obtained from (A.23b)-(A.23c) by setting $y_1 = x_1 = 0$, resulting in the subsystem $\dot{x}_2 = -x_2$, $\dot{x}_3 = -x_3$ which is also globally exponentially stable. Hence, the system (A.22) with the control law $u_1 = -f(x_1) - x_1$ is globally minimum phase with both its external dynamics and its zero dynamics being globally exponentially stable. However, (A.23) is identical to an instance of the family of counterexamples to the Markus-Yamabe conjecture proposed by Cima *et al.* [45]. The system (A.23) is obtained from this system, recited in (4.42), by using $a = b = m = 1$, $\ell = k = 2$, $c = 1$ and the state transformation $x_1 = z_3$, $x_2 = z_2$, $x_3 = z_1$. Cima *et al.* also provide a formula for the explicit solution of (4.42), see [45], from which it follows that (A.23) admits the explicit solution $x_1(t) = \exp(-t)$, $x_2(t) = 180\exp(4t)$, $x_3(t) = -150\exp(5t)$. Hence, both x_2 and x_3 diverge exponentially, despite the exponentially decaying x_1 state which acts as the input to the internal dynamics (A.23b)-(A.23c), so (A.22) is globally, but not strongly minimum phase.

A.5 Parameters of the 4WD Model for Control Design

The parameters of the $\mathcal{M}_7$ model used for the 4WD TCS design are depicted in Table A.1.

Table A.1: Parameters of the $\mathcal{M}_7$ model.

Name	Description	Value	Unit
τ_m	Motor time constant	0.02	s
τ_e	Motor time constant of the ETC	0.02	s
J_c	Aggregated inertia of the drive side	0.23	$\mathrm{kg\,m^2}$
J_r, J_f	Rear and front axle moment of inertia	2.1	$\mathrm{kg\,m^2}$
r_r, r_f	Radius of the rear and front wheels	0.33	m
m	Vehicle mass	2200	kg
k_c	Aggregated drivetrain torsional stiffness	5300	$\mathrm{N\,m/rad}$
d_c	Aggregated drivetrain damping constant	15	$\mathrm{N\,m\,s/rad}$
ρ	Air density	1.1	$\mathrm{kg/m^3}$
A_{st}	Vehicle frontal area	2.37	$\mathrm{m^2}$
c_w	Aerodynamic drag coefficient	0.3	–
g	Gravitational acceleration	9.81	$\mathrm{m/s^2}$
i_a	Automatic transmission gear ratio (2. gear)	3.2	–
i_r, i_f	Rear and front differential gear ratio	3.15	–
l_f	Distance front axle to COG	1.45	m
l_r	Distance rear axle to COG	1.55	m
B_r, B_f	Pacejka stiffness factor of the rear and front tires	10.5	–
C_r, C_f	Pacejka shape factor of the rear and front tires	1.6	–

From these parameters, the total gear ratio between main engine and rear axle is given by $i_G = i_a i_r = 10.08$ for the second gear. An example set consisting of the main controller parameters for the 4WD TCS is listed in Table A.2. Here, the index e denotes the parameters of the ETC, for example b_0 is the gain of the reference model of the controller on the ECU, responsible for the rear axle, while $b_{0,e}$ is the reference model gain of the ETC controller for the front axle. The sample times are $\tau_s = 0.01\,\mathrm{s}$ and $\tau_{s,e} = 0.005\,\mathrm{s}$, while the filter time constants used for computing the required derivatives are $\tau_d = 0.045\,\mathrm{s}$ and $\tau_{d,e} = 0.01\,\mathrm{s}$ while $a_0 = a_{0,e} = 0$.

Table A.2: Example controller parameters of the 4WD traction control system.

Name	Description	Value
k_p	Main engine proportional gain	12
k_i	Main engine integral gain	20
k_d	Main engine derivative gain	0.7
b_0	Main engine reference model gain	267.3
a_1	Main engine reference model inverse time constant	50
$k_{p,e}$	ETC proportional gain	3
$k_{i,e}$	ETC integral gain	1
$k_{d,e}$	ETC derivative gain	0.1
$b_{0,e}$	ETC reference model gain	280
$a_{1,e}$	ETC reference model inverse time constant	5

A.6 State Space Representation of the Linearized TCS

The overall linearized and discretized closed loop LTI system of the 2WD TCS is given by

$$\boldsymbol{x}_{\mathrm{cl}}(k+1) = \boldsymbol{A}_{\mathrm{cl}}\boldsymbol{x}_{\mathrm{cl}}(k) + \boldsymbol{B}_{\mathrm{cl}}\boldsymbol{u}_{\mathrm{cl}}(k) \tag{A.24a}$$

$$y_{\mathrm{cl}}(k) = \boldsymbol{C}_{\mathrm{cl}}\boldsymbol{x}_{\mathrm{cl}}(k) \tag{A.24b}$$

with $\boldsymbol{u}_{\mathrm{cl}}^T = \begin{bmatrix} r_1 & \mu \end{bmatrix}$, $y_{\mathrm{cl}} = y_1$, $\boldsymbol{x}_{\mathrm{cl}}^T = \begin{bmatrix} \delta x_1 & \delta x_2 & \delta x_3 & \delta x_4 & x_{a,d} & x_i & x_d & x_{F_1} & x_{F_2} & x_a \end{bmatrix}$. The first four states are plant states, $x_{a,d}$ is the state from the actuator time delay, x_i and x_d are the states of the PID controller, while x_{F_1} and x_{F_2} are the states of the F_{y_1} and the F_{x_4} filter and x_a is the actuator model state after resolving the feedback loop (see below for details). Moreover,

$$\boldsymbol{A}_{\mathrm{cl}} = \begin{bmatrix} A_{11} & b_0 k_1 d_a \boldsymbol{b}_{p,1}\boldsymbol{c}_c & d_a(k_3 - a_1 k_1)\boldsymbol{b}_{p,1}\boldsymbol{c}_1 & -d_a k_3 \boldsymbol{b}_{p,1}\boldsymbol{c}_2 & \boldsymbol{b}_{p,1}\boldsymbol{c}_a \\ -\boldsymbol{b}_c\boldsymbol{c}_{p,1} & \boldsymbol{A}_c & \boldsymbol{0}_{n_c\times n_1} & \boldsymbol{0}_{n_c\times n_2} & \boldsymbol{0}_{n_c\times n_a} \\ \boldsymbol{b}_1\boldsymbol{c}_{p,1} & \boldsymbol{0}_{n_1\times n_c} & \boldsymbol{A}_1 & \boldsymbol{0}_{n_1\times n_2} & \boldsymbol{0}_{n_1\times n_a} \\ \boldsymbol{b}_2\boldsymbol{c}_{p,2} & \boldsymbol{0}_{n_2\times n_c} & \boldsymbol{0}_{n_2\times n_1} & \boldsymbol{A}_2 & \boldsymbol{0}_{n_2\times n_a} \\ A_{41} & b_0 k_1 \boldsymbol{b}_a\boldsymbol{c}_c & (k_3 - a_1 k_1)\boldsymbol{b}_a\boldsymbol{c}_1 & -k_3\boldsymbol{b}_a\boldsymbol{c}_2 & \boldsymbol{A}_a \end{bmatrix} \tag{A.25a}$$

$$\boldsymbol{B}_{\mathrm{cl}} = \begin{bmatrix} b_0 k_1 d_a d_c \boldsymbol{b}_{p,1} & \boldsymbol{b}_{p,2} \\ \boldsymbol{b}_c & \boldsymbol{0}_{n_c\times 1} \\ \boldsymbol{0}_{n_1\times 1} & \boldsymbol{0}_{n_1\times 1} \\ \boldsymbol{0}_{n_2\times 1} & \boldsymbol{0}_{n_2\times 1} \\ b_0 k_1 d_c \boldsymbol{b}_a & \boldsymbol{0}_{n_a\times 1} \end{bmatrix}, \boldsymbol{C}_{\mathrm{cl}} = \begin{bmatrix} \boldsymbol{c}_{p,1} & \boldsymbol{0}_{1\times n_c} & \boldsymbol{0}_{1\times n_1} & \boldsymbol{0}_{1\times n_2} & \boldsymbol{0}_{1\times n_a} \end{bmatrix} \tag{A.25b}$$

$$A_{11} = \boldsymbol{A}_p - \boldsymbol{b}_{p,1} d_a \big(k_1 \boldsymbol{c}_{p,1}(a_0 + d_1 a_1 + d_c b_0) - k_2(\boldsymbol{c}_{p,1} - \boldsymbol{c}_{p,2}) + k_3(\boldsymbol{c}_{p,2} d_2 - \boldsymbol{c}_{p,1} d_1) \big) \tag{A.25c}$$

$$A_{41} = -\boldsymbol{b}_a \big(k_1 \boldsymbol{c}_{p,1}(a_0 + d_2 a_1 + d_c b_0) - k_2(\boldsymbol{c}_{p,1} - \boldsymbol{c}_{p,2}) + k_3(\boldsymbol{c}_{p,2} d_2 - \boldsymbol{c}_{p,1} d_1) \big) . \tag{A.25d}$$

Here, $\boldsymbol{A}_p$, $\boldsymbol{B}_p = \begin{bmatrix} \boldsymbol{b}_{p,1} & \boldsymbol{b}_{p,2} \end{bmatrix}$, $\boldsymbol{C}_p^T = \begin{bmatrix} \boldsymbol{c}_{p,1}^T & \boldsymbol{c}_{p,2}^T \end{bmatrix}$ are given by the zero order hold discretization of $\boldsymbol{A}$, $\boldsymbol{B} = \begin{bmatrix} \boldsymbol{b} & \boldsymbol{b}_d \end{bmatrix}$, $\boldsymbol{C}$ from (6.6) using the sample time $\tau_s = 0.01\,\mathrm{s}$ after adding an input delay of $\tau_{m,d} = 0.01\,\mathrm{s}$ to the first input channel. The matrices $\boldsymbol{A}_p'$, $\boldsymbol{B}_p'$ and $\boldsymbol{C}_p'$ (without delay state) are

$$\begin{bmatrix} \boldsymbol{A}_p' & \boldsymbol{B}_p' \\ \boldsymbol{0}_{m\times n} & \boldsymbol{I}_m \end{bmatrix} = \exp\Big(\begin{bmatrix} \boldsymbol{A} & \boldsymbol{B} \\ \boldsymbol{0}_{m\times n} & \boldsymbol{0}_{m\times m} \end{bmatrix} \tau_s \Big) = \exp(\boldsymbol{M}) \tag{A.26}$$

and $\boldsymbol{C}_p' = \boldsymbol{C}$, where $\exp(\boldsymbol{M}) = \sum_{i=0}^{\infty} \boldsymbol{M}^i/(i!)$ is the matrix exponential of the $(n+m)\times(n+m)$ matrix $\boldsymbol{M}$, with the definition that $\boldsymbol{M}^0 = \boldsymbol{I}_{n+m}$, see [56, pp. 215–216]. By absorbing the input delay of the first input channel into the system dynamic, the discretized plant matrices including this delay are

$$\boldsymbol{A}_p = \begin{bmatrix} \boldsymbol{A}_p' & \boldsymbol{b}_{p,1}' \\ \boldsymbol{0}_{1\times n} & 0 \end{bmatrix}, \boldsymbol{B}_p = \begin{bmatrix} \boldsymbol{0}_{n\times 1} & \boldsymbol{b}_{p,2}' \\ 1 & 0 \end{bmatrix}, \boldsymbol{C}_p = \begin{bmatrix} \boldsymbol{C}_p' & \boldsymbol{0}_{p_p\times 1} \end{bmatrix} . \tag{A.27}$$

where $\begin{bmatrix} \boldsymbol{b}_{p,1}' & \boldsymbol{b}_{p,2}' \end{bmatrix} = \boldsymbol{B}_p'$. Therefore, $\boldsymbol{A}_p \in \mathbb{R}^{n_p\times n_p}$, $\boldsymbol{B}_p = \begin{bmatrix} \boldsymbol{b}_{p,1} & \boldsymbol{b}_{p,2} \end{bmatrix} \in \mathbb{R}^{n_p\times m}$ and $\boldsymbol{C}_p \in \mathbb{R}^{p_p\times n_p}$ where $m = 2$, $p_p = 2$, $n_p = n+1$ and $n = 4$. The controller dynamics are discretized by applying the Tustin transformation the the corresponding continuous transfer functions of the PID controller (3.110b) and derivative filters (3.114) by substituting s by

$$s \mapsto \frac{2(z-1)}{\tau_s(z+1)} , \tag{A.28}$$

where s is the Laplace variable and z^{-1} represents a unit delay. Converting the discretized transfer functions back to state space form then gives $\boldsymbol{A}_c \in \mathbb{R}^{n_c\times n_c}$, $\boldsymbol{b}_c \in \mathbb{R}^{n_c\times 1}$, $\boldsymbol{c}_c \in \mathbb{R}^{1\times n_c}$ with $n_c = 2$ for the PID controller, $\boldsymbol{A}_1 \in \mathbb{R}^{n_1\times n_1}$, $\boldsymbol{b}_1 \in \mathbb{R}^{n_1\times 1}$, $\boldsymbol{c}_1 \in \mathbb{R}^{1\times n_1}$ with $n_1 = 1$ for the F_{y_1} filter and $\boldsymbol{A}_2 \in \mathbb{R}^{n_2\times n_2}$, $\boldsymbol{b}_2 \in \mathbb{R}^{n_2\times 1}$, $\boldsymbol{c}_2 \in \mathbb{R}^{1\times n_2}$ with $n_2 = 1$ for the F_{x_4} filter. The actuator model is also discretized using the Tustin transformation (A.28) but in (A.25), the actuator model feedback loop is already resolved. This means that $\boldsymbol{A}_a \in \mathbb{R}^{n_a\times n_a}$, $\boldsymbol{b}_a \in \mathbb{R}^{n_a\times 1}$, $\boldsymbol{c}_a \in \mathbb{R}^{1\times n_a}$ with $n_a = 1$ in (A.25) represent the state space matrices of $1/(1 - G_a(z))$ where $G_a(z)$ is the discrete version obtained by applying (A.28) to $G_a(s) = 1/(\tau_{s,e}s + 1)$, see also Section 6.2.1 and Figure 6.2.

Bibliography

[1] Ackermann, J., Blue, P., Bünte, T., Güvenç, L., Kaesbauer, D., Kordt, M., Muhler, M., and Odenthal, D. (2002). *Robust control: the parameter space approach*. Springer, London.

[2] Adamy, J. (2014). *Nichtlineare Systeme und Regelungen. 2., bearbeitete und erweiterte Auflage*. Springer, Berlin, 2 edition.

[3] Ahmad, N. S., Carrasco, J., and Heath, W. P. (2015). A less conservative LMI condition for stability of discrete-time systems with slope-restricted nonlinearities. *IEEE Transactions on Automatic Control*, 60(6):1692–1697.

[4] Ahmadi, A. A., Krstic, M., and Parrilo, P. A. (2011). A globally asymptotically stable polynomial vector field with no polynomial Lyapunov function. In *Proceedings of the 50th IEEE Conference on Decision and Control*, pages 7579–7580, Orlando. IEEE.

[5] Aizerman, M. A. (1949). On a problem concerning the stability "in the large" of dynamical systems. *Uspekhi Matematicheskikh Nauk*, 4(4):187–188.

[6] Aizerman, M. A. and Gantmacher, F. R. (1964). *Absolute stability of regulator systems*. Holden-Day, San Francisco.

[7] Akiba, T., Shirato, R., Fujita, T., and Tamura, J. (2007). A study of novel traction control method for electric motor driven vehicle. In *Proceedings of the 2007 Power Conversion Conference (PCC), Nagoya*, pages 699–704. IEEE.

[8] Alexander, A. and Vacca, A. (2017). Real-time parameter setpoint optimization for electro-hydraulic traction control systems. In *Proceedings of the 15th Scandinavian International Conference on Fluid Power, 2017*, number 144, pages 104–114, Linköping. Linköping University Electronic Press.

[9] Amada, J. and Fujimoto, H. (2012). Torque based direct driving force control method with driving stiffness estimation for electric vehicle with in-wheel motor. In *Proceedings of the 38th Annual Conference of the IEEE Industrial Electronics Society (IECON)*, pages 4904–4909, Montreal. IEEE.

[10] Amann, N., Bocker, J., and Prenner, F. (2004). Active damping of drive train oscillations for an electrically driven vehicle. *IEEE/ASME Transactions on Mechatronics*, 9(4):697–700.

[11] Amodeo, M., Ferrara, A., Terzaghi, R., and Vecchio, C. (2010). Wheel slip control via second-order sliding-mode generation. *IEEE Transactions on Intelligent Transportation Systems*, 11(1):122–131.

[12] Asami, K., Nomura, Y., and Naganawa, T. (1989). Traction control (TRC) system for 1987 Toyota Crown. *SAE Technical Paper 890833*.

[13] Backus, J. W. (1959). The syntax and semantics of the proposed international algebraic language of the Zurich ACM-GAMM conference. In *Proceedings of the International Conference on Information Processing*, pages 125–132, Paris.

[14] Backus, J. W., Bauer, F. L., Green, J., Katz, C., McCarthy, J., Naur, P., Perlis, A. J., Rutishauser, H., Samelson, K., Vauquois, B., Wegstein, J. H., van Wijngaarden, A., and Woodger, M. (1963). Revised report on the algorithmic language ALGOL 60. *The Computer Journal*, 5(4):349–367.

[15] Banks, C. (2002). Searching for Lyapunov functions using genetic programming. Virginia Polytech Institute and State University, Blacksburg, Virginia. Available at: `http://www.aerojockey.com/files/lyapunovgp.pdf`. Accessed: 24.05.2018.

[16] Barabanov, N. E. (1988). On the Kalman problem. *Siberian Mathematical Journal*, 29(3):333–341.

[17] Baumann, J., Torkzadeh, D. D., Ramstein, A., Kiencke, U., and Schlegl, T. (2004). Model-based predictive anti-jerk control. *IFAC Proceedings Volumes*, 37(22):53–58.

[18] Bleckmann, H.-W., Fennel, H., Gräber, J., and Seibert, W. W. (1986). Traction control system with Teves ABS Mark II. *SAE Technical Paper 860506*.

[19] Bobiti, R. and Lazar, M. (2018). Automated-sampling-based stability verification and DOA estimation for nonlinear systems. *IEEE Transactions on Automatic Control*, 63(11):3659–3674.

[20] Bocquillon, B., Feyel, P., Sandou, G., and Rodriguez-Ayerbe, P. (2020). Efficient construction of neural networks Lyapunov functions with domain of attraction maximization. In *17th International Conference on Informatics in Control, Automation and Robotics (ICINCO)*, pages 174–180, Online.

[21] Borrelli, F., Bemporad, A., Fodor, M., and Hrovat, D. (2006). An MPC/hybrid system approach to traction control. *IEEE Transactions on Control Systems Technology*, 14(3):541–552.

[22] Bragin, V. O., Vagaitsev, V. I., Kuznetsov, N. V., and Leonov, G. A. (2011). Algorithms for finding hidden oscillations in nonlinear systems. The Aizerman and Kalman conjectures and Chua's circuits. *Journal of Computer and Systems Sciences International*, 50(4):511–543.

[23] Brayton, R. and Tong, C. (1979). Stability of dynamical systems: A constructive approach. *IEEE Transactions on Circuits and Systems*, 26(4):224–234.

[24] Brockett, R. W. (1978). Feedback invariants for nonlinear systems. *IFAC Proceedings Volumes*, 11(1):1115–1120.

[25] Brogliato, B., Lozano, R., Maschke, B., and Egeland, O. (2007). *Dissipative systems analysis and control*. Springer, London, 2 edition.

[26] Buhmann, M. D. and Pinkus, A. (1995). On a recovery problem. In *Research Report/Seminar für Angewandte Mathematik*, volume 1995. Eidgenössische Technische Hochschule.

[27] Burckhardt, M. (1993). *Fahrwerktechnik: Radschlupf-Regelsysteme*. Vogel-Verlag, Würzburg.

[28] Byrnes, C. I. and Isidori, A. (1989). New results and examples in nonlinear feedback stabilization. *Systems & Control Letters*, 12(5):437–442.

[29] Cai, Z., Ma, C., and Zhao, Q. (2010). Acceleration-to-torque ratio based anti-skid control for electric vehicles. In *Proceedings of the 2010 IEEE/ASME International Conference on Mechatronic and Embedded Systems and Applications*, pages 577–581, Qingdao. IEEE.

[30] Canudas de Wit, C. and Tsiotras, P. (1999). Dynamic tire friction models for vehicle traction control. In *Proceedings of the 38th IEEE Conference on Decision and Control (Cat. No. 99CH36304)*, volume 4, pages 3746–3751, Phoenix, AZ. IEEE.

[31] Canudas de Wit, C., Tsiotras, P., Velenis, E., Basset, M., and Gissinger, G. (2003). Dynamic friction models for road/tire longitudinal interaction. *Vehicle System Dynamics*, 39(3):189–226.

[32] Carlson, C. R. and Gerdes, J. C. (2005). Consistent nonlinear estimation of longitudinal tire stiffness and effective radius. *IEEE Transactions on Control Systems Technology*, 13(6):1010–1020.

[33] Carrasco, J. and Heath, W. P. (2017). Comment on "Absolute stability analysis for negative-imaginary systems"[Automatica 67 (2016) 107–113]. *Automatica*, 85:486–488.

[34] Carrasco, J., Turner, M. C., and Heath, W. P. (2016). Zames–Falb multipliers for absolute stability: From O'Shea's contribution to convex searches. *European Journal of Control*, 28:1–19.

[35] Castañeda, Á. and Guíñez, V. (2011). The discrete and continuous Markus-Yamabe stability conjectures. Available online (last visit 21.04.2021): arXiv:1106.0755 [math.DS].

[36] Chapuis, C., Bideaux, E., Brun, X., and Minoiu-Enache, N. (2013). Comparison of feedback linearization and flatness control for anti-slip regulation (ASR) of an hybrid vehicle: From theory to experimental results. In *Proceedings of the 2013 European Control Conference (ECC)*, pages 446–451, Zurich. IEEE.

[37] Chapuis, C., Brun, X., Bideaux, E., and Minoiu-Enache, N. (2012). Anti-skid regulation (ASR) of an electric vehicle using flatness control. In *Proceedings of the 11th International Symposium on Advanced Vehicle Control*, pages 130–151, Seoul.

[38] Chen, B. and Harker, P. T. (1993). A non-interior-point continuation method for linear complementarity problems. *SIAM Journal on Matrix Analysis and Applications*, 14(4):1168–1190.

[39] Chen, C. and Mangasarian, O. L. (1996). A class of smoothing functions for nonlinear and mixed complementarity problems. *Computational Optimization and Applications*, 5:97–138.

[40] Chen, L., Xi, G., and Sun, J. (2012). Torque coordination control during mode transition for a series–parallel hybrid electric vehicle. *IEEE Transactions on Vehicular Technology*, 61(7):2936–2949.

[41] Chen, X. (2000). Smoothing methods for complementarity problems and their applications: a survey. *Journal of the Operations Research Society of Japan*, 43(1):32–47.

[42] Chesi, G. (2005). Domain of attraction: estimates for non-polynomial systems via LMIs. In *Proceedings of the 16th IFAC World Congress on Automatic Control*, Prague.

[43] Cho, Y.-S. and Narendra, K. (1968). An off-axis circle criterion for stability of feedback systems with a monotonic nonlinearity. *IEEE Transactions on Automatic Control*, 13(4):413–416.

[44] Cima, A., Essen, A. v. d., Gasull, A., Hubbers, E., and Mañosas, F. (1997a). A polynomial counterexample to the Markus-Yamabe conjecture. *Advances in Mathematics*, 131(2):453–457.

[45] Cima, A., Gasull, A., and Mañosas, F. (1997b). A polynomial class of Markus-Yamabe counterexamples. *Publicacions Matemàtiques*, pages 85–100.

[46] Clover, C. L. and Bernard, J. E. (1998). Longitudinal tire dynamics. *Vehicle System Dynamics*, 29(4):231–260.

[47] Colli, V., Tomassi, G., and Scarano, M. (2006). Single wheel longitudinal traction control for electric vehicles. *IEEE Transactions on Power Electronics*, 21(3):799–808.

[48] Crossley, P. R. (1988). Anti-spin control. *SAE Technical Paper 885106*.

[49] Dahmani, H., Pagès, O., and El Hajjaji, A. (2015). Traction control system using a fuzzy representation of the vehicle model. In *Proceedings of the IEEE American Control Conference (ACC)*, pages 5712–5717, Chicago. IEEE.

[50] Dahmani, H., Pagès, O., El Hajjaji, A., and Daraoui, N. (2013). Observer-based tracking control of the vehicle lateral dynamics using four-wheel active steering. In *Proceedings of the 16th International IEEE Conference on Intelligent Transportation Systems (ITSC 2013)*, pages 360–365, The Hague. IEEE.

[51] De Bruin, J. C. A., Doris, A., van de Wouw, N., Heemels, W. P. M. H., and Nijmeijer, H. (2009). Control of mechanical motion systems with non-collocation of actuation and friction: A Popov criterion approach for input-to-state stability and set-valued nonlinearities. *Automatica*, 45(2):405–415.

[52] De Castro, R., Araújo, R. E., and Freitas, D. (2013). Wheel slip control of EVs based on sliding mode technique with conditional integrators. *IEEE Transactions on Industrial Electronics*, 60(8):3256–3271.

[53] De Pinto, S., Chatzikomis, C., Sorniotti, A., and Mantriota, G. (2017). Comparison of traction controllers for electric vehicles with on-board drivetrains. *IEEE Transactions on Vehicular Technology*, 66(8):6715–6727.

[54] Debes, M., Herb, E., Müller, R., Sokoll, G., and Straub, A. (1997a). Dynamische Stabilitäts Control DSC der Baureihe 7 von BMW-Teil 1. *ATZ Automobiltechnische Zeitschrift*, 99(3):134–140.

[55] Debes, M., Herb, E., Müller, R., Sokoll, G., and Straub, A. (1997b). Dynamische Stabilitäts Control DSC der Baureihe 7 von BMW-Teil 2. *ATZ Automobiltechnische Zeitschrift*, 99(4):208–213.

[56] DeCarlo, R. A. (1989). *Linear systems: a state variable approach with numerical implementation*. Prentice Hall, Englewood Cliffs, NJ.

[57] Degel, W., Lupberger, S., Odenthal, D., and Bajcinca, N. (2020). Two degrees of freedom slip controller with lateral torque distribution. *IFAC-PapersOnLine*, 53(2):14450–14455.

[58] Degel, W., Lupberger, S., Odenthal, D., and Bajcinca, N. (2021). Scalable slip control with torque vectoring including input-to-state stability analysis. *IEEE Transactions on Control Systems Technology*. To appear.

[59] Dewey, A. and Jury, E. (1965). A note on Aizerman's conjecture. *IEEE Transactions on Automatic Control*, 10(4):482–483.

[60] Doyle, J. C., Francis, B. A., and Tannenbaum, A. R. (1992). *Feedback control theory*. Macmillan, New York.

[61] Duriez, T., Brunton, S. L., and Noack, B. R. (2016). *Machine Learning Control - Taming Nonlinear Dynamics and Turbulence*. Springer, Cham.

[62] Ewin, N. (2016). *Traction control for electric vehicles with independently driven wheels*. PhD thesis, University of Oxford.

[63] Fan, Z., Koren, Y., and Wehe, D. (1995). A simple traction control for tracked vehicles. In *Proceedings of the 1995 American Control Conference (ACC)*, volume 2, pages 1176–1177, Seattle, WA. IEEE.

[64] Farmer, C. M. (2004). Effect of electronic stability control on automobile crash risk. *Traffic injury prevention*, 5(4):317–325.

[65] Ferrara, A. and Vecchio, C. (2007). Low vibration vehicle traction control to solve fastest acceleration/deceleration problems via second order sliding modes. In *Proceedings of the 2007 American Control Conference (ACC)*, pages 5236–5241, New York. IEEE.

[66] Fertik, H. A. and Ross, C. W. (1967). Direct digital control algorithm with anti-windup feature. *ISA Transactions*, 6(4):317–328.

[67] Feßler, R. (1995). A proof of the two-dimensional Markus-Yamabe stability conjecture and a generalization. *Annales Polonici Mathematici*, 62:45–74.

[68] Fitts, R. (1966). Two counterexamples to Aizerman's conjecture. *IEEE Transactions on Automatic Control*, 11(3):553–556.

[69] Fodor, M., Yester, J., and Hrovat, D. (1998). Active control of vehicle dynamics. In *17th DASC. AIAA/IEEE/SAE. Digital Avionics Systems Conference. Proceedings (Cat. No.98CH36267)*, volume 2, pages I14/1–I14/8, Bellevue, WA. IEEE.

[70] Franklin, G. F., Powell, J. D., and Emami-Naeini, A. (2019). *Feedback control of dynamic systems*. Pearson Education, Limited, Harlow, UK, 8 edition.

[71] Fujii, K. and Fujimoto, H. (2007). Traction control based on slip ratio estimation without detecting vehicle speed for electric vehicle. In *2007 Power Conversion Conference*, pages 688–693, Nagoya. IEEE.

[72] Fujimoto, H., Amada, J., and Maeda, K. (2012). Review of traction and braking control for electric vehicle. In *Proceedings of the 2012 IEEE Vehicle Power and Propulsion Conference*, pages 1292–1299, Seoul. IEEE.

[73] Fujimoto, H., Fujii, K., and Takahashi, N. (2007). Traction and yaw-rate control of electric vehicle with slip-ratio and cornering stiffness estimation. In *Proceedings of the 2007 American control conference (ACC)*, pages 5742–5747, New York. IEEE.

[74] Fujimoto, H., Saito, T., and Noguchi, T. (2004a). Motion stabilization control of electric vehicle under snowy conditions based on yaw-moment observer. In *Proceedings of the 8th IEEE International Workshop on Advanced Motion Control, 2004. AMC'04.*, pages 35–40, Kawasaki. IEEE.

[75] Fujimoto, H., Saito, T., Tsumasaka, A., and Noguchi, T. (2004b). Motion control and road condition estimation of electric vehicles with two in-wheel motors. In *Proceedings of the IEEE International Conference on Control Applications*, volume 2, pages 1266–1271, Taipei. IEEE.

[76] Geamanu, M. S., Mounier, H., Niculescu, S.-I., Cela, A., and LeSolliec, G. (2012). Longitudinal control for an all-electric vehicle. In *Proceedings of the 2012 IEEE International Electric Vehicle Conference (IEVC)*, pages 1–6, Greenville, SC. IEEE.

[77] General Motors Corporation (1970). Section A, Max-Trac System, 45-46-48-49000 series. *1971 Buick chassis service manual*, pages 66–1–66–10. Available at: `https://www.buick-riviera.com/servicemanual.html`. Accessed: 24.08.2019.

[78] Genesio, R., Tartaglia, M., and Vicino, A. (1985). On the estimation of asymptotic stability regions: State of the art and new proposals. *IEEE Transactions on Automatic Control*, 30(8):747–755.

[79] Gerstenmeier, J. (1986). Traction control (ASR)-An extension of the anti-lock braking system (ABS). *SAE Technical Paper 861033*.

[80] Giesl, P. (2007). *Construction of global Lyapunov functions using radial basis functions*, volume 1904 of *Lecture Notes in Mathematics*. Springer, Berlin.

[81] Giesl, P. and Hafstein, S. (2015). Review on computational methods for Lyapunov functions. *Discrete and Continuous Dynamical Systems, Series B*, 20(8):2291–2331.

[82] Giesl, P., Osborne, C., and Hafstein, S. (2020). Automatic determination of connected sublevel sets of CPA Lyapunov functions. *SIAM Journal on Applied Dynamical Systems*, 19(2):1029–1056.

[83] Gillespie, T. D. (1992). *Fundamentals of vehicle dynamics*. Society of Automotive Engineers, Warrendale, PA.

[84] Glassman, E., Desbiens, A. L., Tobenkin, M., Cutkosky, M., and Tedrake, R. (2012). Region of attraction estimation for a perching aircraft: A Lyapunov method exploiting barrier certificates. In *Proceedings of the 2012 IEEE International Conference on Robotics and Automation (ICRA)*, pages 2235–2242, Saint Paul, MN. IEEE.

[85] Glover, F. W. and Kochenberger, G. A. (2006). *Handbook of metaheuristics*. Springer, Boston, MA.

[86] Glutsuk, A. A. (1994). The complete solution of the Jacobian problem for planar vector fields. *Russian Mathematical Surveys*, 49(3):185–186.

[87] Glutsuk, A. A. (1996). Asymptotic stability of linearizations of a vector field in $\mathbb{R}^3$ with a singular point does not imply global stability. In *Comunicaciones del CIMAT*, Guanajuato, Mexico. Preprint 1995.

[88] Gordon, W. B. (1972). On the diffeomorphisms of Euclidean space. *The American Mathematical Monthly*, 79(7):755–759.

[89] Grosman, B. and Lewin, D. R. (2005). Automatic generation of Lyapunov functions using genetic programming. *IFAC Proceedings Volumes*, 38(1):75–80.

[90] Götting, G. (2004). *Dynamische Antriebsregelung von Elektrostraßenfahrzeugen unter Berücksichtigung eines schwingungsfähigen Antriebsstrangs*. PhD thesis, RWTH Aachen University, Germany.

[91] Götting, G. and De Doncker, R. W. (2004). Active drive control of electric vehicles using a modal state observer. In *2004 IEEE 35th Annual Power Electronics Specialists Conference (IEEE Cat. No. 04CH37551)*, volume 6, pages 4585–4590, Aachen. IEEE.

[92] Guíñez, V. and Castañeda, Á. (2011). A polynomial class of Markus–Yamabe counterexamples and examples in $\mathbb{R}^3$. *Applicable Analysis*, 90(5):787–798.

[93] Guo, H., Yu, R., Qiang, W., and Chen, H. (2014). Optimal slip based traction control for electric vehicles using feedback linearization. In *Proceedings of the 2014 International Conference on Mechatronics and Control (ICMC)*, pages 1159–1164, Jinzhou. IEEE.

[94] Gurel, O. and Lapidus, L. (1969). A guide to methods for the generation of Liapunov functions. *Industrial & Engineering Chemistry*, 61(3):30–41.

[95] Gustafsson, F. (1997). Slip-based tire-road friction estimation. *Automatica*, 33(6):1087–1099.

[96] Gutiérrez, C. (1995). A solution to the bidimensional global asymptotic stability conjecture. *Annales de l'Institut Henri Poincaré C, Analyse non linéaire*, 12(6):627–671.

[97] Ha, I.-J., Tugcu, A. K., and Boustany, N. M. (1989). Feedback linearizing control of vehicle longitudinal acceleration. *IEEE Transactions on Automatic Control*, 34(7):689–698.

[98] Hafstein, S. (2007). An algorithm for constructing Lyapunov functions. *Electronic Journal of Differential Equations*, Monograph 8:1–100.

[99] Hahn, W. (1967). *Stability of motion*, volume 138 of *Die Grundlehren der mathematischen Wissenschaften*. Springer, Berlin, Heidelberg.

[100] Ham, H. and Lee, H. (2011). Sliding mode control strategy for the four wheel drive vehicles. In *Proceedings of the 37th Annual Conference of the IEEE Industrial Electronics Society (IECON)*, pages 746–750, Melbourne, VIC. IEEE.

[101] Hamzah, N., Aripin, M. K., Sam, Y. M., Selamat, H., and Ghazali, R. (2012). Second order sliding mode controller for longitudinal wheel slip control. In *2012 IEEE 8th International Colloquium on Signal Processing and its Applications*, pages 138–143, Malacca. IEEE.

[102] Han, K., Choi, M., Lee, B., and Choi, S. B. (2017). Development of a traction control system using a special type of sliding mode controller for hybrid 4WD vehicles. *IEEE Transactions on Vehicular Technology*, 67(1):264–274.

[103] Harifi, A., Aghagolzadeh, A., Alizadeh, G., and Sadeghi, M. (2008). Designing a sliding mode controller for slip control of antilock brake systems. *Transportation Research Part C: Emerging Technologies*, 16(6):731–741.

[104] Haupt, R. L. and Haupt, S. E. (2004). *Practical genetic algorithms*. Wiley, New York, 2 edition.

[105] He, H., Peng, J., Xiong, R., and Fan, H. (2014). An acceleration slip regulation strategy for four-wheel drive electric vehicles based on sliding mode control. *Energies*, 7(6):3748–3763.

[106] He, P. and Hori, Y. (2006). Optimum traction force distribution for stability improvement of 4WD EV in critical driving condition. In *9th IEEE International Workshop on Advanced Motion Control, 2006.*, pages 596–601. IEEE.

[107] He, Y., Lu, C., Shen, J., and Yuan, C. (2019). Design and analysis of output feedback constraint control for antilock braking system with time-varying slip ratio. *Mathematical Problems in Engineering*, 2019:1–11.

[108] Heath, W. P. and Li, G. (2009). Lyapunov functions for the multivariable Popov criterion with indefinite multipliers. *Automatica*, 45(12):2977–2981.

[109] Heath, W. P. and Wills, A. G. (2007). Zames-Falb multipliers for quadratic programming. *IEEE Transactions on Automatic Control*, 52(10):1948–1951.

[110] Holland, J. H. (1975). *Adaptation in natural and artificial systems*. University of Michigan Press, Ann Arbor, MI.

[111] Hori, Y. (1996). A review of torsional vibration control methods and a proposal of disturbance observer-based new techniques. *IFAC Proceedings Volumes*, 29(1):990–995.

[112] Hori, Y. (2002). Future vehicle driven by electricity and control-research on four wheel motored "UOT Electric March II". In *Proceedings of the 7th International Workshop on Advanced Motion Control (Cat. No. 02TH8623)*, pages 1–14, Maribor. IEEE.

[113] Hori, Y., Toyoda, Y., and Tsuruoka, Y. (1998). Traction control of electric vehicle: basic experimental results using the test EV "UOT Electric March". *IEEE Transactions on Industry Applications*, 34(5):1131–1138.

[114] Hrovat, D., Asgari, J., and Fodor, M. (2000). Automotive mechatronic systems. In *Mechatronic systems techniques and applications*, pages 1–98. Gordon & Breach, New York.

[115] Hrovat, D. and Fodor, M. (2014). Automotive engine-based traction control. In *The Impact of Control Technology, 2nd edition*, pages 17–18. IEEE Control Systems Society, New York. Available at: `http://ieeecss.org/impact-control-technology-2nd-edition`. Accessed: 07.07.2021.

[116] Hu, J. J., He, Z. B., Ge, P., and Qin, D. T. (2011). Research on control strategy of traction control for four wheel drive vehicle. In *Frontiers of Manufacturing Science and Measuring Technology*, volume 230 of *Advanced Materials Research*, pages 1242–1249. Trans Tech Publications.

[117] Hu, J.-S. and Yin, D. (2011). MTTE-based motion stabilization control for in-wheel motor electric vehicles. In *SICE Annual Conference 2011*, pages 312–317, Tokyo. IEEE.

[118] Hurwitz, A. (1895). Ueber die Bedingungen, unter welchen eine Gleichung nur Wurzeln mit negativen reellen Theilen besitzt. *Mathematische Annalen*, 46:273–284.

[119] Ilchmann, A. and Schuster, H. (2009). PI-funnel control for two mass systems. *IEEE Transactions on Automatic Control*, 54(4):918–923.

[120] Ise, K., Fujita, K., Inoue, Y., and Masutomi, S. (1990). The "Lexus" traction control (TRAC) system. *SAE Transactions*, 99:319–326.

[121] Isermann, R. (2006). *Fahrdynamik-Regelung: Modellbildung, Fahrerassistenzsysteme, Mechatronik*. Vieweg, Wiesbaden.

[122] Isermann, R. (2014). *Engine modeling and control*. Springer, Berlin, Heidelberg.

[123] Isidori, A. (1995). *Nonlinear Control Systems*. Springer, London, 3 edition.

[124] Isidori, A. (1999). *Nonlinear Control Systems II*. Springer, London.

[125] Isidori, A. (2017). *Lectures in feedback design for multivariable systems*. Advanced Textbooks in Control and Signal Processing. Springer, Cham.

[126] Isidori, A. and Krener, A. (1982). On feedback equivalence of nonlinear systems. *Systems & Control Letters*, 2(2):118–121.

[127] Isidori, A. and Ruberti, A. (1984). On the synthesis of linear input-output responses for nonlinear systems. *Systems & Control Letters*, 4(1):17–22.

[128] Ivanov, V. (2017). *Advanced automotive active safety systems: Focus on integrated chassis control for conventional and electric vehicles with identification of road conditions*. Habilitation thesis, Technical University of Ilmenau.

[129] Ivanov, V., Savitski, D., and Shyrokau, B. (2015). A survey of traction control and antilock braking systems of full electric vehicles with individually controlled electric motors. *IEEE Transactions on Vehicular Technology*, 64(9):3878–3896.

[130] Jaime, R.-P., Kästner, F., Erban, A., and Knödler, K. (2014). Algorithms for recuperation and traction in electric vehicles. *ATZelektronik Worldwide*, 9(2):4–9.

[131] Jalali, K., Uchida, T., Lambert, S., and McPhee, J. (2013). Development of an advanced torque vectoring control system for an electric vehicle with in-wheel motors using soft computing techniques. *SAE International Journal of Alternative Powertrains*, 2(2):261–278.

[132] Jalali, K., Uchida, T., McPhee, J., and Lambert, S. (2012). Development of a fuzzy slip control system for electric vehicles with in-wheel motors. *SAE International Journal of Alternative Powertrains*, 1(1):46–64.

[133] Jalili-Kharaajoo, M. and Besharati, F. (2003). Sliding mode traction control of an electric vehicle with four separate wheel drives. In *Proceedings of the IEEE Conference on Emerging Technologies and Factory Automation (EFTA)*, volume 2, pages 291–296, Lisbon. IEEE.

[134] Jayawardhana, B., Logemann, H., and Ryan, E. P. (2011). The circle criterion and input-to-state stability. *IEEE Control Systems Magazine*, 31(4):32–67.

[135] Jin, L.-Q., Ling, M., and Yue, W. (2017). Tire-road friction estimation and traction control strategy for motorized electric vehicle. *PloS one*, 12(6):e0179526.

[136] Johansen, T. A., Petersen, I., Kalkkuhl, J., and Ludemann, J. (2003). Gain-scheduled wheel slip control in automotive brake systems. *IEEE Transactions on Control Systems Technology*, 11(6):799–811.

[137] Johansson, M. and Rantzer, A. (1997). Computation of piecewise quadratic Lyapunov functions for hybrid systems. In *Proceedings of the 1997 European Control Conference (ECC)*, pages 2005–2010, Brussels. IEEE.

[138] John, S. and Pedro, J. O. (2013). Hybrid feedback linearization slip control for anti-lock braking system. *Acta Polytechnica Hungarica*, 10(1):81–99.

[139] Jones, M., Mohammadi, H., and Peet, M. M. (2017). Estimating the region of attraction using polynomial optimization: A converse Lyapunov result. In *Proceedings of the 56th Conference on Decision and Control (CDC)*, pages 1796–1802, Melbourne, VIC. IEEE.

[140] Jonsson, U. (1997). A nonlinear Popov criterion. In *Proceedings of the 36th Conference on Decision and Control (CDC)*, volume 4, pages 3523–3527, San Diego, CA. IEEE.

[141] Kabganian, M. and Kazemi, R. (2001). A new strategy for traction control in turning via engine modeling. *IEEE Transactions on Vehicular Technology*, 50(6):1540–1548.

[142] Kachroo, P. and Tomizuka, M. (1994). Vehicle traction control and its applications. Technical report, Institute of Transportation Studies, UC Berkeley.

[143] Kalman, R. E. (1957). Physical and mathematical mechanisms of instability in nonlinear automatic control systems. *Transactions of ASME*, 79(3):553–566.

[144] Kalman, R. E. (1963). Lyapunov functions for the problem of Lur'e in automatic control. *Proceedings of the National Academy of Sciences of the United States of America*, 49(2):201–205.

[145] Kanzow, C. (1996). Some noninterior continuation methods for linear complementarity problems. *SIAM Journal on Matrix Analysis and Applications*, 17(4):851–868.

[146] Kapinski, J., Deshmukh, J. V., Sankaranarayanan, S., and Arechiga, N. (2014). Simulation-guided Lyapunov analysis for hybrid dynamical systems. In *Proceedings of the 17th international conference on Hybrid systems: computation and control*, pages 133–142, Berlin. ACM.

[147] Kawabe, T. (2012). Slip suppression of electric vehicles using model predictive PID controller. *International Journal of World Academy of Science, Engineering and Technology*, 67:524–529.

[148] Kececi, E. F. and Tao, G. (2006). Adaptive vehicle skid control. *Mechatronics*, 16(5):291–301.

[149] Khalil, H. K. (1996). *Nonlinear Systems*. Prentice Hall, Upper Saddle River, NJ, 3 edition.

[150] Khatun, P., Bingham, C. M., Schofield, N., and Mellor, P. H. (2003). Application of fuzzy control algorithms for electric vehicle antilock braking/traction control systems. *IEEE Transactions on Vehicular Technology*, 52(5):1356–1364.

[151] Kiencke, U. and Nielsen, L. (2005). *Automotive control systems: for engine, driveline, and vehicle*. Springer, Berlin, Heidelberg, 2 edition.

[152] Kirchner, W. T. and Southward, S. C. (2013). Adaptive vehicle traction control: combined longitudinal and lateral motion. *International Journal of Dynamics and Control*, 1(3):239–253.

[153] König, L., Merlein, D., Schindele, F., and Zimmermann, A. (2019a). Integrierte Traktionsregelung mit modellbasierter Vorsteuerung. *ATZ Automobiltechnische Zeitschrift*, 121(1):46–51.

[154] König, L., Schindele, F., and Ghosh, J. (2019b). ITC–model-based feed forward traction control. In *9th International Munich Chassis Symposium 2018*, pages 265–283, Munich. Springer Vieweg, Wiesbaden.

[155] Kothare, M. V. and Morari, M. (1999). Multiplier theory for stability analysis of anti-windup control systems. *Automatica*, 35(5):917–928.

[156] Kotwicki, A. J. (1982). Dynamic models for torque converter equipped vehicles. *SAE Transactions*, 91:1595–1609.

[157] Koza, J. R. (1992). *Genetic programming: on the programming of computers by means of natural selection*. MIT press, Cambridge, MA.

[158] Koza, J. R. (1994). Genetic programming as a means for programming computers by natural selection. *Statistics and Computing*, 4(2):87–112.

[159] Koza, J. R., Keane, M. A., Yu, J., Bennett, F. H., Mydlowec, W., and Stiffelman, O. (1999). Automatic synthesis of both the topology and parameters for a robust controller for a nonminimal phase plant and a three-lag plant by means of genetic programming. In *Proceedings of the 38th IEEE Conference on Decision and Control (Cat. No. 99CH36304)*, volume 5, pages 5292–5300, Phoenix, AZ. IEEE.

[160] Koza, J. R., Keane, M. A., Yu, J., Mydlowec, W., and Bennett, F. H. (2000). Automatic synthesis of both the topology and parameters for a controller for a three-lag plant with a five-second delay using genetic programming. In *Real-World Applications of Evolutionary Computing*, volume 1803, pages 168–177, Berlin, Heidelberg. Springer.

[161] Krantz, S. G. and Parks, H. R. (2003). *The implicit function theorem: History, theory, and applications*. Springer, Boston, MA.

[162] Krener, A. J. (2013). *Feedback Linearization of Nonlinear Systems*, pages 1–14. Encyclopedia of Systems and Control. Springer, London.

[163] Kuntanapreeda, S. (2014). Traction control of electric vehicles using sliding-mode controller with tractive force observer. *International Journal of Vehicular Technology*, 2014:1–10.

[164] Kuntanapreeda, S. (2015). Super-twisting sliding-mode traction control of vehicles with tractive force observer. *Control Engineering Practice*, 38:26–36.

[165] Lagarias, J. C., Reeds, J. A., Wright, M. H., and Wright, P. E. (1998). Convergence properties of the Nelder–Mead simplex method in low dimensions. *SIAM Journal on Optimization*, 9(1):112–147.

[166] Lee, H. (2006). Four-wheel drive control system using a clutchless centre limited slip differential. *Proceedings of the Institution of Mechanical Engineers, Part D: Journal of Automobile Engineering*, 220(6):665–681.

[167] Lee, H. and Tomizuka, M. (2003). Adaptive vehicle traction force control for intelligent vehicle highway systems (IVHSs). *IEEE Transactions on Industrial Electronics*, 50(1):37–47.

[168] Lee, J. H. and Yoo, W. S. (2012). Non-singular slip (NSS) method for longitudinal tire force calculations in a sudden braking simulation. *International Journal of Automotive Technology*, 13(2):215–222.

[169] Leonov, G. A., Burkin, I. M., and Shepeljavyi, A. I. (1996). *Frequency methods in oscillation theory*, volume 357. Kluwer Academic Publishers, Dordrecht.

[170] Li, C., Ryoo, C.-S., Li, N., and Cao, L. (2009a). Estimating the domain of attraction via moment matrices. *Bulletin of the Korean Mathematical Society*, 46(6):1237–1248.

[171] Li, G., Heath, W. P., and Lennox, B. (2007). An improved stability criterion for a class of Lur'e systems. In *Proceedings of the 46th Conference on Decision and Control (CDC)*, pages 4483–4488, New Orleans, LA. IEEE.

[172] Li, H., Li, L., Song, J., Wu, K., Qiao, Y., Liu, X., and Xia, Y. (2012a). Algorithm for calculating torque base in vehicle traction control system. *Chinese Journal of Mechanical Engineering*, 25(6):1130–1137.

[173] Li, H.-Z., Li, L., He, L., Kang, M.-X., Song, J., Yu, L.-Y., and Wu, C. (2012b). PID plus fuzzy logic method for torque control in traction control system. *International Journal of Automotive Technology*, 13(3):441–450.

[174] Li, J., Song, Z., Shuai, Z., Xu, L., and Ouyang, M. (2015). Wheel slip control using sliding-mode technique and maximum transmissible torque estimation. *Journal of Dynamic Systems, Measurement, and Control*, 137(11):111010–1–111010–10.

[175] Li, K.-C. (1992). On principal Hessian directions for data visualization and dimension reduction: Another application of Stein's lemma. *Journal of the American Statistical Association*, 87(420):1025–1039.

[176] Li, L., Kodama, S., and Hori, Y. (2004). Anti-skid control for EV using dynamic model error based on back-EMF observer. In *Proceedings of the 30th Annual Conference of the IEEE Industrial Electronics Society (IECON)*, volume 2, pages 1700–1704, Busan. IEEE.

[177] Li, S., Liao, C., Chen, S., and Wang, L. (2009b). Traction control of hybrid electric vehicle. In *Proceedings of the 2009 IEEE Vehicle Power and Propulsion Conference*, pages 1535–1540, Dearborn, MI. IEEE.

[178] Lie, A., Tingvall, C., Krafft, M., and Kullgren, A. (2006). The effectiveness of electronic stability control (ESC) in reducing real life crashes and injuries. *Traffic Injury Prevention*, 7(1):38–43.

[179] Liu, G. and Jin, L. (2016). A study of coordinated vehicle traction control system based on optimal slip ratio algorithm. *Mathematical Problems in Engineering*, 2016:1–10.

[180] Logan, B. F. and Shepp, L. A. (1975). Optimal reconstruction of a function from its projections. *Duke Mathematical Journal*, 42(4):645–659.

[181] Loof, J., Besselink, I., and Nijmeijer, H. (2014). Traction control of an electric formula student racing car. In *Proceedings of the 35th FISITA World Automotive Congress*, Maastricht.

[182] Lupberger, S., Degel, W., Odenthal, D., and Bajcinca, N. (2020). Control allocation for hybrid braking considering dynamic battery behaviour. *IFAC-PapersOnLine*, 53(2):14085–14090.

[183] Lupberger, S., Degel, W., Odenthal, D., and Bajcinca, N. (2021). Nonlinear control design for regenerative and hybrid antilock braking in electric vehicles. *IEEE Transactions on Control Systems Technology*, pages 1–15. Early Access.

[184] Lur'e, A. I. and Postnikov, V. N. (1944). On the theory of stability of control systems. *Applied Mathematics and Mechanics*, 8(3):246–248. In Russian.

[185] Lyapunov, A. M. (1992). *The general problem of the stability of motion.* Taylor & Francis, London. English translation by A.T. Fuller, original work published in Russian in 1892.

[186] Maeda, K., Fujimoto, H., and Hori, Y. (2012). Four-wheel driving-force distribution method for instantaneous or split slippery roads for electric vehicle with in-wheel motors. In *Proceedings of the 12th IEEE International Workshop on Advanced Motion Control (AMC)*, pages 1–6, Sarajevo. IEEE.

[187] Magallan, G. A., De Angelo, C. H., and Garcia, G. O. (2010). Maximization of the traction forces in a 2WD electric vehicle. *IEEE Transactions on Vehicular Technology*, 60(2):369–380.

[188] Maisch, W., Jonner, W.-D., and Sigl, A. (1987). ASR–traction control–a logical extension of ABS. *SAE Transactions*, 96:1487–1493.

[189] Marino, P., Meo, S., and Scarano, M. (1993). A stochastic controller for anti-skidding microprocessor system. In *Proceedings of the 5th European Conference on Power Electronics and Applications*, pages 162–166, Brighton. IET.

[190] Markus, L. and Yamabe, H. (1960). Global stability criteria for differential systems. *Osaka Mathematical Journal*, 12(2):305–317.

[191] Materassi, D. and Salapaka, M. V. (2009). Attraction domain estimates combining Lyapunov functions. In *Proceedings of the 2009 American Control Conference (ACC)*, pages 4007–4012, St. Louis, MO. IEEE.

[192] Matthews, M. L. and Williams, C. M. (2012). Region of attraction estimation of biological continuous Boolean models. In *Proceedings of the IEEE International Conference on Systems, Man and Cybernetics*, pages 1700–1705, Seoul. IEEE.

[193] Max Trac (n.d.). Information and brochure from 1971 about the Buick Riviera Max-Trac System. Webpage. Available at: `https://www.buick-riviera.com/maxtrac.html`. Accessed: 24.08.2019.

[194] McGough, J. S., Christianson, A. W., and Hoover, R. C. (2010). Symbolic computation of Lyapunov functions using evolutionary algorithms. In *Proceedings of the 12th IASTED International Conference*, volume 15, pages 508–515, Banff, Alberta.

[195] McKay, R. I., Hoai, N. X., Whigham, P. A., Shan, Y., and O'Neill, M. (2010). Grammar-based genetic programming: a survey. *Genetic Programming and Evolvable Machines*, 11(3):365–396.

[196] Megretski, A. and Rantzer, A. (1997). System analysis via integral quadratic constraints. *IEEE Transactions on Automatic Control*, 42(6):819–830.

[197] Meisters, G. H. (1996). A biography of the Markus-Yamabe conjecture. *Aspects of Mathematics: Algebra, Geometry and Several Complex Variables*. Available at: `https://math.unl.edu/~gmeisters1/papers/HK1996.pdf`. Accessed: 01.05.2021.

[198] Mirzaeinejad, H. and Mirzaei, M. (2010). A novel method for non-linear control of wheel slip in anti-lock braking systems. *Control Engineering Practice*, 18(8):918–926.

[199] Mitchell, M. (1998). *An introduction to genetic algorithms*. MIT press, Cambridge, MA.

[200] Mitschke, M. and Wallentowitz, H. (2014). *Dynamik der Kraftfahrzeuge*, volume 5. Springer Vieweg, Wiesbaden.

[201] Müller, A., Achenberg, W., Schindler, E., Wohland, T., and Mohn, F.-W. (1994). Das neue Fahrsicherheitssystem Electronic Stability Program von Mercedes-Benz. *ATZ Automobiltechnische Zeitschrift*, 96(11):656–670.

[202] Mousavi, A., Davaie-Markazi, A. H., and Masoudi, S. (2018). Comparison of adaptive fuzzy sliding-mode pulse width modulation control with common model-based nonlinear controllers for slip control in antilock braking systems. *Journal of Dynamic Systems, Measurement, and Control*, 140(1):011014–1–011014–15.

[203] Muller, S., Uchanski, M., and Hedrick, K. (2003). Estimation of the maximum tire-road friction coefficient. *Journal of Dynamic systems, Measurement, and Control*, 125(4):607–617.

[204] Najafi, E., Babuška, R., and Lopes, G. A. D. (2016). A fast sampling method for estimating the domain of attraction. *Nonlinear Dynamics*, 86(2):823–834.

[205] Nakakuki, T., Shen, T., and Tamura, K. (2008). Adaptive control approach to uncertain longitudinal tire slip in traction control of vehicles. *Asian Journal of Control*, 10(1):67–73.

[206] Nam, K., Fujimoto, H., and Hori, Y. (2015a). Design of an adaptive sliding mode controller for robust yaw stabilisation of in-wheel-motor-driven electric vehicles. *International Journal of Vehicle Design*, 67(1):98–113.

[207] Nam, K., Hori, Y., and Lee, C. (2015b). Wheel slip control for improving traction-ability and energy efficiency of a personal electric vehicle. *Energies*, 8(7):6820–6840.

[208] Nelder, J. A. and Mead, R. (1965). A simplex method for function minimization. *The Computer Journal*, 7(4):308–313.

[209] Nijholt, A. (1980). *Context-free grammars: covers, normal forms, and parsing*. Number 93 in Lecture Notes in Computer Science. Springer, Berlin, Heidelberg.

[210] Ningfeng, H., Hongyan, G., and Hong, C. (2015). Braking controller design for electrical vehicle using feedback linearization method. In *Proceedings of the 34th Chinese Control Conference (CCC)*, pages 8085–8090, Hangzhou. IEEE.

[211] Nyandoro, O. T., Pedro, J. O., Dahunsi, O. A., and Dwolatzky, B. (2011a). Linear slip control formulation for vehicular anti-lock braking system with suspension effects. *IFAC Proceedings Volumes*, 44(1):4779–4784.

[212] Nyandoro, O. T., Pedro, J. O., Dwolatzky, B., and Dahunsi, O. A. (2011b). State feedback based linear slip control formulation for vehicular antilock braking system. In *Proceedings of the World Congress on Engineering*, volume 1, London.

[213] Nyquist, H. (1932). Regeneration theory. *Bell System Technical Journal*, 11(1):126–147.

[214] Odenthal, D. (2002). *Ein robustes Fahrdynamik-Regelungskonzept für die Kippvermeidung von Kraftfahrzeugen*. PhD thesis, Technical University of Munich.

[215] Odenthal, D. and Blue, P. (2000). Mapping of frequency response performance specifications into parameter space. *IFAC Proceedings Volumes*, 33(14):531–536.

[216] Ogata, K. (2010). *Modern control engineering*. Prentice Hall, Upper Saddle River, NJ, 5 edition.

[217] O'Neill, M. and Ryan, C. (2001). Grammatical evolution. *IEEE Transactions on Evolutionary Computation*, 5(4):349–358.

[218] Orend, R. (2007). *Integrierte Fahrdynamikregelung mit Einzelradaktorik: Ein Konzept zur Darstellung des fahrdynamischen Optimums*. PhD thesis, Friedrich-Alexander-Universität Erlangen-Nürnberg.

[219] Pacejka, H. B. (2005). *Tyre and vehicle dynamics*. Butterworth-Heinemann, Oxford, 2 edition.

[220] Panzani, G., Corno, M., Tanelli, M., Zappavigna, A., Savaresi, S. M., Fortina, A., and Campo, S. (2010). Designing on-demand four-wheel-drive vehicles via active control of the central transfer case. *IEEE Transactions on Intelligent Transportation Systems*, 11(4):931–941.

[221] Park, J. H. and Kim, C. Y. (1999). Wheel slip control in traction control system for vehicle stability. *Vehicle System Dynamics*, 31(4):263–278.

[222] Park, P. (1997). A revisited Popov criterion for nonlinear Lur'e systems with sector-restrictions. *International Journal of Control*, 68(3):461–470.

[223] Parrilo, P. A. and Lall, S. (2003). Semidefinite programming relaxations and algebraic optimization in control. *European Journal of Control*, 9(2-3):307–321.

[224] Perantoni, G. and Limebeer, D. J. N. (2014). Optimal control for a Formula One car with variable parameters. *Vehicle System Dynamics*, 52(5):653–678.

[225] Pinkus, A. (1997). Approximating by ridge functions. *Surface Fitting and Multiresolution Methods*, pages 279–292.

[226] Pinkus, A. (2015). *Ridge functions*, volume 205 of *Cambridge Tracts in Mathematics*. Cambridge University Press, Cambridge, UK.

[227] Piyabongkarn, D., Grogg, J., Yuan, Q., Lew, J., and Rajamani, R. (2006). Dynamic modeling of torque-biasing devices for vehicle yaw control. *SAE Technical Paper 2006-01-1963*.

[228] Piyabongkarn, D., Lew, J., Rajamani, R., and Grogg, J. (2010). Active driveline torque-management systems. *IEEE Control Systems Magazine*, 30(4):86–102.

[229] Piyabongkarn, D., Lew, J., Rajamani, R., Grogg, J., and Yuan, Q. (2007). On the use of torque-biasing systems for electronic stability control: Limitations and possibilities. *IEEE Transactions on Control Systems Technology*, 15(3):581–589.

[230] Pliss, V. A. (1965). *Certain problems in the theory of stability of motion in the whole*. National Aeronautics and Space Administration, Washington, D.C. English translation by W. G. Vogt, original work published in Russian in 1958.

[231] Poli, R., Langdon, W. B., and McPhee, N. F. (2008). *A field guide to genetic programming*. Published via `http://lulu.com`. Available at: `http://www.gp-field-guide.org.uk`. Accessed: 24.05.2018. (With contributions by Koza, J. R.).

[232] Popov, V. M. (1962). Absolute stability of nonlinear systems of automatic control. *Automation and Remote Control*, 22(8):857–875.

[233] Popov, V. M. (1973). *Hyperstability of control systems*. Springer, Berlin.

[234] Prajna, S., Papachristodoulou, A., and Parrilo, P. A. (2002). Introducing SOSTOOLS: A general purpose sum of squares programming solver. In *Proceedings of the 41th Conference on Decision and Control (CDC)*, volume 1, pages 741–746, Las Vegas, NV. IEEE.

[235] Radac, M.-B., Precup, R.-E., Preitl, S., Tar, J. K., Fodor, J., and Petriu, E. M. (2008). Gain-scheduling and iterative feedback tuning of PI controllers for longitudinal slip control. In *2008 IEEE International Conference on Computational Cybernetics*, pages 183–188, Stara Lesna. IEEE.

[236] Rajamani, R., Phanomchoeng, G., Piyabongkarn, D., and Lew, J. Y. (2012). Algorithms for real-time estimation of individual wheel tire-road friction coefficients. *IEEE/ASME Transactions on Mechatronics*, 17(6):1183–1195.

[237] Rall, L. B. (1981). *Automatic differentiation: Techniques and applications*, volume 120 of *Lecture Notes in Computer Science*. Springer, Berlin, Heidelberg.

[238] Rantzer, A. and Megretski, A. (1996). Stability criteria based on integral quadratic constraints. In *Proceedings of the 35th Conference on Decision and Control (CDC)*, volume 1, pages 215–220, Kobe. IEEE.

[239] Ratiroch-Anant, P., Hirata, H., Anabuki, M., and Ouchi, S. (2006). Adaptive controller design for anti-slip system of EV. In *2006 IEEE Conference on Robotics, Automation and Mechatronics*, pages 1–6, Bangkok. IEEE.

[240] Rebouh, S., Kaddouri, A., Abdessemed, R., and Haddoun, A. (2007). Nonlinear control by input-output linearization scheme for EV permanent magnet synchronous motor. In *2007 IEEE Vehicle Power and Propulsion Conference*, pages 185–190, Arlington, TX. IEEE.

[241] Riekert, P. and Schunck, T. E. (1940). Zur Fahrmechanik des gummibereiften Kraftfahrzeugs. *Ingenieur-Archiv*, 11(3):210–224.

[242] Rill, G. (1994). *Simulation von Kraftfahrzeugen*. Vieweg, Braunschweig.

[243] Rill, G. (2007). Wheel dynamics. In *Proceedings of the XII International Symposium on Dynamic Problems of Mechanics (DINAME)*, Ilhabela, SP. ABCM.

[244] Rivera, D. E., Morari, M., and Skogestad, S. (1986). Internal model control. 4. PID controller design. *Industrial and Engineering Chemistry. Process Design and Development*, 25(1):252–265.

[245] Rodríguez, J. M., Meneses, R., and Orús, J. (2013). Active vibration control for electric vehicle compliant drivetrains. In *Proceedings of the 39th Annual Conference of the IEEE Industrial Electronics Society (IECON)*, pages 2590–2595, Vienna. IEEE.

[246] Routh, E. J. (1877). *A treatise on the stability of a given state of motion*. Macmillan, London.

[247] Rundqwist, L. (1991). *Anti-reset windup for PID controllers*. PhD thesis, Lund Institute of Technology, Sweden.

[248] Safonov, M. G. and Kulkarni, V. V. (2000). Zames–Falb multipliers for MIMO nonlinearities. *International Journal of Robust and Nonlinear Control*, 10(11-12):1025–1038.

[249] Sakai, S.-I., Sado, H., and Hori, Y. (2000). Anti-skid control with motor in electric vehicle. In *Proceedings pf the 6th International Workshop on Advanced Motion Control (Cat. No. 00TH8494)*, pages 317–322, Nagoya. IEEE.

[250] Sandberg, I. W. (1964). A frequency-domain condition for the stability of feedback systems containing a single time-varying nonlinear element. *Bell System Technical Journal*, 43(4):1601–1608.

[251] Schröder, D. (2015). *Elektrische Antriebe-Regelung von Antriebssystemen*. Springer, Berlin Heidelberg, 4 edition.

[252] Schuster, H., Westermaier, C., and Schröder, D. (2006). Non-identifier-based adaptive speed control for a two-mass flexible servo system: consideration of stability and steady state accuracy. In *14th Mediterranean Conference on Control and Automation*, pages 1–6, Ancona. IEEE.

[253] Siampis, E., Velenis, E., Gariuolo, S., and Longo, S. (2018). A real-time nonlinear model predictive control strategy for stabilization of an electric vehicle at the limits of handling. *IEEE Transactions on Control Systems Technology*, 26(6):1982–1994.

[254] Sigl, A. and Demel, H. (1990). ASR-traction control, state of the art and some prospects. *SAE Technical Paper 900204*.

[255] Silverman, L. (1969). Inversion of multivariable linear systems. *IEEE Transactions on Automatic Control*, 14(3):270–276.

[256] Slotine, J.-J. E. and Li, W. (1991). *Applied nonlinear control*. Prentice Hall, Englewood Cliffs, NJ.

[257] Smale, S. (1986). Algorithms for solving equations. In *Proceedings of the International Congress of Mathematicians*, volume 1, pages 172–195, Berkeley, CA. World Scientific.

[258] Sontag, E. D. (1989). Smooth stabilization implies coprime factorization. *IEEE Transactions on Automatic Control*, 34(4):435–443.

[259] Sontag, E. D. (2008). Input to state stability: Basic concepts and results. In *Nonlinear and Optimal Control Theory. Lecture Notes in Mathematics*, volume 1932, pages 163–220. Springer, Berlin, Heidelberg.

[260] Soute, I. A. C., van de Molengraft, M. J. G., and Angelis, G. Z. (2001). Using genetic programming to find Lyapunov functions. In *Proceedings of the Genetic and Evolutionary Computation Conference (GECCO)*, pages 449–452, San Francisco, CA.

[261] Stellet, J. E., Giessler, M., Gauterin, F., and León, F. P. (2014). Model-based traction control for electric vehicles. *ATZelektronik Worldwide*, 9(2):44–50.

[262] Åström, K. J. (2002). Control system design, Lecture Notes for ME 155a. Department of Mechanical and Environmental Engineering, University of California, Santa Barbara.

[263] Sussmann, H. J. and Kokotovic, P. V. (1991). The peaking phenomenon and the global stabilization of nonlinear systems. *IEEE Transactions on Automatic Control*, 36(4):424–440.

[264] Syrnik, R. (2015). *Untersuchung der fahrdynamischen Potenziale eines elektromotorischen Traktionsantriebs*. PhD thesis, Technical University of Munich.

[265] Tai, M. and Tomizuka, M. (2000). Robust longitudinal velocity tracking of vehicles using traction and brake control. In *Proceedings of the 6th International Workshop on Advanced Motion Control (Cat. No. 00TH8494)*, pages 305–310, Nagoya. IEEE.

[266] Tan, H.-S. and Chin, Y.-K. (1991). Vehicle traction control: variable-structure control approach. *Journal of Dynamic Systems, Measurement, and Control*, 113(2):223–230.

[267] Tan, H.-S. and Tomizuka, M. (1990). Discrete-time controller design for robust vehicle traction. *IEEE Control Systems Magazine*, 10(3):107–113.

[268] Tibken, B. (2000). Estimation of the domain of attraction for polynomial systems via LMIs. In *Proceedings of the 39th Conference on Decision and Control (CDC)*, pages 3860–3864, Sydney, NSW. IEEE.

[269] Tiganasu, A. and Lazar, C. (2015). LabVIEW traction control dynamic simulator. In *Proceedings of the 19th International Conference on System Theory, Control and Computing (ICSTCC)*, pages 791–796, Cheile Gradistei. IEEE.

[270] Torii, S., Yaguchi, E., Ozaki, K., Jindoh, T., Owada, M., and Naitoh, G. (1986). Electronically controlled torque split system, for 4WD vehicles. *SAE Technical Paper 861349*.

[271] Tseng, C.-S., Chen, B.-S., and Uang, H.-J. (2001). Fuzzy tracking control design for nonlinear dynamic systems via TS fuzzy model. *IEEE Transactions on Fuzzy Systems*, 9(3):381–392.

[272] Uzunsoy, E. (2018). A brief review on fuzzy logic used in vehicle dynamics control. *Journal of Innovative Science and Engineering (JISE)*, 2(1):1–7.

[273] Vaezi, M., Hesam, E. S. J., and Anwar, S. (2015). IMC-PID traction control system for an automobile via engine torque control. In *Proceedings of the IEEE International Conference on Industrial Technology (ICIT)*, pages 296–302, Seville. IEEE.

[274] Van Zanten, A. T. (2002). Evolution of electronic control systems for improving the vehicle dynamic behavior. In *Proceedings of the 6th International Symposium on Advanced Vehicle Control (AVEC)*, pages 7–15, Hiroshima.

[275] Van Zanten, A. T., Erhardt, R., and Pfaff, G. (1995). VDC, the vehicle dynamics control system of Bosch. *SAE Transactions*, 104:1419–1436.

[276] Van Zanten, A. T., Erhardt, R., Pfaff, G., Kost, F., Hartmann, U., and Ehret, T. (1996). Control aspects of the Bosch-VDC. In *Proceedings of the 3rd International Symposium on Advanced Vehicle Control (AVEC)*, pages 576–607, Aachen.

[277] Vasiljevic, G., Griparic, K., and Bogdan, S. (2012). Slip-based traction control system with an on-line road condition estimation for electric vehicles. In *Proceedings of the IEEE International Conference on Control Applications*, pages 395–400, Dubrovnik. IEEE.

[278] Vasiljevic, G., Griparic, K., and Bogdan, S. (2013). Experimental testing of a traction control system with on-line road condition estimation for electric vehicles. In *21st Mediterranean Conference on Control and Automation*, pages 296–302, Platanias. IEEE.

[279] Warthenpfuhl, S., Tibken, B., and Mayer, S. (2010). An interval arithmetic approach for the estimation of the domain of attraction. In *Proceedings of the IEEE International Symposium on Computer-Aided Control System Design (CACSD)*, pages 1999–2004, Yokohama. IEEE.

[280] Willems, J. C. (1972). Dissipative dynamical systems part I: General theory. *Archive for Rational Mechanics and Analysis*, 45(5):321–351.

[281] World Health Organization (2015). *Global status report on road safety 2015*. WHO Press, Geneva.

[282] Wu, L., Gou, J., Wang, L., and Zhang, J. (2015). Acceleration slip regulation strategy for distributed drive electric vehicles with independent front axle drive motors. *Energies*, 8(5):4043–4072.

[283] Yakubovich, V. A. (1977). S-procedure in nonlinear control theory. *Vestnik, Leningrad University*, 4:73–93. English translation, original work published 1971.

[284] Yakubovitch, V. A. (1962). The solution of some matrix inequalities encountered in automatic control theory. In *Doklady Akademii Nauk SSSR*, volume 143, pages 1304–1307.

[285] Yeap, K. Z. and Müller, S. (2016). Characterising the interaction of individual-wheel drives with traction by linear parameter-varying model: a method for analysing the role of traction in torsional vibrations in wheel drives and active damping. *Vehicle System Dynamics*, 54(2):258–280.

[286] Yi, J., Alvarez, L., and Horowitz, R. (2002). Adaptive emergency braking control with underestimation of friction coefficient. *IEEE Transactions on Control Systems Technology*, 10(3):381–392.

[287] Yin, D., Oh, S., and Hori, Y. (2009). A novel traction control for EV based on maximum transmissible torque estimation. *IEEE Transactions on Industrial Electronics*, 56(6):2086–2094.

[288] Zames, G. (1966). On the input-output stability of time-varying nonlinear feedback systems part one: Conditions derived using concepts of loop gain, conicity, and positivity. *IEEE Transactions on Automatic Control*, 11(2):228–238.

[289] Zames, G. and Falb, P. L. (1968). Stability conditions for systems with monotone and slope-restricted nonlinearities. *SIAM Journal on Control*, 6(1):89–108.

[290] Zech, A., Eberl, T., Marx, C., and Müller, S. (2019). Analysis of the potential of a new control approach for traction control considering a P2-Hybrid drivetrain. In *9th International Munich Chassis Symposium 2018*, pages 285–303, Munich. Springer Vieweg, Wiesbaden.

[291] Zech, A., Eberl, T., and Müller, S. (2017). Analyse einer neuen kaskadierten Reglerstruktur für die Antriebsschlupfbegrenzung hochdynamischer Fahrzeugantriebe. In *8. VDI/VDE Fachtagung, "AUTOREG 2017 - Automatisiertes Fahren und vernetzte Mobilität"*, volume 2292 of *VDI-Berichte*, pages 287–297, Berlin. VDI-Verlag, Düsseldorf.

[292] Zhang, C. and Ordonez, R. (2007). Numerical optimization-based extremum seeking control with application to ABS design. *IEEE Transactions on Automatic Control*, 52(3):454–467.

[293] Zhao, J., Zhang, J., and Zhu, B. (2016). Coordinative traction control of vehicles based on identification of the tyre-road friction coefficient. *Proceedings of the Institution of Mechanical Engineers, Part D: Journal of Automobile Engineering*, 230(12):1585–1604.

[294] Zhou, H., Jia, F., Jing, H., Liu, Z., and Güvenç, L. (2018). Coordinated longitudinal and lateral motion control for four wheel independent motor-drive electric vehicle. *IEEE Transactions on Vehicular Technology*, 67(5):3782–3790.

[295] Zhou, L., Xiong, L., and Yu, Z. P. (2013). A research on anti-slip regulation for 4WD electric vehicle with in-wheel motors. In *Instruments, Measurement, Electronics and Information Engineering*, volume 347 of *Applied Mechanics and Materials*, pages 753–757. Trans Tech Publications.

[296] Zubov, V. I. (1964). *Methods of A.M. Lyapunov and their application.* P. Noordhoff, Groningen.

Supervised Student Projects

[297] Degel, W. (2018). Nonlinear multi-slip control for scalable driving concepts. Master's thesis, Technical University of Munich.

[298] Meier, A. (2017). Identifkation nichtlinearer Zusammenhänge mittels Genetischer Programmierung. Internship report, Technical University of Munich.

[299] Meier, A. (2018). Klassifizierung von dynamischen Fahrzuständen mittels Genetic Programming. Master's thesis, Technical University of Munich.

Own Publications

[300] Reichensdörfer, E., Degel, W., Odenthal, D., and Wollherr, D. (2019a). Nonlinear traction control design, stability analysis and experiments for vehicles with on-demand 4WD torque bias systems. In *Proceedings of the 58th Conference on Decision and Control (CDC)*, pages 6669–6674, Nice. IEEE.

[301] Reichensdörfer, E., Odenthal, D., and Wollherr, D. (2017). Grammatical evolution of robust controller structures using Wilson scoring and criticality ranking. In *European Conference on Genetic Programming*, volume 10196 of *Lecture Notes in Computer Science*, pages 194–209, Amsterdam. Springer, Cham.

[302] Reichensdörfer, E., Odenthal, D., and Wollherr, D. (2018). Nonlinear control structure design using grammatical evolution and Lyapunov equation based optimization. In *Proceedings of the 15th International Conference on Informatics in Control, Automation and Robotics - Volume 1: ICINCO*, pages 55–65, Porto. INSTICC, SciTePress, Setúbal.

[303] Reichensdörfer, E., Odenthal, D., and Wollherr, D. (2019b). Automated nonlinear control structure design by domain of attraction maximization with eigenvalue and frequency domain specifications. In *Informatics in Control, Automation and Robotics*, volume 613 of *Lecture Notes in Electrical Engineering*, pages 118–141. Springer, Cham.

[304] Reichensdörfer, E., Odenthal, D., and Wollherr, D. (2020a). Engine-based input-output linearization for traction control systems. *IFAC-PapersOnLine*, 53(2):14055–14060.

[305] Reichensdörfer, E., Odenthal, D., and Wollherr, D. (2020b). On the stability of nonlinear wheel-slip zero dynamics in traction control systems. *IEEE Transactions on Control Systems Technology*, 28(2):489–504. Publication year 2018.

[306] Reichensdörfer, E., Odenthal, D., and Wollherr, D. (2021). On the frontier between Kalman conjecture and Markus-Yamabe conjecture. *IEEE Control Systems Letters*, 5(4):1309–1314.

[307] Zech, A., Eberl, T., Reichensdörfer, E., Odenthal, D., and Müller, S. (2018). Method for developing tire slip controllers regarding a new cascaded controller structure. In *Proceedings of the 14th International Symposium on Advanced Vehicle Control (AVEC)*, pages 302–307, Beijing.